

OBSERVING AND SIMULATING GALAXY EVOLUTION

- from X-ray to millimeter wavelengths

Dissertation submitted for the degree of
PHILOSOPHIÆ DOCTOR

to the PhD School of The Faculty of Science, University of Copenhagen

on April 10 2015, by

Karen Pardos Olsen

Supervisors: *Sune Toft* and *Thomas Greve*



Dark Cosmology Centre



Cover art:

Nut, goddess of the sky in ancient Egyptian religion. Contrary to most other religions, the sky was feminine and her brother, Geb, personified the Earth. At dusk, Nut would swallow the sun god, Ra, who would pass through her belly during the night and be reborn at dawn. Sometimes she was depicted as a cow, but most of the time as a star-covered nude woman arching over, and protecting, the Earth.

OBSERVING AND SIMULATING GALAXY EVOLUTION

- from X-ray to millimeter wavelengths

ABSTRACT

It remains a quest for modern astronomy to answer what main mechanisms set the star formation rate (SFR) of galaxies. Massive galaxies present a good starting point for such a quest due to their relatively easy detection at every redshift. Since stars form out of cold and dense gas, a comprehensive model for galaxy evolution should explain any observed connection between SFR and the amount and properties of the molecular gas of the interstellar medium (ISM). In proposed models of that kind, an active galactic nucleus (AGN) phase is often invoked as the cause for the decrease or cease of star formation. This thesis consists of models and observations of gas and AGNs in massive galaxies at $z \sim 2$, and how they may affect the overall SFR and the subsequent evolutionary trajectory of massive galaxies to $z = 0$.

In this work, a new method and code is presented; Simulator of GALaxy Millimeter/submillimeter Emission (SÍGAME), the aim of which is to improve our understanding of the connection between emission lines from the gas and the underlying ISM physics. By post-processing the outputs of cosmological simulations of galaxy formation with sub-grid physics recipes, SÍGAME divides the ISM into different gas phases and derives density and temperature structure, with locally resolved radiation fields. In the **first study**, SÍGAME is combined with the radiative transfer code LIME to model the spectral line energy distribution (SLED) of the CO molecule. A CO SLED close to that of the Milky Way is found for normal star-forming massive galaxies at $z \sim 2$, but 50 % smaller CO-H₂ conversion factors, with the latter decreasing towards the center of each model galaxy. In a **second study**, SÍGAME is adapted to model the fine-structure line of singly ionized carbon, [CII] at 158 μm , the most powerful emission line of neutral ISM. Most [CII] emission in the same type of $z \sim 2$ galaxies is revealed to trace mainly the molecular part of their ISM. The observed relation between [CII] luminosity and SFR at $z > 0.5$ is reproduced and a similar relation is established on kpc scales for the first time theoretically.

A **third study** uncovers the presence of AGNs among massive galaxies at $z \sim 2$, and sheds light on the AGN-host co-evolution by connecting the fraction and luminosity of AGNs with galaxy properties. By analyzing a large survey in X-ray, AGNs of high and low X-ray luminosity are extracted among massive galaxies at $z \sim 2$ via AGN classification methods and stacking techniques in X-ray. It is found that about every fifth massive galaxy, quenched or not, contain an X-ray luminous AGN. Interestingly, an even higher fraction of low-luminosity AGNs reside in the X-ray undetected galaxies, and preferentially in the quenched ones, lending support to the importance of AGNs in impeding star formation during galaxy evolution.

CONTENTS

Abstract	iii
Contents	iv
1 Background	1
1.0.1 Setting the scale	1
1.0.2 The cosmic web of galaxies	2
1.1 ‘Normal star-forming galaxies’	2
1.1.1 The turning point at $z \sim 2$	4
1.1.2 The case of ‘massive galaxies’	4
1.2 The Interstellar Medium (ISM)	5
1.2.1 Chemical composition	6
1.2.2 Distribution and density	7
1.2.3 Thermal state	8
1.3 The Active Galactic Nucleus (AGN)	11
1.3.1 Unification models	11
1.4 The ‘spectral fingerprint’ of a galaxy	12
1.5 An exciting time for observations	14
1.5.1 Radio Telescopes	14
1.5.2 X-ray Telescopes	15
1.6 Galaxy simulations	17
1.6.1 ‘Zoom-in’ simulations	18
1.6.2 The calibration to $z = 0$	19
1.7 References	19
2 Introduction to this thesis	21
2.1 Evolution of massive galaxies across cosmic time	21
2.1.1 High-redshift massive galaxy populations	21
2.1.2 Observing galaxies at $z > 4$ via their gas emission lines	23
2.1.3 The red and blue galaxies	23
2.1.4 Quenching star formation	24
2.1.5 Connecting the dots	25
2.2 This thesis	27
2.2.1 All eyes on the gas	28
2.2.2 Quick summary of my projects	30
2.3 References	30

3	CO emission lines from galaxies	35
3.1	Probing the molecular gas	35
3.2	Observations of CO line emission from different types of galaxies at $z \gtrsim 2$	36
3.2.1	The X_{CO} factor	36
3.3	Modeling of CO emission lines	37
4	Simulating CO line emission from massive star-forming galaxies at $z = 2$ (Paper I)	40
4.1	Aim of this project	40
4.2	Cosmological Simulations	41
4.2.1	SPH simulations	41
4.2.2	The model galaxies	41
4.3	Modeling the ISM with SÍGAME	45
4.3.1	Methodology overview	45
4.3.2	The Warm and Cold Neutral Medium	45
4.3.3	HI to H ₂ conversion	47
4.3.4	Structure of the molecular gas	49
4.3.5	Radiative transfer of CO lines	56
4.4	Simulating massive $z = 2$ main sequence galaxies	58
4.4.1	Total molecular gas content and H ₂ surface density maps	58
4.4.2	CO line emission maps and resolved excitation conditions	60
4.4.3	The CO-to-H ₂ conversion factor	61
4.4.4	Global CO line luminosities and spectral line energy distributions	62
4.5	Testing different ISM models	65
4.6	Comparison with other models	66
4.7	Summary	70
4.8	References	72
5	[CII] line emission from galaxies	75
5.1	Probing the neutral and ionized gas	75
5.2	Observations of [CII] emission in galaxies at high and low redshift	75
5.2.1	The [CII] deficit	76
5.2.2	Contributing gas phases to the [CII] emission	77
5.2.3	[CII] as a star formation rate tracer	77
5.3	Modeling [CII] emission	78
6	Understanding the $L_{[\text{CII}]}$-SFR relation with simulations (Paper II)	79
6.1	Aim of this project	79
6.2	Methodology overview	79
6.3	SPH Simulations	81
6.3.1	SPH simulations of $z = 2$ MS galaxies	82
6.4	Modeling the ISM	82
6.4.1	GMCs	84
6.4.2	The ionized gas	90
6.5	The [CII] line emission	90
6.6	Results and discussion	92

6.6.1	Radial [CII] luminosity profiles	92
6.6.2	The integrated $L_{\text{[CII]}} - \text{SFR}$ relation	97
6.6.3	The resolved $\Sigma_{\text{[CII]}} - \Sigma_{\text{SFR}}$ relation	99
6.6.4	Physical underpinnings of the $L_{\text{[CII]}} - \text{SFR}$ relation	101
6.7	Comparing with other [CII] simulations	103
6.8	Conclusion	107
7	Outlook	109
7.1	Improvements on SÍGAME	109
7.1.1	Dust temperatures with a radiative transfer code	109
7.1.2	Modeling of asymmetric GMCs	109
7.1.3	Including heating by X-rays and turbulent dissipation	110
7.2	Going to higher redshift	110
7.2.1	The evolution of X_{CO} with redshift	110
7.2.2	The full calibration to normal galaxies at $z \sim 2$	110
7.2.3	Galaxies during the epoch of re-ionization	110
7.3	References	112
II	THE AGN-GALAXY CO-EVOLUTION AT $z \sim 2$	117
8	How to detect an AGN	119
8.1	Dissecting the X-ray emission from an AGN	120
8.1.1	The AGN fraction at $z \gtrsim 2$ from observations in X-ray	122
9	On the prevalence of AGN at $z \sim 2$ (Paper III)	123
9.1	Aim of this project	123
9.2	Our method and galaxy sample	123
9.2.1	X-ray data and stacking analysis	124
9.2.2	Luminous AGN Identification	126
9.2.3	X-ray Inferred SFR	127
9.3	An overwhelmingly large AGN population	129
9.3.1	Luminous AGN Fraction	129
9.3.2	Importance of Low-luminosity AGNs	130
9.3.3	Contribution from Hot Gas Halos	131
9.3.4	Quenching of Star Formation by AGNs?	133
9.4	Conclusions	134
10	Outlook	136
10.1	The AGN-morphology connection	136
10.2	Direct observations of AGN feedback	137
10.3	Future directions: Discerning variability with time	137
10.4	References	139
	Summary	142
	Sammenfatning	144

Acknowledgments	146
Appendices	147
A Appendix to Chapter 4	149
A.1 Thermal balance of the atomic gas phase	149
A.2 Thermal balance of the molecular gas phase	150
A.3 GMC models	152
A.4 Testing SÍGAME on MW-like galaxies	158
B Appendix to Chapter 6	161
B.1 Density of singly ionized carbon	161
B.2 Electron fraction	163
B.3 [CII] excitation and emission	163
B.4 References	167

1

BACKGROUND

*Do not feel lonely, the entire Universe is inside you. - Rumi*¹

While Europeans were taking their medieval nap, Arabs carried astronomy forward. Not only did they collect and combine the astronomy from e.g. Greece, Egypt and India into one mathematical language, they also made contributions to the Ptolemaic system and created instruments such as celestial globes, astrolabs and large observatories. Their motivation was mostly a practical one of wanting to determine prayer times and the direction to Mecca to high accuracy. But what might the Arabs have thought for themselves while looking up at the stars? While this will remain unknown, we now know that most of that twinkling in the sky comes from our home, the Milky Way. Stars in the Milky Way are organized in a slowly rotating disk of spiral arms, embraced by an additional spheroidal component, the bulge. If you are lucky, you can even see a diffuse and ‘milky’ band going across the night sky, and that is the combined light from millions of unresolved stars in the Milky Way disk. What you cannot see with your naked eye, is all the gas and dust out of which new stars are born. Nor can you see the dark matter, emitting no light at all and believed to inhabit a large sphere embracing the Milky Way entirely. Such assemblies of baryonic and dark matter we call galaxies, and the Universe is full of them. Understanding how these galaxies form and evolve while making room for life², is one of the fundamental aims of modern astronomy. This thesis is about the gas and the black hole component in galaxies. A theoretical model is developed to simulate the amount and state of gas in galaxies as well as its light emission in the infrared. A separate study uncovers the fraction of massive galaxies dominated by the powerful energetics associated with their central black hole, during an important cosmic epoch. Together, these projects offer a better view of galaxy evolution and will be useful for predicting and interpreting future observations.

1.0.1 SETTING THE SCALE

The finite speed of light is of great value to astronomers, because it allows us to look back in time. In fact, astronomical distances, both within and between galaxies, are measured in light years (ly; the distance light can travel in 1 year) or parsecs (1 pc = 3.26 ly). On top of that, the expansion of the Universe causes light to ‘stretch’ as it traverses the great expanses between galaxies. The amount of ‘stretching’ serves as a label on every photon, saying how far it has been traveling. We call this ‘the redshift of light’, z , and often use it as a measure of

¹Persian poet and Sufi mystic of the 13th century

²In at least one case

distance from us or age of the Universe. Fig. 1.1 provides a quick calibration between age of the Universe and redshift.

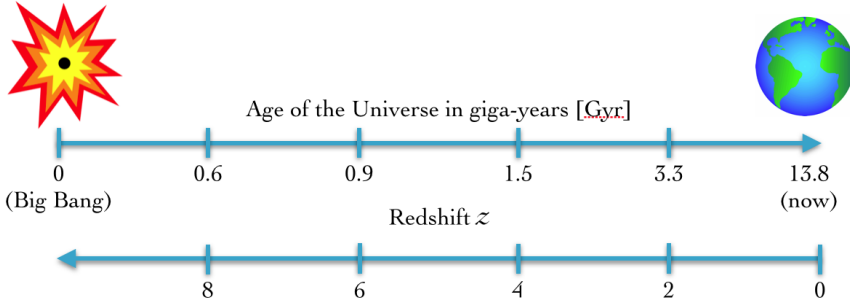


Figure 1.1 A scale comparing age of the Universe with redshift, across its total lifespan of ~ 13.8 Gyr. Note that the redshift drops with age in an exponential-like behaviour, meaning that the Universe reached half its age at quite low redshift, $z \approx 0.7$. Photons decoupled from matter at $z = 1,100$, only $\sim 378,000$ yr after the Big Bang, and that is as far back as we can observe. The ages have been calculated according to the now generally accepted spatially flat Λ CDM cosmology model, that describes the composition of the Universe with just six parameters (fixed here to the most recent results by the Planck Collaboration et al., 2015).

1.0.2 THE COSMIC WEB OF GALAXIES

Galaxies are not evenly distributed in space, but rather follow the underlying cosmic web of dark matter that attracts the gas via gravitation. Fig. 1.2 is a map carried out by Colless et al. (2001) of galaxies close to the MW and out to $z \approx 0.3$ over a total sky area of 2000 deg^2 or almost 5% of the total sky. Like a Swiss cheese, there are regions with very low density of galaxies (so-called voids) and other regions with many galaxies living close together (clusters) connected by filaments and sheets. It has been confirmed by observations, that in the latter, highly concentrated regions, galaxies are prone to interact and possibly merge into even bigger ones. Galaxies are therefore not isolated systems that go about their own business, but are constantly influenced by their surroundings via e.g. mergers, tidal strippings and gas inflow from the Intra Cluster Medium (ICM). In some of the following sections we will describe their internal components and inner workings, treating them as isolated systems, but one should never forget that galaxies in general interact with their surroundings.

1.1 ‘NORMAL STAR-FORMING GALAXIES’

Galaxies come in a great variety from containing few stars (dwarf galaxies) to containing many stars (massive galaxies), from compact to extended, from star-forming to inactive (quiescent in the following) and with different compositions of stars, gas, dust and dark matter. That said, most of them follow a basic rule: The more stars they have, the more stars they form. In other words, plotted in a star formation rate (SFR) vs. stellar mass (M_*) diagram, most galaxies fall on a power law relation called the ‘main sequence’ (MS). The evolution of this sequence with cosmic time has been investigated recently by Speagle et al. (2014) who compiled 25 studies from the existing literature to find that the MS evolves towards higher SFR as we look back in time. This is shown in Fig. 1.3 with best fits to the observations at different redshifts, without plotting individual galaxies for the sake of simplicity.

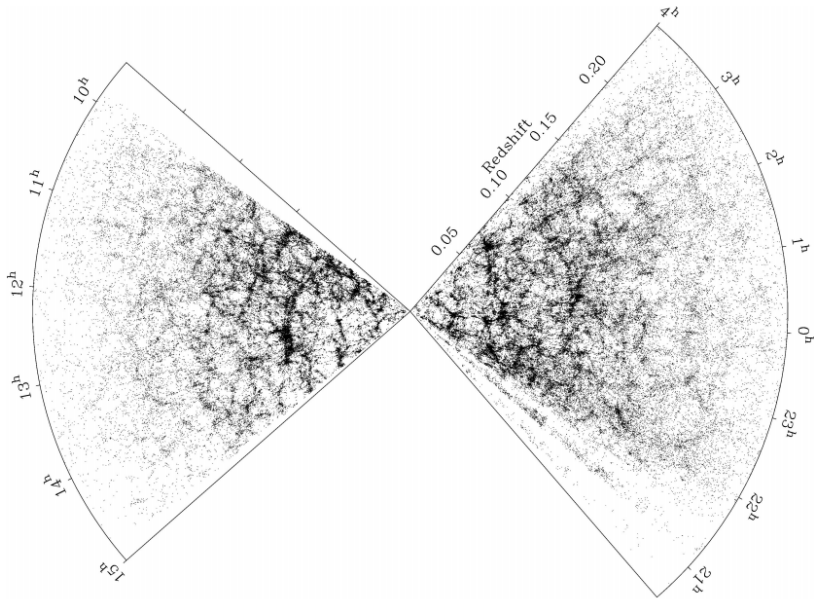


Figure 1.2 Map of galaxies around us and out to $z \approx 0.3$ from the 2dF Galaxy Redshift Survey by (Colless et al., 2001) who studied two strips on the sky, one in the northern (left) and one in the southern (right) hemisphere.

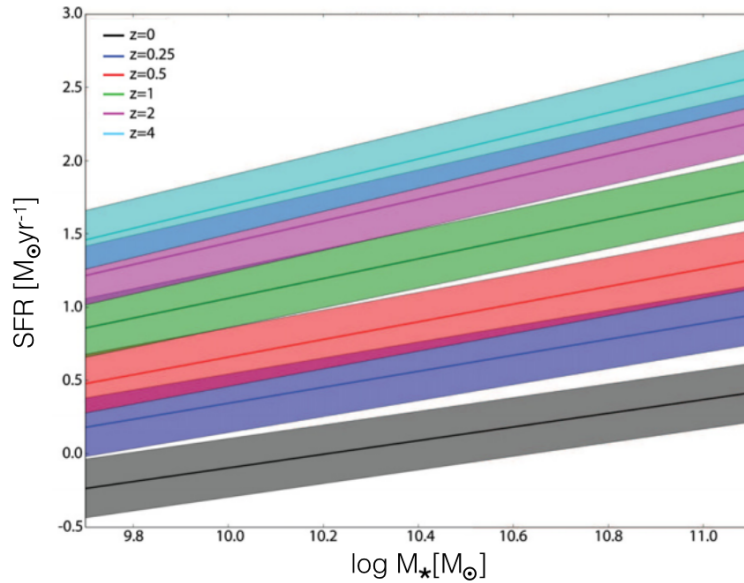


Figure 1.3 Main sequence evolution. Power law fits to star-forming galaxies in different redshift bins from the compilation study of Speagle et al. (2014). Shaded areas show an estimated ‘true’ scatter of 0.2 dex.

Hence, like in crazy adolescent years, back in the day galaxies used to produce stars at much higher rates. The slope of the SFR- M_* relations shown in Fig. 1.3 is also called the specific star formation rate, $SSFR = SFR/M_*$, and with very few galaxies at high-redshift, it is still hard to say whether the SSFR continues to rise with redshift or reaches a ‘plateau’ (Behroozi et al.,

1.1.1 THE TURNING POINT AT $z \sim 2$

If one measures SFR per volume, there is a maximum in cosmic SFR density, SFRD, at $z \sim 2$ after which it starts to decline again as shown in Fig. 1.4. The epoch around $z \sim 2$, or about 10 billion years ago, is therefore an interesting one of phase change and one that we are just now beginning to uncover with modern telescopes (see Section 1.5).

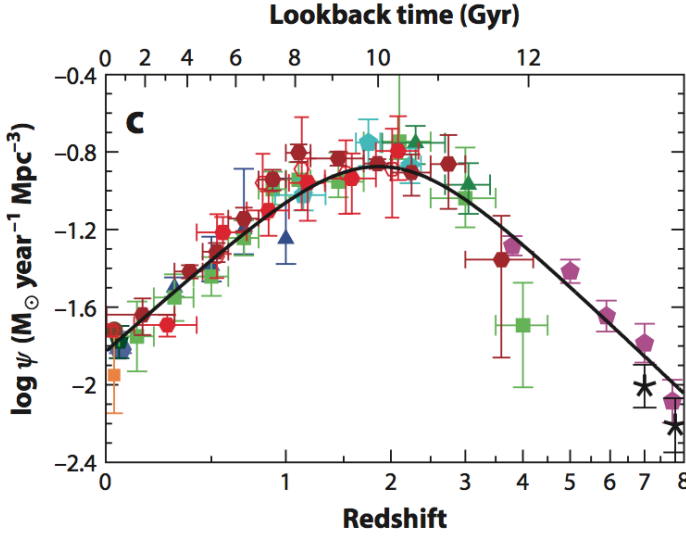


Figure 1.4 The evolution of cosmic SFR density (SFRD) with redshift from the review of Madau & Dickinson (2014).

1.1.2 THE CASE OF ‘MASSIVE GALAXIES’

To understand how galaxies evolved since their formation some million years after the Big Bang, we need observations of all types of galaxies from high redshift until now. This task is impeded by the difficulty of resolving a galaxy very far away, because galaxies start to appear very dim and small. The degree at which a large survey (such as the 2dF Survey in Fig. 1.2) is capturing all galaxies of a certain mass, is referred to as ‘completeness’. The state-of-the-art Cosmic Assembly Near-IR Deep Extragalactic Legacy Survey (CANDELS), carried out with the Hubble Space Telescope (HST), looks all the way back to the high-redshift universe ($z \sim 8$) with observations of different exposure time (depth). But even in the deep fields of GOODS-South/North, a typical lower mass limit of 10^{10} M_\odot must be adopted to ensure 100 % completeness for studies going out to $z \sim 2.5$ (see e.g. Wuyts et al., 2012). In the smaller Ultra Deep Fields (UDFs), CANDELS can reach the same mass out to $z \sim 3$ due to longer exposure times³ (Hartley et al., 2013). But galaxies with stellar masses below these limits may exist that these surveys are incapable of detecting with available telescopes and integration time. For this reason, massive (i.e. with high stellar mass) galaxies represent a convenient sample, because

³see http://candels.ucolick.org/survey/files/ferguson_STUC1102_v2.pdf

they are relatively easy to detect at all redshifts. My work concerns mainly massive galaxies, so this denomination will occur frequently in the present dissertation and the exact mass range will always be defined for each particular study.

1.2 THE INTERSTELLAR MEDIUM (ISM)

Let's return for a moment to the sparkling stars that you may observe on a clear night. What you can't see with your naked eye is all the material filling out the vast spaces in between those stars, the Interstellar Medium or ISM. But it is out of this mixture of gas and dust that stars are born, the stars that expel heavier elements during their explosive deaths, thereby providing the universe with the atoms that we are ultimately made of. Carl Sagan once said that *'we are made of starstuff'*, yet stars would never have been formed had it not been for the gas that was already there. Fig. 1.5 shows an example of what surprises lie in wait once telescopes are tuned to the frequencies at which the gas lights up in the ISM. The blue image is made of stellar light emission from the Antennae Galaxies – two colliding spiral galaxies about 70 million ly away from us – and the red image is a composite of observations with the interferometric array ALMA (to be described in section 1.5).

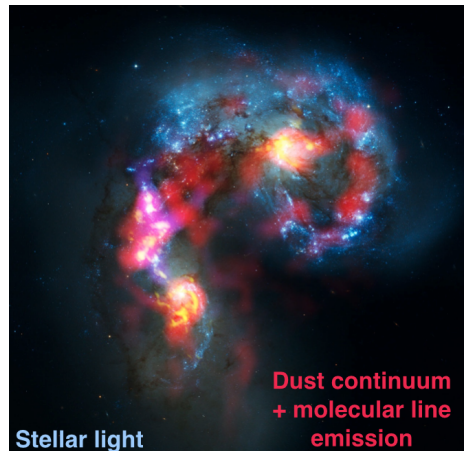


Figure 1.5 The Antennae Galaxies, credit: NASA/ESA HST for the optical image, and ALMA (ESO/NAOJ/NRAO) first science results for the observations of gas and dust at sub-mm wavelengths.

Whether a cloud of gas in a galaxy can fragment and collapse to a density that allows fusion, i.e. the ignition of a new star, depends on the properties of that gas. The efficiency by which the gas forms stars is characterised by the gas depletion time, t_{dep} :

$$t_{\text{dep}} = m_{\text{gas}}/\text{SFR} \quad (1.1)$$

that is, the time it would take to use up a cloud of mass m_{gas} if the current SFR stayed constant. Naively, one might expect that t_{dep} would be close to the time it takes a cloud to collapse onto itself under the influence of gravity only, also called the free-fall time, t_{ff} . But observations show that t_{dep} is typically 1-3 orders of magnitude longer than t_{ff} , requiring the existence of processes that slow down the star formation rate resulting from pure gravitation. These processes are broadly gathered under the term 'feedback' from either nearby star formation (see review by Krumholz et al., 2014) or the powerful radiation from an Active Galactic Nucleus (see Section 1.3.1).

Feedback on star formation is a whole topic in itself under fierce exploration with observations and theoretical models. An example of one strong type of feedback, is the ionizing field from young stars. Stars of masses $> 10 M_{\odot}$ emit large quantities of ionizing photons creating large bubbles of expanding hot, ionized gas, that can hit nearby cold clouds and prevent them from collapsing in a type of explosive feedback (Krumholz et al., 2014; Dale et al., 2012).

However, recent simulations by Dale et al. (2012) show that the effect of expanding regions of ionized gas in turbulent clouds depends strongly on the escape velocities in the gas. Fig. 1.6 illustrates, with snapshots from their simulations, how photoionization only has a significant impact in clouds of escape velocities, as set by the cloud mass and size, below about 10 km s^{-1} . This example shows that feedback from star formation involves many intercoupled processes. Other types of stellar feedback include those of protostellar outflows, radiation pressure from massive stars, winds from hot stars, supernovae explosions and the mere thermal energy injected into the gas as gravitational potential energy is released during the collapse. In addition, nature most likely combines these mechanisms with the influence of magnetic fields (e.g. Price & Bate, 2009).

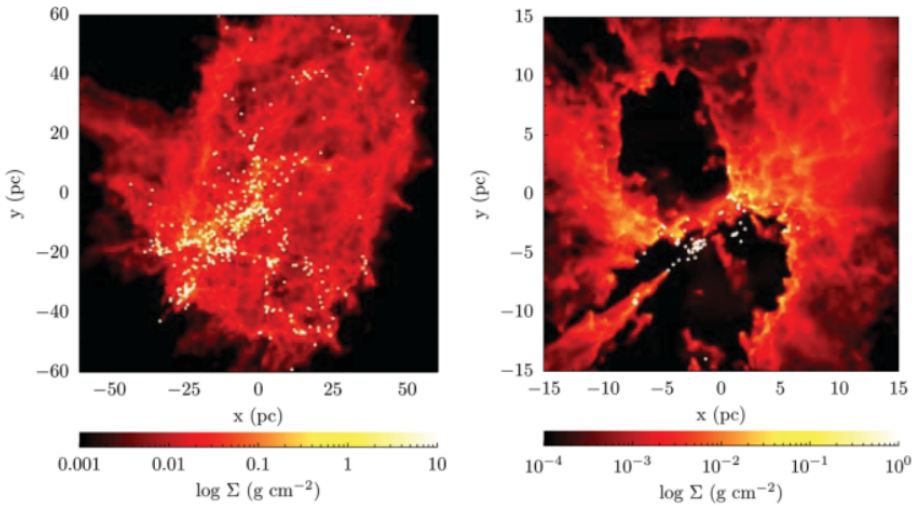


Figure 1.6 *Left*: Column density map of a simulation of star cluster formation in a gas cloud with escape velocity $> 10 \text{ km s}^{-1}$. White dots represent individual stars. *Right*: The same but for an escape velocity of $< 10 \text{ km s}^{-1}$, in which case star formation is suppressed. Adapted from Krumholz et al. (2014).

In principle, being able to observe the composition, turbulence, temperature, density and magnetic fields of the same gas cloud to high angular precision, would provide the building blocks for uniquely defining star formation on small ($< 50 \text{ pc}$) scales. Therefore, *being able to characterise the gas in terms of these properties will help explain why some massive galaxies at $z \sim 2$ are quiescent while others are even more star-forming than their local counterparts.*

1.2.1 CHEMICAL COMPOSITION

Before galaxies formed, the universe was pervaded by a primordial gas of only 4 atomic species; hydrogen (H), helium (He) and a trace of lithium (Li) and beryllium (Be), as well as a few of their isotopes. These were created from about 10 seconds to 20 minutes after the Big Bang⁴, but any elements heavier than Lithium and Beryllium had to wait for the formation of the first stars a few hundreds of million years later, in order to be produced. Today, hydrogen and helium continue to be the dominant species found in the local ISM of the MW, with gas mass fractions

⁴see <http://www.astro.ucla.edu/~wright/BBNS.html>

of $\sim 71.5\%$ and $\sim 27.1\%$ respectively, compared to only 1.4% of heavier elements denoted ‘metals’ (e.g. Przybilla et al., 2008).

All atoms in the ISM can exist in atomic form or be ionized to several degrees or be combined in molecules of increasing complexity (see Tielens 2013 for an overview of just how complicated these molecules can get). For the general life of a galaxy however, only a subset of these species needs to be considered for the structure and thermal state of the ISM relevant for star formation, as we shall see in the next subsections.

1.2.2 DISTRIBUTION AND DENSITY

Stars form generally in clusters as the simulated one depicted in Fig. 1.6 (Krumholz et al., 2014). Such constructions of dense knots and long filaments are collectively called Giant Molecular Clouds (GMCs) and are observed to have radii from about 5 to ~ 100 pc in the MW and local galaxies (Blitz et al., 2007). From measuring the broadening of emission lines from the gas and converting those into velocity dispersions, one can get an estimate of the mass, by assuming the cloud to be in virial equilibrium (Roman-Duval et al., 2010):

$$M_{\text{vir}} = \frac{1.3\sigma_v^2 R}{G} \Rightarrow M_{\text{vir}}[M_\odot] = 905 \cdot (\sigma_{v,1D}[\text{km s}^{-1}])^2 \cdot R[\text{pc}] \quad (1.2)$$

This was done by for example Blitz et al. (2007), who found the mass spectrum shown to the left in Fig. 1.7, the data of which can be fitted with a power law of slope -1.71 in the outer MW.

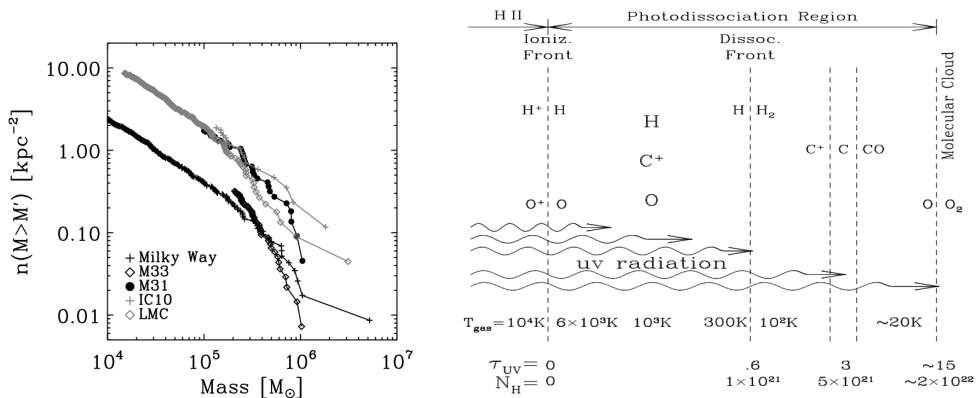


Figure 1.7 *Left*: Mass spectrum of GMCs in the MW and local galaxies (Blitz et al., 2007). *Right*: Schematic overview of the chemical stratification taking place in the PDR of a GMC, from Papadopoulos & Thi (2013).

The reason why all gas in the galaxy is not neutral and forming molecules, is mainly the strong far-ultraviolet (FUV) radiation field from young stars, which ionizes the gas and creates a stratification of the ISM as illustrated on the right-hand side of Fig. 1.7. The region of stratified layers is also referred to as the Photodissociation Region (PDR). In addition to ionizing, the FUV radiation penetrates into the gas and determines its thermal and chemical state. This results in a set of distinct phases of the ISM, that have been observationally identified and are listed in Table 1.1. After the dense, molecular gas, comes the warm and cold neutral medium, often collectively named ‘WCNM’, and finally, the least dense, ionized gas (HII).

If we take a look at the densities listed in Table 1.1, it is clear that the ISM is in general *very*

Chemical state	Gas phase	n [cm ⁻³]	T_k [K]
Molecular gas (17% of total mass)	Diffuse H ₂	~ 100	~ 50
	Dense H ₂	$10^3 - 10^6$	$10 - 50$
Atomic gas (60% of total mass)	Warm HI (WNM)	~ 0.6	~ 5000
	Cold HI (CNM)	30	~ 100
Ionized gas (23% of total mass)	Coronal gas (HIM)	0.004	$10^{5.5}$
	HII gas	$0.3 - 10^4$	10^4

Table 1.1 Gas mass fractions, densities and temperatures of the different phases of interstellar gas, adapted from Draine (2011).

diffuse. You would need a cube of $700 \times 700 \times 700$ meters of the densest H₂ gas phase (with density $n_H \sim 10^6$ cm⁻³) in order to have the same gas mass as present in 1 cm³ of air at sea level on Earth (with density $\rho \approx 1.2$ kg m⁻³).

Gas mass and SFR are related via the Kennicutt-Schmidt (KS) law, which is an observed tight relation between surface density of SFR, Σ_{SFR} , and gas, Σ_{gas} . As will be explained in further detail in Part I, the line emission from the CO molecule is particularly well suited for estimating the total gas mass. The KS-law for low and high- z star-forming galaxies was estimated by Genzel et al. (2010) using a large data base of CO line observations and SFRs based on several SFR indicators:

$$\log \Sigma_{\text{SFR}} [\text{M}_{\odot} \text{ yr}^{-1} \text{ kpc}^{-2}] = 1.17 \times \log \Sigma_{\text{gas}} [\text{M}_{\odot} \text{ pc}^{-2}] - 3.48 \quad (1.3)$$

However, recent observations show that this correlation might break down already on scales of ~ 100 pc (Xu et al., 2015).

1.2.3 THERMAL STATE

The thermal state of the ISM is complicated by the fact that the ISM is never in thermodynamic equilibrium, but rather always subject to a flow of energy. It is constantly being heated, primarily by FUV radiation from young stars, while radiating away the heat via dust emission in the infrared and (mostly FIR) gas emission lines (see Section 1.4 for more on the spectrum of a galaxy). To derive the gas kinetic temperature, T_k , one must therefore consider all relevant heating and cooling mechanisms, calculate their energy rates and search for an equilibrium temperature.

Out in the hot, ionized HII regions (see Table 1.1), gas is heated by photo-ionization of HI gas. FUV photons ionize the hydrogen atoms and the free electrons convert their kinetic energy to heat via collisions with other gas particles. Cosmic rays are very energetic protons, most likely produced in supernovae (Ackermann et al., 2013), and they represent a second radiation field that can heat the gas and penetrate even further into it than FUV photons due to their high energies (\sim GeV). Like FUV photons, cosmic rays can ionize the atomic gas and release electrons with kinetic energy, but cosmic rays can also interact with the free electrons, transferring kinetic energy directly via Coulomb interactions.

As for cooling, the gas has several options. First of all, emission lines from hydrogen and heavier elements, in their atomic and ionized states, can remove a great deal of energy, especially at $T_k > 10^4$ K. The cooling rates as function of T_k for the most important elements are shown in Fig. 1.8. The sudden rise in cooling rate at $T_k \sim 10^4$ K makes sure that the temperature

of the HII gas hardly ever exceeds 10^4 K.

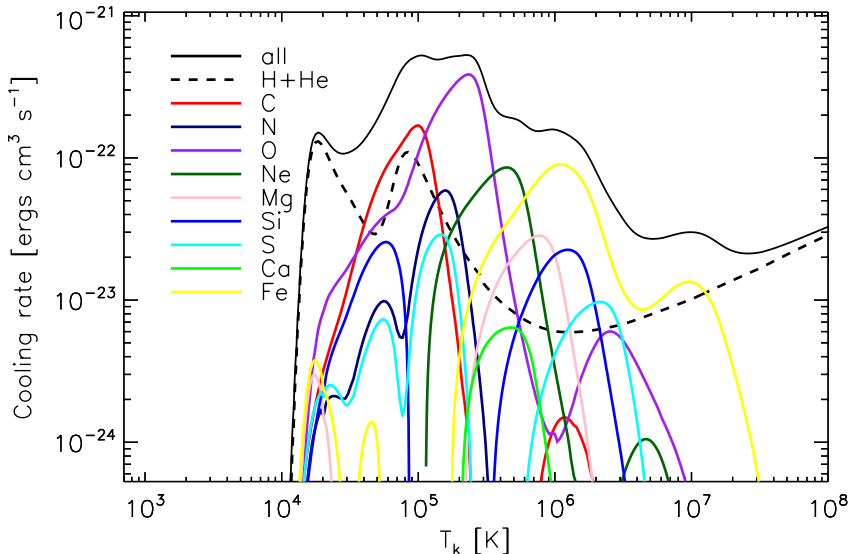


Figure 1.8 Cooling rates of all (black) and individual atoms and ions in the hot ISM as function of temperature. Made with the publicly available code of Wiersma et al. (2009) which includes both collisional- and photo-ionization, though collisional ionization equilibrium (CIE) has been used for this plot. The code takes T_k and n_H as input of which n_H is set to 0.01 cm^{-3} here, and solar abundances are adopted.

In addition to these emission lines, electron recombination with ions can cool the gas, as recombining electrons take away kinetic energy from the plasma, a process which is important at temperatures $> 10^3$ K (Wolfire et al., 2003). At similar high temperatures another important cooling mechanism is the scattering of free electrons off of other free ions, whereby free-free emission removes energy from the gas (Draine, 2011).

Combining all of the above heating and cooling mechanisms, we arrive at one equation that describes the balance between the energy rates of heating and cooling:

$$\Gamma_{\text{PI}} + \Gamma_{\text{CR,HI}} = \Lambda_{\text{ions+atoms}} + \Lambda_{\text{rec}} + \Lambda_{\text{f-f}} \quad (1.4)$$

where Γ_{PI} and $\Gamma_{\text{CR,HI}}$ are the heating rates for photo-ionization and cosmic ray ionization, respectively, whereas $\Lambda_{\text{ions+atoms}}$ is the combined cooling rate from the elements shown in Fig. 1.8. Finally, Λ_{rec} and $\Lambda_{\text{f-f}}$ are the cooling rates due to recombination and free-free interactions as described above.

In the denser and colder ($T_k < 10^4$ K) WCNM, other heating and cooling mechanisms take over. Rather than photo-ionizing the gas, FUV photons now heat the gas more efficiently via the photo-electric effect consisting of a FUV photon knocking loose an electron from the surface of a dust grain, with the same net result: The escaping electron can deposit its kinetic energy as heat in the surrounding gas. The dominating cooling mechanisms in neutral gas are fine-structure line emission from ionised carbon, [CII], to be discussed in more detail in Section 5.1

in Part I, and from neutral atomic oxygen, [OI], leading to the following energy rate equation:

$$\Gamma_{\text{PE}} + \Gamma_{\text{CR,HI}} = \Lambda_{\text{CII}} + \Lambda_{\text{OI}} \quad (1.5)$$

where Γ_{PE} is the heating rate due to the photo-electric effect on dust grains, Λ_{CII} is the cooling rate due to [CII] line emission and Λ_{OI} is the cooling rate due to [OI] line emission. In addition, the Lyman alpha (Ly- α) line of hydrogen at 1216 Å is important in the warm part of the WCNM.

In molecular gas, most of the FUV radiation will be attenuated by dust and self-shielding molecules, leaving in some cases cosmic rays as the dominant source of heating. Indeed, it has been suggested that cosmic rays control the initial conditions for star formation in regions of high SFR density where the sites for star formation might be completely UV-shielded (Papadopoulos et al., 2011; Papadopoulos & Thi, 2013). The prescription for cosmic ray heating per hydrogen atom in molecular gas is in principle different from its form in neutral gas, but the two turn out to be very similar (Stahler & Palla, 2005) (though see Glassgold et al., 2012, who find higher heating rates in molecular gas by a factor 2-3). At increasingly higher temperature, [CII] line cooling gives way for CO line cooling, and at very high densities ($> 10^4 \text{ cm}^{-3}$), cooling by interactions between gas and dust particles can become dominating, as the gas approaches the dust temperature. In molecular gas, line cooling from molecular hydrogen and atomic oxygen also contributes to the cooling rate with typically smaller amounts. Summarized in one equation, the thermal equilibrium in molecular gas can hence be approximated by:

$$\Gamma_{\text{PE}} + \Gamma_{\text{CR,H}_2} = \Lambda_{\text{H}_2} + \Lambda_{\text{CO}} + \Lambda_{\text{OI}} + \Lambda_{\text{CII}} + \Lambda_{\text{gas-dust}} \quad (1.6)$$

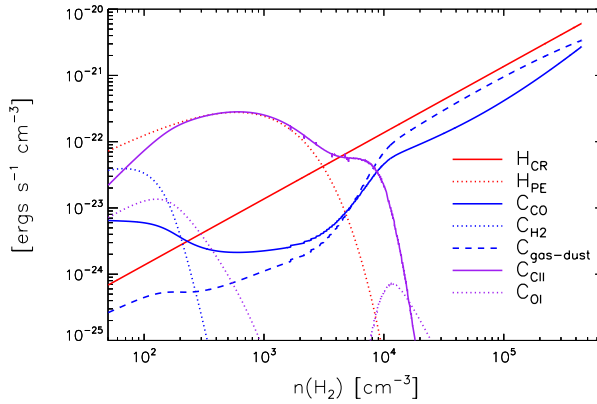


Figure 1.9 Heating and cooling rates in molecular gas. The energy rates shown are calculated at the equilibrium temperature for that density. Calculated for a GMC of mass $m_{\text{GMC}} = 10^4 M_{\odot}$, solar metallicity, an interstellar FUV field of 16 Habing units and a cosmic ray ionization rate of $8 \times 10^{-16} \text{ s}^{-1}$. In the outskirts (low density) of the cloud, [CII] line cooling and photo-electric heating dominate, while in the inner regions (high density), gas-dust cooling and CR heating take over, of which the latter is proportional to the density and hence a straight line of slope 1 (Stahler & Palla, 2005). Made with the `SÍGAME` code (to be described in Part I).

Fig. 1.9 gives an example of the dominant heating and cooling mechanisms mentioned above as functions of density for the interior of a model GMC of mass $m_{\text{GMC}} = 10^4 M_{\odot}$ and solar metallicity, immersed in an interstellar FUV field of 16 Habing units and a cosmic ray

ionization rate of $8 \times 10^{-16} \text{ s}^{-1}$.

1.3 THE ACTIVE GALACTIC NUCLEUS (AGN)

Apart from the gas, dust, stars and dark matter that I mentioned in the beginning of this introduction, there is a fifth component in the MW: black holes. A particularly big one or ‘supermassive black hole’ (SMBH) is hiding at the very center of the MW, and most likely every galaxy, as it became clear in the 90’s (Magorrian et al., 1998).

The strong gravitational pull from a SMBH creates a rotating accretion disk of matter (yellow part in Fig. 1.10) from its host galaxy. As gravitational energy is converted into mechanical and electromagnetic energy, gas in the accretion disk is heated to very high temperatures and starts to radiate fiercely over a broad range of energies, from radio to X-ray (see Krawczynski & Treister, 2013, for a review of the inner workings of these central engines).

Galaxies in which the spectra are dominated by this type of central energy source, are called Active Galactic Nuclei (AGNs). Observationally, AGNs have been classified into two main groups; (Seyfert) type I and type II based on the width of their optical emission lines. Type I AGNs show strong broad emission lines, while type II AGNs have relatively narrow emission lines and softer X-ray emission. In some cases, relativistic jets are produced perpendicularly to the accretion disk and their strong synchrotron radiation in radio has led to the classification ‘radio-loud’ AGNs. AGNs for which the optical light from the host galaxy is outshined by the central disk itself are dubbed quasars (QSOs).

1.3.1 UNIFICATION MODELS

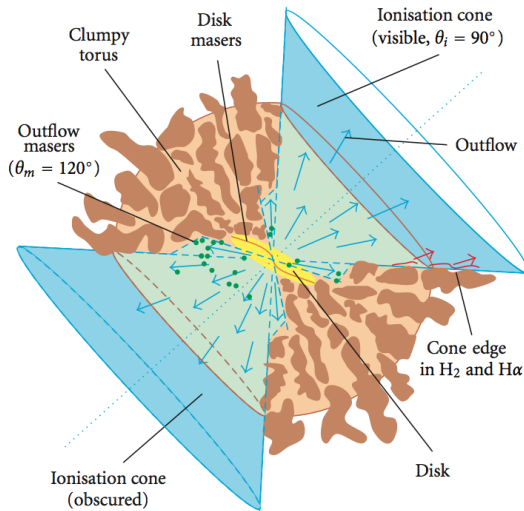


Figure 1.10 Drawing, from the review of (Bianchi et al., 2012), of the inner engine emitting the strong radiation of an AGN, including the disk (yellow) of matter accreting onto the SMBH, the surrounding clumpy torus (brown) and ionization cones (blue), also containing the relativistic jets.

Over the past two decades, observations have led to the Standard Unified Model suggesting that type I and type II AGNs are intrinsically the same class of objects, but viewed from different angles, as pictured in Fig. 1.10 (Bianchi et al., 2012). In this picture, the accretion disk is surrounded by a clumpy torus of gas and dust, and outflow is mainly allowed within the ionization cone encircling the relativistic jets. A type I AGN is a galaxy inclined so that we see the inner parts of the accretion disk where high orbital speeds result in relatively broad lines. A type II AGN is orientated so that the inner accretion disk is obscured by the clumpy torus and only narrow lines from more distant cold material can be observed.

A tight correlation between optical and X-ray emission of unobscured quasars suggest that all luminous AGNs are intrinsically also X-ray bright (e.g. Steffen et al.,

2006; Gibson et al., 2008). But high amounts of obscuring gas and dust in the torus and elsewhere in the host galaxy can decrease the X-ray luminosity or change the spectral slope of the X-ray emission that actually escapes the galaxy, to be discussed further in Section 1.3.1. Alternative sources for strong X-ray emission in a galaxy are High-Mass X-ray Binary systems (HMXBs), which may be significant in case of high SFR (Ranalli et al., 2003), and halos of hot gas (Mulchaey & Jeltrema, 2010).

1.4 THE ‘SPECTRAL FINGERPRINT’ OF A GALAXY

The best way to measure the conditions of gas in the ISM is by taking a ‘spectral fingerprint’. Fig. 1.11 is a cartoon version of the spectral energy distribution (SED) of a galaxy if we were able to measure its emission from the smallest wavelengths (x-ray) to the longest (~ 1 cm) of interest for the ISM. Furthermore, the SED is shown in the ‘rest frame’ of the galaxy rather than in the observers frame, in which the SED would be red-shifted to longer wavelengths if the galaxy happened to be at high redshift. The unit is Jansky ($= \text{Jy} = 10^{-26} \frac{\text{W}}{\text{m}^2 \cdot \text{Hz}}$) which is a typical flux unit in radio astronomy. The SED shown in Fig. 1.11 is that of a typical star-forming spiral galaxy, taken from the publicly available SED templates of Kirkpatrick et al. (2012), with an additional imaginative X-ray flux measurement corresponding to an X-ray luminosity of $L_{0.5-8 \text{ keV}} = 10^{44} \text{ ergs/s}$.

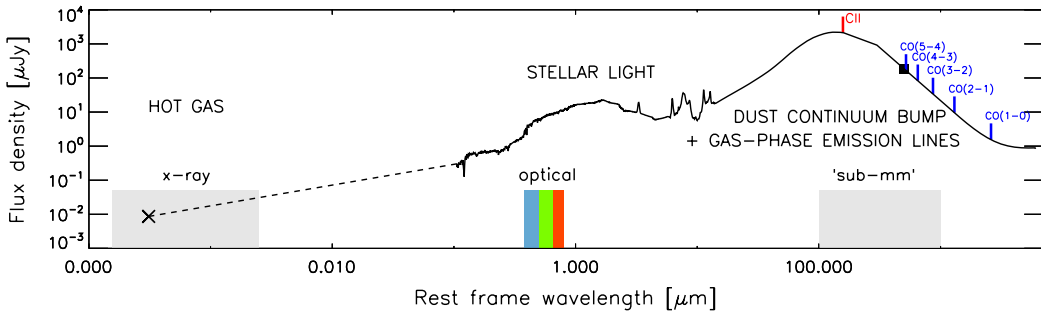


Figure 1.11 The SED of a typical star-forming galaxy at $z = 0$ with indications of the different components contributing to its shape. Also shown are the positions of some important emission lines from the gas, to be described in Part I. The flux has been scaled to the observed $500 \mu\text{m}$ luminosity of local galaxies for a mass of $10^{10} M_{\odot}$ as marked with a black square (Groves et al., 2015). SED template of Kirkpatrick et al. (2012): <http://www.astro.umass.edu/~pope/Kirkpatrick2012/>.

First noticeable are the two ‘bumps’ at wavelengths around $1 \mu\text{m}$ and $100 \mu\text{m}$. The first one is dominated by direct stellar light at ultraviolet (UV) to near-infrared (NIR) wavelengths. The UV light is mainly produced by young massive stars recently formed and therefore traces the current SFR well, since massive stars have relatively short lifetimes. On the other hand, the NIR flux is primarily consisting of light from old, less massive stars, making NIR luminosity a good tracer of total stellar mass. Good estimates of SFR and M_{*} can be made simultaneously by fitting the entire SED with stellar population synthesis models, typically only requiring assumptions about the initial mass function (IMF) of stars as they are born, the SFR history and the metallicity. For example, the SFRs in Fig. 1.4 were created assuming a Salpeter IMF (Salpeter, 1955).

The second bump is caused by dust that absorbs light at many wavelengths, but it is a

particularly powerful absorber of far-ultraviolet (FUV; $\sim 100\text{-}200\text{ nm}$) radiation, which is re-emitted again in the infrared (IR; $\sim 1\text{-}1000\text{ }\mu\text{m}$), thus ‘reprocessing’ the emitted starlight. The shape of the dust ‘bump’ can most of the time be approximated by a combination of a modified blackbody (a ‘greybody’), fixed at the temperature of the dust, and a power law in the mid-infrared (MIR) as described in detail by Casey (2012) and shown with an example in Fig. 1.12. On top of the dust peak a few important gas emission lines are shown, namely the CO (blue) and [CII] (red) lines, that will be described in detail in Part I.

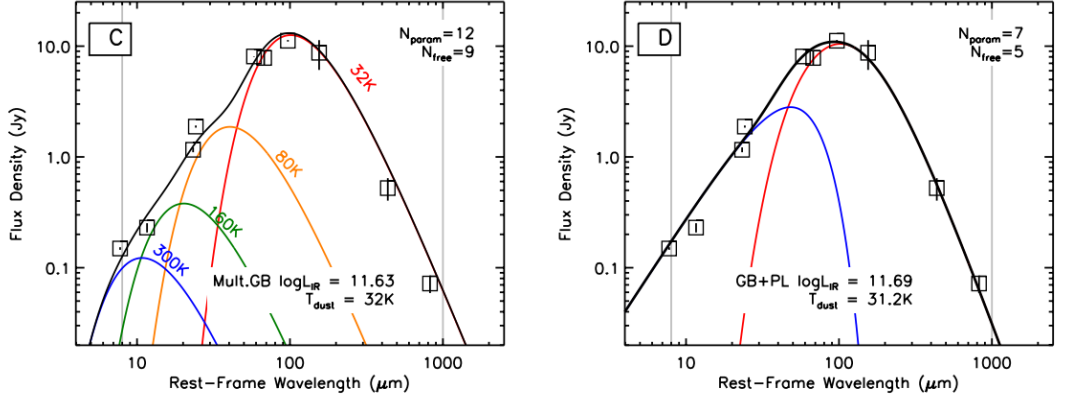


Figure 1.12 Examples of how the spectra in MIR to FIR, caused by dust in a galaxy, can be approximated by either several ‘greybodies’ of different dust temperature (left) or one greybody combined with a power law at high energies (right). Adapted from Casey (2012) who presented the latter, simplified FIR SED fitting technique.

In order to analyze the gas component of a galaxy, there are basically two relevant regimes in wavelength, both of which are indicated with grey areas in the figure:

X-ray regime: Thermal emission from galactic and extra-galactic hot, ionized gas.

Sub-mm regime: Gas emission lines from colder, more neutral gas.

This thesis implements observational and theoretical techniques in both of these regimes, as will be summarized in Section 2.2.

1.5 AN EXCITING TIME FOR OBSERVATIONS

Facilities for observing gas and dust in galaxies accross cosmic time are experiencing a true revolution, that is gradually opening our eyes towards normal galaxies at high redshifts. Here, I will briefly go through the most important radio and X-ray telescopes in use or preparation.

1.5.1 RADIO TELESCOPES

Probably the most impressive effort in this regard has been the Atacama Large Millimeter Array (ALMA), even if still under contruction. For an idea of its capabilities already in 2011 when the first scientific observations with ALMA began, see the image in Fig. 1.5 made with only 12 antennas. When completed, ALMA will comprise 50 antennas of 12 metres in diameter, acting as a single telescope and with a very high spatial resolution thanks to the art of interferometry. An additional 4 12-m and 12 7-m antennas will create a compact array in the centre. Together, the 66 antennas (each weighing > 100 tons!) can be moved with special designed vehicles into different configurations with maximum antenna distances from 150 m to an astonishing 16 km.



Figure 1.13 A photo of 19 ALMA antennas as they stood ready for the ALMA Early Science cycle. The array is located on the Chajnantor Plateau at 5000 m above sea level in Atacama desert of northern Chile. Credit: ALMA (ESO/NAOJ/NRAO)/W. Garnier (ALMA).

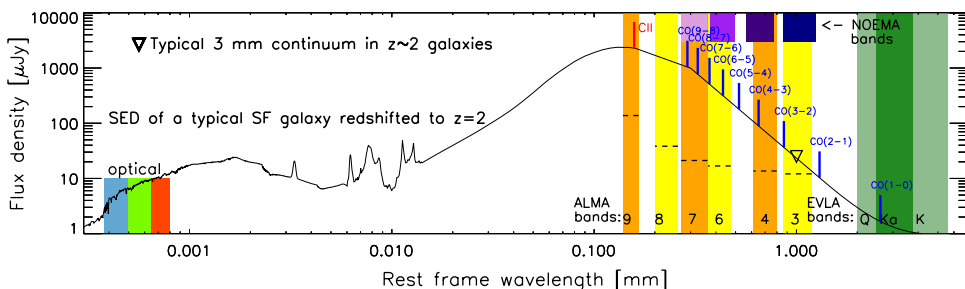
A more extended configuration corresponds to a higher spatial resolution, but also a lower sensitivity towards larger (more extended) sources on the sky, a trade-off that must be considered when planning observations. With bands of high spectral resolution from $312 \mu\text{m}$ to 3.56 mm (and 2 extra bands going down to about 7.4 mm possibly added in the future), ALMA will be able to detect [CII] and CO lines in a normal galaxy at $z = 3$ in a matter of hours. For the next cycle of observations (Cycle 3, starting in October 2015), ALMA is anticipated to encompass a total of 48 antennas with most receiver bands available.

In the Northern Hemisphere, The NOrthern Extended Millimeter Array (NOEMA⁵, former PdBI) will be, upon completion in 2019, the facility in the Northern Hemisphere that comes closest to the capabilities of ALMA, with bands for observing in the $808 \mu\text{m}$ - 3.7 mm range. At longer wavelengths, the Jansky Very Large Array (JVLA) is currently the superior radio interferometer, covering from 0.6 to 30 cm with 27 antennas of diameter 25 m (Napier, 2006). A number of single-dish radio telescopes can also target gas and dust emission at high redshifts; the LMT, IRAM-30m, GBT, Onsala 20+25m, ARO, NMA and APEX to name a few.

An overview of ALMA, EVLA and NOEMA is intended with Fig. 1.14, comparing the position of their frequency bands with the SED (including [CII] and CO lines) of a typical star-forming galaxy at $z = 2$.

The James Webb Space Telescope (JWST), scheduled to launch in 2018, will be an improved version of the famous Hubble Space Telescope (HST, expected to stay in operation until 2020), covering 0.6 to $28 \mu\text{m}$ with the same resolution in NIR as HST has in the optical.

⁵<http://www.iram.fr/IRAMFR/GILDAS/doc/html/noema-intro-html/noema-intro.html>



(Reynolds et al., 2014). Astrosat is India's first dedicated astronomy satellite and has the advantage of allowing simultaneous multi-wavelength observations at UV and X-ray wavelengths. It will have two bands for detecting X-rays (3-80 keV and 10-150 keV), and a large effective area in the hard X-ray band to facilitate studies of highly variable sources such as AGN (Paul, 2013).

1.6 GALAXY SIMULATIONS

With so many coupled mechanisms in a galaxy on scales from sub-parsecs to kilo-parsecs, the advantage of running numerical simulations of galaxy evolution has proven tremendous. Galaxy simulations can be roughly divided into two kinds: Cosmological simulations that start out with the small density perturbations of dark matter shortly after the Big Bang, and more idealized disk simulations that start out with an analytical density profile for the galaxy and allow gravitational and electromagnetic forces to perturb the galaxy in time. I will focus on the former kind as that is what my theoretical projects build on (see Parts I and II).

The series of images in Fig. 1.16 illustrate how a cosmological simulation works, with snapshots, from high redshift ($z = 4$) and until now ($z = 0$), of the dark matter structures and the resulting gas mass distribution. In the present Λ CDM cosmological model, dark matter formed structures (or ‘minihalos’) before baryonic gas could cool and collapse. Cosmological simulations therefore focus on modeling an underlying dark matter structure (left-hand side of Fig. 1.16) at the same time as the baryonic component of the universe is allowed to condense in these structures via gravity, dissipation and radiation (right-hand side of Fig. 1.16). As the universe ages, filaments and knots in the dark matter density distribution become more pronounced and infalling gas cools enough to form stars and galaxies in regions of high concentration.

The universe is then believed to have proceeded via hierarchical structure formation, in which small gravitationally bound structures, such as stars and galaxies, form first, followed by groups, clusters and superclusters of galaxies, not to mention the cosmic web in between them (c.f. Fig 1.2).

It was soon realized though, that these large-scale simulations with resolutions going down to kpc-scales, could not capture the actual physics inside galaxies, where the most important processes take place on < 1 pc scales. In particular, simulations on smaller scales proved that localized feedback is needed in order to avoid overpredicting the star formation rate and to agree with the observed IMF of star clusters (Tasker, 2011; Krumholz et al., 2011; Hopkins et al., 2011). Made possible by an increasing computing power and technology, cosmological galaxy simulations have seen two big ‘revolutions’ since their beginning in the early 90’s as

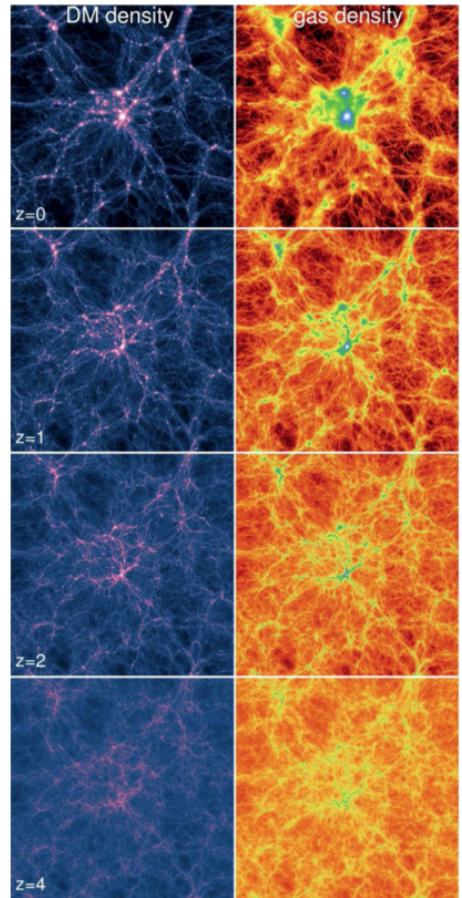


Figure 1.16 106.5 Mpc wide on each side, column density maps are shown of simulated dark matter (left) and gas column densities (right) from $z = 4$ until now (bottom to top). Brightest colors in the column density plot correspond to a density of $\sim 10^4 M_{\odot}/\text{kpc}^3$. The images are from the Illustris Project – one of the most comprehensive cosmological hydrodynamical simulations of galaxy formation to date (Vogelsberger et al., 2014). The recently developed moving-mesh code AREPO (Springel, 2010) was used to follow DM and gas dynamics.

illustrated in Fig. 1.17, of which we are in the middle of the last one, the ‘zoom-in’ simulations.

1.6.1 ‘ZOOM-IN’ SIMULATIONS

The concept behind ‘zoom-in’ simulations is to select a galaxy at low redshift in a cosmological simulation of low resolution ($\gtrsim 1$ kpc), and trace the particles (or cells) comprising it back in time to the beginning of the simulation. A re-simulation is then initiated with much higher resolution, but only following the particles/cells that end up in the galaxy of interest. This re-simulation may take days or months, but provides the opportunity to follow star formation on realistic scales, while staying in agreement with the overall large scale structure. Two computational techniques exist for treating the gas hydrodynamically at the necessary resolution: **Smoothed Particle Hydrodynamic (SPH) simulations:** The gas is represented by particles with properties such as mass, density and temperature in addition to a smoothing kernel that roughly speaking smears the particles out across a volume in space. Resolution is increased simply by increasing the number of particles while reducing their mass in order to keep mass conservation.

Adaptive Mesh Refinement (AMR) simulations: The gas is divided into cells that can be subdivided in areas where higher resolution is needed. All interactions between gas cells take place as mass/temperature/pressure exchange through the cell partition walls.

Examples of SPH codes include `GADGET` and `GASOLINE`, whereas `ART`, `ENZO` and `RAMSES` are AMR codes. Kim et al. (2014) presented, with the AGORA project, a comparison of these in terms of resolution, physics of the ISM, feedback and galactic outflows. But see also Springel (2010) for a novel combination of the two methods.

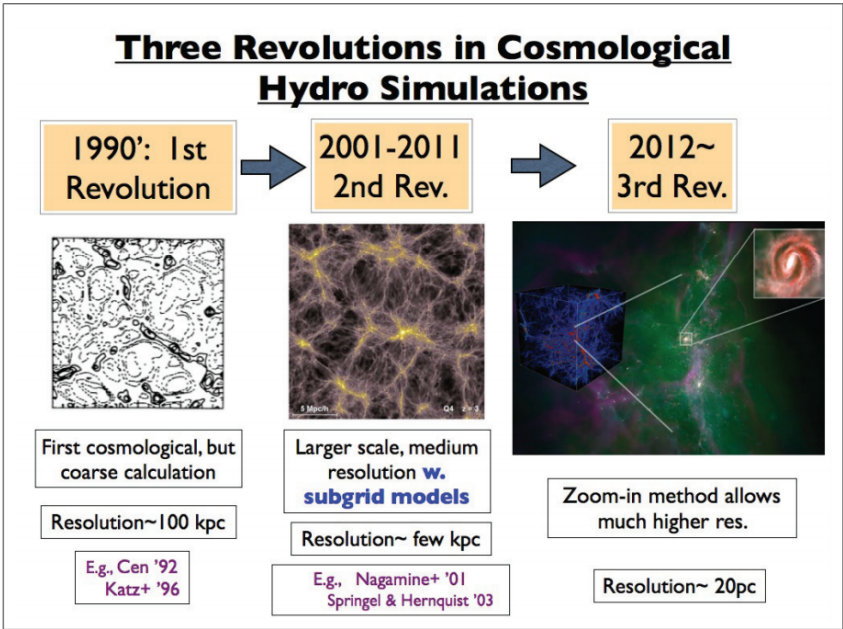


Figure 1.17 Schematic overview of the history of cosmological galaxy simulations and their improvements over the past two decades, with references, as presented in the review by Nagamine (2014).

1.6.2 THE CALIBRATION TO $z = 0$

While the initial conditions for galaxy formation and evolution are relatively strict, by e.g. measurements of the Cosmic Microwave Background (CMB), and the final endpoint is anchored with $z = 0$ observations, what goes on in between is less well-defined by observations. Common tests for the evaluation of a cosmological simulation focus on how well it can reproduce the observed main sequence and luminosity functions at low- to high- z . Although simulations on the whole agree with observations, a discrepancy still persists at the time of maximum cosmic star formation ($1 \lesssim z \lesssim 3$), where the simulated main sequence is a factor $\sim 2 - 3$ below the observed one (e.g. Furlong et al., 2014). Possible explanations include an IMF that changes with redshift and galaxy properties (rather than staying fixed to the locally observed one as most simulations assume), or feedback from stellar winds, supernovae and AGN that is not properly accounted for in simulations (e.g. Davé, 2008; Narayanan & Davé, 2012; Sparre et al., 2015). Until more resolved observations of ISM at $z \gtrsim 2$ are obtained, simulations of galaxy evolution are forced to make, and be inhibited by, extrapolations to high- z of local ISM physics and star-formation laws. Some of these restrictions will be discussed in Part I.

1.7 REFERENCES

- Ackermann, M., Ajello, M., Allafort, A., et al. 2013, *Science*, 339, 807
Bauer, F. E., Alexander, D. M., Brandt, W. N., et al. 2004, *AJ*, 128, 2048
Behroozi, P. S., Wechsler, R. H., & Conroy, C. 2013, *ApJ*, 770, 57
Bianchi, S., Maiolino, R., & Risaliti, G. 2012, *Advances in Astronomy*, 2012, 17
Blitz, L., Fukui, Y., Kawamura, A., et al. 2007, *Protostars and Planets V*, 81
Casey, C. M. 2012, *MNRAS*, 425, 3094
Colless, M., Dalton, G., Maddox, S., et al. 2001, *MNRAS*, 328, 1039
Dale, J. E., Ercolano, B., & Bonnell, I. A. 2012, *MNRAS*, 424, 377
Dannerbauer, H., Daddi, E., Riechers, D. A., et al. 2009, *ApJL*, 698, L178
Davé, R. 2008, *MNRAS*, 385, 147
Draine, B. T. 2011, *Physics of the Interstellar and Intergalactic Medium*
Furlong, M., Bower, R. G., Theuns, T., et al. 2014, *ArXiv e-prints*
Genzel, R., Tacconi, L. J., Gracia-Carpio, J., et al. 2010, *MNRAS*, 407, 2091
Gibson, R. R., Brandt, W. N., & Schneider, D. P. 2008, *ApJ*, 685, 773
Glassgold, A. E., Galli, D., & Padovani, M. 2012, *ApJ*, 756, 157
Goicoechea, J. R., & Nakagawa, T. 2011, in *EAS Publications Series*, Vol. 52, EAS Publications Series, ed. M. Rölli, R. Simon, V. Ossenkopf, & J. Stutzki, 253–258
Groves, B. A., Schinnerer, E., Leroy, A., et al. 2015, *ApJ*, 799, 96
Hartley, W. G., Almaini, O., Mortlock, A., et al. 2013, *MNRAS*, 431, 3045
Hopkins, P. F., Quataert, E., & Murray, N. 2011, *MNRAS*, 417, 950
Kim, J.-h., Abel, T., Agertz, O., et al. 2014, *ApJS*, 210, 14
Kirkpatrick, A., Pope, A., Alexander, D. M., et al. 2012, *ApJ*, 759, 139
Krawczynski, H., & Treister, E. 2013, *Frontiers of Physics*, 8, 609
Krumholz, M. R., Klein, R. I., & McKee, C. F. 2011, *ApJ*, 740, 74
Krumholz, M. R., Bate, M. R., Arce, H. G., et al. 2014, *Protostars and Planets VI*, 243
Madau, P., & Dickinson, M. 2014, *ARA&A*, 52, 415
Magorrian, J., Tremaine, S., Richstone, D., et al. 1998, *AJ*, 115, 2285
Mulchaey, J. S., & Jelte, T. E. 2010, *ApJ*, 715, L1

- Nagamine, K. 2014, in American Institute of Physics Conference Series, Vol. 1594, American Institute of Physics Conference Series, ed. S. Jeong, N. Imai, H. Miyatake, & T. Kajino, 41–45
- Napier, P. J. 2006, in Astronomical Society of the Pacific Conference Series, Vol. 356, *Revealing the Molecular Universe: One Antenna is Never Enough*, ed. D. C. Backer, J. M. Moran, & J. L. Turner, 65
- Narayanan, D., & Davé, R. 2012, *MNRAS*, 423, 3601
- Papadopoulos, P. P., & Thi, W.-F. 2013, in *Advances in Solid State Physics*, Vol. 34, *Cosmic Rays in Star-Forming Environments*, ed. D. F. Torres & O. Reimer, 41
- Papadopoulos, P. P., Thi, W.-F., Miniati, F., & Viti, S. 2011, *MNRAS*, 414, 1705
- Paul, B. 2013, *International Journal of Modern Physics D*, 22, 41009
- Planck Collaboration, Ade, P. A. R., Aghanim, N., et al. 2015, ArXiv e-prints
- Price, D. J., & Bate, M. R. 2009, *MNRAS*, 398, 33
- Przybilla, N., Nieva, M.-F., & Butler, K. 2008, *ApJ*, 688, L103
- Ranalli, P., Comastri, A., & Setti, G. 2003, *A&A*, 399, 39
- Reynolds, C., Ueda, Y., Awaki, H., et al. 2014, ArXiv e-prints
- Roman-Duval, J., Jackson, J. M., Heyer, M., Rathborne, J., & Simon, R. 2010, *ApJ*, 723, 492
- Salpeter, E. E. 1955, *ApJ*, 121, 161
- Sparre, M., Hayward, C. C., Springel, V., et al. 2015, *MNRAS*, 447, 3548
- Speagle, J. S., Steinhardt, C. L., Capak, P. L., & Silverman, J. D. 2014, *ApJS*, 214, 15
- Springel, V. 2010, *MNRAS*, 401, 791
- Stahler, S. W., & Palla, F. 2005, *The Formation of Stars* (Wiley)
- Steffen, A. T., Strateva, I., Brandt, W. N., et al. 2006, *AJ*, 131, 2826
- Tasker, E. J. 2011, *ApJ*, 730, 11
- Tielens, A. G. G. M. 2013, *Reviews of Modern Physics*, 85, 1021
- Vogelsberger, M., Genel, S., Springel, V., et al. 2014, *MNRAS*, 444, 1518
- Wiersma, R. P. C., Schaye, J., & Smith, B. D. 2009, *MNRAS*, 393, 99
- Wolfire, M. G., McKee, C. F., Hollenbach, D., & Tielens, A. G. G. M. 2003, *ApJ*, 587, 278
- Wuyts, S., Förster Schreiber, N. M., Genzel, R., et al. 2012, *ApJ*, 753, 114
- Xu, C. K., Cao, C., Lu, N., et al. 2015, *ApJ*, 799, 11
- Xue, Y. Q., Luo, B., Brandt, W. N., et al. 2011, *ApJS*, 195, 10

2

INTRODUCTION TO THIS THESIS

2.1 EVOLUTION OF MASSIVE GALAXIES ACROSS COSMIC TIME

With the previous brief description of the internal composition of galaxies and the observational and theoretical tools used for characterising them, we are now ready to take a look at the populations of massive galaxies so far uncovered and the current status on creating a consistent picture for their evolution with cosmic time.

2.1.1 HIGH-REDSHIFT MASSIVE GALAXY POPULATIONS

An important fact to bear in mind when studying galaxy evolution, is that we are never observing *the same* galaxy at various epochs in the life of the universe. At each redshift, the most we can do is observe galaxies in a snapshot of their lifetime, and often any evolutionary connection between galaxies observed at different redshifts is hampered by different selection techniques and incompleteness (we cannot detect all galaxies at every redshift, cf. Section 1.1.2).

The ideal way of classifying galaxies at all redshifts would be to measure their entire SED (like the one shown in Fig. 1.11) via spectroscopy. But since this would be very time-consuming, clever methods have been developed to first select a candidate group of the galaxies that might be of interest, and then perform high-resolution spectroscopy on these. Such methods typically build on photometry – measuring the total flux through a limited set of photometric bands by applying filters that only allow certain ranges in wavelength. For selecting galaxies of a certain mass, the *K*-band (centered on $2.2\ \mu\text{m}$ in the NIR) is particularly useful since it captures light from primarily old stellar populations that dominate the mass budget of most galaxies. Therefore, a lower cut in *K*-band luminosity directly translates into a minimum stellar mass Cimatti (2003). Follow-up spectroscopy can then determine the redshift, stellar mass and SFR to higher precision with SED fitting methods (see Man et al., 2012; Cimatti et al., 2004, for applications of this method). This method works out to $z \sim 4$ where the *K*-band starts to trace rest-frame UV light, which unlike NIR or optical, is dominated by the strong radiation from young stars, and is therefore a tracer of the amount of current star formation rather than stellar mass.

At $z \gtrsim 3$, another way to classify galaxies is typically via their current amount of star formation. This star formation can be either un-obscured, as revealed in rest-frame UV, or – in galaxies of high dust amount – obscured resulting in high FIR luminosities (dust continuum ‘bump’ in Fig. 1.11), or a combination of the two. Two examples of the first approach are the

Lyman Break Galaxies (LBGs) and BzK-selected galaxies, whereas the second approach has revealed a group of very dusty galaxies, the Sub-mm Galaxies (SMGs) or nowadays, Dusty Star-forming Galaxies (DSFGs; Casey et al., 2014).

LBGs are selected to have a strong break and reduced flux at the wavelength $< \lambda = 912 \text{ \AA}$. This break is caused by neutral hydrogen gas residing inside the galaxy and in the Inter Galactic Medium (IGM), absorbing light at wavelengths below 912 \AA , the threshold for ionizing hydrogen. The LBG technique requires that the galaxy be UV bright (relatively star-forming) and not dust-obscured (Steidel et al., 2003). The advantage of the LBG technique is that it makes a preselection of not only SFR but also redshift, by restricting the location of the break. Carilli et al. (2008) used a method called ‘stacking’ (see application of this in X-ray in Part II), to find that LBGs at $z \sim 3$ have SFRs of $31 \pm 7 M_{\odot} \text{ yr}^{-1}$, that is, not very high on the MS at that redshift (c.f. Fig. 1.3).

The BzK-selection takes advantage of absorption in stellar atmospheres creating a strong break at $\sim 4000 \text{ \AA}$ so that three photometric bands (B , z and K) can effectively be used to select galaxies at $1.4 \lesssim z \lesssim 2.5$ and roughly estimate their SFR (Daddi et al., 2004). Similar groups of color-selected galaxies are those of ‘BX’ and ‘BM’ galaxies, selected via their color in the three UV and optical filters U_n , G and R (Adelberger et al., 2004; Steidel et al., 2004). The color criteria for ‘BX’ galaxies restricts them to lie at $2.0 \leq z \leq 2.5$, while the ‘BM’ galaxies lie at $1.5 \leq z \leq 2.0$. Both techniques give rise to slightly higher SFRs than the BzK-selection would, as shown by Reddy et al. (2005) using X-ray inferred bolometric SFRs.

SMGs on the other hand, are selected for having a strong rest-frame NIR emission, and were first detected with the ground-based instrument SCUBA at $850 \mu\text{m}$ (e.g. Smail et al., 1997; Hughes et al., 1998; Barger et al., 1999), soon followed by surveys including the use of instruments such as MAMBO at 1.2 mm and AzTEC at 1.1 mm (Coppin et al., 2005; Chapman et al., 2005; Greve et al., 2008; Perera et al., 2008). The advantage of looking in the rest-frame $1 - 3 \text{ mm}$ wavelength range at high redshift, is that the flux stays roughly the same owing to the effect of ‘negative K -correction’ as illustrated in Fig. 2.1. Due to this effect, SMGs have been identified mainly at $z \sim 2$ but with a tail extending up to $z \sim 5$ (Chapman et al., 2005; Wardlow et al., 2011; Simpson et al., 2014). Converting the high IR luminosities to dust-obscured SFRs, implies SFRs of $\sim 100 - 1000 M_{\odot} \text{ yr}^{-1}$ (Karim et al., 2013). For the most part, SMGs display disturbed stellar morphologies and/or kinematics as compared to normal non-interacting rotating disks, suggesting recent or ongoing merger events (e.g. Conselice et al., 2003; Chen et al., 2015). The disturbed signatures are backed up by molecular emission line observations of clumps of dense and highly star-forming gas in SMGs (e.g. Tacconi et al., 2008; Riechers et al., 2011; Hodge et al., 2012).

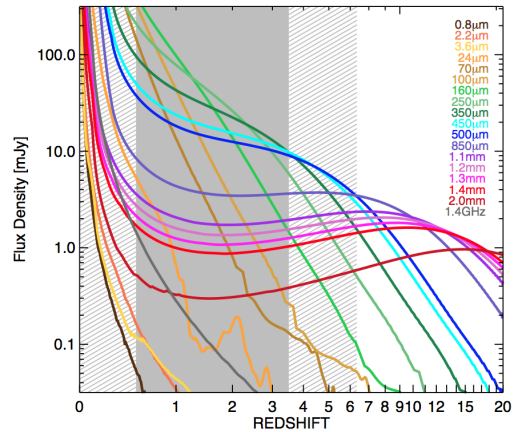


Figure 2.1 Observed flux densities for a typical dusty, star-forming galaxy as presented in the review by Casey et al. (2014). Note the nearly-constant flux density in the $\sim 1 \text{ mm}$ bands across $1 \lesssim z \lesssim 10$ redshift range.

2.1.2 OBSERVING GALAXIES AT $z > 4$ VIA THEIR GAS EMISSION LINES

In the early ($z > 4$) universe, very few normal star-forming galaxies have so far been detected, typically via the LBG technique (see Behroozi et al., 2013, for a compilation), and even fewer quiescent galaxies have been discovered at $z \gtrsim 2.5$, with the most distant ones at $z \sim 3$ (Gobat et al., 2012; Fan et al., 2013). Only one galaxy at $z > 7$ has so far had its redshift determined from spectroscopy of its stellar continuum. But the galaxy A1689-zD1 at $z = 7.5 \pm 0.2$, has now been detected in dust emission with ALMA resulting in a combined (UV+IR) SFR of $\sim 12 M_{\odot} \text{ yr}^{-1}$ (Watson et al., 2015), i.e. a normal star-forming galaxy. In addition to dust continuum, ALMA can also detect line emission from the gas, thereby determining redshifts and characterizing the ISM at the same time for normal star-forming galaxies (see more on this in the Outlook section of Part I). An example of such an emission line, is [CII] from singly ionized carbon, which is expected to be the most luminous cooling line in neutral gas. We return with a more detailed description of [CII] in Chapter 6, but mention here that at $z \sim 5-7$, the [CII] line falls in bands 6-7 of ALMA, currently the most sensitive millimeter interferometer by an order of magnitude, and therefore a promising tool for detecting [CII] in normal star-forming galaxies at $z \sim 6$. Indeed, it has been detected in and around normal star-forming galaxies at $z \sim 5-7$ (Maiolino et al., 2015; Capak et al., 2015). *Our only way of characterizing the ISM of high- z galaxies might very well be to observe emission lines from the gas.*

2.1.3 THE RED AND BLUE GALAXIES

The local galaxy population is bimodal in terms of UV-to-optical color, with a distinct group of blue, star-forming galaxies and another of red, quiescent galaxies (Strateva et al., 2001; Schawinski et al., 2014). This is shown with color-mass diagrams in Fig. 2.2 for low redshift galaxies. The connection between color and star formation activity is a result of younger stars having relatively bluer colors than old stars, which emit their light predominantly at longer (optical and NIR) wavelengths. Historically, the red and blue galaxies are also called ‘early’ and ‘late’-type galaxies from the morphological classification of Hubble (1926). In general, late type galaxies display stellar disks with spiral arms and exponential light profiles whereas the stellar light from early-type galaxies (or sometimes named ellipticals) is more concentrated with even structures and no clear sign of spiral arms. But detailed observations of their stellar populations have later shown that this naming makes sense, since the nearby red galaxies most likely formed much earlier than the blue ones (e.g. Kartaltepe et al., 2014). As always, dust plays an important role and can make star-forming galaxies appear red by absorbing the blue light and re-emitting it in the FIR. Indeed Sodr  et al. (2013) showed that some local galaxies with extremely red colors, are reddened by dust more than by older (redder) stellar populations. But the diagrams in Fig. 2.2 have been corrected for reddening by dust, by measuring the dust extinction in optical light.

In between the red and the blue group, lies the ‘green valley’ with very few galaxies. There is a discussion about how many of these green galaxies are actually late-type galaxies being quenched (Pan et al., 2013; Schawinski et al., 2007) and how many are early-type galaxies with star formation initiated recently in a sort of ‘rejuvenation’ (Fang et al., 2012). In Section 1.1 the main sequence (MS) of star formation was introduced, and Fig. 1.3 showed how the MS grows towards higher SFR with redshift. Blue galaxies lie on the MS relation, whereas red galaxies lie below and typically at high stellar mass. One of the biggest quest in astronomy for understanding galaxy evolution is; *Why did blue galaxies form more stars at higher redshift?*

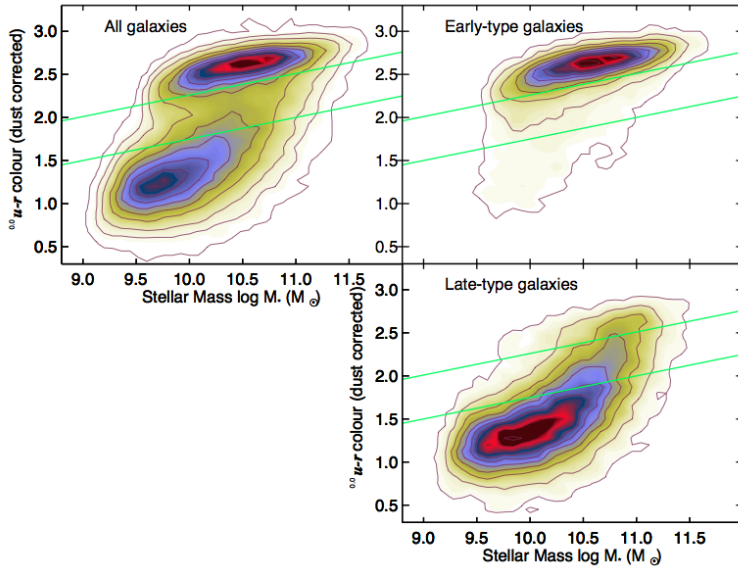


Figure 2.2 The UV-optical color bimodality of $0.02 < z < 0.05$ galaxies, as measured by Schawinski et al. (2014) using the SDSS+GALEX+Galaxy Zoo data. The ‘0.0’ in $^{0.0}u$ refers to the K -correction of the observed color to $z = 0$ (see Section 2.1.1). Green lines indicate the ‘green valley’ in between the two galaxy populations.

By now, the division into quiescent or star-forming has been observationally confirmed out to $z \sim 3$, (Kriek et al., 2008; Williams et al., 2009; Viero et al., 2013; Man et al., 2014), leading to a second, equally important, question: *When did the onset of the red sequence take place and what caused it?*

2.1.4 QUENCHING STAR FORMATION

AGNs are one of the preferred hypothesized mechanisms for quenching star formation, as radiation, winds and jets from the central accreting black hole can remove the gas or heat it so that contraction of molecular clouds cannot take place (see Fabian 2012 and McNamara & Nulsen 2007 for a reviews on models and observational evidence). A distinction is made between ‘quasar mode’, by which feedback from an AGN ejects all gas from the galaxies (Granato et al., 2004), and ‘radio mode’, during which powerful jets heat the circumgalactic medium to such high temperatures that further accretion of cold gas onto the galaxy is prevented (Croton et al., 2006). Semi-analytical simulations, by e.g. Di Matteo et al. (2005), show how reasonable descriptions of the AGN feedback on star formation in elliptical galaxies can reproduce the observed local mass function.

In addition to quenching by AGNs (possibly ignited by a major merger), the environment in which the galaxy lives is believed to raise further quenching mechanisms. This suspicion came from observations showing that galaxies in clusters are in general more quenched and passive than field galaxies (Verdugo et al., 2008). Similar to AGNs, most of these proposed internal/external mechanisms have to do with the removal, distribution or heating of gas, i.e. the fuel for further star formation. This can happen via galaxy-galaxy interactions or influence by the Intra Cluster Medium (ICM) itself. The following are some of the more popular environmental quenching mechanisms, but see reviews by e.g. Boselli & Gavazzi (2006) and Blanton &

Moustakas (2009) for a much more complete overview: i) Harassment, when during close encounters or direct mergers, galaxies alter each others' morphology (Moore et al., 1998); ii) Ram pressure stripping, where galaxies traveling through the ICM at high speed have their ISM shock-heated and eventually stripped off, ending up in the cluster as seen in observations of individual cases and proposed by several simulations (e.g. Steinhauser et al., 2012; Bösch et al., 2013; Ebeling et al., 2014); iii) Tidal stripping, by which galaxies passing through the ICM feel the global tidal field of their host, significantly altering their morphologies (Villalobos et al., 2014); iv) Cosmological 'starvation' or 'strangulation', when the hot gas halo around a galaxy is removed due to hydrodynamical interactions with the ICM, and further infall of gas is prevented causing the galaxy to slowly run out of fuel on time scales of a few Gyr (Balogh et al., 2000; Bekki et al., 2002; Feldmann & Mayer, 2015); v) Compactness quenching, as suggested by observations of satellites in the outskirts of haloes, that show a strong correlation between quenching and compactness of the galaxy (Woo et al., 2015).

These last types of quenching mechanisms are also referred to collectively as 'satellite quenching', because they primarily happen to satellite galaxies in a cluster. However, it has been hypothesized that satellite quenching and that of AGN (also called 'mass-quenching'), are actually manifestations of the same underlying process (Carollo et al., 2014; Knobel et al., 2015).

2.1.5 CONNECTING THE DOTS

The fact that the red sequence is already in place at $z \sim 2$, means that we have to push even further out in redshift in order to find the onset of this 'dead' population, and with that, hopefully also the 'murder weapon'. In addition, half of the most massive galaxies ($M_* > 10^{11} M_\odot$) at $z \approx 2$ are already compact and quiescent galaxies (CQGs) with old stellar populations (e.g. Toft et al., 2007; van Dokkum et al., 2008; Szomoru et al., 2012). The stellar spectra suggest that major starburst events took place in CQGs some 1-2 Gyr prior to the time of observation, but were quenched by mechanisms either internal or external (or both) to the galaxy (e.g. Gobat et al., 2012; Whitaker et al., 2013; van de Sande et al., 2013). So far, very few CQGs have been found in the present-day universe (e.g. Trujillo et al., 2009; Taylor et al., 2010), though see also Graham et al. (2015) who suggest that CQGs could be hiding in the local universe as the bulges of spheroidal galaxies having grown an additional (2D) disk over the past 9-11 Gyr.

It is still an open question what kind of galaxy evolution leads to the CQGs observed at $z \sim 2$, and how they increased in size, without increasing their SFR significantly, down to $z \sim 0$, for which a size increase by a factor of $\sim 3 - 6$ is required (e.g. Trujillo et al., 2006; Toft et al., 2007; Szomoru et al., 2012). Basically, three formation scenarios have been put forth: i) Massive CQGs formed in a monolithic way, assembling most of their mass at $z > 2 - 3$ and then 'puffed up' (by adiabatic expansion) into the big, red ellipticals we see today (e.g. Bezanson et al., 2009; Damjanov et al., 2009).

ii) A similar scenario to i), but CQGs enhanced their size from $z \sim 2$ to 0 by inside-out growth, most likely due to merging with other small galaxies (minor merging), following a type of hierarchical structure formation like the dark matter (Naab et al., 2009; Oser et al., 2012). The minor merging scenario is in good agreement with the observed metallicity gradients (Kim & Im, 2013) and stellar kinematics (e.g. van de Sande et al., 2013; Arnold et al., 2014) in $z = 0$ quiescent galaxies.

iii) The third possibility, requires a bit more thought. Compared to star-forming galaxies, local quiescent galaxies are more massive at the same SFR but also slightly smaller at the same mass,

for redshifts out to $z \sim 2$. This can be seen in Fig. 2.3 which shows the main sequence of galaxies, including the quiescent ones below it, from $z \sim 0$ to $z \sim 2$. The average size of the quiescent population could grow with time simply if recently quenched (larger) star-forming galaxies are constantly being added to the sample as time moves forward (Trujillo et al., 2012; Poggianti et al., 2013; Krogager et al., 2014, e.g.). This hypothesis also goes under the name ‘progenitor bias’. However, Belli et al. (2015) argued that, for at least half of all CQGs at $z = 2$, the increase in size until $z = 1.5$ must have taken place via growth rather than additions of increasingly larger galaxies to the sample.

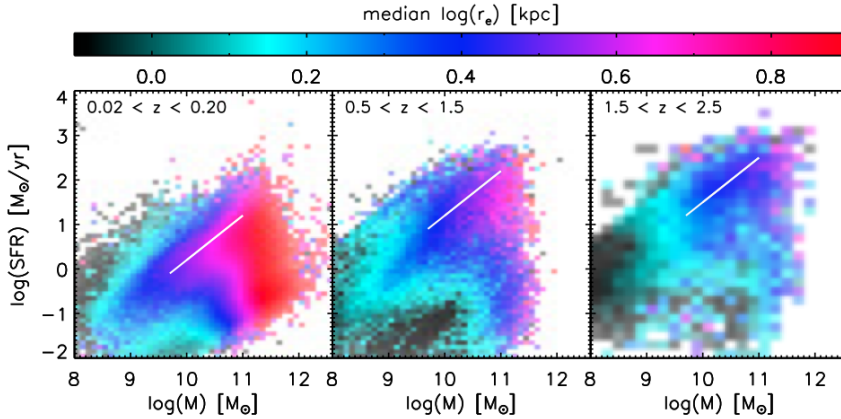


Figure 2.3 Galaxy SFR-mass diagrams in three redshift bins, color-coded by size which is expressed as a circularized effective radius from fitting a Sérsic profile to the rest frame visible or NIR depending on redshift. From Wuyts et al. (2011), who study galaxies from various large samples, including CANDELS (see Section 1.1.2).

The potential quenching by AGNs has led to the idea of a fast evolutionary path from compact star-bursting galaxy at $z \sim 3$ to a galaxy quenched by AGN feedback some 1 – 2 Gyr later and, via size-growth, to a larger, however still quiescent galaxy at $z = 0$. This is illustrated in Fig. 2.4 as an ‘early-track’ route (Barro et al., 2013). In addition, Barro et al. (2013) suggest a late-track evolutionary path, by which larger $z \sim 2$ star-forming galaxies slowly turn off star formation between $z = 2$ and $z = 0$, without passing through a compact phase. This idea was expanded upon by Williams et al. (2014), who suggest that massive, compact galaxies take the fast route and quench sooner than the normally-sized LBGs at $z \sim 2 - 3$.

Galaxy mergers present the kind of violent events that are required for the ‘early-track’ route. In particular, simulations have shown that gas-rich (wet) mergers can lead to bursts of star formation, but that gas is driven towards the center via dissipation and may ignite an AGN. Wet mergers can increase the stellar mass but leave a more compact remnant, whereas gas-poor (dry) mergers can build up a galaxy in mass and size without altering star formation too much (see Lin et al., 2008,

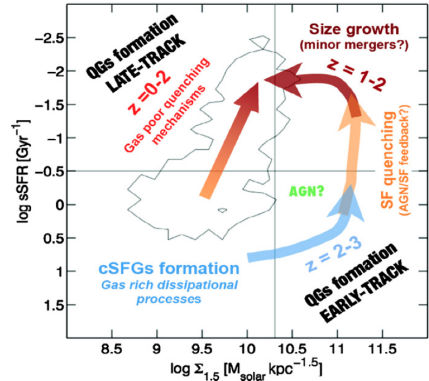


Figure 2.4 Two suggested evolutionary paths from star-forming galaxies at $z = 2 - 3$ to quiescent galaxies at $z = 0$ (Barro et al., 2013).

and references therein). In addition, major mergers are those between galaxies of similar mass whereas minor mergers are those in which the stellar masses differ by a factor of at least ~ 4 (Man et al., 2014).

In order to find the actual progenitors (and descendants for that matter) of the CQGs, we have to look outside the MS, consisting of normal galaxies. Fig. 2.5 illustrates an evolutionary sequence connecting $z \gtrsim 3$ SMGs through compact quiescent $z \sim 2$ galaxies to local elliptical ones (Hopkins et al., 2006; Ricciardelli et al., 2010; Toft et al., 2014; Marchesini et al., 2014). Here, gas-rich major mergers in the early universe trigger a short time period (42_{-29}^{+40} Myr) of high SFR in the form of a nuclear dust-enshrouded starbursts, that we observe as an SMG. That star formation is subsequently quenched either due to gas exhaustion, feedback from the starburst itself or the ignition of an AGN. What is left behind, is a compact stellar remnant that is observed as a CQG about a Gyr after, at $z \sim 2$. Finally, the CQGs grow gradually, and primarily through minor merging, into the elliptical galaxies that we observe today.

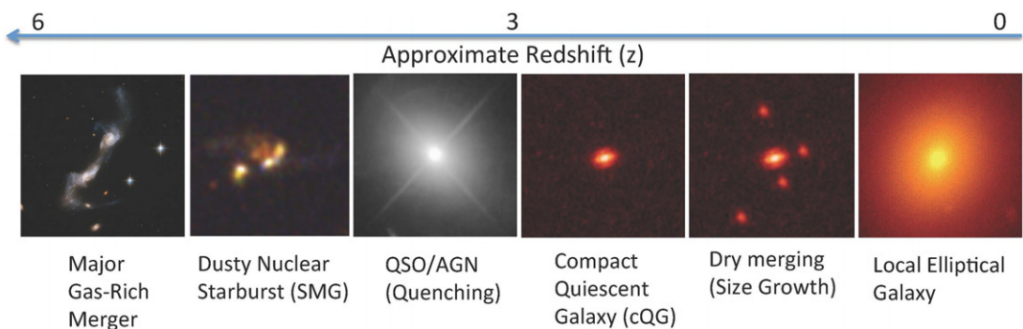


Figure 2.5 The proposed evolutionary sequence by Toft et al. (2014) going from major gas-rich mergers at high redshift (left) to local elliptical quiescent galaxies (right).

But observations of merger rates in massive galaxies at $z \sim 3 - 0$ show that major and minor merging is not enough to bring the CQGs to the sizes of locally observed early-type galaxies, suggesting that other mechanisms are needed for the size growth (Man et al., 2014). And, as summarized in Section 2.1.4, there are many alternative ways to quench star formation in addition to the powerful feedback of an AGN. In order to understand evolution of massive galaxies at high redshifts, it is fundamental to find out which of these mechanisms dominate and when.

2.2 THIS THESIS

The two fundamental questions about galaxy evolution, that were posed in the beginning of this chapter, in Section 2.1.3, could both be related to the observed main sequence of star formation (MS; see Section 1.1):

- 1) *Why does the MS evolve towards higher SFR with redshift?*
- 2) *What causes some galaxies to be outliers to the MS, or ‘quiescent’ galaxies?*

These issues are illustrated in Fig. 2.6, and compose the focus of this thesis. Stars form out of gas, and it would therefore seem natural that these questions translate into: *At what rate did galaxies acquire and use up their gas mass?* The larger part of my thesis focuses on the gas content of galaxies, on which the following subsection expands upon.

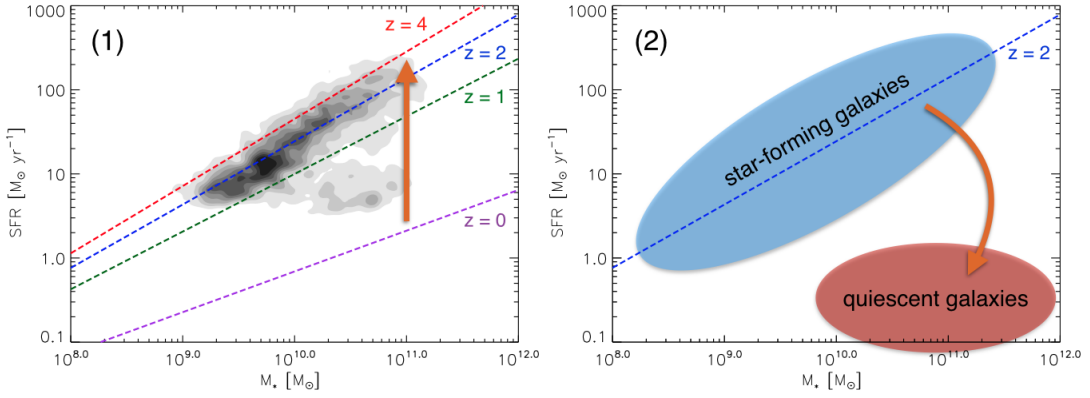


Figure 2.6 Plots showing the MS at various redshifts from Speagle et al. (2014), illustrating the two open questions that need to be answered in order to understand galaxy evolution across cosmic time: 1) Why the MS evolves towards higher SFR with redshift and, 2) Why some galaxies are hardly forming stars, creating a group of red, quiescent galaxies observed all the way out to redshift 3. Contours in the left-hand plot show the position of star-forming galaxies at $1.4 < z < 2.5$ from the NEWFIRM Medium-Band Survey (Whitaker et al., 2011).

2.2.1 ALL EYES ON THE GAS

Most of the above-mentioned mechanisms depend in one way or another on gas amount, as summarized below:

- The gas content together with the amount of in/outflow of gas sets the fuel available for star formation and thereby a 1st order estimate of how long the galaxy can continue producing stars at the current SFR.
- Removal or heating of this gas is what quenches star formation, and is an important milestone in the life of massive galaxies.
- Mergers and the resulting triggering of an AGN, are often invoked as a quenching mechanism, but the outcome of a merger depends critically on how gas-rich the merging galaxies are.

As mentioned in section 1.1, typical galaxies spend 95 % of their lifetime since $z = 1$ within a factor 4 of their average SFR at a given M_* (Noeske et al., 2007). In light of this, most of the evolution in the MS, where galaxies spend most of their lives, might be due to a rising gas mass fraction with redshift. The general consensus is that galaxies at higher redshift were definitely more gas-rich, but the very few observations at $z > 3$ make this statement hard to quantify, as Fig. 2.7 illustrates. This figure shows the gas mass fraction defined as $f_{\text{gas}} = M_{\text{gas}} / (M_{\text{gas}} + M_*)$ as a function of redshift and reveals the uncertainty in its evolution at $z \gtrsim 2$.

Another topic related to the gas and under current debate, is whether the KS law (introduced in Section 1.2.2) might be different in normal galaxies compared to starburst galaxies or mergers, as shown in Fig. 2.8 (though such conclusions depend critically on how the gas mass is determined, a topic we return to in Part I).

A huge missing piece to the puzzle is therefore knowledge of the gas (and dust) in massive galaxies, especially at $z \gtrsim 2$. The premonition, shared by several research groups, is that future observations of the gas and dust content, morphology and dynamics in high- z MS and quiescent galaxies, will solve the puzzle (Carilli & Walter, 2013; Blain, 2015). As put by Glazebrook (2013): ‘...we need to consider the fuel as well as the fire’. As mentioned in 1.5, it is now possible with radio telescopes such as ALMA, JVLA and NOEMA to access the high-redshift domain

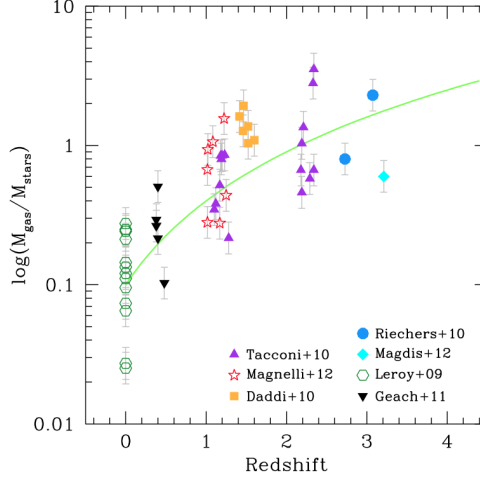


Figure 2.7 Evolution of the gas to stellar mass ratio, M_{gas}/M_* , with redshift for star-forming disk galaxies with $M_* > 10^{10} M_\odot$ (Carilli & Walter, 2013).

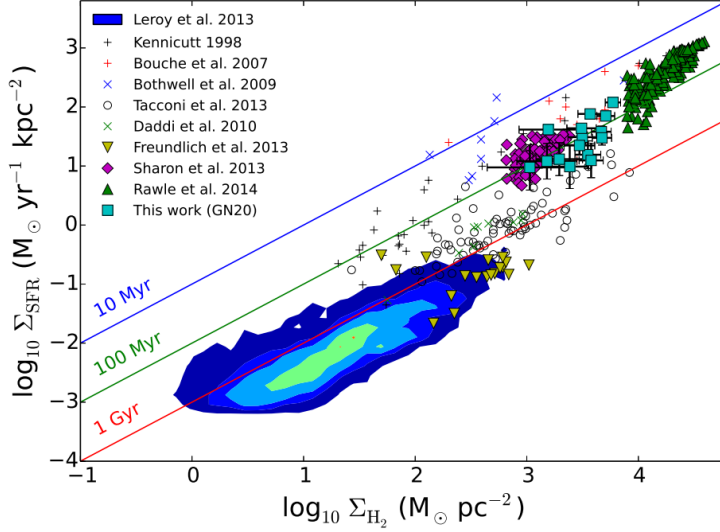


Figure 2.8 The KS law for different galaxy types at high and low redshift from the work of Hodge et al. (2015) who carried out resolved CO(2-1) observations of the $z = 4.05$ SMG GN20, shown with cyan squares. GN20 lies significantly above the relation for local MS galaxies (contours), together with two other strongly lensed, resolved SMGs (magenta diamonds and green triangles), unresolved SMGs (blue crosses and red plus-signs) and local ultraluminous infrared galaxies (ULIRGs; black plus-signs). Close to the local MS galaxies are $z \sim 1.2$ massive star-forming galaxies (yellow upside-down triangles), $z \sim 1 - 3$ color-selected galaxies (black open circles) and $z \sim 1.5$ BzK galaxies (green crosses). See references for these observations in Hodge et al. (2015).

where the red sequence must have formed.

To answer the above questions, we not only need to observe the gas at high redshift in more detail, we also need to know how to interpret those observations better.

2.2.2 QUICK SUMMARY OF MY PROJECTS

I have worked on improving our knowledge of the evolutionary state of massive galaxies at $z = 2$, with regard to 3 aspects:

- Amount and distribution of molecular gas in the ISM
A key species for studying the gas in the ISM was already introduced in Chapter 1 (Section 1.2.2) and will be described in detail in Part I: carbonmonoxide (CO). I used galaxy simulations and developed sub-grid procedures that could be combined with radiative transfer calculations in order to improve predictions for the use of CO lines to estimate the amount and distribution of molecular gas in the ISM of normal star-forming galaxies at $z \sim 2$ (SÍGAME, see Part I Chapter 3).
- Tracing SFR on local and global scales
The line emission of C^+ has been used to trace SFR and various phases of the ISM, including neutral and ionized gas, but it holds many mysteries with its exact origin still unknown. Combining galaxy simulations with sub-grid procedures, I developed a method for modeling [CII] line emission in order to study its origin in the ISM, and make predictions for its use as a star formation tracer at $z \sim 2$ (SÍGAME, see Part I Chapter 5).
- Importance of AGNs in massive galaxies at $z \sim 2$
By analyzing *Chandra* X-ray data from a sample of galaxies at $1.5 \lesssim z \lesssim 2.5$, including the stacked signal from low-luminosity sources, I derive the fraction of luminous and low-luminosity AGNs in star-forming as well as in quiescent massive galaxies (see Part II).

At the beginning of the following chapters some additional background is provided on the specific techniques used in the above listed project, and each chapter will be followed by a list of references.

2.3 REFERENCES

- Adelberger, K. L., Steidel, C. C., Shapley, A. E., et al. 2004, *ApJ*, 607, 226
Arnold, J. A., Romanowsky, A. J., Brodie, J. P., et al. 2014, *ApJ*, 791, 80
Balogh, M. L., Navarro, J. F., & Morris, S. L. 2000, *ApJ*, 540, 113
Barger, A. J., Cowie, L. L., Smail, I., et al. 1999, *AJ*, 117, 2656
Barro, G., Faber, S. M., Pérez-González, P. G., et al. 2013, *ApJ*, 765, 104
Behroozi, P. S., Wechsler, R. H., & Conroy, C. 2013, *ApJ*, 770, 57
Bekki, K., Couch, W. J., & Shioya, Y. 2002, *ApJ*, 577, 651
Belli, S., Newman, A. B., & Ellis, R. S. 2015, *ApJ*, 799, 206
Bezanson, R., van Dokkum, P. G., Tal, T., et al. 2009, *ApJ*, 697, 1290
Blain, A. W. 2015, ArXiv e-prints
Blanton, M. R., & Moustakas, J. 2009, *ARA&A*, 47, 159
Bösch, B., Böhm, A., Wolf, C., et al. 2013, *A&A*, 549, A142
Boselli, A., & Gavazzi, G. 2006, *PASP*, 118, 517
Capak, P. L., Carilli, C., Jones, G., et al. 2015, ArXiv e-prints
Carilli, C. L., & Walter, F. 2013, *ARA&A*, 51, 105
Carilli, C. L., Lee, N., Capak, P., et al. 2008, *ApJ*, 689, 883
Carollo, C. M., Cibinel, A., Lilly, S. J., et al. 2014, ArXiv e-prints

- Casey, C. M., Narayanan, D., & Cooray, A. 2014, *Phys. Rep.*, 541, 45
- Chapman, S. C., Blain, A. W., Smail, I., & Ivison, R. J. 2005, *ApJ*, 622, 772
- Chen, C.-C., Smail, I., Swinbank, A. M., et al. 2015, *ApJ*, 799, 194
- Cimatti, A. 2003, in *The Mass of Galaxies at Low and High Redshift*, ed. R. Bender & A. Renzini, 124
- Cimatti, A., Daddi, E., Renzini, A., et al. 2004, *Nature*, 430, 184
- Conselice, C. J., Chapman, S. C., & Windhorst, R. A. 2003, *ApJ*, 596, L5
- Coppin, K., Halpern, M., Scott, D., Borys, C., & Chapman, S. 2005, *MNRAS*, 357, 1022
- Croton, D. J., Springel, V., White, S. D. M., et al. 2006, *MNRAS*, 365, 11
- Daddi, E., Cimatti, A., Renzini, A., et al. 2004, *ApJ*, 617, 746
- Damjanov, I., McCarthy, P. J., Abraham, R. G., et al. 2009, *ApJ*, 695, 101
- Di Matteo, T., Springel, V., & Hernquist, L. 2005, *Nature*, 433, 604
- Ebeling, H., Stephenson, L. N., & Edge, A. C. 2014, *ApJ*, 781, L40
- Fabian, A. C. 2012, *ARA&A*, 50, 455
- Fan, L., Fang, G., Chen, Y., et al. 2013, *ApJ*, 771, L40
- Fang, J. J., Faber, S. M., Salim, S., Graves, G. J., & Rich, R. M. 2012, *ApJ*, 761, 23
- Feldmann, R., & Mayer, L. 2015, *MNRAS*, 446, 1939
- Glazebrook, K. 2013, in *IAU Symposium*, Vol. 295, *IAU Symposium*, ed. D. Thomas, A. Pasquali, & I. Ferreras, 368–375
- Gobat, R., Strazzullo, V., Daddi, E., et al. 2012, *ApJ*, 759, L44
- Graham, A. W., Dullo, B. T., & Savorgnan, G. A. D. 2015, *ArXiv e-prints*
- Granato, G. L., De Zotti, G., Silva, L., Bressan, A., & Danese, L. 2004, *ApJ*, 600, 580
- Greve, T. R., Pope, A., Scott, D., et al. 2008, *MNRAS*, 389, 1489
- Hodge, J. A., Carilli, C. L., Walter, F., et al. 2012, *ApJ*, 760, 11
- Hodge, J. A., Riechers, D., Decarli, R., et al. 2015, *ApJ*, 798, L18
- Hopkins, P. F., Hernquist, L., Cox, T. J., et al. 2006, *ApJS*, 163, 1
- Hubble, E. P. 1926, *ApJ*, 64, 321
- Hughes, D. H., Serjeant, S., Dunlop, J., et al. 1998, *Nature*, 394, 241
- Karim, A., Swinbank, A. M., Hodge, J. A., et al. 2013, *MNRAS*, 432, 2
- Kartaltepe, J. S., Mozena, M., Kocevski, D., et al. 2014, *ArXiv e-prints*
- Kim, D., & Im, M. 2013, *ApJ*, 766, 109
- Knobel, C., Lilly, S. J., Woo, J., & Kovač, K. 2015, *ApJ*, 800, 24
- Kriek, M., van der Wel, A., van Dokkum, P. G., Franx, M., & Illingworth, G. D. 2008, *ApJ*, 682, 896
- Krogager, J.-K., Zirm, A. W., Toft, S., Man, A., & Brammer, G. 2014, *ApJ*, 797, 17
- Lin, L., Patton, D. R., Koo, D. C., et al. 2008, *ApJ*, 681, 232
- Maiolino, R., Carniani, S., Fontana, A., et al. 2015, *ArXiv e-prints*
- Man, A. W. S., Toft, S., Zirm, A. W., Wuyts, S., & van der Wel, A. 2012, *ApJ*, 744, 85
- Man, A. W. S., Zirm, A. W., & Toft, S. 2014, *ArXiv e-prints*
- Marchesini, D., Muzzin, A., Stefanon, M., et al. 2014, *ApJ*, 794, 65
- McNamara, B. R., & Nulsen, P. E. J. 2007, *ARA&A*, 45, 117
- Moore, B., Lake, G., & Katz, N. 1998, *ApJ*, 495, 139
- Naab, T., Johansson, P. H., & Ostriker, J. P. 2009, *ApJ*, 699, L178
- Noeske, K. G., Weiner, B. J., Faber, S. M., et al. 2007, *ApJ*, 660, L43
- Oser, L., Naab, T., Ostriker, J. P., & Johansson, P. H. 2012, *ApJ*, 744, 63
- Pan, Z., Kong, X., & Fan, L. 2013, *ApJ*, 776, 14
- Perera, T. A., Chapin, E. L., Austermann, J. E., et al. 2008, *MNRAS*, 391, 1227

Poggianti, B. M., Moretti, A., Calvi, R., et al. 2013, *ApJ*, 777, 125
 Reddy, N. A., Erb, D. K., Steidel, C. C., et al. 2005, *ApJ*, 633, 748
 Ricciardelli, E., Trujillo, I., Buitrago, F., & Conselice, C. J. 2010, *MNRAS*, 406, 230
 Riechers, D. A., Carilli, L. C., Walter, F., et al. 2011, *ApJ*, 733, L11
 Schawinski, K., Thomas, D., Sarzi, M., et al. 2007, *MNRAS*, 382, 1415
 Schawinski, K., Urry, C. M., Simmons, B. D., et al. 2014, *MNRAS*, 440, 889
 Simpson, J. M., Swinbank, A. M., Smail, I., et al. 2014, *ApJ*, 788, 125
 Smail, I., Ivison, R. J., & Blain, A. W. 1997, *ApJ*, 490, L5
 Sodré, L., Ribeiro da Silva, A., & Santos, W. A. 2013, *MNRAS*, 434, 2503
 Speagle, J. S., Steinhardt, C. L., Capak, P. L., & Silverman, J. D. 2014, *ApJS*, 214, 15
 Steidel, C. C., Adelberger, K. L., Shapley, A. E., et al. 2003, *ApJ*, 592, 728
 Steidel, C. C., Shapley, A. E., Pettini, M., et al. 2004, *ApJ*, 604, 534
 Steinhauser, D., Haider, M., Kapferer, W., & Schindler, S. 2012, *A&A*, 544, A54
 Strateva, I., Ivezić, Ž., Knapp, G. R., et al. 2001, *AJ*, 122, 1861
 Szomoru, D., Franx, M., & van Dokkum, P. G. 2012, *ApJ*, 749, 121
 Tacconi, L. J., Genzel, R., Smail, I., et al. 2008, *ApJ*, 680, 246
 Taylor, E. N., Franx, M., Glazebrook, K., et al. 2010, *ApJ*, 720, 723
 Toft, S., van Dokkum, P., Franx, M., et al. 2007, *ApJ*, 671, 285
 Toft, S., Smolčić, V., Magnelli, B., et al. 2014, *ApJ*, 782, 68
 Trujillo, I., Carrasco, E. R., & Ferré-Mateu, A. 2012, *ApJ*, 751, 45
 Trujillo, I., Cenarro, A. J., de Lorenzo-Cáceres, A., et al. 2009, *ApJ*, 692, L118
 Trujillo, I., Förster Schreiber, N. M., Rudnick, G., et al. 2006, *ApJ*, 650, 18
 van de Sande, J., Kriek, M., Franx, M., et al. 2013, *ApJ*, 771, 85
 van Dokkum, P. G., Franx, M., Kriek, M., et al. 2008, *ApJ*, 677, L5
 Verdugo, M., Ziegler, B. L., & Gerken, B. 2008, *A&A*, 486, 9
 Viero, M. P., Monceli, L., Quadri, R. F., et al. 2013, *ApJ*, 779, 32
 Villalobos, Á., De Lucia, G., & Murante, G. 2014, *MNRAS*, 444, 313
 Wardlow, J. L., Smail, I., Coppin, K. E. K., et al. 2011, *MNRAS*, 415, 1479
 Watson, D., Christensen, L., Knudsen, K. K., et al. 2015, *Nature*, 519, 327
 Whitaker, K. E., Labbé, I., van Dokkum, P. G., et al. 2011, *ApJ*, 735, 86
 Whitaker, K. E., van Dokkum, P. G., Brammer, G., et al. 2013, *ApJ*, 770, L39
 Williams, C. C., Giavalisco, M., Cassata, P., et al. 2014, *ApJ*, 780, 1
 Williams, R. J., Quadri, R. F., Franx, M., van Dokkum, P., & Labbé, I. 2009, *ApJ*, 691, 1879
 Woo, J., Dekel, A., Faber, S. M., & Koo, D. C. 2015, *MNRAS*, 448, 237
 Wuyts, S., Förster Schreiber, N. M., van der Wel, A., et al. 2011, *ApJ*, 742, 96

Part I

Modeling the ISM of $z \sim 2$ galaxies with SÍGAME

3

CO EMISSION LINES FROM GALAXIES

3.1 PROBING THE MOLECULAR GAS

Due to the high abundance of hydrogen, the most common molecule to find in the ISM, is by far H_2 . But in terms of observing cold molecular gas, H_2 is practically invisible, because the lack of an electric dipole moment means that the lowest possible rotational transitions of H_2 are electric quadrupole moments with very high energy. The first rotational transition, $S(0)$, is at 510 K, meaning that even the lowest rotational transitions can only be excited in shock waves, FUV-rich PDRs or regions affected by turbulent dissipation (Ingalls et al., 2011).

The second most abundant molecule is carbonmonoxide, CO, consisting of one carbon and one oxygen atom. The abundance relative to H_2 , $[\text{CO}/\text{H}_2]$, is roughly 10^{-4} in MW ISM as has been determined via observations of early cold cores in the MW (Glover & Mac Low, 2011; Liu et al., 2013) and simulations of molecular clouds with $n_{\text{H}} \gtrsim 1000 \text{ cm}^{-3}$ (Glover & Mac Low, 2011).

CO is the most used molecule for observing molecular gas, since its rotational transitions conveniently sample the typical densities and temperatures inside GMCs. To probe the very densest parts of GMCs, other molecular tracers exist with higher critical densities (again see Tielens 2013 for an overview of most detected molecules, and Aalto 2013 for a subset of the denser gas tracers), but the low CO lines have proven excellent for capturing the majority of the molecular gas.

Fig. 3.1 provides an illustration of the rotating CO molecule, together with the frequencies and critical densities of the first 5 transitions. Also, the positions of the first 5 transitions on a typical SED can be seen in Fig. 1.11. In GMCs, the excitation of CO molecules to higher rotational levels is believed to come mainly from collisions with H_2 molecules. The population of the various rotational levels are therefore deter-

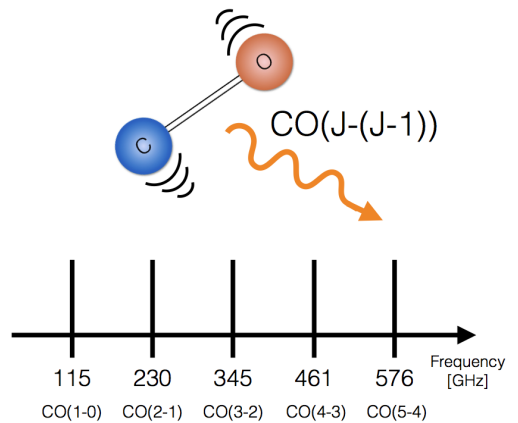


Figure 3.1 Illustration of the rotating CO molecules together with the frequencies of the first 5 rotational lines of the CO molecular are shown. Below are the corresponding critical densities ($n_{\text{crit}} = A_{ul} \sum_{i \neq u} C_{ui}$) as calculated by Greve et al. (2014) for a kinetic temperature of $T_k = 40 \text{ K}$ and assuming H_2 to be the main collision partner.

mined by density and temperature (how fast the molecules are moving) of the gas. The amount of flux in each rotational transition creates a CO Spectral Line Energy Distribution (SLED) or ‘CO ladder’ which can take on different shapes depending on the gas properties.

3.2 OBSERVATIONS OF CO LINE EMISSION FROM DIFFERENT TYPES OF GALAXIES AT $z \gtrsim 2$

At $z \sim 2$, the vast majority of CO observations have been of extreme galaxies, such as submillimeter galaxies (SMGs) with very high SFRs or quasi-stellar objects (QSOs) containing powerful AGNs. Only a few galaxies on the “main sequence of star formation” (MS, e.g. Wuyts et al., 2011), have been observed in CO. These are typically massive ($10^{10} - 10^{11} M_{\odot}$) galaxies selected by the BzK technique to be moderately star-forming with $\text{SFR} \simeq 10 - 500 M_{\odot} \text{ yr}^{-1}$, i.e. specific SFR (SSFR) of around 0.5 Gyr^{-1} . The molecular gas of SMGs and QSOs is highly excited with peak fluxes at the CO(5-4) and CO(6-5) transitions, which is evidence of dense and possibly warm gas (Papadopoulos et al., 2012), but little is known for the normal star-forming galaxies observed in CO to date. The only such galaxies, with 4 observed CO transitions, are the BzK-selected galaxies BzK-4171, BzK-16000 and BzK-21000 (Daddi et al., 2015). These galaxies were previously believed to contain mainly gas reminiscent to that of the Milky Way (MW) (Dannerbauer et al., 2009; Aravena et al., 2014), but new CO(5-4) observations by Daddi et al. (2015) require a second component of higher density and possibly higher temperature.

With instruments of high spatial resolution, it has recently become possible to resolve galaxies at $z \gtrsim 2$ on kiloparsec scales, as shown with the VLA by e.g. Walter et al. (2007) when observing low- J CO transitions. Scales of 1 kpc require a resolution of $\sim 0.1''$ at $z = 2$, achievable with ALMA for higher CO lines that are not redshifted below its bands.

When measuring the CO ladder of galaxies with different compositions, SFR and AGN activity, a huge variety emerges. Fig. 3.2 compares the rather low-excitation ladder of the MW to the CO ladders of SMGs and QSOs which peak at increasingly higher J -values. An upper limit as to how steep the ladder can be, is reached if the gas is in Local Thermal Equilibrium (LTE), in which case the level populations just follow a Boltzmann distribution set by the gas kinetic temperature and no radiative transitions are considered. For gas in LTE and of kinetic temperature above that of the upper level transition level, the CO ladder would grow as J^2 as indicated in Fig. 3.2 in blue. But in general, this upper limit is not reached by the local kinetic temperature and the high J -levels are less populated.

3.2.1 THE X_{CO} FACTOR

Probably the widest use of CO emission lines, is the estimation of total molecular gas mass. The low critical density ($\sim 300 \text{ cm}^{-3}$) of the first CO(1-0) transition makes it a tracer of most gas in a GMC. In order to convert from CO(1-0) line intensity and column density of H_2 , the CO- H_2 conversion factor (X_{CO} or ‘ X -factor’) gives the H_2 column density per CO(1-0) intensity unit:

$$X_{\text{CO}} [\text{cm}^{-2}/(\text{K km s}^{-1})^{-1}] = N(\text{H}_2)/W_{\text{CO}(1-0)} \quad (3.1)$$

A similar conversion factor exists between total H_2 gas mass amount and CO line luminosity:

$$\alpha_{\text{CO}} [M_{\odot}/(\text{K km pc}^{-2})^{-1}] = M(\text{H}_2)/L_{\text{CO}(1-0)} \quad (3.2)$$

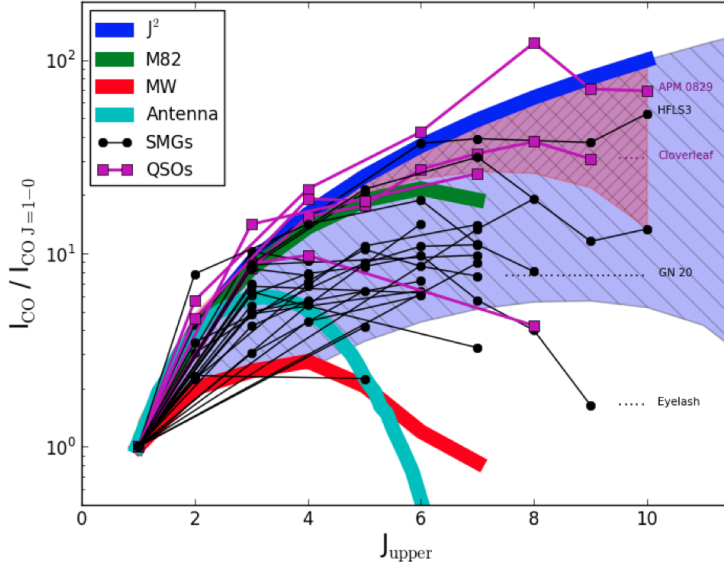


Figure 3.2 Observed CO ladders for different galaxies, normalized to the CO(1-0) transition. From the review of Casey et al. (2014).

The most common way of inferring their values, is to estimate the gas mass from either (i) the CO line width assuming the GMCs are in virial equilibrium (cf. eq. 1.2), (ii) the dust mass assuming a dust-to-gas mass ratio, or (iii) γ -ray emission from cosmic ray interactions with H_2 (see references in Narayanan et al., 2012). In the inner disk of the MW, they are relatively constant at $X_{\text{CO}} \approx 2 \times 10^{20} \text{ cm}^{-2} / (\text{K km s}^{-1})^{-1}$ and $\alpha_{\text{CO}} \approx 4.3 \text{ M}_{\odot} / (\text{K km pc}^{-2})^{-1}$ (from the comprehensive review on the X -factor by Bolatto et al., 2013).

But recent observations, at low and high redshift, show that X_{CO} must be lower in galaxies of high-surface density environments, and larger in low-metallicity environments. This has led to the belief that maybe there exists two versions of the KS star formation relation, one for gas-rich mergers and another for star-forming normal disk galaxies (Genzel et al., 2010). Based on detailed modeling, Narayanan et al. (2012) came up with a function for X_{CO} that depends on CO line luminosity and metallicity. With this prescription for X_{CO} a single continuous KS star formation relation can be drawn for starbursts and normal disk galaxies at low and high redshift as shown in Fig. 3.3. However, see the work of Hodge et al. (2015), implying that SMGs really can have more efficient star formation on small scales, regardless of the choice of conversion factor.

3.3 MODELING OF CO EMISSION LINES

The CO ladder of a galaxy can be modeled by combining galaxy simulations (either zoom-in versions of cosmological simulations or isolated galaxy models, cf. Section 1.6) with sub-grid prescriptions for the GMC structure and radiative transfer codes or LVG models for the transport of CO line emission through the ISM. Over the past decade in particular, detailed modeling of CO emission has been developed, the basic steps of which can be summarised as follows: (1) Simulate a galaxy with dark matter, stars and atomic gas (if possible, with a multiphase molec-

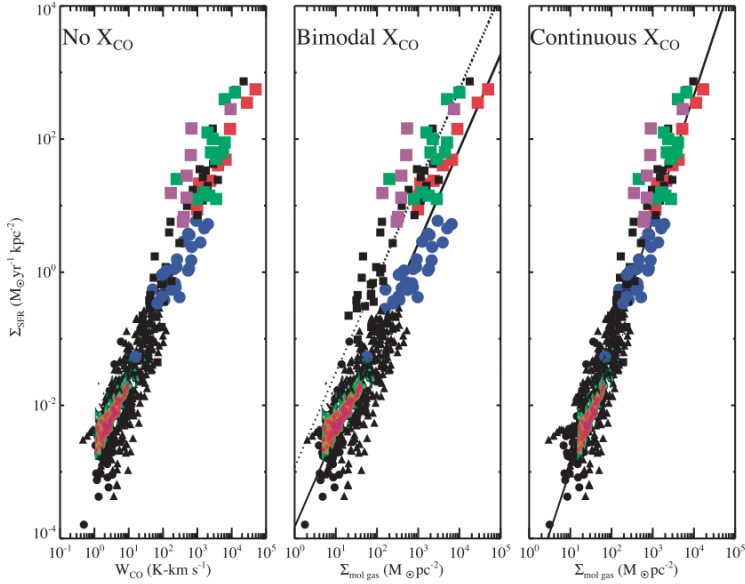


Figure 3.3 The effect of using an effectively bimodal X_{CO} factor (mid panel; $\alpha_{\text{CO}} = 4.5$ for local disks, 3.6 for high- z disks and $0.8 M_{\odot} / (\text{K km pc}^{-2})^{-1}$ for mergers) or a continuous one (right panel) on the KS law (Narayanan et al., 2012).

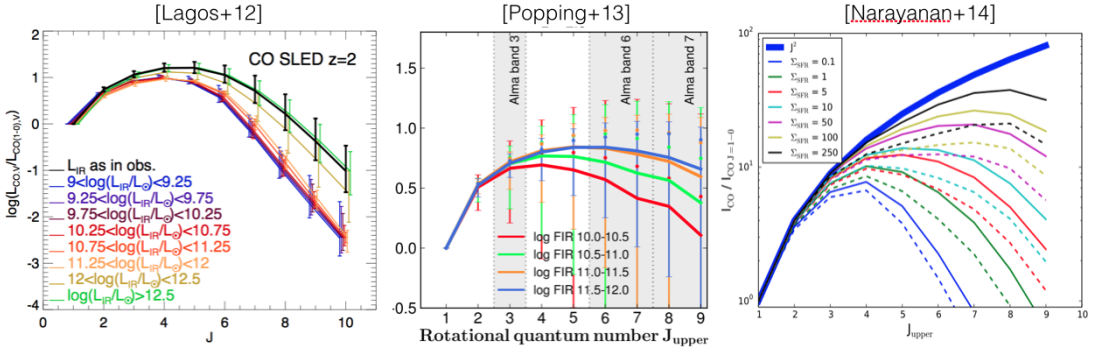


Figure 3.4 Examples of simulated CO ladders for different galaxy types. *Left*: The shape of CO ladders for $z = 2$ galaxies, binned according to infrared ($8 - 1000 \mu\text{m}$) luminosity, L_{IR} , as predicted by Lagos et al. (2012), *Middle*: The same as in the left panel according to the method of Popping et al. (2014), *Right*: CO ladders parameterized by Σ_{SFR} for simulations of resolved (solid) and unresolved (dashed) cases, as derived by Narayanan & Krumholz (2014).

ular gas), (2) Apply semi-analytical physical recipes to estimate the amount and state of dust and molecular gas, (3) Calculate the radiative transfer of selected CO lines. A full description of such a process can be found in Narayanan et al. (2008b), who investigated the signatures in CO morphology and line profile of outflows created by active galactic nuclei (AGNs) and starbursts. The same method has been used to study other aspects of the ISM, such as the Kennicutt-Schmidt relation and the X_{CO} factor which relates velocity-integrated CO line intensity to H_2 column density, in low- and high-redshift galaxies (e.g., Narayanan et al., 2011; Narayanan & Hopkins, 2013). By running smoothed particle hydrodynamical (SPH) simulations with the GADGET-3 code, Narayanan et al. (2011) were able to follow the evolution with

time of a multiphase ISM in isolated disk galaxies undergoing a merger, allowing the gas to cool down to temperatures of ~ 10 K. Lagos et al. (2012) simulated the CO emission of quiescently star-forming as well as starburst galaxies at redshifts ranging from $z = 0$ to $z = 6$ by coupling cosmological galaxy formation simulations with the tabulated output of a code describing photon dominated regions (PDRs). Lagos et al. (2012) found that the global velocity-integrated CO line intensity peaks at higher rotational transitions with increasing infrared (IR) luminosity (J -level 4 to 5 when median L_{IR} of the sample goes from about $1.3 \sim 10^9$ to $8 \times 10^{12} L_{\odot}$). In a similar study, Popping et al. (2014) found that models of normal star-forming galaxies at high redshift have much higher rotational transitions than their local counterparts. Finally, the modeling of CO lines from a large set of simulated disk galaxies, recently carried out by Narayanan & Krumholz (2014) showed that the CO line energy distribution can be parameterised better with respect to SFR surface density compared to total SFR. Simulated CO SLEDs in in Fig. 3.4 provide examples of these previous works. However simulations of resolved CO line emission have been lacking.

4

SIMULATING CO LINE EMISSION FROM MASSIVE STAR-FORMING GALAXIES AT $z = 2$ (PAPER I)

4.1 AIM OF THIS PROJECT

We wanted to expand on previous modeling done by other groups of CO emission lines from galaxies at high redshift by developing a method that focuses on radial gradients of the X_{CO} factor and CO line ratios. The aim of the project was therefore to serve as a preview of what astronomers might one day observe in ‘normal’ star-forming galaxies at $z \sim 2$ with new and upcoming instruments.

For that purpose, we created a new numerical framework for simulating the line emission of normal star-forming galaxies. The code – Simulator of GALaxy Millimeter/submillimeter Emission (SÍGAME¹) – combines (non-)cosmological simulations of galaxy formation with sub-grid prescriptions for the H_2/HI fraction and thermal balance throughout the ISM, down to parsec scales. SÍGAME accounts for a FUV and cosmic ray intensity field that vary with local SFR density within the galaxy. SÍGAME can be applied to any galaxy simulated in the SPH formalism, though currently restricted to galaxies dominated by star formation processes rather than AGN and with mean metallicities above about $0.01Z_{\odot}$. Here, we adapt the code to cosmological SPH simulations of three massive, normal star-forming galaxies at $z = 2$ (i.e., so-called main-sequence galaxies), and model their CO rotational line spectrum using a publicly available 3D radiative transfer code. We show that SÍGAME reproduces observed low- J CO line luminosities and provides new estimates of the X_{CO} factor for main-sequence galaxies at $z \sim 2$, while at the same time predicting their CO line luminosities at high- J ($J_{\text{up}} > 6$) transitions where observations are yet to be made.

The structure of this chapter is as follows. Section 4.2 describes the cosmological SPH simulations used, along with the basic properties of the three star-forming galaxies extracted from the simulations. A detailed description of SÍGAME is presented in Section 4.3. The CO emission maps and spectra obtained after applying SÍGAME to the three simulated galaxies are presented in Section 4.4, where we also compare to actual CO observations of similar galaxies at $z \sim 2$. Section 4.6 discusses the strengths and weaknesses of SÍGAME in the context of other molec-

¹SÍGAME in Spanish translates as ‘follow me’ - which in this context refers to the pursue of line emission through a galaxy.

ular line (CO) simulations and recent observations. Finally, in Section 4.7 we summarise the main steps of SÍGAME, and list its main findings and predictions regarding the CO line emission from massive, star-forming galaxies at $z \simeq 2$. We adopt a flat cold dark matter (Λ CDM) scenario with $\Omega_m = 0.3$, $\Omega_\Lambda = 0.7$ and $h = 0.65$.

4.2 COSMOLOGICAL SIMULATIONS

4.2.1 SPH SIMULATIONS

We employ a cosmological TreeSPH code for simulating galaxy formation and evolution, though in principle, grid-based hydrodynamic simulations could be incorporated equally well. The TreeSPH code used for the simulations is in most respects similar to the one described in Sommer-Larsen et al. (2005) and Romeo et al. (2006). A cosmic baryon fraction of $f_b = 0.15$ is assumed, and simulations are initiated at a redshift of $z = 39$. The implementation of star formation and stellar feedback, however, has been manifestly changed.

Star formation is assumed to take place in cold gas ($T_k \lesssim 10^4$ K) at densities $n_H > 1 \text{ cm}^{-3}$. The star formation efficiency (or probability that a gas particle will form stars) is formally set to 0.1, but is, due to effects of self-regulation, considerably lower. Star formation takes place in a stochastic way, and in a star formation event, 1 SPH gas particle is converted completely into 1 stellar SPH particle, representing the instantaneous birth of a population of stars according to a Chabrier (2003) stellar initial mass function (IMF; Chabrier 2003) – see further below.

The implementation of stellar feedback is based on a sub-grid super-wind model, somewhat similar to the ‘high-feedback’ models by Stinson et al. (2006). These models, though, build on a supernova blast-wave approach rather than super-wind models. Both types of models invoke a Chabrier (2003) IMF, which is somewhat more top-heavy in terms of energy and heavy-element feedback than, e.g., the standard Salpeter IMF. The present models result in galaxies characterised by reasonable $z = 0$ cold gas fractions, abundances and circum-galactic medium abundance properties. They also improve considerably on the “angular momentum problem” relative to the models presented in, e.g., Sommer-Larsen et al. (2003). The models will be described in detail in a forthcoming paper.

4.2.2 THE MODEL GALAXIES

Three model galaxies, hereafter referred to as G1, G2 and G3 in order of increasing SFR, were extracted from the above SPH simulation and re-simulated using the ‘zoom-in’ technique described in (e.g., Sommer-Larsen et al., 2003). The emphasis in this study is on massive ($M_* \gtrsim 5 \times 10^{10} M_\odot$) galaxies, and the three galaxies analysed are therefore larger, rescaled versions of galaxies formed in the $10/h$ Mpc cosmological simulation described in Sommer-Larsen et al. (2003). The linear scale-factor is of the order 1.5, and since the CDM power spectrum is fairly constant over this limited mass range the rescaling is a reasonable approximation.

Galaxy G1 was simulated at fairly high resolution, using a total of 1.2×10^6 SPH and dark matter particles, while about 9×10^5 and 1.1×10^6 particles were used in the simulations of G2 and G3, respectively. For the G1 simulation, the masses of individual SPH gas, stellar and dark matter particles are $m_{\text{SPH}} = m_* \approx 6.3 \times 10^5 h^{-1} M_\odot$ and $m_{\text{DM}} = 3.5 \times 10^6 h^{-1} M_\odot$, respectively. Gravitational (cubic spline) softening lengths of 310, 310 and $560 h^{-1} \text{ pc}$, respectively, were employed. Minimum gas smoothing lengths were about $50 h^{-1} \text{ pc}$. For the lower resolution simulations of galaxies G2 and G3, the corresponding particle masses are $m_{\text{SPH}} = m_* \approx 4.7 \times$

Table 4.1 Physical properties of the three simulated galaxies G1, G2, and G3

	SFR [$M_{\odot} \text{ yr}^{-1}$]	M_{*} [$10^{11} M_{\odot}$]	M_{SPH} [$10^{10} M_{\odot}$]	f_{SPH}	Z'	R_{cut} [kpc]
G1	40	0.53	2.07	28%	1.16	20
G2	80	1.49	2.63	15%	1.97	15
G3	142	2.11	4.66	18%	1.36	20

Notes. All quantities are determined within a radius R_{cut} , which is the radius where the cumulative radial stellar mass function of each galaxy becomes flat. The gas mass (M_{SPH}) is the total SPH gas mass within R_{cut} . The metallicity ($Z' = Z/Z_{\odot}$) is the mean of all SPH gas particles within R_{cut} .

$10^6 h^{-1} M_{\odot}$ and $m_{\text{DM}} = 2.6 \times 10^7 h^{-1} M_{\odot}$, respectively, and the gravitational softening lengths were 610, 610 and $1090 h^{-1} \text{pc}$. Minimum gas smoothing lengths were about $100 h^{-1} \text{pc}$.

Due to effects of gravitational softening, typical velocities in the innermost parts of the galaxies (typically at radii less than about $2\epsilon_{\text{SPH}}$, where ϵ_{SPH} is the SPH and star particle gravitational softening length) are somewhat below dynamical values (see, e.g. Sommer-Larsen et al., 1998). The dynamical velocities will be of the order $v_{\text{dyn}} = \sqrt{GM(R)/R}$, where G is the gravitational constant, R is the radial distance from the centre of the galaxy and $M(R)$ is the total mass located inside of R . Indeed, it turns out that for the simulated galaxies considered in this project SPH particle velocities inside of $2\epsilon_{\text{SPH}}$ are only about 60-70% of what should be expected from dynamics. To coarsely correct for this adverse numerical effect, for SPH particles inside of $2\epsilon_{\text{SPH}}$ the velocities are corrected as follows: For SPH particles of total velocity less than v_{dyn} , the tangential component of the velocity is increased such that the total velocity becomes equal to v_{dyn} . Only the tangential component is increased in order not to create spurious signatures of merging. With this correction implemented, the average ratio of total space velocity to dynamical velocity of all SPH particles inside of $2\epsilon_{\text{SPH}}$ equals unity.

Figure 4.1 shows surface density maps of the SPH gas in G1, G2, and G3, i.e., prior to any post-processing by *SÍGAME*. The gas is seen to be strongly concentrated towards the centre of each galaxy and structured in spiral arms containing clumps of denser gas. The spiral arms reach out to a radius of about 20 kpc in G1 and G3, with G2 showing a more compact structure that does not exceed $R \sim 15 \text{ kpc}$. Table 4.1 lists key properties of the simulated galaxies, namely their SFR, stellar mass (M_{*}), SPH gas mass (M_{SPH}), SPH gas mass fraction ($f_{\text{SPH}} = M_{\text{SPH}}/(M_{*} + M_{\text{SPH}})$), and metallicity Z' . These quantities were measured within a radius (R_{cut} , also given in Table 4.1) corresponding to where the radial cumulative stellar mass function has flattened out. The metallicity is in units of solar metallicity and is calculated from the abundances of C, N, O, Mg, Si, S, Ca and Fe in the SPH simulations, and adjusted for the fact that not all heavy metals have been included according to the solar element abundancies measured by Asplund et al. (2009).

The location of our three model galaxies in the SFR- M_{*} diagram is shown in Figure 4.2 along with a sample of 3754 $1.4 < z < 2.5$ main-sequence galaxies selected in near-IR from the NEWFIRM Medium-Band Survey (Whitaker et al., 2011). The latter used a Kroupa IMF but given its similarity with a Chabrier IMF no conversion in the stellar mass and SFR was made (cf., Papovich et al. (2011) and Zahid et al. (2012) who use conversion factors of 1.06 and 1.13, respectively). Also shown is the determination of the main-sequence relation at $z \simeq 2$ by

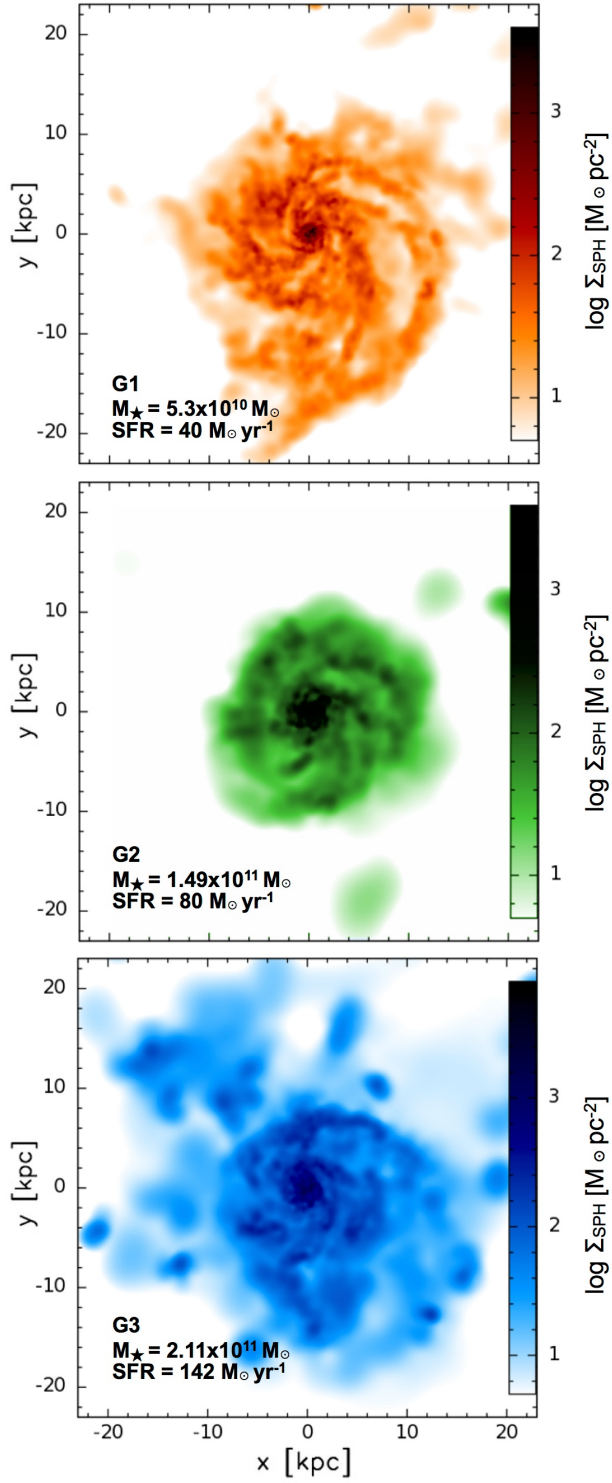


Figure 4.1 SPH gas surface density maps of the three model galaxies G1 (top), G2 (middle), and G3 (bottom) viewed face-on. The stellar masses and SFRs of each galaxy are indicated (see also Table 4.1). The maps have been rendered with the visualization tool SPLASH version 2.4.0 (Price, 2007) using the gas smoothing lengths provided by the simulations.

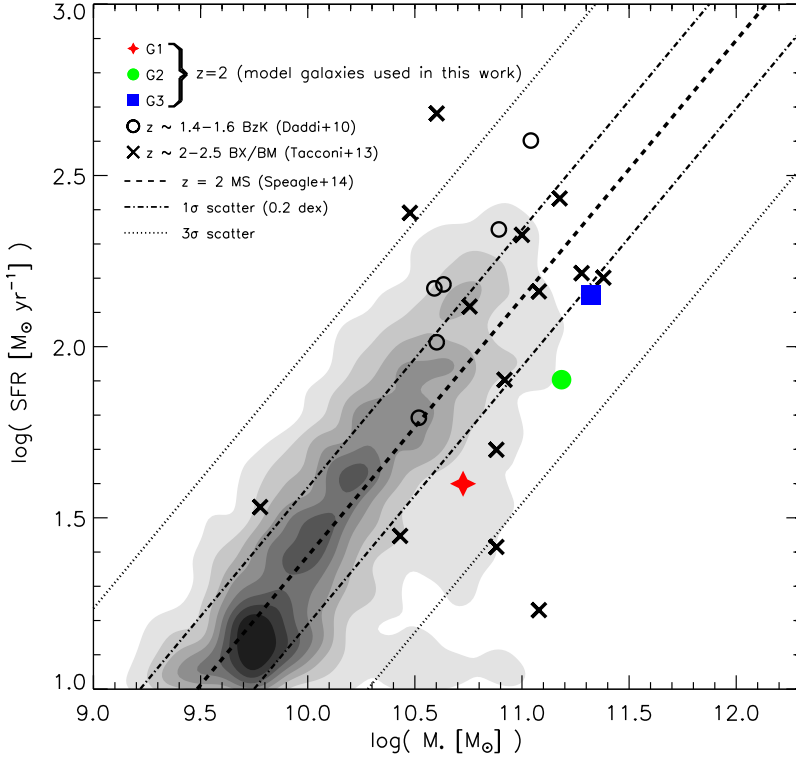


Figure 4.2 Position of the three model galaxies studied here (G1, G2 and G3 with filled a red star, a green circle and a blue square respectively), on a SFR- M_* diagram. The grey filled contours show the $z \sim 2$ number density of 3754 $1.4 < z < 2.5$ galaxies from the NEWFIRM Medium-Band Survey (Whitaker et al., 2011). The SFR - M_* relation at $z \sim 2$ as determined by Speagle et al. (2014) is indicated by the dashed line, with the 1σ and 3σ scatter of the relation shown by the dot-dashed and dotted lines, respectively. Also shown are six $z \sim 1.4 - 1.6$ BzK galaxies (black circles; Daddi et al. 2010) and 14 $z \sim 2 - 2.5$ Bx/BM galaxies (black crosses; Tacconi et al. 2013). The BzK galaxies are from top to bottom: BzK-12591, BzK-21000, BzK-16000, BzK-17999, BzK-4171 and BzK-2553 (following the naming convention of Daddi et al. 2010).

Speagle et al. (2014), and the 1 and 3σ scatter around it. G1, G2, and G3 are seen to lie within the 3σ scatter around the $z \sim 2$ main sequence, albeit offset somewhat towards lower SFRs. This latter tendency is also found among a subset of CO-detected Bx/BM galaxies at $z \sim 2 - 2.5$ (Tacconi et al., 2013), highlighted in Figure 4.2 along with a handful of $z \sim 1.5$ BzK galaxies also detected in CO (Daddi et al., 2010). The Bx/BM galaxies are selected by a UGR colour criteria (Adelberger et al., 2004), while the BzK galaxies are selected by the BzK colour criteria (Daddi et al., 2004). Based on the above we conclude that, in terms of stellar mass and SFR, our three model galaxies are representative of the star-forming galaxy population detected in CO at $z \sim 2$.

4.3 MODELING THE ISM WITH SÍGAME

4.3.1 METHODOLOGY OVERVIEW

Here we give an overview of the major steps that go into SÍGAME, along with a brief description of each. The full details of each step are given in subsequent sections and in appendices A.1 through A.3. We stress, that SÍGAME operates entirely in the post-processing stage of an SPH simulation, and can in principle easily be adapted to any given SPH galaxy simulation as long as certain basic quantities are known for each SPH particle in the simulation, namely: position (r), velocity (\vec{v}), atomic hydrogen density (n_{H}), metallicity (Z'), kinetic temperature (T_{k}), smoothing length (h), and star formation rate (SFR). The key steps involved in SÍGAME are:

1. Cooling of the SPH gas. The initially hot ($T_{\text{k}} \sim 10^{3-7}$ K) SPH gas particles are cooled to temperatures typical of the warm neutral medium ($\lesssim 10^4$ K) by atomic and ionic cooling lines primarily.
2. Inference of the molecular gas mass fraction ($f'_{\text{mol}} = m_{\text{H}_2}/m_{\text{SPH}}$) of each SPH particle after the initial cooling in step 1. f'_{mol} for a given SPH particle is calculated by taking into account its temperature, metallicity, and the local CR and FUV radiation field impinging on it.
3. Distribution of the molecular gas into GMCs. Cloud masses and sizes are obtained from random sampling of the observed GMC mass-spectrum in nearby quiescent galaxies and applying the local GMC mass-size relation.
4. GMC thermal structure. A radial density profile is adopted for each GMC and used to calculate the temperature structure throughout individual clouds, taking into account heating and cooling mechanisms relevant for neutral and molecular gas, when exposed to the local CR and attenuated FUV fields.
5. Radiative transport of CO lines. Finally, the CO line spectra are calculated separately for each GMC with a radiative transfer code and accumulated on a common velocity axis for the entire galaxy.

Determining the temperature (i) and the molecular gas mass fraction (ii) of a warm neutral gas SPH particle cannot be done independently of each other, but must be solved for simultaneously in an iterative fashion (see Sections 4.3.2 and 4.3.3). As already mentioned, we shall apply SÍGAME to the SPH simulations of galaxies G1, G2, and G3 described in Section 4.2, and in doing so we will use them to illustrate the workings of the code.

4.3.2 THE WARM AND COLD NEUTRAL MEDIUM

In SPH simulations of galaxies the gas is typically not cooled to temperatures below a few thousand Kelvin (Springel & Hernquist, 2003). This is illustrated in Figure 4.3, which shows the SPH gas temperature distribution (dashed histogram) in G1 (for clarity we have not shown the corresponding temperature distributions for G2 and G3, both of which are similar to that of G1). Minimum SPH gas temperatures in G1, G2 and G3 are about 1200 K, 3100 K and 3200 K, respectively, and while temperatures span the range $\sim 10^{3-7}$ K, the bulk ($\sim 80 - 90\%$) of the gas mass in all three galaxies is at $T_{\text{k}} \lesssim 10^5$ K.

At these temperatures the gas will be in atomic or ionised form, and H atoms that attach to dust grain surfaces via chemical bonds (chemisorbed) will evaporate from the grains before H_2 can be formed. H_2 can effectively only exist at temperatures below $\sim 10^3$ K, assuming a realistic desorption energy of 3×10^4 K for chemisorbed H atoms (see Cazaux & Spaans, 2004). The first step of SÍGAME is therefore to cool some portion of the hot SPH gas down to $T_k \lesssim 10^3$ K, i.e., a temperature range characteristic of a warm and cold neutral medium for which we can meaningfully employ a prescription for the formation of H_2 .

SÍGAME employs the standard cooling and heating mechanisms pertaining to a hot, partially ionised gas. Cooling occurs primarily via emission lines from H, He, C, O, N, Ne, Mg, Si, S, Ca, and Fe in their atomic and ionised states, with the relative importance of these radiative cooling lines depending on the temperature (Wiersma et al., 2009). In addition to these emission lines, electron recombination with ions can cool the gas, as recombining electrons take away kinetic energy from the plasma, a process which is important at temperatures $> 10^3$ K (Wolfire et al., 2003). At similar high temperatures another important cooling mechanism is the scattering of free electrons off other free ions, whereby free-free emission removes energy from the gas (Draine, 2011). Working against the cooling is heating caused by cosmic rays via the expulsion of bound electrons from atoms or the direct kinetic transfer to free electrons via Coulomb interactions (Simnett & McDonald, 1969). By ignoring heating of the gas by photoionization, we shall adopt an assumption typically used for galactic ISM (Gnat & Sternberg, 2007; Smith et al., 2008), though see Wiersma et al. (2009) who demonstrate how cooling rates are reduced when including photoionization in the intergalactic medium and proto-galaxies.

We arrive at a first estimate of the temperature of the neutral medium by requiring energy rate equilibrium between the above mentioned heating and cooling mechanisms:

$$\Gamma_{\text{CR,HI}} = \Lambda_{\text{ions+atoms}} + \Lambda_{\text{rec}} + \Lambda_{\text{f-f}}, \quad (4.1)$$

where $\Lambda_{\text{ions+atoms}}$ is the cooling rate due to atomic and ionic emission lines, Λ_{rec} and $\Lambda_{\text{f-f}}$ are the cooling rates from recombination processes and free-free emission as described above, and $\Gamma_{\text{CR,HI}}$ is the CR heating rate in atomic, partly ionised, gas. The detailed analytical expressions employed by SÍGAME for these heating and cooling rates are given in appendix A.1.

The abundances of the atoms and ions included in $\Lambda_{\text{ions+atoms}}$ either have to be calculated in a self-consistent manner as part of the SPH simulation or set by hand. For our set of galaxies, the SPH simulations follow the abundances of H, C, N, O, Mg, Si, S, Ca and Fe, while for the abundances of He and Ne, we adopt solar mass fractions of 0.2806 and 10^{-4} , respectively, as used in Wiersma et al. (2009).

$\Gamma_{\text{CR,HI}}$ depends on the *primary* CR ionization rate (ζ_{CR}), a quantity that is set by the number density of supernovae since they are thought to be the main source of CRs (Ackermann et al., 2013). In SÍGAME, this is accounted for by parameterizing ζ_{CR} as a function of the *local* star formation rate density (SFRD) as it varies across the simulated galaxy. The details of this parameterization are deferred to Section 4.3.4.

In eq.4.1, all terms but $\Lambda_{\text{ions+atoms}}$ depend on the ionization fraction ($x_e = n_e/n_{\text{HI}}$) of the gas, which in turn depends on the *total* CR ionization rate (i.e., ζ_{CR} corrected for secondary ionizations of H and He), the gas temperature (T_k), and the HI density (n_{HI}) (see appendix A.1). The ionization fraction is calculated taking into account the ionization of H and He (with a procedure kindly provided by I. Pelupessy; see also Pelupessy (2005)). Since, n_{HI} is set by the molecular gas mass fraction (f'_{mol}), which in turn also depends on T_k (see Section 4.3.3 on how

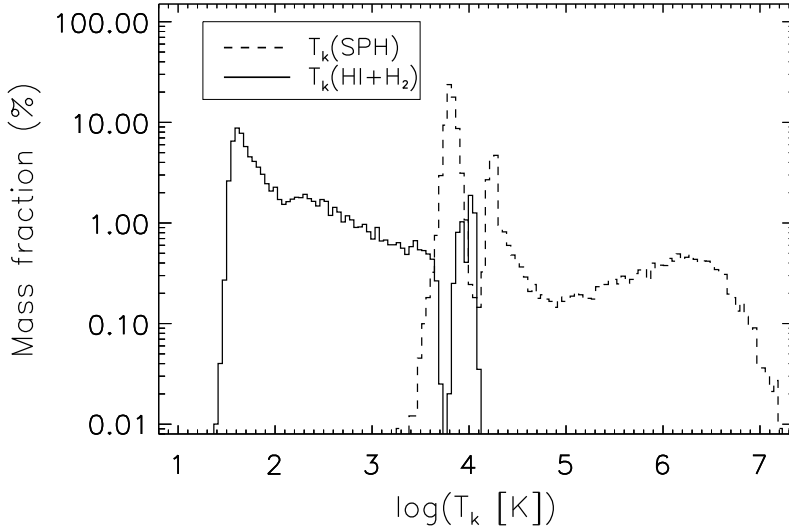


Figure 4.3 The distributions of gas kinetic temperature before (dashed histogram) and after (solid histogram) applying the heating and cooling mechanisms of eq. 4.1 to galaxy G1. The original hot SPH gas is seen to span a temperature range from about 10^3 K up to $\sim 10^7$ K, while once the gas has been cooled the temperature distribution only barely exceeds $\sim 10^4$ K.

f'_{mol} is calculated), eq. 4.1 has to be solved in an iterative fashion until consistent values for T_k , n_e , and f'_{mol} are reached. Example solutions are given in Figure A.1 in Appendix A.1.

The temperature distribution that results from solving eq. 4.1 for every SPH particle in the G1 simulation is shown in Figure 4.3 (very similar distributions are obtained for G2 and G3). The gas has been cooled to $T_k \lesssim 10^4$ K, with temperatures extending down to ~ 25 K. This new gas phase represents both the warm neutral medium (WNM) and the cold neutral medium (CNM), and from it we derive the molecular gas phase.

4.3.3 HI TO H₂ CONVERSION

For the determination of the molecular gas mass fraction associated with each SPH gas particle, a prescription of Pelupessy et al. (2006) is used, inferred by equating the formation rate of H₂ on dust grains with the photodissociation rate of H₂ by Lyman-Werner band photons, and taking into account the self-shielding capacity of H₂ and dust extinction. We ignore H₂ production in the gas phase (cf., Christensen et al., 2012) since only in diffuse low metallicity ($\lesssim 0.1 Z_\odot$) gas is this thought to be the dominant formation route (Norman & Spaans, 1997), and so should not be relevant in our model galaxies that have mean metallicities $Z' > 1$ (see Table 4.1) and very little gas with $Z' < 0.1$ (see Figure A.3 in Appendix A.3). We adopt a steady-state for the HI→H₂ transition, meaning that we ignore any time dependence owing to temporal changes in the UV field strength and/or disruptions of GMCs, both of which can occur on similar time scales as the H₂ formation. This has been shown to be a reasonable assumption for environments with metallicities $\gtrsim 0.01 Z_\odot$ (Narayanan et al., 2011; Krumholz & Gnedin, 2011).

The first step is to derive the FUV field strength, G_0 , which sets the HI→H₂ equilibrium. In

SÍGAME, G_0 consists of a spatially varying component that scales with the local SFRD ($\text{SFRD}_{\text{local}}$) in different parts of the galaxy on top of a constant component set by the total stellar mass of the galaxy. This is motivated by Seon et al. (2011) who measured the average FUV field strength in the MW ($G'_{0,\text{MW}}$) and found that about half comes from star light directly with the remainder coming from diffuse background light. We shall assume that in the MW the direct stellar contribution to $G'_{0,\text{MW}}$ is determined by the average SFRD (SFRD_{MW}), while the diffuse component is fixed by the stellar mass ($M_{*,\text{MW}}$). From this assumption, i.e., by calibrating to MW values, we derive the desired scaling relation for G_0 in our simulations:

$$G_0 = G'_{0,\text{MW}} \left(0.5 \frac{\text{SFRD}_{\text{local}}}{\text{SFRD}_{\text{MW}}} + 0.5 \frac{M_*}{M_{*,\text{MW}}} \right), \quad (4.2)$$

where $G'_{0,\text{MW}} = 0.6$ Habing (Seon et al., 2011), and $M_{*,\text{MW}} = 6 \times 10^{10} M_\odot$ (McMillan, 2011). For SFRD_{MW} we adopt $0.0024 M_\odot \text{ yr}^{-1} \text{ kpc}^{-3}$, inferred from the average SFR within the central 10 kpc of the MW ($0.3 M_\odot \text{ yr}^{-1}$; Heiderman et al., 2010) and within a column of height equal to the scale height of the young stellar disk (0.2 kpc; Bovy et al., 2012) of the MW disk. $\text{SFRD}_{\text{local}}$ is the SFRD ascribed to a given SPH particle, and is calculated as the volume-averaged SFR of all SPH particles within a 5 kpc radius. Note, that the stellar mass sets a lower limit on G_0 , which for G1, G2, and G3 are 0.22, 0.62, and 0.88 Habing, respectively.

Next, the gas upon which the FUV field impinges is assumed to reside in logotropic clouds, i.e., clouds with radial density profiles given by $n(r) = n_{\text{H,ext}} (r/R)^{-1}$, where $n_{\text{H,ext}}$ is the density at the cloud radius R . For a logotropic density profile, the external density is given by $n_{\text{H,ext}} = 2/3 \langle n_{\text{H}} \rangle$, where we approximate $\langle n_{\text{H}} \rangle$ with the original SPH gas density. From Pelupessy et al. (2006) we then have that the molecular gas mass fraction, including heavier elements than hydrogen, of each cloud is given by²:

$$f'_{\text{mol}} \equiv \frac{m_{\text{mol}}}{m_{\text{SPH}}} = \exp \left[-4 \frac{A_{\text{v}}^{(\text{tr})}}{\langle A_{\text{v}} \rangle} \right]. \quad (4.3)$$

Here $\langle A_{\text{v}} \rangle$ is the area-averaged visual extinction of the cloud and $A_{\text{v}}^{(\text{tr})}$ is the extinction through the outer layer of neutral hydrogen. The area-averaged extinction, $\langle A_{\text{v}} \rangle$, is calculated from the metallicity and average cloud density, $\langle n_{\text{H}} \rangle$:

$$\langle A_{\text{v}} \rangle = 7.21 \times 10^{-22} Z' \langle n_{\text{H}} \rangle R, \quad (4.4)$$

where $\langle n_{\text{H}} \rangle R$ is set by the well known density-size scaling relation for virialised clouds, normalised by the external boundary pressure, P_{ext} , i.e.:

$$\langle n_{\text{H}} \rangle = n_{\text{ds}} \left(\frac{P_{\text{ext}}/k_{\text{B}}}{10^4 \text{ cm}^{-3} \text{ K}} \right)^{1/2} \left(\frac{R}{\text{pc}} \right)^{-1}. \quad (4.5)$$

For the normalization constant we adopt $n_{\text{ds}} = 10^3 \text{ cm}^{-3}$, as inferred from studies of molecular clouds in the MW (Larson, 1981; Wolfire et al., 2003; Heyer & Brunt, 2004), although we note that Pelupessy et al. (2006) uses 1520 cm^{-2} . The external hydrostatic pressure for a rotating

²We will use lower case m when dealing with individual SPH particles. Furthermore, f'_{mol} is not to be confused with f_{mol} describing the total molecular gas mass fraction of a galaxy and to be introduced in Section 4.4.

disk of gas and stars is calculated at mid-plane following Swinbank et al. (2011):

$$P_{\text{tot}} \approx \frac{\pi}{2} G \Sigma_{\text{gas}} \left[\Sigma_{\text{gas}} + \left(\frac{\sigma_{\text{gas}\perp}}{\sigma_{*\perp}} \right) \Sigma_* \right], \quad (4.6)$$

where $\sigma_{\text{gas}\perp}$ and $\sigma_{*\perp}$ are the local vertical velocity dispersions of gas and stars respectively, and Σ denotes surface densities of the same. These quantities are all calculated directly from the simulation output, using the neighbouring SPH particles within 5 kpc, weighted by mass, density and the cubic spline kernel (see also Monaghan, 2005). The external cloud pressure that enters in eq. 4.5, is assumed to be equal to $P_{\text{tot}}/(1 + \alpha_0 + \beta_0)$ for relative cosmic and magnetic pressure contributions of $\alpha_0 = 0.4$ and $\beta_0 = 0.25$ (Elmegreen, 1989; Swinbank et al., 2011). For the MW, $P_{\text{ext}}/k_B \sim 10^4 \text{ cm}^{-3} \text{ K}$ (Elmegreen, 1989), but as shown in Figure A.3 in Appendix A.3, our model galaxies span a wide range in P_{ext}/k_B of $\sim 10^2 - 10^7 \text{ cm}^{-3} \text{ K}$.

For $A_v^{(\text{tr})}$, the following expression is provided by Pelupessy et al. (2006):

$$A_v^{(\text{tr})} = 1.086 \nu \xi_{\text{FUV}}^{-1} \times \ln \left[1 + \frac{\frac{G'_0}{\nu \mu S_H(T_k)} \sqrt{\frac{\xi_{\text{FUV}}}{Z' T_k}}}{n_{\text{H,ext}}/135 \text{ cm}^{-3}} \right], \quad (4.7)$$

where ξ_{FUV} is the ratio between dust FUV absorption cross section (σ) and the effective grain surface area (σ_d), and is set to $\xi_{\text{FUV}} = \sigma/\sigma_d = 3$. $S_H = (1 + 0.01 T_k)^{-2}$ is the probability that HI atoms stick to grain surfaces, where T_k is the kinetic gas temperature (determined in an iterative way as explained in Section 4.3.2). Furthermore, $\nu = n_{\text{H,ext}} R \sigma (1 + n_{\text{H,ext}} R \sigma)^{-1}$, and μ (set to 3.5 as suggested by Pelupessy et al., 2006) is a parameter which incorporates the uncertainties associated with primarily S_H and σ_d .

Following the above prescription `SÍGAME` determines the molecular gas mass fraction and thus the molecular gas mass ($m_{\text{mol}} = f'_{\text{mol}} m_{\text{SPH}}$) associated with each SPH particle. Depending on the environment (e.g., G_0 , Z' , T_k , P_{ext} , ...), the fraction of the SPH gas converted into H_2 can take on any value between 0 and 1, as seen from the f'_{mol} distribution of G1 in Figure 4.4. Overall, the total mass fraction of the SPH gas in G1, G2, and G3 (i.e., within R_{cut}) that is converted to molecular gas is 29 %, 52 % and 34 %, respectively.

4.3.4 STRUCTURE OF THE MOLECULAR GAS

Having determined the molecular gas mass fractions, `SÍGAME` proceeds by distributing the molecular gas into GMCs, and calculates their masses and sizes, along with internal density and temperature structures, as described in the following.

GMC masses and sizes

The molecular gas associated with a given SPH particle is divided into GMCs by randomly sampling a power-law mass spectrum of the form:

$$\frac{dN}{dm_{\text{GMC}}} \propto m_{\text{GMC}}^{-\beta}. \quad (4.8)$$

For GMCs in the MW disk and Local Group galaxies $\beta \simeq 1.8$ (Blitz et al., 2007), and is the value adopted by `SÍGAME` in this work unless otherwise stated. Lower and upper mass cut-offs at

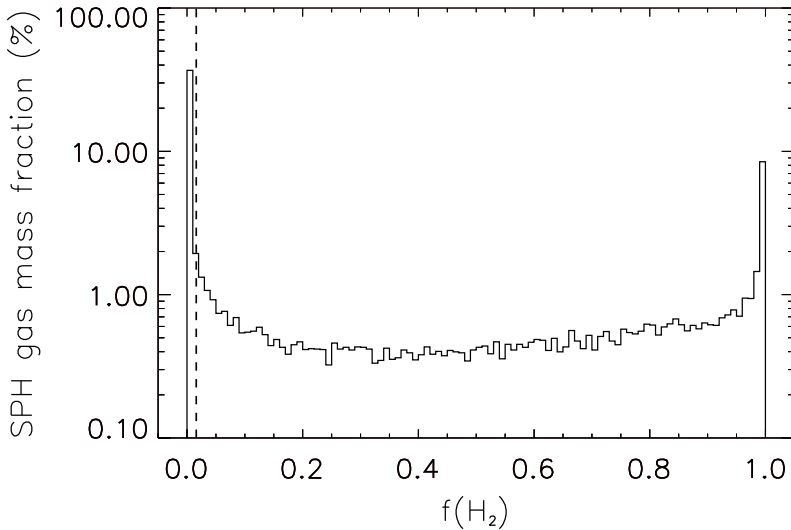


Figure 4.4 The distribution of the H_2 gas mass fraction of the SPH particles in G1 calculated according to eq. 4.3 (solid line histogram). Similar distributions are found for G2 and G3. The lower limit on f'_{mol} , defined as described in Section 4.3.4, is indicated by the dashed vertical line.

$10^4 M_\odot$ and $10^6 M_\odot$, respectively, are enforced in order to span the mass range observed by Blitz et al. (2007). A similar approach was adopted by Narayanan et al. (2008b,a). Note that, in the case of G1 the upper cut-off on the GMC masses is in fact set by the mass resolution of the SPH simulation ($6.3 \times 10^5 h^{-1} M_\odot$). For G1, typically $\lesssim 30$ GMCs are created in this way per SPH particle, while for G2 and G3, which were run with SPH gas particles masses almost an order of magnitude higher, as much as ~ 100 GMCs can be extracted from a given SPH particle for $\beta = 1.8$. Figure 4.5 shows the resulting mass distribution of all the GMCs in G1, along with the distribution of molecular mass associated with the SPH gas particles prior to it being divided into GMCs. The net effect of re-distributing the H_2 mass into GMCs is a mass distribution dominated by relatively low cloud masses, which is in contrast to the relatively flat SPH H_2 mass distribution. Note, the lower cut-off at $m_{\text{GMC}} = 10^4 M_\odot$ implies that if the molecular gas mass associated with an SPH particle (i.e., $m_{\text{mol}} = f'_{\text{mol}} m_{\text{SPH}}$) is less than this lower limit it will not be re-distributed into GMCs. Since m_{SPH} is constant in our simulations ($6.3 \times 10^5 h^{-1} M_\odot$ for G1 and $4.7 \times 10^6 h^{-1} M_\odot$ for G2 and G3) the lower limit imposed on m_{GMC} translates directly into a lower limit on f'_{mol} (0.016 for G1 and 0.002 for G2 and G3, shown as a dashed vertical line for G1 in Figure 4.4). As a consequence, 0.2, 0.005 and 0.01 % of the molecular gas in G1, G2, and G3, respectively, does not end up in GMCs. These are negligible fractions and the molecular gas they represent can therefore be safely ignored.

The GMC sizes are derived from the virial theorem, which relates the radius of a GMC (R_{eff}) to its mass and external pressure (P_{ext}) according to:

$$\frac{R_{\text{eff}}}{\text{pc}} = \left(\frac{P_{\text{ext}}/k_{\text{B}}}{10^4 \text{ cm}^{-3} \text{ K}} \right)^{-1/4} \left(\frac{m_{\text{GMC}}}{290 M_\odot} \right)^{1/2}. \quad (4.9)$$

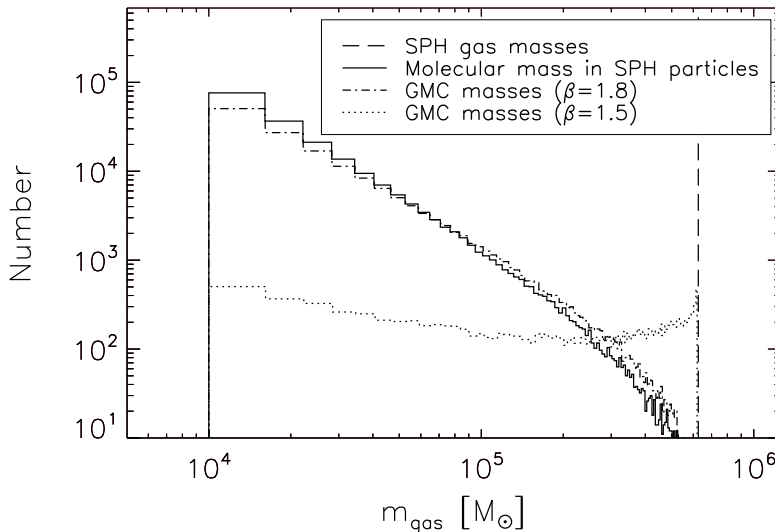


Figure 4.5 The distribution of GMC masses in G1 obtained by applying eq. 4.8, with $\beta = 1.8$ (solid histogram) and $\beta = 1.5$ (dash-dotted histogram), compared to the total molecular gas masses associated with SPH particles (distribution shown as dotted histogram). The dashed vertical line indicates the SPH gas mass resolution of the simulation ($= 6.3 \times 10^5 h^{-1} M_{\odot}$ in the case of G1).

Similarly, the internal velocity dispersion (σ_v) of the clouds is given by:

$$\frac{\sigma_v}{\text{km s}^{-1}} = 1.2 \left(\frac{P_{\text{ext}}/k_B}{10^4 \text{ cm}^{-3} \text{ K}} \right)^{1/4} \left(\frac{R_{\text{eff}}}{\text{pc}} \right)^{1/2} \quad (4.10)$$

(e.g., Elmegreen, 1989; Swinbank et al., 2011). Figure 4.6 shows the resulting distribution of GMC radii in G1 (solid histogram). The minimum and maximal cloud radii found in G1 are $\sim 0.07 \text{ pc}$ and $\sim 100 \text{ pc}$, respectively, and are set by the pressure and the imposed limits on m_{GMC} .

Observations have indicated that the shape of the GMC mass spectrum might be different in gas-rich systems where a high-pressure ISM leads to the characteristic mass of star-forming clumps of molecular gas being much higher than what is observed in normal spirals (e.g. Swinbank et al., 2011; Leroy et al., 2015). In Section 4.5 we therefore examine the effects of adopting a more top-heavy GMC mass distribution, corresponding to $\beta = 1.5$ (shown as dot-dashed histogram in Figure 4.5). The total amount of molecular gas in our galaxies does not change significantly between $\beta = 1.8$ and $\beta = 1.5$, and the CO simulation results are robust against (reasonable) changes in the mass-spectrum.

The GMCs are placed randomly around the position of their ‘parent’ SPH particle, albeit with an inverse proportionality between radial displacement and mass of the GMC. The latter is done in order to retain the mass distribution of the original galaxy simulation as best as possible. The GMCs are assigned the same bulk velocity, \bar{v} , Z' , G_0 and ζ_{CR} as their ‘parent’ SPH particle.

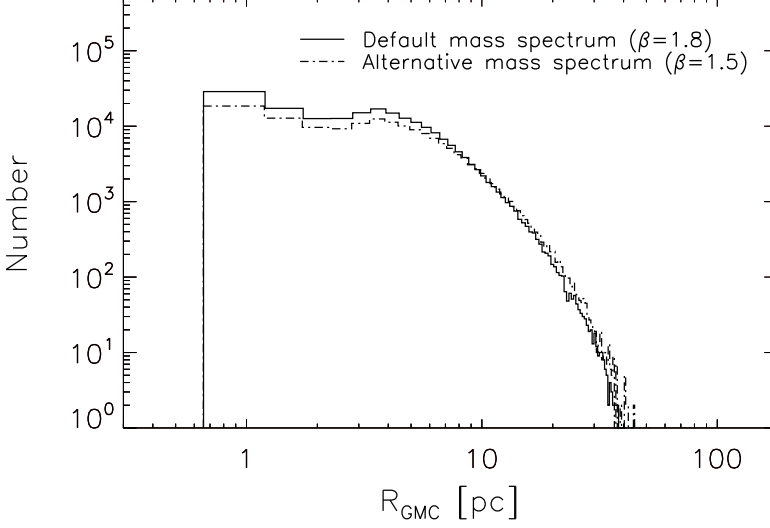


Figure 4.6 The distribution of GMC radii in G1 for the adopted cloud mass spectrum with $\beta = 1.8$ (solid histogram) and for a slightly modified spectrum with $\beta = 1.5$ (dash-dotted histogram). Similar distributions are found for G2 and G3.

GMC density structure

In order to ensure a finite central density in our GMCs, *SÍGAME* adopts a Plummer radial density profile (e.g., Plummer, 1911; Whitworth & Ward-Thompson, 2001):

$$\frac{n_{\text{H}_2}(R)}{\text{cm}^{-3}} = 3.55 \left(\frac{m_{\text{GMC}}}{M_{\odot}} \right) \left(\frac{R_p}{\text{pc}} \right)^{-3} \left(1 + \frac{R^2}{R_p^2} \right)^{-5/2}, \quad (4.11)$$

where R_p is the so-called Plummer radius, which we set to $R_p = 0.1 R_{\text{eff}}$. The latter allows for a broad range in gas densities throughout the clouds, from $\sim 10^5 \text{ cm}^{-3}$ in the central parts to a few 10 cm^{-3} further out. Note, eq. 4.11 accounts for the presence of helium in the GMC.

In Section 4.5 we examine the impact on our simulation results if a steeper GMC density profile with an exponent of $-7/2$ is adopted instead of the default $-5/2$ in eq. 4.11. This modified Plummer profile, as well as the default profile, are shown in Figure 4.7 for a GMC with mass of $10^4 M_{\odot}$ and external pressure 10^4 K cm^{-3} .

GMC thermal structure

Having established the masses, sizes, and density structure of the GMCs, *SÍGAME* solves for the kinetic temperature throughout the clouds by balancing the relevant heating and cooling mechanisms as a function of cloud radius.

GMCs are predominantly heated by FUV photons (via the photo-electric effect) and cosmic rays. For the strength of the FUV field impinging on the GMCs, we take the previously calculated values at the SPH gas particle position (eq. 4.2). We shall assume that the CR ionization rate scales in a similar manner, since CRs have their origin in supernovae and are therefore

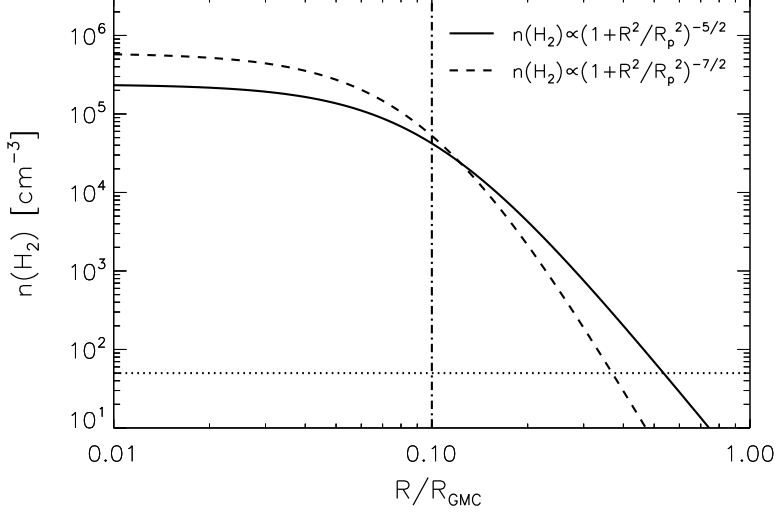


Figure 4.7 Plummer density profiles (eq. 4.11) with exponents $-5/2$ (solid line) and $-7/2$ (dashed line) for a GMC mass of $10^4 M_\odot$ and an external pressure of $P_{\text{ext}}/k_B = 10^4 \text{ K cm}^{-3}$. The corresponding cloud radius is $R_{\text{cloud}} = 5.9 \text{ pc}$ (eq. 4.9). The vertical dash-dotted line marks the Plummer radius ($= 0.1 R_{\text{GMC}}$), and the horizontal dotted line the n_{H_2} value (50 cm^{-3}) below which CO is assumed to photo-dissociate in our simulations.

related to the star formation and the total stellar mass of the galaxy:

$$\zeta_{\text{CR}} = \zeta_{\text{CR,MW}} \left(0.5 \frac{\text{SFRD}_{\text{local}}}{\text{SFRD}_{\text{MW}}} + 0.5 \frac{M_*}{M_{*,\text{MW}}} \right) \quad (4.12)$$

where $\text{SFRD}_{\text{local}}$, SFRD_{MW} and $M_{*,\text{MW}}$ are as described in Section 4.3.3, and ζ_{CR} is scaled to the ‘canonical’ MW value of $\zeta_{\text{CR,MW}} = 3 \times 10^{-17} \text{ s}^{-1}$ (e.g. Webber, 1998). While the FUV radiation is attenuated by dust and therefore does not heat the GMC centres significantly, cosmic rays can penetrate these dense regions and heat the gas there (Papadopoulos et al., 2011). For this reason *SÍGAME* attenuates the FUV field throughout the GMCs, while the CR ionization rate remains constant for a given cloud. The extinction of the FUV field at a certain point within a GMC is derived by integrating the Plummer density profile from that point and out to R_{eff} . This H column density is converted into a visual extinction ($A_V = N_{\text{H}}/2.2 \times 10^{21} \text{ cm}^{-2}$) so that the attenuated FUV field becomes:

$$G_{0,\text{att}} = G_0 e^{-1.8 A_V}, \quad (4.13)$$

where the factor of 1.8 is the adopted conversion from visual to FUV extinction (Black & Dalgarno, 1977).

SÍGAME calculates the gas kinetic temperature throughout each GMC via the following heating and cooling rate balance:

$$\Gamma_{\text{PE}} + \Gamma_{\text{CR,H}_2} = \Lambda_{\text{H}_2} + \Lambda_{\text{CO}} + \Lambda_{\text{OI}} + \Lambda_{\text{CII}} + \Lambda_{\text{gas-dust}}. \quad (4.14)$$

Γ_{PE} is the photo-electric heating by FUV photons, and $\Gamma_{\text{CR,H}_2}$ is the cosmic ray heating in

molecular gas. Λ_{H_2} is the cooling rate of the two lowest H_2 rotational lines (S(0) and S(1)), and Λ_{CO} is the cooling rate of the combined CO rotational ladder. $\Lambda_{\text{gas-dust}}$ is the cooling rate due to interactions between gas molecules and dust particles, which only becomes important at densities above 10^4 cm^{-3} (e.g., Goldsmith, 2001; Glover & Clark, 2012). Λ_{CII} and Λ_{OI} are the cooling rates due to [CII] and OI line emission, respectively. The abundances of carbon and oxygen used in the prescriptions for their cooling rates, scale with the cloud metallicity, while the CO cooling scales with the relative CO to neutral carbon abundance ratio, set by the molecular density (see Appendix A.2).

$\Lambda_{\text{gas-dust}}$ depends on the temperature difference between the gas and the dust (see eq. A.13). The dust temperature, T_{dust} , is set by the equilibrium between the absorption of FUV and the emission of IR radiation by the dust grains. We adopt the approximation given by Tielens (2005):

$$\frac{T_{\text{dust}}}{\text{K}} \simeq 33.5 \left(\frac{a}{1 \mu\text{m}} \right)^{-0.2} \left(\frac{G_{0,\text{att}}}{10^4 \text{ Habing}} \right)^{0.2}, \quad (4.15)$$

where $G_{0,\text{att}}$ is the dust-attenuated FUV field (eq. 4.13) and a is the grain size, which we set to $1 \mu\text{m}$ for simplicity. Values for T_{dust} using eq. 4.15 range from 0 to 8.9 K, but we enforce a lower limit on T_{dust} equal to the $z = 2$ CMB temperature of 8.175 K. T_{dust} is therefore essentially constant ($\sim 8 - 9$ K) throughout the inner region of the GMC models, similar to the value of $T_{\text{dust}} = 8$ K adopted by Papadopoulos & Thi (2013) for CR-dominated cores. Analytical expressions for all of the above heating and cooling rates are given in Appendix A.2, which also shows their relative strengths as a function of density for two example GMCs (Figure A.2).

Figure A.4 in Appendix A.3 shows the resulting T_{k} versus n_{H_2} behaviour for 80 GMCs spanning a broad range of GMC masses, metallicities, and star formation rate densities. As seen in the displayed GMC models, some general trends can be inferred from the $T_{\text{k}} - n_{\text{H}_2}$ diagrams. At fixed metallicity and mass, an increase in G_0 (and therefore also in ζ_{CR}), leads to higher temperatures throughout the models. In the outer regions this is due primarily to the increased photoelectric heating, while in the inner regions, heating by the unattenuated cosmic rays takes over as the dominating heating mechanism (Figure A.2). Keeping G_0 (and ζ_{CR}) fixed, lower T_{k} -levels and shallower $T_{\text{k}} - n_{\text{H}_2}$ gradients are found in GMCs with higher metallicities. Both these trends are explained by the fact that the [CII] and OI cooling rates scale linearly with Z' (see Appendix A.2).

Moving from the outskirts and inward towards the GMC centres, T_{k} drops as the attenuation of G_0 reduces the photoelectric heating. However, the transition from cooling via [CII] to the less efficient cooling mechanism by CO lines, causes a local increase in T_{k} at $n_{\text{H}_2} \sim 10^3 - 10^{4.5} \text{ cm}^{-3}$, as also seen in the detailed GMC simulations by Glover & Clark (2012). The exact density at which this ‘bump’ in T_{k} occurs depends strongly on the mass of the GMC. Our choice of the Plummer model for the radial density profile means that the extinction, A_{V} , at a certain density increases with GMC mass. This in turn decreases the FUV heating, and as a result the $T_{\text{k}} - n_{\text{H}_2}$ curve moves to lower densities with increasing GMC mass.

As the density increases towards the cloud centres (i.e., $n_{\text{H}_2} \gtrsim 10^{4.5} \text{ cm}^{-3}$) molecular line cooling and also gas-dust interactions become increasingly efficient and start to dominate the cooling budget. The $T_{\text{k}} - n_{\text{H}_2}$ curves are seen to be insensitive to changes in Z' , which is expected since the dominant heating and cooling mechanisms in these regions do not depend on Z' . Eventually, in the very central regions of the clouds, the gas reaches temperatures close to that of the ambient CMB radiation field, irrespective of the overall GMC properties and the

Table 4.2 Parameters, global and local, used by $\mathcal{S}\acute{\mathcal{I}}\mathcal{G}\mathcal{A}\mathcal{M}\mathcal{E}$, together with relevant equations in this work.

Global parameters	[CO/H ₂], β (GMC mass spectrum), GMC density profile	Eqs. 4.8 and 4.11
Local parameters	$m_{\text{GMC}}, G_0, \zeta_{\text{CR}}, Z', P_{\text{ext}}, \text{SFRD}$	Eqs. 4.8, 4.2, 4.2 and 4.6
Derived internal GMC parameters	$n_{\text{H}}, T_{\text{k}}, x_{\text{e}}, \sigma_{\text{v}}$	Eqs. 4.11 and 4.14

conditions at the surface (Figure A.2).

GMC grid models

The $T_{\text{k}} - n_{\text{H}_2}$ curve for a given GMC is determined by the following quantities:

- G_0 and ζ_{CR} , which govern the gas heating and are set by the local star formation rate density ($\text{SFRD}_{\text{local}}$) and the total stellar mass (M_*) according to eqs. 4.2 and 4.12.
- m_{GMC} and P_{ext} which determine the effective radius of a cloud (eq. 4.9) and thus its density profile (eq. 4.11).
- The local metallicity (Z'), which influences the fraction of H₂ gas and plays an important role in cooling the gas.

These local parameters together with the most important global parameters used by $\mathcal{S}\acute{\mathcal{I}}\mathcal{G}\mathcal{A}\mathcal{M}\mathcal{E}$ are listed in Table 4.2. The GMC ensemble distributions of G_0 , ζ_{CR} , m_{GMC} , $P_{\text{ext}}/k_{\text{B}}$, and Z' for each of the galaxies G1, G2 and G3 are shown in Figure A.3.

There are more than 100,000 GMCs in a single model galaxy and, as Figure A.3 shows, they span a wide range in G_0 , ζ_{CR} , m_{GMC} , $P_{\text{ext}}/k_{\text{B}}$, and Z' . Thus, in order to shorten the computing time, we calculated $T_{\text{k}} - n_{\text{H}_2}$ curves for a set of 630 GMCs, chosen to appropriately sample the distributions at certain grid values (listed in Table 4.3, and marked by vertical black lines in Figure A.3). Every GMC in our simulations was subsequently assigned the $T_{\text{k}} - n_{\text{H}_2}$ curve of the GMC grid model closest to it in the $(G_0, m_{\text{GMC}}, Z')$ parameter space. In the default GMC grid, we keep $P_{\text{ext}}/k_{\text{B}}$ fixed to a MW-like value of 10^4 K cm^{-3} , thereby also anchoring the scaling relations in eq. 4.9 and 4.10 for size and velocity dispersion. This is done to minimise the number of radiative transfer calculations, effectively keeping the amount of molecular gas mass dependent on local pressure, but removing local pressure as a free parameter in, and hence simplifying, the calculation of CO emission.

In addition to the default grid described above, we made two separate tests to explore the GMC parameter space more fully. These tests are described in the following and results of their application are presented in Section 4.5. The external cloud pressure, $P_{\text{ext}}/k_{\text{B}}$, spans a wide range from $\sim 10^3$ to 10^9 K cm^{-3} as shown in Figure A.3. In a separate test, we therefore constructed the same GMC grid, but for fixed pressures of $P_{\text{ext}}/k_{\text{B}} = 10^{5.5}$ and $10^{6.5} \text{ K cm}^{-3}$ and interpolated among the resulting three values of $P_{\text{ext}}/k_{\text{B}}$ ($[10^4, 10^{5.5}, 10^{6.5}] \text{ K cm}^{-3}$) as a demonstration of how to incorporate local pressure in $\mathcal{S}\acute{\mathcal{I}}\mathcal{G}\mathcal{A}\mathcal{M}\mathcal{E}$. We also test the effect of adopting the alternative radial GMC density profile defined in Section 4.3.4. $T_{\text{k}} - n_{\text{H}_2}$ curves were calculated for each possible combination of the parameter grid values listed in Table 4.3 for both density profiles, giving us a total of $3 \times 2 \times 630 = 3780$ GMC grid models.

Table 4.3 Grid parameter values

G_0 [Habing]	0.5, 1, 4, 7, 10, 13, 16, 19, 23, 27
$\log(m_{\text{GMC}} [\text{M}_\odot])$	4.0, 4.25, 4.5, 4.75, 5.0, 5.25, 5.5, 5.75, 6.0
$\log(Z/Z_\odot)$	-1, -0.5, 0, 0.5, 1, 1.4, 1.8
$\log(P_{\text{ext}}/k_B [\text{K cm}^{-3}])$	4.0, 5.5, 6.5

4.3.5 RADIATIVE TRANSFER OF CO LINES

`SÍGAME` assumes a fixed CO abundance equal to the Galactic value of $[\text{CO}/\text{H}_2] = 2 \times 10^{-4}$ (Lee et al., 1996; Sofia et al., 2004, and see Section 4.6 for a justification of this value) everywhere in the GMCs except for $n_{\text{H}_2} < 50 \text{ cm}^{-3}$, where CO is not expected to survive photo-dissociation processes (e.g. Narayanan et al., 2008a). `SÍGAME` calculates the CO line radiative transfer for each GMC individually and derives the CO line emission from the entire galaxy.

Individual GMCs

For the CO radiative transfer calculations we use a slightly modified version of the LIne Modeling Engine (`LIME` ver. 1.4; Brinch & Hogerheijde, 2010) - a 3D molecular excitation and radiative transfer code. `LIME` has been modified in order to take into account the redshift dependence of the CMB temperature, which is used as boundary condition for the radiation field during photon transport, and we have also introduced a redshift correction in the calculation of physical sizes as a function of distance. We use collision rates for CO (assuming H_2 is the main collision partner) from Yang et al. (2010). In `LIME`, photons are propagated along grid lines defined by Delaunay triangulation around a set of appropriately chosen sample points in the gas, each of which contain information on n_{H_2} , T_k , σ_v , $[\text{CO}/\text{H}_2]$ and v . `SÍGAME` constructs such a set of sample points throughout each GMC: about 5000 points distributed randomly out to a radius of 50 pc, i.e., beyond the effective radius of typical GMCs in G1, G2, and G3 (Figure 4.6) and in a density regime below the threshold density of 50 cm^{-3} adopted for CO survival (see previous paragraph). The concentration of sample points is set to increase towards the centre of each GMC where the density and temperature vary more drastically.

For each GMC, `LIME` generates a CO line data cube, i.e., a series of CO intensity maps as a function of velocity. The velocity-axis consists of 50 channels, each with a spectral resolution of 1.0 km s^{-1} , thus covering the velocity range $v = [-25, +25] \text{ km s}^{-1}$. The maps are 100 pc on a side and split into 200 pixels, corresponding to a linear resolution of 0.5 pc/pixel (or an angular resolution of $5.9 \times 10^{-5} ''/\text{pixel}$ at $z = 2$). Intensities are corrected for arrival time delay and redshifting of photons.

Figure A.5 shows the area- and velocity-integrated CO Spectral Line Energy Distributions (SLEDs) for the same 80 GMCs used in Section 4.3.4 to highlight the $T_k - n_{\text{H}_2}$ profiles (Figure A.4). The first thing to note is that the CO line fluxes increase with m_{GMC} , which is due to the increase in size, i.e., surface area of the emitting gas, with cloud mass (Section 4.3.4). Turning to the shape of the CO SLEDs, a stronger G_0 (and ζ_{CR}) increases the gas temperature and thus drives the SLEDs to peak at higher J -transitions. Only the higher, $J_{\text{up}} > 4$, transitions are also affected by metallicity, displaying increased flux with increased Z' . For GMCs with high G_0 , the high metallicity levels thus cause the CO SLED to peak at $J_{\text{up}} > 8$.

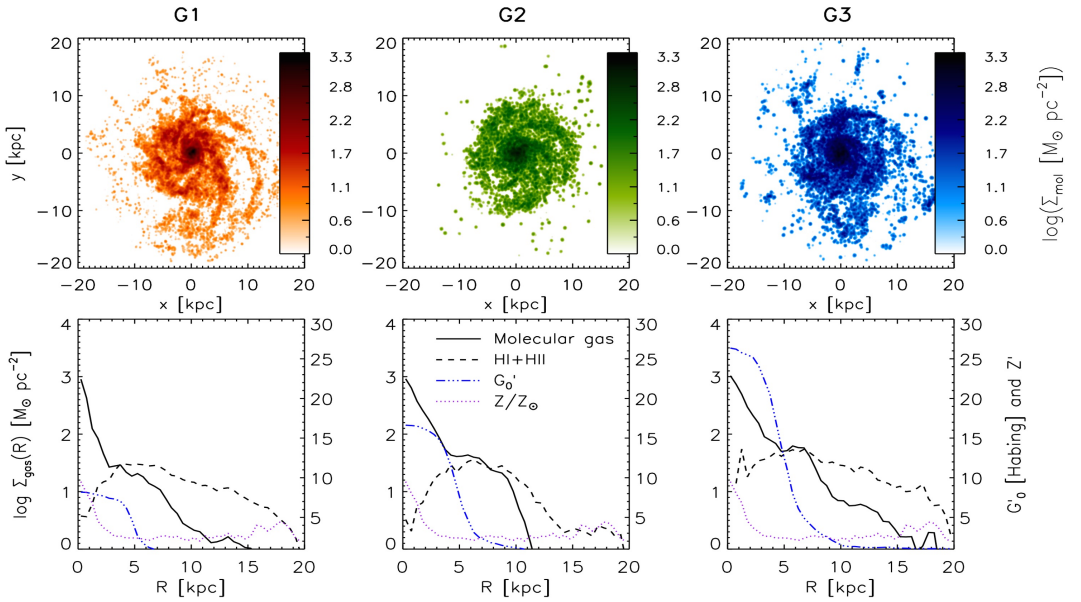


Figure 4.8 Top row: Molecular surface density maps of our model galaxies seen face-on. The maps have been smoothed using a circular Gaussian with full width at half maximum (FWHM) of 3 pixels corresponding to 0.24 kpc. The molecular gas surface density maps are seen to trace the spiral arms and inner disk as well as a few dense clumps further out. Bottom row: azimuthally averaged radial profiles of the molecular (solid curve) and HI + HII (dashed curve) gas surface densities, of the mean metallicity (dotted curve) and of G_0 (dot-dashed curve) – determined from 50 radial bins stretching from 0 to 15 kpc from the centre of each galaxy. The molecular gas is the result of applying the recipes in Section 4.3.3 to the SPH simulations presented in Section 4.2.2, while the HI + HII gas is the initial SPH gas mass minus the derived molecular gas mass (both include the contribution from helium). We estimate G_0 by averaging over the FUV fields impinging on all GMCs in each radial bin.

The effects of dust

Dust absorbs the UV light from young O and B stars and re-emits in the far-IR, leading to possible ‘IR pumping’ of molecular infrared sources. However, due to the large vibrational level spacing of CO, the molecular gas has to be at a temperature of at least 159 K, for significant IR pumping of the CO rotational lines to take place, when assuming a maximum filling factor of 1, as shown by Carroll & Goldsmith (1981). Most of the gas in our GMC models is at temperatures below 100 K, with only a small fraction of the gas, in the very outskirts, of the GMCs reaching $T_k > 159$ K, as seen in Figure A.4 in Appendix A.3. This happens only if the metallicity is low ($Z' \leq 0.1$) or in case of a combination between high FUV field ($G_0 \geq 4$) and moderate metallicity.

In principle, the high- J CO lines could be subject to extinction by dust, but this effect is significant only in extremely dust-enshrouded sources (Papadopoulos et al., 2010), and therefore unlikely to be relevant for our simulations.

While LIME is capable of including dust in the radiative transfer calculations, provided that a table of dust opacities as function of wavelength be supplied together with the input model, we have chosen not to include dust in the simulations presented here.

CO emission maps

A given GMC is assigned the CO emission line profile of the GMC model that corresponds to the nearest grid point in the $(G_0, m_{\text{GMC}}, Z')$ parameter space. A spatial grid of 400×400 pixels is overlaid on each galaxy viewed face-on, and the line profiles of all GMCs within each pixel are added to a common velocity axis, thus resulting in a position-velocity datacube. CO moment 0 maps are then constructed by integrating the flux within each pixel in velocity. These maps are 40 kpc on each side and thus have a resolution of ~ 100 pc/pixel. By expanding the pixel size to encompass the entire galaxy, the global CO SLED is derived.

The approach described above assumes that the molecular line emission from each GMC is radiatively decoupled from all other GMCs, due to the significant velocity gradients across the galaxies ($\sim 200 - 500 \text{ km s}^{-1}$) and the relatively small internal line widths of the individual GMCs ($\sim 2 - 34 \text{ km s}^{-1}$ for the GMCs in G1, G2 and G3).

4.4 SIMULATING MASSIVE $z = 2$ MAIN SEQUENCE GALAXIES

In this section we examine the H_2 surface density and CO emission maps resulting from applying SÍGAME to the three SPH galaxy simulations G1, G2, and G3 at $z = 2$ (Section 4.2), and we compare with existing CO observations of main sequence galaxies at $z \sim 1 - 2.5$. We also tested SÍGAME on three MW-like galaxies (see Appendix A.4), finding a general agreement with the CO line observations of MW and other similar local galaxies. As mentioned in previous sections, our default grid will be that corresponding to a Plummer density profile and a pressure of $P_{\text{ext}}/k_{\text{B}} = 10^4 \text{ cm}^{-3} \text{ K}$, combined with a GMC mass spectrum of slope $\beta = 1.8$, unless otherwise stated.

4.4.1 TOTAL MOLECULAR GAS CONTENT AND H_2 SURFACE DENSITY MAPS

The total molecular gas masses of G1, G2 and G3 – obtained by summing up the GMC masses associated with all SPH particles within each galaxy (i.e., $M_{\text{mol}} = \sum m_{\text{GMC}} = \sum f'_{\text{mol}} m_{\text{SPH}}$) – are 7.1×10^9 , 1.7×10^{10} , and $2.1 \times 10^{10} M_{\odot}$, respectively, corresponding to about 34, 59 and 45 % of the original total SPH gas masses of the galaxies within $R_{\text{cut}} = 20 \text{ kpc}$.³ The global molecular gas mass fractions (i.e., $f_{\text{mol}} = M_{\text{mol}}/(M_{\star} + M_{\text{mol}})$) are 11.8, 10.2 and 9.1 % for G1, G2, and G3, respectively.

This is $\sim 4 - 5\times$ below the typical molecular gas mass fraction ($\sim 40 - 60\%$) inferred from CO observations of main sequence galaxies at $z \sim 1 - 3$ with similar stellar masses and star formation rates as our simulations (e.g., Daddi et al., 2010; Magnelli et al., 2012; Tacconi et al., 2013).

The reason for this discrepancy is the low SPH gas mass fractions of our simulated galaxies to begin with ($f_{\text{SPH}} = M_{\text{SPH}}/(M_{\star} + M_{\text{SPH}}) = 18 - 28\%$), which obviously restricts f_{mol} to lower values. Such low gas fractions have been observed in local star forming galaxies. For example, assuming a MW-like α_{CO} factor, Saintonge et al. (2011) derived $f_{\text{mol}} \sim 6.7 \pm 4.5\%$ for a sample of 119 CO(1 – 0) detected normal star forming galaxies and a stack of 103 non-detections.

Figure 4.8 (top panels) shows the molecular gas surface density (Σ_{mol}) maps of G1, G2, and G3, where Σ_{mol} is calculated over pixels $80 \text{ pc} \times 80 \text{ pc}$ in size. The pixel size was chosen in order to avoid resolving the GMCs, which typically have sizes $\lesssim 40 \text{ pc}$ (see Figure 4.6). The

³These global molecular-to-SPH gas mass fractions are calculated as $M_{\text{mol}}/M_{\text{SPH}} = \sum m_{\text{GMC}} / \sum m_{\text{SPH}}$, where the sums are over all SPH particles.

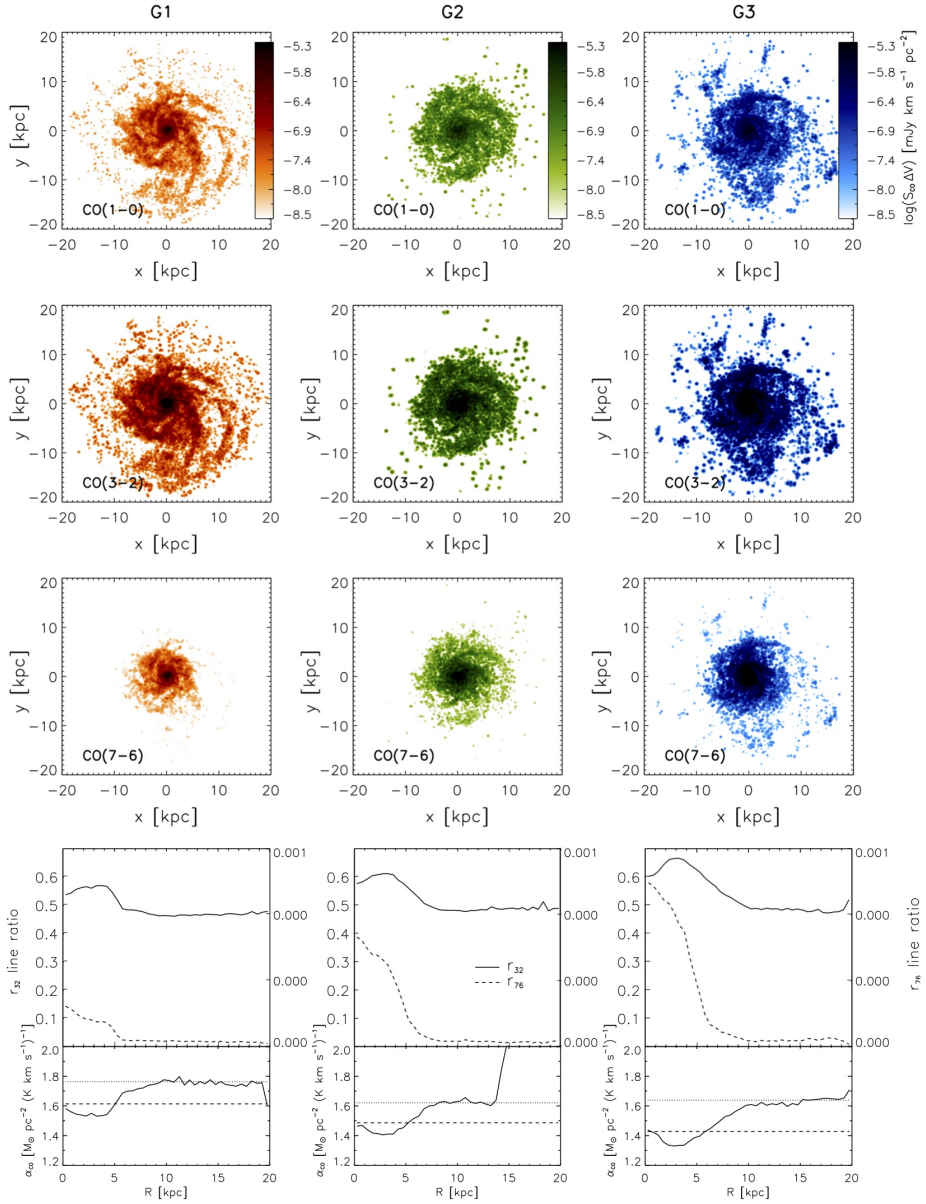


Figure 4.9 The top three rows show the moment 0 maps of the CO(1–0), CO(3–2) and CO(7–6) emission from G1, G2 and G3. The CO maps have been smoothed using a circular Gaussian with full width at half maximum (FWHM) of 3 pixels corresponding to 0.24 kpc, and as with the SPH and molecular gas surface density maps, a logarithmic scale has been applied in order to better display extended emission. The bottom row shows the azimuthally averaged CO 3–2/1–0 and 7–6/1–0 brightness temperature line ratios (denoted r_{32} and r_{76} , respectively) as functions of projected radius for each of the three galaxies. A radial bin-size of 0.5 kpc was used. Also shown are the azimuthally averaged radial profiles of CO-to-H₂ conversion factor $\alpha_{\text{CO}}(R) = \Sigma_{\text{H}_2}/I_{\text{CO}(1-0)}$ in units of $\text{M}_{\odot} \text{ pc}^{-2} (\text{K km s}^{-1})^{-1}$ with a dashed line indicating the global α_{CO} factor and a dotted line for the disk-averaged α_{CO} factor (see Section 4.4.2).

molecular gas is seen to extend out to radii of ~ 10 kpc and beyond, but generally the molecular

gas concentrates within the inner regions of each galaxy. The distribution of molecular gas broadly follows the central disk and spiral arms where the SPH surface density (Σ_{SPH}) is also the highest (Figure 4.1). The correspondence is far from one-to-one, however, as seen by the much larger extent of the SPH gas, i.e., regions where H_2 has not formed despite the presence of atomic and ionised gas. This point is further corroborated in the bottom panels of Figure 4.8, which show azimuthally-averaged radial surface density profiles of the molecular gas and of the $\text{HI} + \text{HII}$ gas. The latter is simply the initial SPH gas mass with the molecular gas mass subtracted, and has been corrected (just like the molecular gas phase) for the mass contribution from helium.

In order to compare $\Sigma_{\text{HI+HII}}$ and Σ_{mol} with observations, we have set the radial bin width to 0.5 kpc – the typical radial bin size used for nearby spirals in the work of Leroy et al. (2008)⁴. The radially binned Σ_{mol} reaches $\sim 800 - 1000 \text{ M}_{\odot} \text{ pc}^{-2}$ in the central regions of our simulated galaxies, which is comparable to observational estimates of Σ_{mol} (of several $100 \text{ M}_{\odot} \text{ pc}^{-2}$) towards the centres of nearby spirals (Leroy et al., 2008). In all three galaxies, the HI+HII surface density dips within the central $\sim 1 - 2 \text{ kpc}$, coinciding with a strong peak in Σ_{mol} . Thus, despite the marked increase in the FUV radiation field towards the centre, the formation of H_2 driven by the increase in gas pressure is able to overcome photodestruction of H_2 through absorption of Lyman or Werner band radiation. The central H_2 surface densities are similar for all galaxies and is a direct consequence of very similar SPH gas surface densities in the centre combined with molecular gas mass fractions approaching 1. From $R \sim 2 \text{ kpc}$ and out to $\sim 10 \text{ kpc}$, the $\text{HI} + \text{HII}$ surface density remains roughly constant with values of ~ 40 , ~ 70 and $\sim 100 \text{ M}_{\odot} \text{ pc}^{-2}$ for G1, G2 and G3, respectively.

Radial profiles of the HI and molecular gas surface density that are qualitatively very similar to our simulations have been observed in several nearby star-forming disk galaxies (e.g., Leroy et al., 2008; Bigiel et al., 2008). In local galaxies, however, the HI surface density, including helium, rarely exceeds $\sim 10 \text{ M}_{\odot} \text{ pc}^{-2}$, while in our simulations we find $\text{HI} + \text{HII}$ surface densities that are $4 - 10\times$ higher, which is due to the substantial fraction of ionised gas in our simulated galaxies.

4.4.2 CO LINE EMISSION MAPS AND RESOLVED EXCITATION CONDITIONS

Moment 0 maps of the $\text{CO}(1-0)$, $\text{CO}(3-2)$ and $\text{CO}(7-6)$ emission from G1, G2 and G3 are shown in Figure 4.9. Both the $\text{CO}(1-0)$ and $\text{CO}(3-2)$ emission are seen to trace the H_2 gas distribution well (Figure 4.8), while the $\text{CO}(7-6)$ emission only trace gas in the central $\sim 7 \text{ kpc}$ of the galaxies.

Also shown in Figure 4.9 (bottom row) are the azimuthally averaged $\text{CO } 3-2/1-0$ and $7-6/1-0$ brightness temperature line ratios (denoted r_{32} and r_{76} , respectively) as a function of radius for G1, G2 and G3. The profiles show that the gas is more excited in the central $\sim 5 \text{ kpc}$, where typical values of r_{32} and r_{76} are $\sim 0.55 - 0.65$ and $\sim 0.02 - 0.08$, respectively, compared to $r_{32} \sim 0.5$ and $r_{76} < 0.01$ further out in the disk. This radial behaviour of the line ratios does not reflect the H_2 gas surface density, which peaks towards the centre rather than flattens, and gradually trails off out to $R \sim 12 \text{ kpc}$ instead of dropping sharply at $R \sim 4 - 6 \text{ kpc}$ (Figure 4.9). Rather, r_{32} and r_{76} seem to mimic the radial behaviour of G_0 (and thus ζ_{CR}), which makes sense since G_0 and ζ_{CR} are the most important factors for the internal GMC temperature

⁴The H_2 surface density maps in Figure 4.8 are averaged over areas $80 \times 80 \text{ pc}$ in size, and therefore give higher peak surface densities than the radial profiles which are averaged over $\sim 0.5 \text{ kpc}$ wide annuli.

distribution (Figure A.4). The central values for r_{32} and r_{76} increase when going from G1 to G3, as expected from the elevated levels of star formation density (and of G_0 and ζ_{CR} , accordingly) in their central regions. Beyond ~ 6 kpc the line ratios are constant (~ 0.5 and < 0.01) and the same for all three galaxies, due to relatively similar G_0 (and ζ_{CR}) there.

The decrease in r_{32} towards the centre has also been observed in nearby galaxies. For M51, a spiral galaxy with a smaller SFR than our model galaxies (see Appendix A.4), Vlahakis et al. (2013) measured a median ratio of $r_{32} = 0.54$ for pixels covering the central kpc region, but typical ratios of $0.2 - 0.4$ in the arm and inter-arm regions. In comparison, our model galaxies display larger r_{32} ratios and a slightly less pronounced drop of 0.1 or less when going from the central kpc region to the outskirts of the disk. Mao et al. (2010) observed 125 nearby galaxies of different types and found global r_{32} values to be 0.61 ± 0.16 in normal galaxies, and > 0.89 in starbursts and (U)LIRGs. Iono et al. (2009) and Papadopoulos et al. (2012) found slightly lower r_{32} in their samples of (U)LIRGs, with mean values of 0.48 ± 0.26 and 0.67 ± 0.62 respectively. The r_{32} profiles of our model galaxies reveal more highly excited gas in their centres than in the disks, with central values similar to the observed values towards (U)LIRGs by Papadopoulos et al. (2012) but below those reported by Mao et al. (2010). Finally, Geach & Papadopoulos (2012) employed Large Velocity Gradient (LVG) radiative transfer models to examine r_{32} in different environments. For quiescent clouds similar to very low-excitation gas clouds found in M31, they showed that r_{32} can be as low as ~ 0.13 , while dense ($n(\text{H}_2) > 10^4 \text{ cm}^{-3}$) star-forming clouds typically have $r_{32} \sim 0.88$. Most likely a result of their moderate star formation rates, the r_{32} radial profiles of our model galaxies lie in between these more extreme cases.

4.4.3 THE CO-TO-H₂ CONVERSION FACTOR

The CO-to-H₂ conversion factor (α_{CO}) connects CO(1–0) line luminosity (in surface brightness temperature units) with the molecular gas mass (M_{mol}) as follows:

$$\alpha_{\text{CO}} = \frac{M_{\text{mol}}}{L'_{\text{CO}(1-0)}}, \quad (4.16)$$

From the CO(1–0) surface brightness and H₂ surface density maps of our simulated galaxies, we calculate the average α_{CO} within radial bins from the galaxy centres (Figure 4.9). The resulting radial profiles show that α_{CO} is essentially constant as a function of radius, taking on values in the range $\sim 1.3 - 1.8 M_{\odot} \text{ pc}^{-2} (\text{K km s}^{-1})^{-1}$ across all three galaxies, except in the outskirts of G2 where α_{CO} shoots up to higher values. The high values of α_{CO} in the outskirts of G2 reflect the very low molecular gas surface densities (see Figure 4.8) and resulting lack of CO line emission, rendering α_{CO} a meaningless quantity in this region. In order to compare with the stellar properties in Table 4.1, we will use only the region within $R = 15$ kpc for the further analysis of CO line emission in G02. Small systematic changes in α_{CO} with radius are seen in all three simulated galaxies as α_{CO} is systematically below (above) the global α_{CO} value, marked with dashed lines, at $\lesssim 5$ kpc ($\gtrsim 5$ kpc). Blanc et al. (2013) measured a drop in α_{CO} by a factor of two when going from $R \sim 7$ kpc to the $R < 2$ kpc central region of the Sc galaxy NGC 628, assuming a constant gas depletion timescale when converting SFR surface densities into gas masses. For comparison, the radial α_{CO} profiles of our model galaxies only drop by about 10% from $R \gtrsim 7$ kpc to the $R < 2$ kpc central region.

Sandstrom et al. (2013) measured and examined the resolved α_{CO} values in a sample of 26 nearby spiral galaxies. A disk-averaged α_{CO} value was calculated for each galaxy, by tiling

them with pixels of spacing $37.5''$ (corresponding to pixel sizes of $0.7 - 3.9 \text{ kpc}^2$) and calculating the mean of α_{CO} values for pixels with a sufficient signal-to-noise ratio. It was found that, on average, the galaxies have a central ($R \leq 1 \text{ kpc}$) α_{CO} value a factor of two below the disk-averaged α_{CO} value. We calculate disk-averaged α_{CO} for our model galaxies in a similar way by tiling the galaxies seen face-on with 1 kpc^2 -sized pixels and taking the average over pixels within the cut-out radii R_{cut} given in Table 4.1. The resulting values are shown with dotted lines in Figure 9 and are no more than $\sim 1.2\times$ the central ($R \leq 1 \text{ kpc}$) α_{CO} . Our simulated galaxies, therefore do not quite reproduce the drop in α_{CO} typically observed when going from the disk to the central regions of local, spiral galaxies. Although, we note that for three galaxies from the Sandstrom et al. (2013) sample (NGC 3938, NGC 3077 and NGC 4536) α_{CO} changes by only $10 - 16\%$ from the disk to the centre, which is in line with our simulations.

The α_{CO} factor is expected to depend on Z' , as higher metallicity means higher C and O abundances as well as more dust that helps shield CO from photodestruction by FUV light, thereby leading to a possibly lowering of α_{CO} . A comparison of the α_{CO} radial profiles with those of G_0 and Z' in the bottom panel of Figure 4.8, suggests that the transition in α_{CO} is caused by a change in G_0 rather than a change in Z' , since α_{CO} and G_0 generally start to drop at around $R \sim 6 \text{ kpc}$ while Z' already drops drastically at 1 kpc from the centre. Our modeling therefore implies that α_{CO} is controlled by G_0 rather than Z' in normal star-forming galaxies at $z \sim 2$, in agreement with the observations by Sandstrom et al. (2013) who do not find a strong correlation with Z' .

From the total molecular gas masses and CO(1 – 0) luminosities of G1, G2, and G3, we derive global α_{CO} factors of $\alpha_{\text{CO}} = 1.6, 1.5$ and $1.4 \text{ M}_{\odot} \text{ pc}^{-2} (\text{K km s}^{-1})^{-1}$, respectively. These values are lower (by a factor ~ 3) than the inner disk MW value ($\alpha_{\text{CO,MW}} \simeq 4.3 \pm 0.1 \text{ M}_{\odot} \text{ pc}^{-2} (\text{K km s}^{-1})^{-1}$), and closer to the typical mergers/starburst α_{CO} -values ($\sim 0.2 \times \alpha_{\text{CO,MW}}$) inferred from CO dynamical studies of local ULIRGs (e.g., Solomon et al., 1997; Downes & Solomon, 1998; Bryant & Scoville, 1999) and $z \sim 2$ SMGs (e.g., Tacconi et al., 2008). Our α_{CO} -values are also below those inferred from dynamical modeling of $z \sim 1.5$ BzKs ($\alpha_{\text{CO}} = 3.6 \pm 0.8 \text{ M}_{\odot} \text{ pc}^{-2} (\text{K km s}^{-1})^{-1}$; Daddi et al., 2010).

The α_{CO} factors of the $z \sim 1 - 1.3$ star-forming galaxies studied by Magnelli et al. (2012) occupy the same region of the M_* –SFR plan as our model galaxies, but have α_{CO} factors at least a factor ~ 6 higher. Their α_{CO} are $\sim 5 - 20 \text{ M}_{\odot} \text{ pc}^{-2} (\text{K km s}^{-1})^{-1}$ when converting dust masses to gas masses using a metallicity-dependent gas-to-dust ratio, and Magnelli et al. (2012) further find that the same galaxies have relatively low dust temperatures of $\lesssim 28 \text{ K}$ compared to the galaxies further above the main sequence of Rodighiero et al. (2010). The fact that the main-sequence galaxies of Magnelli et al. (2012) are all of near-solar metallicity as ours, cf. Table 4.1, suggests that other factors, such as dust temperature caused by strong FUV radiation, can be more important than metallicity in regulating α_{CO} , in line with our study of the α_{CO} radial profiles.

4.4.4 GLOBAL CO LINE LUMINOSITIES AND SPECTRAL LINE ENERGY DISTRIBUTIONS

The global CO SLEDs of G1, G2 and G3 are shown in Figure 4.10 in three different incarnations: 1) total CO line luminosities ($L'_{\text{CO}_{J,J-1}}$), 2) brightness temperature ratios ($T_{\text{B,CO}_{J,J-1}}/T_{\text{B,CO}_{1,0}} = L'_{\text{CO}_{J,J-1}}/L'_{\text{CO}_{1,0}}$) and 3) line intensity ratios ($I_{\text{CO}_{J,J-1}}/I_{\text{CO}_{1,0}} = L'_{\text{CO}_{J,J-1}}/L'_{\text{CO}_{1,0}} \times (\nu_{\text{CO}_{J,J-1}}/\nu_{\text{CO}_{1,0}})^2$). We have also compiled relevant CO observations of normal star-forming galaxies at $z \sim 1 - 3$

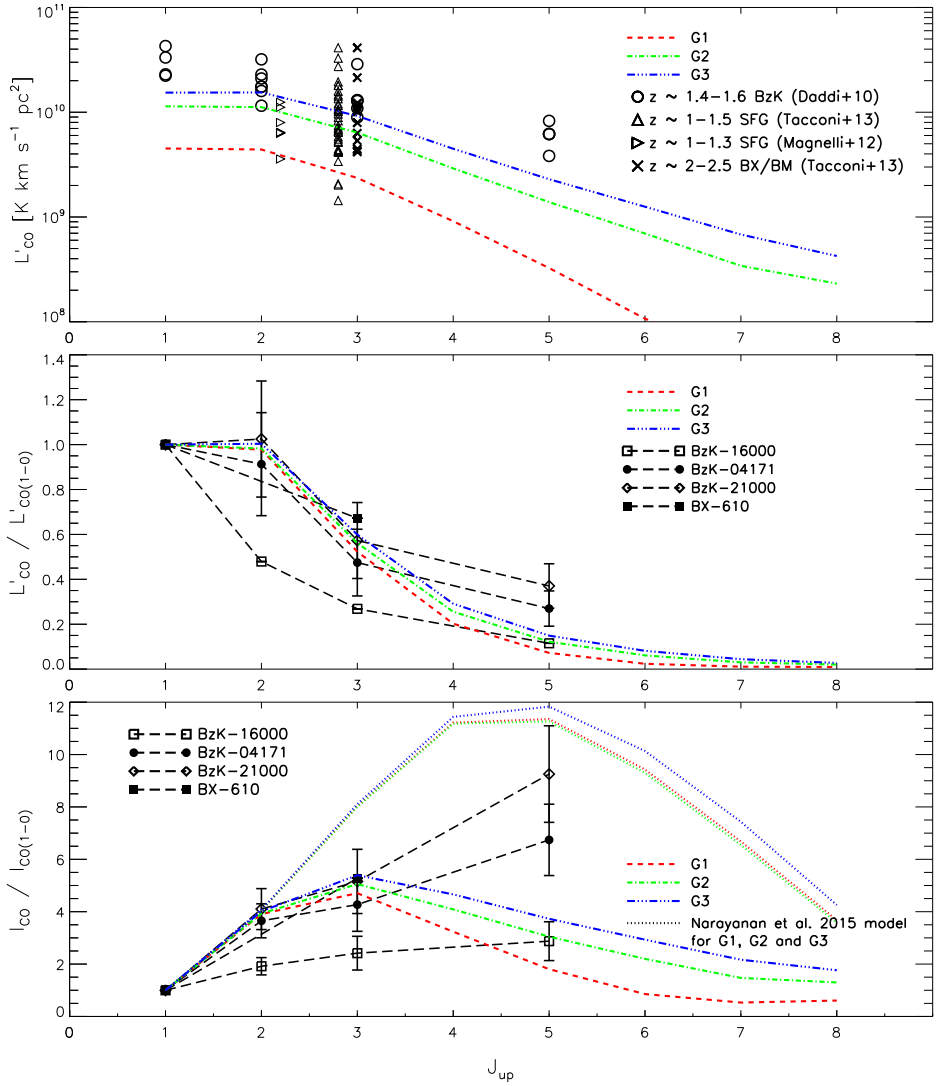


Figure 4.10 Global CO SLEDs of our three model galaxies G1, G2 and G3 shown as red (dashed), green (dash-dot) and blue (dash-dot-dot-dot) curves, respectively. The SLEDs are given as absolute line luminosities in units of $\text{K km s}^{-1} \text{pc}^2$ (top panel), as brightness temperature ratios normalised to the CO(1–0) transition (middle panel), and as velocity-integrated intensity ratios normalised to CO(1–0) (bottom panel). The model CO SLEDs are compared with observations of $z \sim 1.4–1.6$ BzK galaxies (open circles; Dannerbauer et al., 2009; Daddi et al., 2010, 2015; Aravena et al., 2010, 2014), $z \sim 1–1.5$ star-forming galaxies (CO(3–2); empty triangles; Tacconi et al., 2013), $z \sim 1–1.3$ star-forming galaxies (CO(1–0) and CO(2–1); right-facing triangles; Magnelli et al., 2012), and $z \sim 2–2.5$ BX/BM galaxies (CO(3–2); crosses; Tacconi et al., 2013). Four BzK galaxies (BzK–16000, BzK–4171, BzK–21000 and BzK–610) have been observed in CO(1–0) and at least one additional transition to date, and are highlighted in the bottom two panels by connecting dashed lines and individual symbols. Also shown in the bottom panel, with dotted lines, are the line ratio predictions of Narayanan & Krumholz (2014) (D14), calculated for the Σ_{SFR} of our galaxies, G1 to G3 from bottom to top (see Section 4.6).

in order to facilitate a comparison with our simulated CO SLEDs. In addition to the $z \sim 1–1.5$

BzK and $z \sim 2 - 2.5$ BX/BM samples by Daddi et al. (2010) and Tacconi et al. (2013), respectively, this includes 7 star-forming galaxies (SFGs) at $z \sim 1.2$ (Magnelli et al., 2012) and 39 SFGs at $z \sim 1 - 1.5$ (Tacconi et al., 2013). The galaxies in the sample from Magnelli et al. (2012) are all detected in CO(2–1) as well as in *Herschel*/PACS bands, and have $\log(M_*/M_\odot) = 10.36 - 11.31$ and $\text{SFR} \sim 29 - 74 M_\odot \text{ yr}^{-1}$. The $z \sim 1 - 1.5$ SFG sample from Tacconi et al. (2013) comes from the Extended Growth Strip International Survey (EGS), is covered by the CANDELS and 3D-HST programs ($J - H$ bands and $H\alpha$ respectively), and has $\log(M_*/M_\odot) = 10.40 - 11.23$ and $\text{SFR} \sim 28 - 630 M_\odot \text{ yr}^{-1}$.

The $z \sim 2 - 2.5$ BX/BM galaxies of Tacconi et al. (2013) are not only closest in redshift to our simulated galaxies but also occupy the same region of the $\text{SFR} - M_*$ plane (see Figure 4.2). We find that G2 and G3, the two most massive ($M_* > 10^{11} M_\odot$) and star-forming ($\text{SFR} \gtrsim 80 M_\odot \text{ yr}^{-1}$) galaxies of our simulations, have CO(3–2) luminosities of 6.4×10^9 and $9.2 \times 10^9 \text{ K km s}^{-1} \text{ pc}^2$, respectively, in the range of CO(3–2) luminosities of the BX/BM galaxies. G1 is just below this range and about a factor of 4 below the average BX/BM luminosity ($\sim 1.2 \pm 0.9 \times 10^{10} \text{ K km s}^{-1} \text{ pc}^2$). All three simulated galaxies have CO(2–1) and CO(3–2) luminosities consistent with those of the $z \simeq 1 - 1.5$ SFGs observed by Magnelli et al. (2012) and Tacconi et al. (2013), which span a range in CO(2–1) and CO(3–2) luminosity of $(3.6 - 12.5) \times 10^9$ and $(1.4 - 41.3) \times 10^9 \text{ K km s}^{-1} \text{ pc}^2$, respectively. Finally, we see that the $z \sim 1.5$ BzK galaxies in general have higher CO line luminosities across all observed CO transitions (up to $J_{\text{up}} = 5$), although at the $J = 2 - 1$ and $J = 3 - 2$ transitions there is overlap with G3. As mentioned in Section 4.4.1, the molecular gas mass fractions of our galaxies is a factor $\sim 4 - 5$ below the mean of the observed galaxies at $z \sim 1 - 2.5$ with which we compare, and we propose this as the main reason for the comparatively low CO luminosities.

Differences in the global CO excitation conditions between G1, G2 and G3 are best seen in the CO(1–0) normalised luminosity (and intensity) ratios, i.e., middle (and bottom) panel in Figure 4.10. The CO SLEDs of all three galaxies follow each other quite closely up to the $J = 3 - 2$ transition where the SLEDs all peak; at $3 < J_{\text{up}} < 7$ the SLEDs gradually diverge. While the metallicity distributions in G1, G2 and G3 are similar (see Figure A.3), the rise in G_0 presents a likely cause to the increasing high- J flux when going from G1 to G3, as higher G_0 leads to more flux primarily in the $J > 4$ transitions (see Figure A.5).

Our simulated galaxies are seen to have CO 2–1/1–0, 3–2/1–0, and 5–4/1–0 brightness temperature ratios of $r_{21} \simeq 1$, $r_{32} \simeq 0.6$, and $r_{54} \simeq 0.15$, respectively. The first two ratios compare extremely well with the line ratios measured for BzK–4171 and BzK–21000, i.e., $r_{21} \simeq 0.9 - 1$, and $r_{32} \simeq 0.5 - 0.6$ (Dannerbauer et al., 2009; Aravena et al., 2010; Daddi et al., 2010, 2015), and suggest that our simulations are able to emulate the typical gas excitation conditions responsible for the excitation of the low- J lines in normal $z \sim 1 - 3$ SFGs. In contrast, $r_{54} = 0.3 - 0.4$ observed in BzK–4171 and BzK–21000 (Daddi et al., 2015), is nearly $2\times$ higher than our model predictions. Daddi et al. (2015) argue that this is evidence for a component of denser and possibly warmer molecular gas, not probed by the low- J lines. In this picture, we would expect CO(4–3) to probe both the cold, low-excitation gas as well as the dense and possibly warm star-forming gas traced by the CO(5–4) line, and we would expect CO(6–5) to be arising purely from this more highly excited phase and thus departing even further from our models.

However, significant scatter in the CO line ratios of main-sequence galaxies is to be expected, as demonstrated by the significantly lower line ratios observed towards BzK–16000: $r_{21} \simeq 0.4$, $r_{32} \simeq 0.3$, and $r_{54} \simeq 0.1$ (Aravena et al., 2010; Daddi et al., 2010, 2015) and, in fact, the average r_{54} for all three BzK galaxies above ($\simeq 0.2$; Daddi et al., 2015) is consistent with

our models. It may be that G2 and G3, and perhaps even G1, are more consistent with the CO SLEDs of the bulk $z \sim 1 - 3$ main-sequence galaxies. We stress, that to date, no $z \sim 1 - 3$ main sequence galaxies have been observed in the $J = 4 - 3$ nor the $6 - 5$ transitions, and observations of these lines, along with low- and high- J lines in many more BzK and main-sequence $z \simeq 1 - 3$ galaxies are needed in order to fully delineate the global CO SLEDs in a statistically robust way.

4.5 TESTING DIFFERENT ISM MODELS

In this section we investigate the effects on our simulation results when adopting i) a more top-heavy GMC mass spectrum with a slope of $\beta = 1.5$, ii) a steeper GMC density profile, i.e., a Plummer profile exponent of $-7/2$, and iii) a GMC model grid that includes P_{ext} as a fourth parameter. In order to carry out option iii), the GMC model grid was produced for $P_{\text{ext}}/k_{\text{B}} = 10^4 \text{ cm}^{-3} \text{ K}$ (default), $10^{5.5} \text{ cm}^{-3} \text{ K}$ and $10^{6.5} \text{ cm}^{-3} \text{ K}$, allowing for a look-up table of CO SLEDs in $(G_0, m_{\text{GMC}}, Z', P_{\text{ext}})$ parameter space.

We examine the effects that options i)-iii) have on the global CO SLED of galaxy G2 (Figure 4.11) and how combinations of option i) and ii) change the values of the global CO-to- H_2 conversion factor for all three simulated galaxies (Table 4.4). Also, we show the impact that changes ii) and iii) have on the CO SLEDs of the individual GMC grid models in Figures A.6 and A.7.

Changing the GMC mass spectrum from $\beta = 1.8$ to 1.5 leaves the CO SLED virtually unchanged with only a marginal increase in the line flux ratios for $J_{\text{up}} \geq 4$. This holds true regardless of what has been assumed for ii) and iii) (compare solid vs. dashed and dot-dashed vs. dotted curves in Figure 4.11). Also, changing β from 1.8 to 1.5 does not lead to any significant change in α_{CO} (Table 4.4).

Adopting the modified Plummer density profile with an exponent of $-7/2$ instead of $-5/2$ results in significantly higher global line ratios for $J_{\text{up}} \geq 3$ (see dotted vs. dashed curve and dot-dashed vs. solid curves in Figure 4.11). This is due to the higher central densities achieved for the modified Plummer profile which, as shown in Figure A.6, leads to an increase in the excitation of the higher J lines relative to that of the low- J lines. Significantly higher α_{CO} values ($\simeq 3.6 \text{ M}_{\odot} \text{ pc}^{-2} (\text{K km s}^{-1})^{-1}$) are obtained when adopting a modified Plummer profile (Table 4.4). These are in excellent agreement with the α_{CO} values inferred for $z \simeq 1.5 - 2$ BzK galaxies by Daddi et al. (2010). In our simulations, the higher α_{CO} values are due the steeper density profile which leads to smaller GMC sizes and therefore smaller CO(1-0) fluxes (Figure A.6) and, ultimately, a lowering of the total CO(1-0) luminosity of the galaxy.

Including external pressures of $P_{\text{ext}}/k_{\text{B}} = 10^{5.5} \text{ cm}^{-3} \text{ K}$ and $10^{6.5} \text{ cm}^{-3} \text{ K}$ in the GMC model grid (see Section 4.3.4), means that these pressure values are assigned to GMCs with $P_{\text{ext}}/k_{\text{B}}$ in the ranges $10^{4.75} - 10^6$ and $> 10^6 \text{ cm}^{-3} \text{ K}$, respectively. The higher pressures now experienced by these subsets of GMCs results in smaller radii since $R_{\text{GMC}} \propto P_{\text{ext}}^{-1/4}$ for a given mass (see eq. 4.9). Their velocity dispersions and densities increase since $\sigma_v \propto P_{\text{ext}}^{1/8}$ and $n_{\text{H}_2}(R = 0) \propto P_{\text{ext}}^{3/4}$ for a given mass (see eqs. 4.10 and 4.11). The net effect this has on the global CO SLED is depicted in the bottom panel of Figure 4.11. Line ratios with $J_{\text{up}} = 3$ are lowered, and increasingly so for higher J , resulting in a steeper decline at high ($J_{\text{up}} \geq 4$) transitions.

Table 4.4 The global H_2 -to-CO conversion factors (in units of $\text{M}_\odot \text{pc}^{-2} (\text{K km s}^{-1})^{-1}$), averaged over G1, G2, and G3, for combinations of assumptions i) and ii). The pressure has been kept fixed at $P_{\text{ext}}/k_B = 10^4 \text{ cm}^{-3} \text{ K}$.

	$\beta = 1.8$	$\beta = 1.5$
Plummer profile	1.5 ± 0.1	1.5 ± 0.1
Modified Plummer profile	3.6 ± 0.4	3.5 ± 0.5

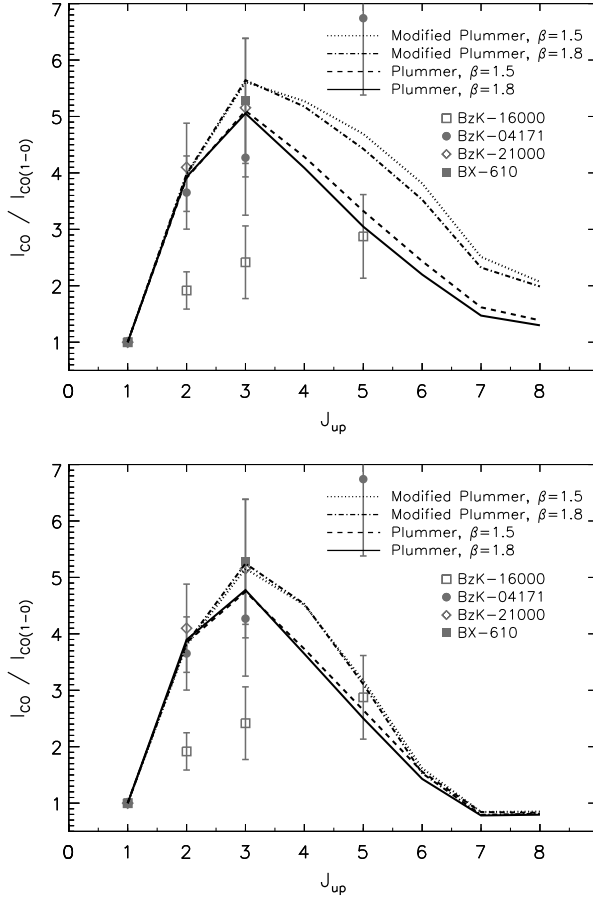


Figure 4.11 Global CO SLEDs of our model galaxy G2 for different choices of ISM prescriptions. *Top*: For a pressure fixed of $10^4 \text{ cm}^{-3} \text{ K}$. *Bottom*: Using the P_{ext} as a fourth parameter in the GMC model grid (see Section 4.3.4).

4.6 COMPARISON WITH OTHER MODELS

The sub-grid physics implemented by SÍGAME assumes that the scaling-laws and thermal balance equations that have been established for GMCs in our own Galaxy can be applied to the ISM conditions in high- z galaxies. In this respect, SÍGAME does not differ from most other numerical simulations of the molecular line emission from galaxies (e.g., Narayanan et al., 2006; Pelupessy et al., 2006; Greve & Sommer-Larsen, 2008; Christensen et al., 2012; Lagos et al., 2012; Muñoz & Furlanetto, 2013; Narayanan & Krumholz, 2014; Lagos et al., 2012; Popping et al., 2014), although there are of course differences in the range and level of detail of the various

sub-grid physics implementations. Here we highlight and discuss some of these differences between *SÍGAME* and other simulations.

First, however, we compare the *SÍGAME* CO SLEDs of G1, G2, and G3 with those predicted by other CO emission simulations of similar main-sequence galaxies. A direct comparison can be made with the models presented by Narayanan & Krumholz (2014), where the global CO SLED is parametrised as a function of the luminosity weighted SFR surface density (Σ_{SFR}). We approximate a luminosity weighted Σ_{SFR} by calculating a mean of Σ_{SFR} for 1 kpc^2 pixels across the galaxies seen face-on, weighted by the total SFR within the pixels. With this procedure, G1, G2 and G3 have Σ_{SFR} of 3.0, 2.9 and $3.8 \text{ M}_{\odot} \text{ yr}^{-1} \text{ kpc}^2$, respectively, and the resulting CO SLEDs inferred from the Narayanan & Krumholz (2014) parametrisation are shown as dotted lines in the bottom panel of Figure 4.10. These are seen to peak at $J_{\text{up}} = 5$ and not 3 as the *SÍGAME* CO SLEDs do. Also, the line flux ratios are significantly higher for all transitions above $J_{\text{up}} = 2$. Both set of models agree on the r_{21} ratio, but follow distinct CO SLED shapes for the remaining transitions. The models also seem to suggest one dominating ISM phase, whereas the observed CO SLED of the BzK galaxies indicate a more complex multi-phased ISM.

Combining a semi-analytical galaxy formation model with a photon-dominated region code, Lagos et al. (2012) made predictions of the CO SLEDs of $z = 2$ galaxies as a function of their IR luminosities. They found that for galaxies with infrared luminosities $L_{\text{IR}} \sim 10^{11.6} - 10^{12.2} L_{\odot}$ – which is the range found for G1, G2, and G3 if one adopts $L_{\text{IR}}/L_{\odot} = \text{SFR}/[\text{M}_{\odot} \text{ yr}^{-1}] \times 10^{10}$ (Kennicutt 1998 for a Chabrier IMF) – the CO SLEDs (when converted to velocity integrated flux ratios in order to compare with the bottom panel of Figure 4.10) peak at $J = 3 - 2$, in agreement with our model galaxies. However, the line ratios of the CO SLEDs of Lagos et al. (2012) are consistently above ours up to $J_{\text{up}} = 7$, but cross over our models at $J_{\text{up}} = 7$ and go below at $J_{\text{up}} = 8$. In terms of CO line luminosity, our model G1 agrees best with the models of Lagos et al. (2012), lying within the 10-90 percentile ranges (80% of their galaxy distribution) for the CO luminosities of their sample for $2 < J_{\text{up}} < 8$, but slightly below for the first two transitions and for $J_{\text{up}} > 7$. G2 and G3, lying roughly a factor 2-4 above G1, are outside the 10-90 percentile ranges of the models from Lagos et al. (2012).

Popping et al. (2014), in their semi-analytical study of MS galaxies at $z = 0, 1.2$ and 2, found that for galaxies with far-infrared (FIR) luminosities of $L_{\text{FIR}} = 10^{11} - 10^{12} L_{\odot}$, the CO SLED peaks at CO(3–2) or CO(4–3) at $z = 0$, but at CO(6–5) at $z = 2$, as a result of denser and warmer gas in their model galaxies. The CO luminosities of our galaxies G2 and G3 are in broad agreement with the corresponding models by Popping et al. (2014) at CO(4–3) and (5–4) for similar SFRs. But at $J_{\text{up}} < 4$ our galaxies are above while at $J_{\text{up}} > 5$, our galaxies are below those of Popping et al. (2014) up until $J_{\text{up}} = 9$ where the SLEDs cross again.

• Implementation of G_0 and ζ_{CR}

SÍGAME stands out from most other simulations to date in the way the FUV radiation field and the CR flux that impinge on the molecular clouds are modelled and implemented. Most simulations adopt a fixed, galaxy-wide value of G_0 and ζ_{CR} , scaled by the total SFR or average gas surface density across the galaxy (e.g., Lagos et al., 2012; Narayanan & Krumholz, 2014). *SÍGAME* refines this scheme by determining a spatially varying G_0 (and ζ_{CR}) set by the local SFRD, as described in Section 4.3.3. By doing so, we ensure that the molecular gas in our simulations is calorimetrically coupled to the star formation in their vicinity. If we adopt the method of Narayanan & Krumholz (2014) and calculate a global value for G_0 by calibrating to the MW value, using $\text{SFR}_{\text{MW}} = 2 \text{ M}_{\odot} \text{ yr}^{-1}$ and $G_{0,\text{MW}} = 0.6 \text{ Habing}$, our galaxies would have G_0 rang-

ing from about 12 to 42, whereas, with the SFR surface density scaling of Lagos et al. (2012), global G_0 values would lie between about 6 and 9. For comparison, the locally determined G_0 in our model galaxies spans a larger range from 0.3 to 27 (see Figure A.3). Narayanan & Krumholz (2014) determine the global value of ζ_{CR} as $2 \times 10^{-17} \text{Z}' \text{s}^{-1}$, corresponding to values of $3.7 - 6.2 \times 10^{-17} \text{s}^{-1}$ in our model galaxies, when using the mass-weighted mean of Z' in each galaxy. Typical values adopted in studies of ISM conditions are around $(1 - 2) \times 10^{-17} \text{s}^{-1}$ (Wolfire et al., 2010; Glover & Clark, 2012), but again, the local values of ζ_{CR} in our galaxies span a larger range, from 1.3×10^{-17} to $1.3 \times 10^{-15} \text{s}^{-1}$. Adopting the method of Narayanan & Krumholz (2014) for G_0 and ζ_{CR} in our galaxies, leads to higher CO luminosities at $J_{\text{up}} > 2$, but very similar CO(1 – 0) luminosities which together with slightly reduced molecular gas masses result in smaller α_{CO} factors by about 7 – 8 %.

• The molecular gas mass fraction

In SÍGAME the molecular gas mass fraction (f'_{mol}) is calculated following the work by Pelupessy et al. (2006) (P06), in which f'_{mol} depends on temperature, metallicity, local FUV field, and boundary pressure on the gas cloud in question. Other methods exist, such as those of Blitz & Rosolowsky (2006) and Krumholz et al. (2009) (K09). The K09 method, which was adopted by e.g. Narayanan & Krumholz (2014), establishes f'_{mol} from local cloud metallicity, dissociating radiation field and column density. In Figure 4.12 we compare the K09 method to that of P06. The gas surface density that enters in the K09 method was estimated within 1 kpc of each SPH particle, as used in our calculation of P_{ext} (see Section 4.3.3).

The two methods agree for molecular gas fractions $\gtrsim 80\%$, which are seen to be dominated by SPH particles with high metallicities (i.e., $\log Z' \gtrsim 0.3$). At lower molecular gas fractions the agreement between the two methods exhibit an increasing scatter. Also, systematic, metallicity dependent differences are seen between the two methods. For high metallicity gas, the P06 method gives systematically higher molecular gas fractions than the K09 method. At low metallicities (i.e., $\log Z' \lesssim 0.2$) the K09 method tends to result in higher molecular gas fractions than P06. The above is the result of the K09 method having a much weaker dependance on Z' Krumholz et al. (2009) than the P06 method (see Section 4.3.3). Despite these differences, we find that using the K09 instead of the P06 method does not change the total molecular gas mass significantly: f_{mol} for G1, G2 and G3 goes from 12.2, 10.0, 9.2 % to 11.4, 10.7 and 10.3 %, respectively.

A common feature of the above $\text{HI} \rightarrow \text{H}_2$ prescriptions is that they assume an instantaneous HI to H_2 conversion. However, as pointed out by Pelupessy et al. (2006), the typical timescales for H_2 cloud formation are of order $\sim 10^7$ yr, which are comparable to the timescales of a number of processes, such as cloud-cloud collisions and star formation, that can potentially alter or even fully disrupt typical molecular clouds and drive H_2 formation/destruction in both directions. Ideally, therefore, a comprehensive modeling of the $\text{HI} \rightarrow \text{H}_2$ transition should be time-dependent. Relying on the findings of Narayanan et al. (2011) and Krumholz & Gnedin (2011), the static solution for H_2 formation is a valid approximation for $Z' > 0.01$, which is the case for the three model galaxies studied here.

• CO abundance

SÍGAME assumes a constant CO abundance relative to H_2 , which for the simulations presented in this work was set to the Galactic CO abundance, i.e., $[\text{CO}/\text{H}_2] = 2 \times 10^{-4}$. In reality, H_2 gas can self-shield better than the CO gas, creating an outer region or envelope of ‘CO-dark’ gas (Bolatto et al., 2008). Observations in the MW by Pineda et al. (2013) indicate that the amount

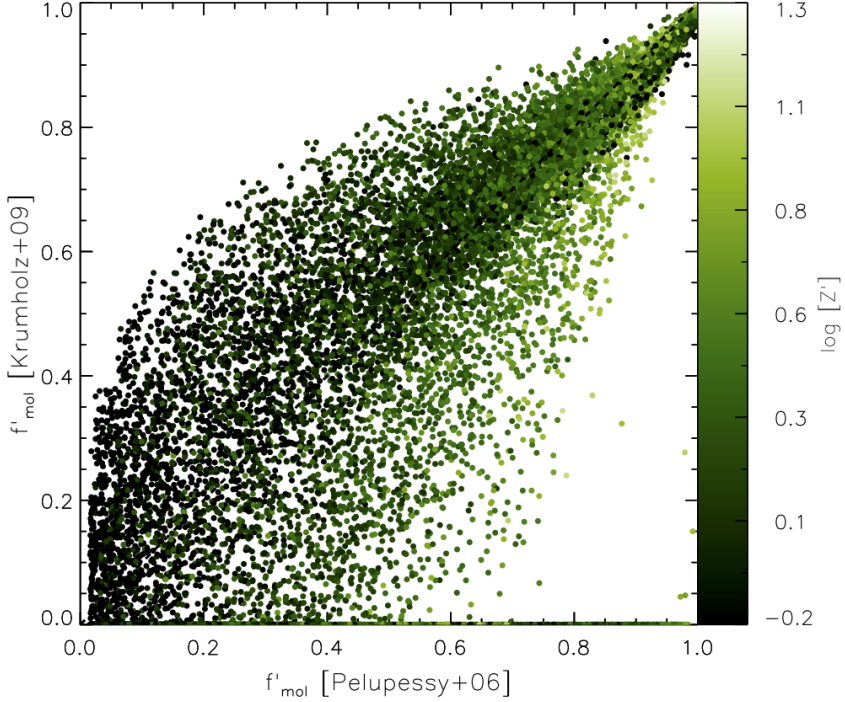


Figure 4.12 Comparison of two methods for calculating the molecular gas mass fraction, f'_{mol} , of SPH particles in G1: That of Pelupessy et al. (2006) with external cloud pressure derived from hydrostatic mid-plane equilibrium as done in this work (abscissa) and that of Krumholz et al. (2009) (ordinate) used by e.g., Narayanan & Krumholz (2014), color-coded by metallicity.

of dark gas grows with decreasing metallicity and the resulting absence of CO molecules. By modeling a dynamically evolving ISM with cooling physics and chemistry incorporated on small scales, Smith et al. (2014) showed that in a typical MW-like disk of gas, the CO-dark gas mass fraction, f_{DG} , defined as having integrated CO intensity $W_{\text{CO}} < 0.1 \text{ K km s}^{-1}$, is about 42 %, but up to 62 % in a radiation field ten times that of the solar neighbourhood. While Smith et al. (2014) kept metallicity fixed to solar, Wolfire et al. (2010) found f_{DG} values of about 0.5 – 0.7 for the low metallicity cases with $Z' = 0.5$ in $10^6 M_{\odot}$ clouds immersed in the local interstellar radiation field. Recently, Bisbas et al. (2015) argued that CR ionization rates of $10 - 50 \times \zeta_{\text{CR,MW}}$ can effectively destroy most CO in GMCs.

Thus, it is expected that $[\text{CO}/\text{H}_2]$ is lower in regions of low metallicity and/or intense FUV and CR fields, effectively leading to underestimates of the α_{CO} conversion factor when not accounted for in models. Since in this work we have restricted our simulations to main-sequence galaxies with solar or higher than solar metallicities, adopting a constant Galactic $[\text{CO}/\text{H}_2]$ seems a reasonable choice, but see Lagos et al. (2012), Narayanan et al. (2012) and Narayanan & Krumholz (2014) for alternative approaches.

• GMC density and thermal structure

When solving for the temperature structure of each GMC, *SÍGAME* includes only the most

dominant atomic and molecular species in terms of heating and cooling efficiencies. `SÍGAME` also ignores heating via X-ray irradiation and turbulence. In particular, it has been shown with models that turbulent heating can completely control the mean temperature of molecular clouds, exceeding the heating from cosmic rays (Pan & Padoan, 2009). Our comparison of observed CO SLEDs at $z = 2$ with those of `SÍGAME`, suggest that our simulations are missing a warm gas component, which could be explained, at least in part, by the exclusion of turbulent heating. We have, however, checked our $T_k - n_{\text{H}_2}$ curves in Figure A.4 against those of Glover & Clark (2012), who performed time-resolved, high-resolution ($\delta m \simeq 0.05 - 0.5 M_\odot$) SPH simulations of individual FUV irradiated molecular clouds using a chemical network of 32 species (see their Figure 2). Overall, there is great similarity in the T_k vs. n_{H_2} behaviour of the two sets of simulations. This includes the same main trend of decreasing temperature with increasing hydrogen density, as well as the local increase in T_k at $\sim 10^3 - 10^4 \text{ cm}^{-3}$ and the subsequent decrease to $T_k < 10 \text{ K}$ at $n_{\text{H}_2} > 10^{5.5} \text{ cm}^{-3}$. Thus, our GMCs models, despite their simplified density profiles and chemistry, seem to agree well with much more detailed simulations.

4.7 SUMMARY

In this chapter we have presented `SÍGAME`, a code that simulates the molecular line emission of galaxies via a detailed post-processing of the outputs from cosmological SPH simulations. A sequence of sub-grid prescriptions are applied to a simulation snapshot in order to derive the molecular gas density and temperature from the SPH particle information, which includes SFR, gas density, temperature and metallicity.

A key aspect of `SÍGAME` is the *localised* coupling between the star formation and the energetics of the ISM, where the strength of the local FUV radiation field and CR ionization rate that impinge and heat a cloud scales with the local star formation rate density. The radial temperature profile of each GMC is calculated by balancing the heating rate with cooling from H_2 , CO, OI, and [CII] lines in addition to gas-dust interactions. In these thermal balance calculations, `SÍGAME` takes into account the local enrichment of the gas, which is a critical parameter for the cooling rates. The CO emission line spectrum from a grid of GMC models is calculated using the 3D radiative transfer code `LIME`.

We used `SÍGAME` to create line emission velocity-cubes of the full CO rotational ladder for three cosmological N-body/SPH simulations of massive ($M_* \gtrsim 10^{10.5} M_\odot$) main-sequence galaxies at $z = 2$.

Molecular gas is produced more efficiently towards the centre of each galaxy, and while HI surface gas densities (including helium) do not exceed $\sim 100 M_\odot \text{ pc}^{-2}$ anywhere in the disk, central molecular gas surface densities reach $\sim 1000 M_\odot \text{ pc}^{-2}$ on spatial scales of $100 \text{ pc} \times 100 \text{ pc}$, in good agreement with observations made at similar spatial resolution. This strong increase in molecular surface density is brought on by a similar increase in total gas surface density, overcoming the increase in photo-dissociating FUV field towards the centre of each galaxy.

Turning to the CO emission, the velocity-integrated moment 0 maps reveal distinct differences in the various transitions as molecular gas tracers. The morphology of molecular gas in our model galaxies is well reproduced in CO(1-0), but going to higher transitions, the region of CO emitting gas shrinks towards the galaxy centres. The global CO SLEDs of our simulated galaxies all peak at $J = 3 - 2$. Recent CO(5 - 4) observations of $z \sim 1.5$ BzK galaxies seem to

suggest that these galaxies actually peak at higher J . The CO(3 – 2) line luminosities of our model galaxies are within the range of corresponding observed samples at redshifts $z \sim 1 - 2.5$, however on the low side. In particular, the model galaxies are below or at the CO luminosities of BzK-selected galaxies of comparable mass and SFR but at $z \sim 1.5$. The low luminosities are most likely a consequence of molecular gas mass fractions in our galaxies being about $\sim 4 - 5$ times below the observed values in the star-forming galaxies at $z = 1 - 2.5$ used to compare with.

Combining the derived H₂ gas masses with the CO(1 – 0) line emission found, we investigate local variations in the CO-H₂ conversion factor α_{CO} . The radial α_{CO} profiles all show a decrease towards the galaxy centres, dropping by a factor of ~ 1.2 in the central $R \leq 2$ kpc region compared to the disk average, the main driver being the FUV field rather than a gradient in density or metallicity. Global α_{CO} factors range from 1.4 to $1.6 \text{ M}_{\odot} \text{ pc}^{-2} (\text{K km s}^{-1})^{-1}$ or about 0.3 times the MW value, but closer to values for $z \sim 1.5$ normal star-forming galaxies identified with the BzK colour criteria. Changing the GMC properties from what is observed in the MW and local galaxies to a steeper GMC density profiles and/or a shallower GMC mass spectra, resulted in elevated α_{CO} values of up to 0.9 times the MW value.

The CO luminosity ratios of CO 3–2/1–0 and 7–6/1–0 (r_{32} and r_{76} respectively) drop off in radius about where the FUV radiation drops in intensity, and are thus likely controlled by the FUV field as is α_{CO} . The global ratios of $r_{21} \simeq 1$ and $r_{32} \simeq 0.6$ agree very well with observations of BzK galaxies, while the r_{54} of about 0.15 is low compared to recent observations in BzK–4171 and BzK–21000. The low flux from high CO transitions in our models compared to observations could be explained, at least in part, by our omission of turbulent heating in SÍGAME. However, more observations of $J_{\text{up}} > 3$ lines towards high- z main-sequence galaxies, such as the BzKs, are still needed in order to determine the turn-over in their CO SLEDs and better constrain the gas excitation.

Finally, we note that SÍGAME in principle is able to simulate the emission from a broad range of molecular and atomic lines in the far-IR/mm wavelength regime provided measured collision rates exist, such as those found in the LAMDA database⁵. For more on future applications of SÍGAME, see the Outlook chapter after the following chapter.

⁵<http://www.strw.leidenuniv.nl/~moldata/>, Schöier et al. (2005)

4.8 REFERENCES

- Aalto, S. 2013, in IAU Symposium, Vol. 292, IAU Symposium, ed. T. Wong & J. Ott, 199–208
- Ackermann, M., Ajello, M., Allafort, A., et al. 2013, *Science*, 339, 807
- Adelberger, K. L., Steidel, C. C., Shapley, A. E., et al. 2004, *ApJ*, 607, 226
- Aravena, M., Carilli, C., Daddi, E., et al. 2010, *ApJ*, 718, 177
- Aravena, M., Hodge, J. A., Wagg, J., et al. 2014, *MNRAS*, 442, 558
- Asplund, M., Grevesse, N., Sauval, A. J., & Scott, P. 2009, *ARA&A*, 47, 481
- Bigiel, F., Leroy, A., Walter, F., et al. 2008, *AJ*, 136, 2846
- Black, J. H., & Dalgarno, A. 1977, *ApJs*, 34, 405
- Blanc, G. A., Schruha, A., Evans, II, N. J., et al. 2013, *ApJ*, 764, 117
- Blitz, L., Fukui, Y., Kawamura, A., et al. 2007, *Protostars and Planets V*, 81
- Blitz, L., & Rosolowsky, E. 2006, *ApJ*, 650, 933
- Bolatto, A. D., Leroy, A. K., Rosolowsky, E., Walter, F., & Blitz, L. 2008, *ApJ*, 686, 948
- Bolatto, A. D., Wolfire, M., & Leroy, A. K. 2013, *ARA&A*, 51, 207
- Bovy, J., Rix, H.-W., & Hogg, D. W. 2012, *ApJ*, 751, 131
- Brinch, C., & Hogerheijde, M. R. 2010, *A&A*, 523, A25
- Bryant, P. M., & Scoville, N. Z. 1999, *AJ*, 117, 2632
- Carroll, T. J., & Goldsmith, P. F. 1981, *ApJ*, 245, 891
- Casey, C. M., Narayanan, D., & Cooray, A. 2014, *Phys. Rep.*, 541, 45
- Cazaux, S., & Spaans, M. 2004, *ApJ*, 611, 40
- Chabrier, G. 2003, *PASP*, 115, 763
- Christensen, C., Quinn, T., Governato, F., et al. 2012, *MNRAS*, 425, 3058
- Daddi, E., Cimatti, A., Renzini, A., et al. 2004, *ApJ*, 617, 746
- Daddi, E., Bournaud, F., Walter, F., et al. 2010, *ApJ*, 713, 686
- Daddi, E., Dannerbauer, H., Liu, D., et al. 2015, *A&A*, 577, A46
- Dannerbauer, H., Daddi, E., Riechers, D. A., et al. 2009, *ApJL*, 698, L178
- Downes, D., & Solomon, P. M. 1998, *ApJ*, 507, 615
- Draine, B. T. 2011, *Physics of the Interstellar and Intergalactic Medium* (Princeton University Press)
- Elmegreen, B. G. 1989, *ApJ*, 344, 306
- Geach, J. E., & Papadopoulos, P. P. 2012, *ApJ*, 757, 156
- Genzel, R., Tacconi, L. J., Gracia-Carpio, J., et al. 2010, *MNRAS*, 407, 2091
- Glover, S. C. O., & Clark, P. C. 2012, *MNRAS*, 421, 9
- Glover, S. C. O., & Mac Low, M.-M. 2011, *MNRAS*, 412, 337
- Gnat, O., & Sternberg, A. 2007, *ApJS*, 168, 213
- Goldsmith, P. F. 2001, *ApJ*, 557, 736
- Greve, T. R., & Sommer-Larsen, J. 2008, *A&A*, 480, 335
- Greve, T. R., Leonidaki, I., Xilouris, E. M., et al. 2014, *ApJ*, 794, 142
- Heiderman, A., Evans, II, N. J., Allen, L. E., Huard, T., & Heyer, M. 2010, *ApJ*, 723, 1019
- Heyer, M. H., & Brunt, C. M. 2004, *ApJL*, 615, L45
- Hodge, J. A., Riechers, D., Decarli, R., et al. 2015, *ApJ*, 798, L18
- Ingalls, J. G., Bania, T. M., Boulanger, F., et al. 2011, *ApJ*, 743, 174
- Iono, D., Wilson, C. D., Yun, M. S., et al. 2009, *ApJ*, 695, 1537
- Kennicutt, Jr., R. C. 1998, *ARA&A*, 36, 189
- Krumholz, M. R., & Gnedin, N. Y. 2011, *ApJ*, 729, 36
- Krumholz, M. R., McKee, C. F., & Tumlinson, J. 2009, *ApJ*, 699, 850

- Lagos, C. d. P., Bayet, E., Baugh, C. M., et al. 2012, MNRAS, 426, 2142
- Larson, R. B. 1981, MNRAS, 194, 809
- Lee, H.-H., Bettens, R. P. A., & Herbst, E. 1996, A&As, 119, 111
- Leroy, A. K., Walter, F., Brinks, E., et al. 2008, AJ, 136, 2782
- Leroy, A. K., Bolatto, A. D., Ostriker, E. C., et al. 2015, ApJ, 801, 25
- Liu, T., Wu, Y., & Zhang, H. 2013, ApJ, 775, L2
- Magnelli, B., Saintonge, A., Lutz, D., et al. 2012, A&A, 548, A22
- Mao, R.-Q., Schulz, A., Henkel, C., et al. 2010, ApJ, 724, 1336
- McMillan, P. J. 2011, MNRAS, 414, 2446
- Monaghan, J. J. 2005, Reports on Progress in Physics, 68, 1703
- Muñoz, J. A., & Furlanetto, S. R. 2013, MNRAS, 435, 2676
- Narayanan, D., Cox, T. J., Shirley, Y., et al. 2008a, ApJ, 684, 996
- Narayanan, D., & Hopkins, P. F. 2013, MNRAS, 433, 1223
- Narayanan, D., Krumholz, M., Ostriker, E. C., & Hernquist, L. 2011, MNRAS, 418, 664
- Narayanan, D., & Krumholz, M. R. 2014, MNRAS, 442, 1411
- Narayanan, D., Krumholz, M. R., Ostriker, E. C., & Hernquist, L. 2012, MNRAS, 421, 3127
- Narayanan, D., Cox, T. J., Robertson, B., et al. 2006, ApJL, 642, L107
- Narayanan, D., Cox, T. J., Kelly, B., et al. 2008b, ApJs, 176, 331
- Norman, C. A., & Spaans, M. 1997, ApJ, 480, 145
- Pan, L., & Padoan, P. 2009, ApJ, 692, 594
- Papadopoulos, P. P., Isaak, K., & van der Werf, P. 2010, ApJ, 711, 757
- Papadopoulos, P. P., & Thi, W.-F. 2013, in Advances in Solid State Physics, Vol. 34, Cosmic Rays in Star-Forming Environments, ed. D. F. Torres & O. Reimer, 41
- Papadopoulos, P. P., Thi, W.-F., Miniati, F., & Viti, S. 2011, MNRAS, 414, 1705
- Papadopoulos, P. P., van der Werf, P. P., Xilouris, E. M., et al. 2012, MNRAS, 426, 2601
- Papovich, C., Finkelstein, S. L., Ferguson, H. C., Lotz, J. M., & Giavalisco, M. 2011, MNRAS, 412, 1123
- Pelupessy, F. I. 2005, PhD thesis, Leiden Observatory, Leiden University, P.O. Box 9513, 2300 RA Leiden, The Netherlands
- Pelupessy, F. I., Papadopoulos, P. P., & van der Werf, P. 2006, ApJ, 645, 1024
- Pineda, J. L., Langer, W. D., Velusamy, T., & Goldsmith, P. F. 2013, A&A, 554, A103
- Plummer, H. C. 1911, MNRAS, 71, 460
- Popping, G., Somerville, R. S., & Trager, S. C. 2014, MNRAS, 442, 2398
- Price, D. J. 2007, Publications of the Astronomical Society of Australia, 24, 159
- Rodighiero, G., Cimatti, A., Gruppioni, C., et al. 2010, A&A, 518, L25
- Romeo, A. D., Sommer-Larsen, J., Portinari, L., & Antonuccio-Delogu, V. 2006, MNRAS, 371, 548
- Saintonge, A., Kauffmann, G., Kramer, C., et al. 2011, MNRAS, 415, 32
- Sandstrom, K. M., Leroy, A. K., Walter, F., et al. 2013, ApJ, 777, 5
- Schöier, F. L., van der Tak, F. F. S., van Dishoeck, E. F., & Black, J. H. 2005, A&A, 432, 369
- Seon, K.-I., Edelstein, J., Korpela, E., et al. 2011, ApJs, 196, 15
- Simnett, G. M., & McDonald, F. B. 1969, ApJ, 157, 1435
- Smith, B., Sigurdsson, S., & Abel, T. 2008, MNRAS, 385, 1443
- Smith, R. J., Glover, S. C. O., Clark, P. C., Klessen, R. S., & Springel, V. 2014, MNRAS, 441, 1628
- Sofia, U. J., Lauroesch, J. T., Meyer, D. M., & Cartledge, S. I. B. 2004, ApJ, 605, 272
- Solomon, P. M., Downes, D., Radford, S. J. E., & Barrett, J. W. 1997, ApJ, 478, 144
- Sommer-Larsen, J., Götz, M., & Portinari, L. 2003, ApJ, 596, 47

- Sommer-Larsen, J., Romeo, A. D., & Portinari, L. 2005, *MNRAS*, 357, 478
- Sommer-Larsen, J., Vedel, H., & Hellsten, U. 1998, *MNRAS*, 294, 485
- Speagle, J. S., Steinhardt, C. L., Capak, P. L., & Silverman, J. D. 2014, *ApJS*, 214, 15
- Springel, V., & Hernquist, L. 2003, *MNRAS*, 339, 289
- Stinson, G., Seth, A., Katz, N., et al. 2006, *MNRAS*, 373, 1074
- Swinbank, A. M., Papadopoulos, P. P., Cox, P., et al. 2011, *ApJ*, 742, 11
- Tacconi, L. J., Genzel, R., Smail, I., et al. 2008, *ApJ*, 680, 246
- Tacconi, L. J., Neri, R., Genzel, R., et al. 2013, *ApJ*, 768, 74
- Tielens, A. G. G. M. 2005, *The Physics and Chemistry of the Interstellar Medium* (Cambridge University Press)
- . 2013, *Reviews of Modern Physics*, 85, 1021
- Vlahakis, C., van der Werf, P., Israel, F. P., & Tilanus, R. P. J. 2013, *MNRAS*, 433, 1837
- Walter, F., Riechers, D. A., Carilli, C. L., et al. 2007, in *Astronomical Society of the Pacific Conference Series*, Vol. 375, *From Z-Machines to ALMA: (Sub)Millimeter Spectroscopy of Galaxies*, ed. A. J. Baker, J. Glenn, A. I. Harris, J. G. Mangum, & M. S. Yun, 182
- Webber, W. R. 1998, *ApJ*, 506, 329
- Whitaker, K. E., Labbé, I., van Dokkum, P. G., et al. 2011, *ApJ*, 735, 86
- Whitworth, A. P., & Ward-Thompson, D. 2001, *ApJ*, 547, 317
- Wiersma, R. P. C., Schaye, J., & Smith, B. D. 2009, *MNRAS*, 393, 99
- Wolfire, M. G., Hollenbach, D., & McKee, C. F. 2010, *ApJ*, 716, 1191
- Wolfire, M. G., McKee, C. F., Hollenbach, D., & Tielens, A. G. G. M. 2003, *ApJ*, 587, 278
- Wuyts, S., Förster Schreiber, N. M., van der Wel, A., et al. 2011, *ApJ*, 742, 96
- Yang, B., Stancil, P. C., Balakrishnan, N., & Forrey, R. C. 2010, *ApJ*, 718, 1062
- Zahid, H. J., Dima, G. I., Kewley, L. J., Erb, D. K., & Davé, R. 2012, *ApJ*, 757, 54

5

[CII] LINE EMISSION FROM GALAXIES

5.1 PROBING THE NEUTRAL AND IONIZED GAS

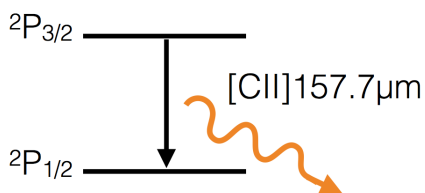


Figure 5.1 The two level system of ionized carbon leading to the line emission at $\sim 158 \mu\text{m}$. The excitation happens via collisions with either electrons, atoms or molecules.

Being the fourth most common element after hydrogen in the Milky Way (MW), it comes as no surprise that carbon is nearly ubiquitous throughout the various phases of the ISM in star-forming galaxies (e.g. Dartois & Muñoz-Caro, 2007; Esteban et al., 2014; James et al., 2014). Much of that carbon is ionized by the ultraviolet (UV) radiation permeating the ISM, due to the low ionization potential of carbon (11.3 eV cf. 13.6 eV for hydrogen). As a result, singly ionized carbon (CII) is found in regions of ionized as well as neutral gas. In both regions, the $^2P_{3/2}-^2P_{1/2}$ fine structure transition of CII can be collisionally excited by electrons (e^-), atoms (H I) or molecules (H_2), depending on the gas phase, resulting in an emission line at $157.714 \mu\text{m}$ or 1900.5369 GHz (hereafter [CII]).

The critical densities of [CII] are only 16 cm^{-3} , 2400 cm^{-3} and 4800 cm^{-3} for collisions with e^- , H I and H_2 respectively at a temperature of 500 K (Goldsmith et al., 2012). Together, these facts are what makes [CII] one of the strongest cooling lines of the ISM, with a line luminosity equivalent to $\sim 0.1 - 1\%$ of the far-infrared (FIR) luminosity of galaxies (e.g. Stacey et al., 1991; Brauher et al., 2008).

5.2 OBSERVATIONS OF [CII] EMISSION IN GALAXIES AT HIGH AND LOW REDSHIFT

Due to high atmospheric opacity at these frequencies, observations of [CII] in the local Universe must be done at high altitudes or in space. Indeed, the very first detections of [CII] towards Galactic objects (Russell et al., 1980; Stacey et al., 1983; Kurtz et al., 1983) and other galaxies (Crawford et al., 1985; Stacey et al., 1991; Madden et al., 1992) were done with airborne observatories such as the NASA Lear Jet and the Kuiper Airborne Observatory. The advent of the Infrared Space Observatory (ISO) allowed for the first systematic [CII] surveys of local galaxies (e.g. Malhotra et al., 1997; Luhman et al., 1998, 2003). Detections of [CII] at high- z have also

become feasible over recent years with ground-based facilities (Hailey-Dunsheath et al., 2010; Stacey et al., 2010), as well as the *Herschel* Space Observatory (see the recent review by Casey et al., 2014).

5.2.1 THE [CII] DEFICIT

Early observations and modeling suggested that [CII] is predominantly associated with Photodissociation Regions (PDRs) in the outskirts of molecular clouds exposed to intense far-ultraviolet (FUV) radiation, hence predicting a strong correlation between [CII] luminosity, $L_{\text{[CII]}}$, and that of reprocessed FUV light as measured in far-infrared (FIR), L_{FIR} (Tielens & Hollenbach, 1985; Crawford et al., 1985). However, a deficit in $L_{\text{[CII]}}$ relative to L_{FIR} was soon observed towards local ultraluminous infrared galaxies (ULIRGs) and high- z galaxies dominated by an AGN (e.g. Malhotra et al., 1997; Luhman et al., 1998; Malhotra et al., 2001; Luhman et al., 2003; Díaz-Santos et al., 2013; Farrah et al., 2013). Some indications suggest that this ‘[CII] deficit’ persists at high- z , with the ratio extending to other FIR lines (e.g. Graciá-Carpio et al., 2011), though the existence of a high- z deficit is debated (Hailey-Dunsheath et al., 2010; Wagg et al., 2010; De Breuck et al., 2011; Ferkinhoff et al., 2011; Swinbank et al., 2012). Magdis et al. (2014) find that intermediate $z \sim 0.3$ ULIRGs actually fall on the relation for local normal galaxies measured by Malhotra et al. (2001), suggesting that high- z ULIRGs are in fact scaled-up versions of local star-forming galaxies, rather than the disturbed systems resulting from mergers that are typically associated with local $z < 0.2$ ULIRGs. The [CII] deficit increases with higher dust temperatures on both global and resolved scales in local galaxies (e.g. Croxall et al., 2012; Díaz-Santos et al., 2013; Herrera-Camus et al., 2015), shown with an example in Fig. 5.2, suggesting that dust plays a crucial role in controlling the $L_{\text{[CII]}}/L_{\text{FIR}}$ ratio.

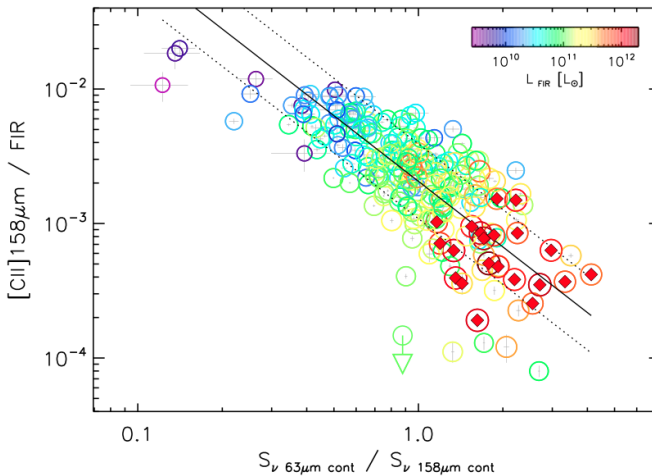


Figure 5.2 The [CII] deficit as investigated and plotted by Díaz-Santos et al. (2013) for local luminous infrared galaxies (LIRGs). Deviation from the global [CII]-FIR relation increases with dust temperature corresponding to increasing 60/100 μm color.

Various scenarios have been put forward as causing the [CII] deficit (see a summary of these in e.g. Malhotra et al., 2001; Herrera-Camus et al., 2015), but a consensus has not been achieved with observations and models so far. Favoured scenarios causing the [CII] deficit are ones in which the efficiency of the FUV light to heat the gas is decreased or obscuring dust absorbs the

FUV radiation before it reaches the potential sources of [CII] emission. Such scenarios include i) large HII regions created by high ionization parameters where most of the FUV radiation is absorbed by dust rather than goes to heating the gas via photo-ionization (e.g. Tielens & Hollenbach, 1985; Abel et al., 2009; Graciá-Carpio et al., 2011; Croxall et al., 2012), ii) high levels of grain charging, primarily in PDRs, which decrease the efficiency of photoelectric heating of the gas by FUV radiation (e.g. Malhotra et al., 2001; Croxall et al., 2012; Ibar et al., 2015), and iii) dust-bounded clouds or PDRs in ULIRGs, where high dust masses in the HII regions absorb most FUV light before it reaches regions with more ionized carbon (Luhman et al., 2003; Farrah et al., 2013; Abel et al., 2009).

5.2.2 CONTRIBUTING GAS PHASES TO THE [CII] EMISSION

Knowing the relative contributions to $L_{\text{[CII]}}$ from different gas phases in the ISM would help sorting out in the possible causes for the [CII] deficit. But observations of [CII] emission alone, will not readily give away information on the different ISM phases contributing, unless combined with some other gas tracer such as [NII] ($122\ \mu\text{m}$) (Malhotra et al., 2001) or HI (21 cm) as well as CO line emission as done by Pineda et al. (2013) for the MW, in order to separate contributions from ionized, neutral and molecular gas. Updated in Pineda et al. (2014), the ISM phases considered are found to contribute with roughly amounts to the total $L_{\text{[CII]}}$ with 30 % from dense PDRs, 25 % from cold HI, 25 % from CO-dark H_2 gas and 20 % from ionized gas. Observing 60 normal, star-forming galaxies in [CII] and [NII], Malhotra et al. (2001) estimated that a rough mean of 50 % of $L_{\text{[CII]}}$ comes from ionized gas and the rest from PDRs. Even larger PDR contributions were found in the giant HII region N11 in the Large Magellanic Cloud (LMC), by Lebouteiller et al. (2012) who conclude, from comparison of [CII] with [NII], that 95 % of $L_{\text{[CII]}}$ arises in diffuse PDRs, whereas dense PDRs are better traced by [OI], also considered the second most important cooling line in neutral gas.

5.2.3 [CII] AS A STAR FORMATION RATE TRACER

Since [CII] is sensitive to the local FUV field which itself probes OB star formation activity, it was early on suggested that $L_{\text{[CII]}}$ correlates with SFR of a galaxy, and observations soon revealed a $L_{\text{[CII]}}$ -SFR correlation for nearby galaxies (Stacey et al., 1991; Leech et al., 1999; Boselli et al., 2002). More comprehensive studies were performed by de Looze et al. (2011); De Looze et al. (2014) and Farrah et al. (2013) for modest star-forming galaxies and ULIRGs in the local Universe. The scatter in the $L_{\text{[CII]}}$ -SFR relation is substantial though, apparently irregardless of the overall galaxy classification (Sargsyan et al., 2012), and increasing towards low metallicity, warm dust temperatures and large filling factors of ionized, diffuse gas (De Looze et al., 2014).

With the Photodetector Array Camera & Spectrometer (PACS) on board *Herschel*, resolved observations of [CII] in local galaxies became possible (e.g. De Looze et al., 2014; Herrera-Camus et al., 2015; Kapala et al., 2015), and the advent of the Atacama Large Millimeter Array (ALMA) promises to make such detections and observations relatively routine, even at high- z (e.g. Wang et al., 2013). The $L_{\text{[CII]}}$ -SFR relation has now also observed on kpc-scales in local galaxies as a kind ‘[CII] KS relation’ between surface density of SFR, Σ_{SFR} , and that of [CII] luminosity, $\Sigma_{\text{[CII]}}$ (e.g. De Looze et al., 2014; Herrera-Camus et al., 2015; Kapala et al., 2015). Kapala et al. (2015) concluded that [CII] traces SFR in the spiral arms of the Andromeda Galaxy (M31) similarly to what is seen in larger samples of more distant galaxies, although with a significant contribution to [CII] from outside star-forming regions. and a shallower slope of the

$\Sigma_{[\text{CII}]}-\Sigma_{\text{SFR}}$ relation on ~ 50 pc scales than on kpc scales. For the MW, Pineda et al. (2014) find that only the combined emission of all gas phases, leads to a slope of the $\Sigma_{[\text{CII}]}-\Sigma_{\text{SFR}}$ relation in agreement with extragalactic observations. But the $\Sigma_{[\text{CII}]}-\Sigma_{\text{SFR}}$ relation for local galaxies also suffers from a great deal of scatter. De Looze et al. (2014) find, when observing 32 local dwarf galaxies on kpc-scales, that this scatter is most likely due to internal ISM conditions, rather than large variations within individual galaxies. Analyzing 46 nearby (mostly spiral) galaxies from the *Herschel* KINGFISH sample, Herrera-Camus et al. (2015) succeeded in reducing the scatter on the $\Sigma_{[\text{CII}]}-\Sigma_{\text{SFR}}$ relation at warm IR colors, by deriving a set of IR color adjustments that can be applied to normal, star-forming galaxies in the absence of strong AGNs. But a firm physical reason for the scatter is still missing.

Metallicity is a potentially important factor for the $L_{[\text{CII}]}-\text{SFR}$, as an increase in metallicity translates into a higher mass fraction of carbon and dust, both of which affect the $L_{[\text{CII}]}-\text{SFR}$ relation. Similar to De Looze et al. (2014), Herrera-Camus et al. (2015) found an increased scatter around the $L_{[\text{CII}]}-\text{SFR}$ relation at low metallicities, implying that at low metallicities, a non-negligible fraction of the neutral gas cooling takes place via the $[\text{OI}]\ 63\ \mu\text{m}$ cooling line instead the $[\text{CII}]$ line. In M31, Kapala et al. (2015) see an increasing trend in $L_{[\text{CII}]} / L_{\text{TIR}}$ with radius as expected if $L_{[\text{CII}]}$ itself depended strongly on metallicity, since M31 exhibits a clearly decreasing metallicity with radius (Sanders et al., 2012). However, Kapala et al. (2015) cannot rule out other factors such as stellar density and radiation field strength. Kramer et al. (2013) found a sharp increase in $L_{[\text{CII}]} / L_{\text{FIR}}$ at $R \sim 4.5$ kpc in M33, but dismiss metallicity as the sole cause, due to the rather shallow metallicity gradient in M33 (Magrini et al., 2010). The effect of low metallicity together with the disruption of molecular clouds is also becoming an important subject for studies of the Epoch of Reionization (EoR) at $z \sim 6$, as a possible explanation for several non-detections of normal star-forming galaxies. Examples include the lensed $\text{Ly}\alpha$ emitter at $z = 6.56$ and the Himiko galaxy at $z \sim 6.5$ forming stars at a rate of ≈ 10 and $\sim 100\ \text{M}_{\odot}\ \text{yr}^{-1}$, respectively (Kanekar et al., 2013; Ouchi et al., 2013), and more recently 3 Lyman Break Galaxies at $z \sim 7$ of $\text{SFR} \sim 10\ \text{M}_{\odot}\ \text{yr}^{-1}$ (Maiolino et al., 2015).

5.3 MODELING $[\text{CII}]$ EMISSION

How the physical conditions of the ISM control the $[\text{CII}]$ emission can be investigated by applying sub-grid treatment to the gas in semi-analytical (Popping et al., 2014a; Muñoz & Furlanetto, 2014) or fully hydrodynamical (Nagamine et al., 2006; Vallini et al., 2013) simulations of galaxy evolution. In their models of $[\text{CII}]$ emission in high- z galaxies Nagamine et al. (2006) found that $[\text{CII}]$ emission depends significantly on the amount of neutral gas. Vallini et al. (2013) improved on the method of Nagamine et al. (2006), by implementing radiative transfer of the UV field and higher resolution simulations of a single $z = 6.6$ $\text{Ly}\alpha$ emitter, though only at two fixed metallicities ($Z = Z_{\odot}$ and $Z = 0.02Z_{\odot}$). Popping et al. (2014a) managed to reproduce the $[\text{CII}]$ deficit for all FIR luminosities at $z > 1$ as well as the $L_{[\text{CII}]}-\text{FIR}$ correlation at $z = 0$, however with the simplification of averaging galaxy properties across annuli in the galactic disks. Muñoz & Furlanetto (2014) modeled $z > 6$ $\text{Ly}\alpha$ emitters, slightly overpredicting the $[\text{CII}]$ while underpredicting the CO line emission, when compared to the few observations available, but demonstrating that line modeling during the Epoch of Reionization is possible. In addition, other works have concentrated on single clouds employing either radiative transfer (Abel et al., 2009) or an escape probability approach (Goldsmith et al., 2012) to derive the $[\text{CII}]$ strength.

6

UNDERSTANDING THE $L_{[\text{CII}]}$ -SFR RELATION WITH SIMULATIONS (PAPER II)

6.1 AIM OF THIS PROJECT

As described in the previous chapter, simulations hold promise in aiding interpretation of the $[\text{CII}]$ emission. In this chapter, an adapted version of our code `SÍGAME` is presented that is capable of incorporating $[\text{CII}]$ emission into smoothed particle hydrodynamics (SPH) simulations of galaxies. We will consider a multi-phased ISM consisting of molecular clouds, whose surface layers are stratified by FUV-radiation from localized star formation, embedded within a neutral medium of atomic gas. In addition, we will include the diffuse ionized gas intrinsic to the SPH simulations as a third ISM phase. The temperatures of the molecular and atomic gas are calculated from thermal balance equations sensitive to the local FUV-radiation and CR ionization rate. `SÍGAME` will be applied to GADGET-3 cosmological SPH simulations of seven star-forming galaxies on the main-sequence (MS) at $z = 2$ in order to simulate the $[\text{CII}]$ emission from normal star-forming galaxies at this epoch, examine the relative contributions to the emission from the molecular, atomic and ionized ISM phases, and the relationship to the star formation activity in the galaxies. Throughout, we adopt a flat cosmology with $\Omega_{\text{M}} = 0.27$, $\Omega_{\Lambda} = 0.73$, and $h = 0.71$ (Spergel et al., 2003).

6.2 METHODOLOGY OVERVIEW

This section gives an overview of our multi-phased ISM model. To a large extent the model follows the steps laid out in Chapter 4, in that it is applied at the post-processing stage of an SPH simulation. As input, the ISM model requires: the position ($[x, y, z]$), velocity ($[v_x, v_y, v_z]$), smoothing length (h), gas mass (m_{SPH}), hydrogen density (n_{H}), gas kinetic temperature (T_{k}), electron fraction ($x_{\text{e}} = n_{\text{e}}/n_{\text{H}}$), SFR, metallicity (Z) as well as the relative abundances of carbon ($[\text{C}/\text{H}]$) and oxygen ($[\text{O}/\text{H}]$). The key steps involved in the post-processing are illustrated in Fig. 6.1 and briefly listed below (with details given in subsequent sections):

The key steps involved in this process are illustrated in Fig. 6.1 and briefly listed below (with full details given in subsequent sections):

1. The SPH gas is separated into its neutral and ionized constituents as dictated by the electron fraction provided by the GADGET-3 simulations.

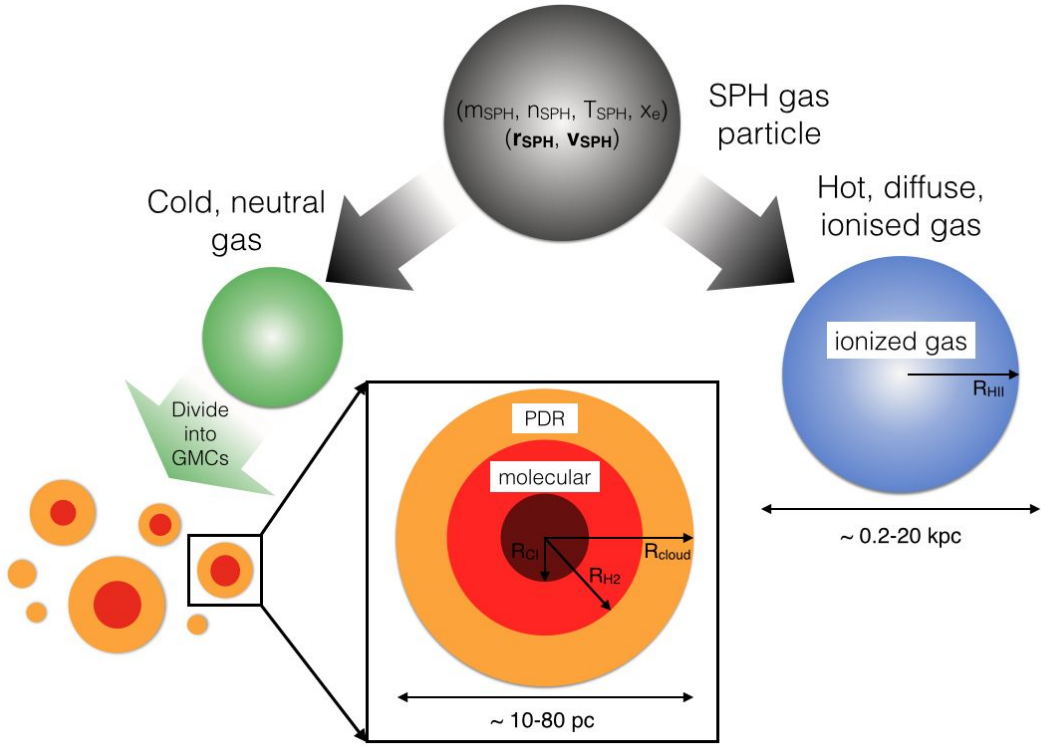


Figure 6.1 Schematic illustrating the sub-grid procedures applied to the SPH simulation in post-processing. Each SPH particle is a hybrid of neutral and ionized gas. The neutral gas associated with each SPH gas particle is divided into GMCs with masses and sizes following the Galactic mass-spectrum and mass-size relation for GMCs. Each GMC has an onion-layer structure, set by the stratification of the impinging FUV-field, which consists of outer layer of PDR/atomic gas of HI and CII, and an inner molecular region where carbon is found in its single ionized state, and in neutral form further in (Section 6.4.1). The ionized gas associated with each SPH particle is assumed to reside in spherical clouds with radii and temperatures given by the SPH smoothing length and gas temperature (Section 6.4.2).

2. The neutral gas is divided into giant molecular clouds (GMCs) according to the observed mass function of GMCs in the Milky Way (MW) and nearby quiescent galaxies. The GMCs are modeled as logotropic spheres with their sizes and internal velocity dispersions derived according to pressure-normalized scaling relations.
3. Each GMC is assumed to consist of three spherically symmetric regions: (1) a FUV-shielded molecular core region where all carbon is locked up in CI and CO; (2) an outer molecular region where both CI and CII can exist; and (3) a largely neutral atomic layer of HI, HII and CII. The last region mimics the FUV-stratified PDRs observed at the surfaces of molecular clouds (Hollenbach & Tielens, 1999). This layer can contain both atomic and ionized gas, but we shall refer to it simply as the PDR gas. The relative extent of these regions within each cloud, and thus the densities at which they occur, ultimately depends on the strength of the impinging FUV-field and CR ionization rate. The latter are set to scale with the local SFR volume density and, by requiring thermal balance with the cooling from line emission (from CII, OI, and H₂), determine the temperatures of the molecular and atomic gas phases.

Table 6.1 Global properties of the seven simulated galaxies used for this work at $z = 2$.

	G1	G2	G3	G4	G5	G6	G7
M_* [$10^{10} M_\odot$]	0.36	0.78	0.95	1.80	4.03	5.52	6.57
M_{gas} [$10^{10} M_\odot$]	0.42	0.68	1.26	1.43	2.59	2.16	1.75
M_{neutral} [$10^{10} M_\odot$]	0.09	0.13	0.57	0.20	0.29	0.29	0.39
M_{ionized} [$10^{10} M_\odot$]	0.33	0.55	0.69	1.23	1.30	1.87	1.36
SFR [$M_\odot \text{ yr}^{-1}$]	4.9	10.0	8.8	25.1	19.9	59.0	37.5
Σ_{SFR} [$M_\odot \text{ yr}^{-1} \text{ kpc}^{-2}$]	0.016	0.032	0.028	0.080	0.063	0.188	0.119
Z'	0.43	0.85	0.64	1.00	1.00	1.67	1.72

All quantities have been calculated at $z = 2$ using a fixed cut-out radius of $R_{\text{cut}} = 10 \text{ kpc}$, which is the radius at which the accumulative stellar mass function of each galaxy flattens. M_{gas} is the total gas mass, and M_{neutral} and M_{ionized} the gas masses in neutral and ionized form, respectively (see Section 6.4). The metallicity ($Z' = Z/Z_\odot$) is the mean of all SPH gas particles within R_{cut} .

4. The remaining ionized gas of the SPH simulation is divided into HII clouds of radius equal to the smoothing lengths, temperature equal to that of the SPH simulation and constant density.
5. The [CII] emission from the molecular, PDR, and diffuse ionized gas is calculated separately and summed to arrive at the total [CII] emission from the galaxy. In doing so it is assumed that there is no radiative coupling between the clouds in the galaxy.

The SPH simulations used in this study, and the galaxies extracted from them, are described in the following section.

6.3 SPH SIMULATIONS

Our simulations are evolved with an updated version of the public GADGET-3 cosmological SPH code (Springel 2005 and S. Huang et al. 2015 in preparation). It includes cooling processes using the primordial abundances as described in Katz et al. (1996), with additional cooling from metal lines assuming photo-ionization equilibrium from Wiersma et al. (2009). We use the more recent ‘pressure-entropy’ formulation of SPH which resolves mixing issues when compared with standard ‘density-entropy’ SPH algorithms (see Saitoh & Makino, 2013; Hopkins, 2013, for further details). Our code additionally implements the time-step limiter of Saitoh & Makino (2009), Durier & Dalla Vecchia (2012) which improves the accuracy of the time integration scheme in situations where there are sudden changes to a particle’s internal energy. To prevent artificial fragmentation (Schaye & Dalla Vecchia, 2008; Robertson & Kravtsov, 2008), we prohibit gas particles from cooling below their effective Jeans temperature which ensures that we are always resolving at least one Jeans mass within a particle’s smoothing length. This is very similar to adding pressure to the ISM as in Springel & Hernquist (2003), Schaye & Dalla Vecchia (2008), except instead of directly pressurizing the gas we prevent it from cooling and fragmenting below the Jeans scale.

We stochastically form stars within the simulation from molecular gas following a Schmidt (1959) law with an efficiency of 1% per local free-fall time (Krumholz & Tan, 2007; Lada et al., 2010). The molecular content of each gas particle is calculated via the equilibrium analytic

model of Krumholz et al. (2008, 2009); McKee & Krumholz (2010). This model allows us to regulate star formation by the local abundance of H_2 rather than the total gas density, which confines star formation to the densest peaks of the ISM. Further implementation details can be found in Thompson et al. (2014). Galactic outflows are implemented using the hybrid energy/momentum-driven wind (ezw) model fully described in Davé et al. (2013); Ford et al. (2015). We also account for metal enrichment from Type II supernovae (SNe), Type Ia SNe, and AGB stars as described in Oppenheimer & Davé (2008).

6.3.1 SPH SIMULATIONS OF $z = 2$ MS GALAXIES

We use the cosmological zoom-in simulations presented in Thompson et al. (2015), and briefly summarized here. Initial conditions were generated using the MUSIC code (Hahn & Abel, 2011) assuming cosmological parameters consistent with constraints from the *Planck* (Planck Collaboration et al., 2014) results, namely $\Omega_m = 0.3$, $\Omega_\Lambda = 0.7$, $H_0 = 70$, $\sigma_8 = 0.8$, $n_s = 0.96$. Six target halos were selected at $z = 2$ from a low-resolution N -body simulation consisting of 256^3 dark-matter particles in a $(16h^{-1}\text{Mpc})^3$ volume with an effective co-moving spatial resolution of $\epsilon = 1.25 h^{-1} \text{ kpc}$. Each target halo is populated with higher resolution particles at $z = 249$, with the size of each high resolution region chosen to be 2.5 times the maximum radius of the original low-resolution halo. The majority of halos in our sample are initialized with a single additional level of refinement ($\epsilon = 0.625 h^{-1} \text{ kpc}$), while the two smallest halos are initialized with two additional levels of refinement ($\epsilon = 0.3125 h^{-1} \text{ kpc}$).

The six halos produce seven star-forming galaxies at $z = 2$ that are free from all low-resolution particles within the virial radius of their parent halo. Their stellar masses (M_*) range from 3.6×10^9 to $6.6 \times 10^{10} M_\odot$ and their SFRs from 5 to $60 M_\odot \text{ yr}^{-1}$ (Table 6.1). We hereafter label the galaxies G1, ..., G7 in order of increasing M_* . Other relevant global properties directly inferred from the SPH simulations, such as total gas mass (M_{gas}), neutral and ionized gas masses (M_{neutral} and M_{ionized} , respectively), average SFR surface density (Σ_{SFR}), and average metallicity (Z'), can also be found in Table 6.1.

Fig. 6.2 shows the locations of G1, ..., G7 in the SFR– M_* diagram. The galaxies are consistent with observational determinations of the $z \sim 2$ MS of star-forming galaxies (Whitaker et al., 2011; Speagle et al., 2014).

6.4 MODELING THE ISM

As illustrated in Fig. 6.1, the first step in modeling the ISM is to split each SPH particle into an ionized and a neutral gas component. This is done using the electron fraction, x_e , associated with each SPH particle, i.e.,:

$$m_{\text{neutral}} = (1 - x_e)m_{\text{SPH}} \quad (6.1)$$

$$m_{\text{ionized}} = x_e m_{\text{SPH}}. \quad (6.2)$$

The electron fraction from GADGET-3 gives the density of electrons relative to that of hydrogen, n_e/n_{H} , and can therefore reach values of ~ 1.16 in the case where helium is also ionized. As a result we re-normalized the distribution of x_e values to a maximal x_e of 1 so as to not exceed the total gas mass in the simulation. Fig. 6.3 shows the distribution of SPH gas particles masses in G4 – chosen for its position near the center of the stellar and gas mass ranges of G1, ..., G7 – along with the mass distributions of the neutral and ionized gas components obtained

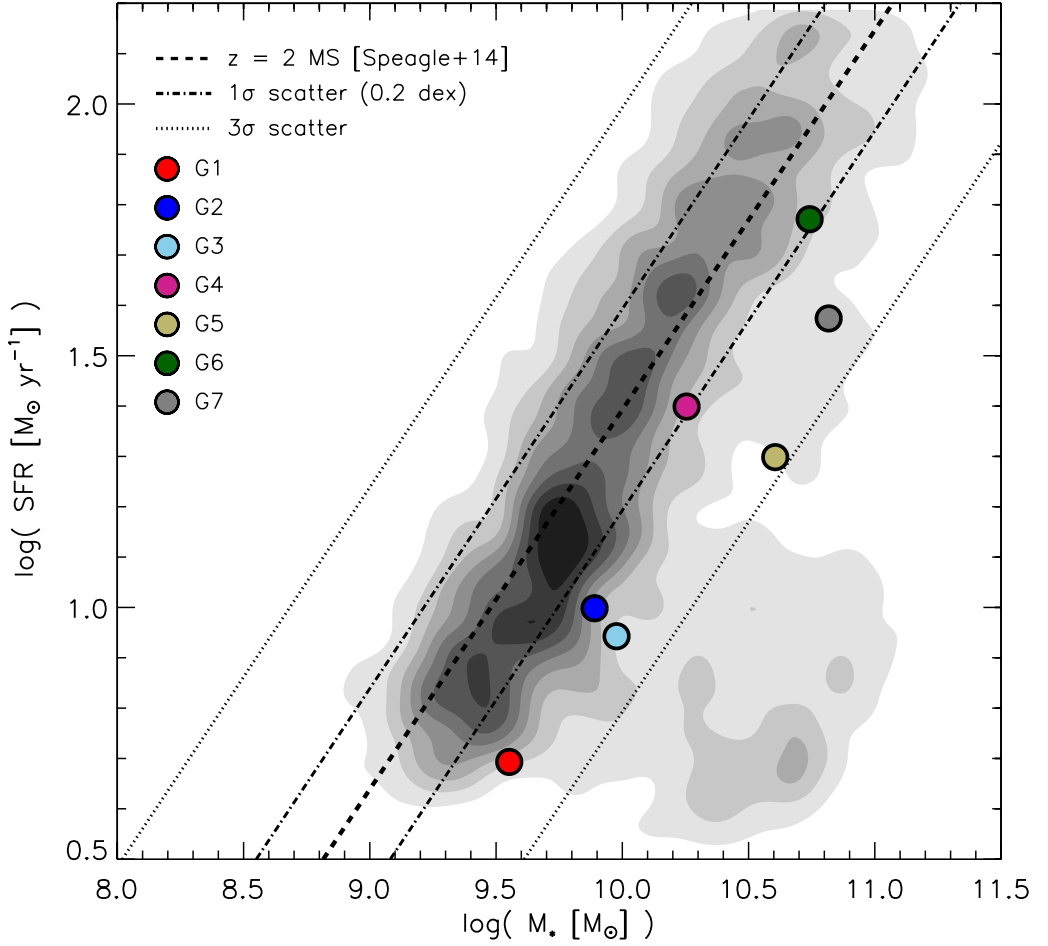


Figure 6.2 The SFR– M_* relation at $z \simeq 2$ as determined by Speagle et al. (2014) (dashed line) with the location of our seven simulated galaxies highlighted (filled circles). Dotted-dashed and dotted lines indicate the 1σ and 3σ scatter around the relation of Speagle et al. (2014). For comparison we also show the locus defined by 3754 $1.4 < z < 2.5$ galaxies from the NEWFIRM Medium-Band Survey (gray filled contours), with masses and SFRs calculated using a Kroupa IMF (Whitaker et al., 2011).

from eqs. 6.1 and 6.2. The ionized gas is seen to have a relatively flat distribution spanning the mass range $\sim 10^{4.3} - 10^{5.8} M_\odot$. The neutral gas, however, peaks at two characteristic masses ($\sim 10^{5.5} M_\odot$ and $\sim 10^{5.8} M_\odot$), where the lower mass peak represents gas particles left over from the first generation of stars in the simulation.

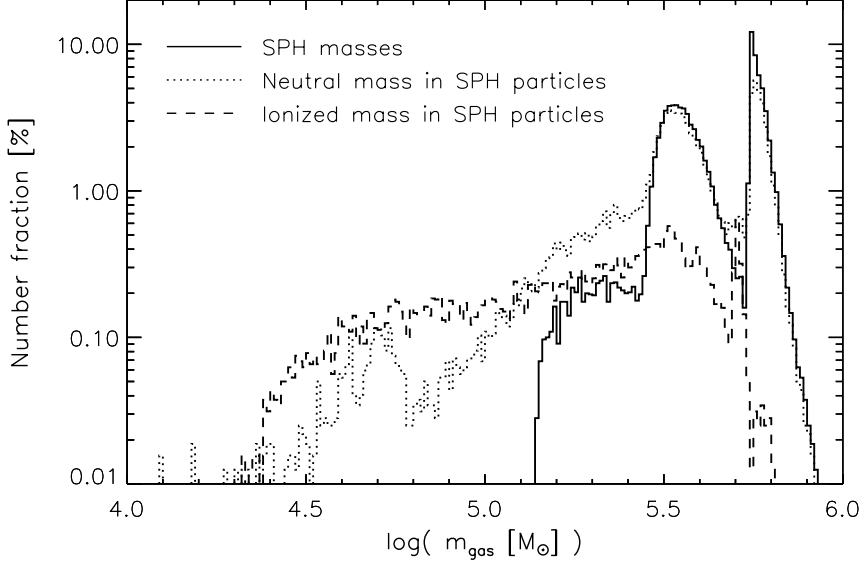


Figure 6.3 The distribution of SPH gas particle masses (solid histogram) in G4. The distribution peaks at two characteristic masses ($\sim 10^{5.5} M_{\odot}$ and $\sim 10^{5.8} M_{\odot}$), where the lower mass peak represents gas particles left over from the first generation of stars in the simulation. Splitting the gas into its neutral and ionized components according to eqs. 6.1 and 6.2 results in the mass distribution given by the dotted and dashed histograms, respectively.

6.4.1 GMCs

Masses, sizes and velocity dispersion

The neutral gas mass, m_{neutral} , associated with a given SPH particle is divided into GMCs by randomly sampling the GMC mass spectrum as observed in the Galactic disk and Local Group galaxies: $\frac{dN}{dm_{\text{GMC}}} \propto m_{\text{GMC}}^{-\beta}$ with $\beta = 1.8$ (Blitz et al., 2007). Similar to Narayanan et al. (2008b,a), a lower and upper cut in mass of $10^4 M_{\odot}$ and $10^6 M_{\odot}$, respectively, are enforced in order to ensure the GMC masses stay within the range observed by Blitz et al. (2007). Up to 40 GMCs are created per SPH particle but typically most ($> 90\%$) of the SPH particles are split into four GMCs or less. While m_{neutral} never exceeds the upper GMC mass limit ($10^6 M_{\odot}$), there are instances where m_{neutral} is below the lower GMC mass limit ($10^4 M_{\odot}$). In those cases we simply discard the gas, i.e., remove it from any further sub-grid processing. For the highest resolution simulations in our sample (G1 and G2), the discarded neutral gas amounts to $\sim 6\%$ of the total neutral gas mass, and $\lesssim 0.02\%$ in the remaining five galaxies. We shall therefore assume that it does not affect our results significantly.

The GMCs are randomly distributed within $0.2 \times$ the smoothing length of the original SPH particle, but with the radial displacement scaling inversely with GMC mass in order to retain the original gas mass distribution as closely as possible. To preserve the overall gas kinematics as best possible, all GMCs associated with a given SPH particle are given the same velocity as that of the SPH particle.

GMC sizes are obtained from the pressure-normalized scaling relations for virialized molec-

ular clouds which relate cloud radius (R_{cloud}) with mass (m_{GMC}) and external pressure (P_{ext}):

$$\frac{R_{\text{cloud}}}{\text{pc}} = \left(\frac{P_{\text{ext}}/k_{\text{B}}}{10^4 \text{ cm}^{-3} \text{ K}} \right)^{-1/4} \left(\frac{m_{\text{GMC}}}{290 M_{\odot}} \right)^{1/2}. \quad (6.3)$$

We assume $P_{\text{ext}} = P_{\text{tot}}/(1 + \alpha_0 + \beta_0)$ for relative cosmic and magnetic pressure contributions of $\alpha_0 = 0.4$ and $\beta_0 = 0.25$ (Elmegreen, 1989). For the total pressure (P_{tot}) we adopt the external hydrostatic pressure at mid-plane for a rotating disk of gas and stars, i.e.,:

$$P_{\text{tot}} \approx \frac{\pi}{2} G \Sigma_{\text{gas}} \left[\Sigma_{\text{gas}} + \left(\frac{\sigma_{\text{gas},\perp}}{\sigma_{*,\perp}} \right) \Sigma_{*} \right], \quad (6.4)$$

where Σ_{gas} and Σ_{*} are the local surface densities of gas and stars, respectively, and $\sigma_{\text{gas},\perp}$ and $\sigma_{*,\perp}$ their local velocity dispersions measured perpendicular to the mid-plane (see e.g., Elmegreen (1989); Swinbank et al. (2011)). For each SPH particle, all of these quantities are calculated directly from the simulation output (using a radius of $R = 1 \text{ kpc}$ from each SPH particle), and it is assumed that the resulting P_{ext} is the external pressure experienced by all of the GMCs generated by the SPH particle. We find that GMCs in our simulated galaxies are subjected to a wide range of external pressures ($P_{\text{ext}}/k_{\text{B}} \sim 10^2 - 10^7 \text{ cm}^{-3} \text{ K}$). For comparison, the range of pressures experienced by clouds in our Galaxy and in Local Group galaxies is $P_{\text{ext}}/k_{\text{B}} \sim 10^3 - 10^7 \text{ cm}^{-3} \text{ K}$ with an average of $P_{\text{ext}}/k_{\text{B}} \sim 10^4 \text{ cm}^{-3} \text{ K}$ in Galactic clouds (Elmegreen, 1989; Blitz et al., 2007). This results in GMC sizes in our simulations ranging from $R_{\text{cloud}} = 1 - 300 \text{ pc}$.

The internal velocity dispersion (σ_v) of the GMCs is inferred from the virial theorem, which provides us with a pressure-normalized $\sigma_v - R_{\text{GMC}}$ relation:

$$\sigma_v = 1.2 \text{ km s}^{-1} \left(\frac{P_{\text{ext}}/k_{\text{B}}}{10^4 \text{ cm}^{-3} \text{ K}} \right)^{1/4} \left(\frac{R_{\text{cloud}}}{\text{pc}} \right)^{1/2}, \quad (6.5)$$

where the normalization of 1.2 km s^{-1} comes from studies of Galactic GMCs (Larson, 1981; Elmegreen, 1989; Swinbank et al., 2011).

GMC density and temperature structure

We assume a truncated logotropic profile for the total hydrogen number density of the GMCs, i.e.,:

$$n_{\text{H}}(R) = n_{\text{H,ext}} \left(\frac{R_{\text{cloud}}}{R} \right), \quad (6.6)$$

where $n_{\text{H}}(R > R_{\text{cloud}}) = 0$. For such a density profile it can be shown that the external density, $n_{\text{H,ext}}$, is 2/3 of the average density:

$$n_{\text{H,ext}} = 2/3 \langle n \rangle = 2/3 \frac{m_{\text{GMC}}}{4/3 \pi m_{\text{H}} R_{\text{cloud}}^3}. \quad (6.7)$$

While the total hydrogen density follows a logotropic profile, the transition from $\text{H}_2 \rightarrow \text{HI}/\text{HII}$ is assumed to be sharp. Similarly for the transition from $\text{CI} \rightarrow \text{CII}$. This is illustrated in Fig. 6.4, which shows an example density profile of a GMC from our simulations. From the center of

the GMC and out to R_{H_2} , hydrogen is in molecular form. Beyond R_{H_2} , hydrogen is found as HI and HII out to R_{cloud} .

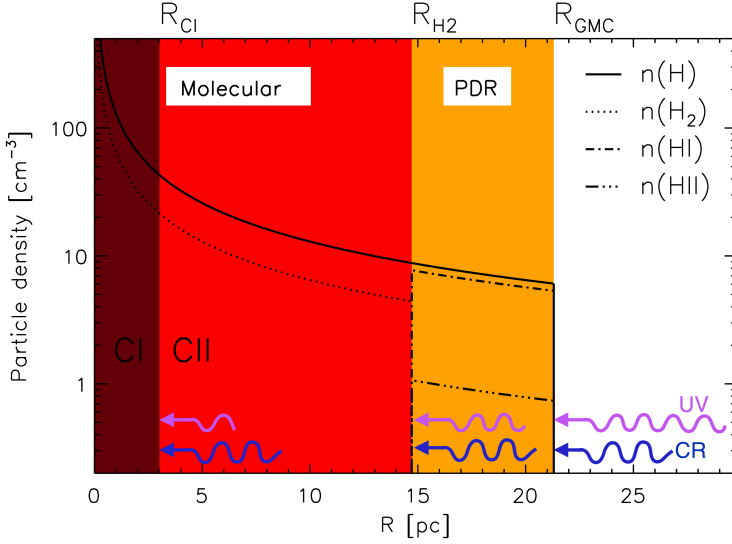


Figure 6.4 Example H number density profile (solid line) for a GMC of mass $m_{\text{GMC}} = 1.3 \times 10^4 M_{\odot}$ and radius $R_{\text{GMC}} = 21$ pc. Also shown are the density profiles of H_2 ($= 0.5n_H$), HI and HII. Note, the transition from molecular to atomic H is assumed to happen instantaneously at R_{H_2} . The total C abundance follows that of H but scaled with the [C/H] abundance (as provided by the ‘parent’ SPH particle, see Section 6.2). CII can exist throughout the cloud except for the very inner region ($R < R_{CI}$; indicated in brown), with the CI to CII transition happening instantaneously at R_{CI} . [CII] emission from the layer $R_{CI} \leq R \leq R_{H_2}$ (indicated in red) is referred to as ‘molecular’ emission, while [CII] emission from $R_{H_2} < R \leq R_{\text{GMC}}$ (indicated in orange) is referred to as ‘PDR’ emission. The relative thickness of these layers is set by the impinging FUV radiation field and cosmic rays (illustrated as purple and blue arrows, respectively), with the former undergoing attenuation further into the cloud.

The size of the molecular region, when adopting the logotropic density profile, is related to the total molecular gas mass fraction (f'_{mol}) of each GMC:

$$f'_{\text{mol}} = \frac{m_{\text{mol}}}{m_{\text{GMC}}} = \frac{\int_0^{R_{H_2}} \rho_{\text{ext}} \frac{R_{\text{GMC}}}{R} 4\pi R^2 dR}{\int_0^{R_{\text{GMC}}} \rho_{\text{ext}} \frac{R_{\text{GMC}}}{R} 4\pi R^2 dR} \quad (6.8)$$

$$= \frac{\int_0^{R_{H_2}} R dR}{\int_0^{R_{\text{GMC}}} R dR} = \left(\frac{R_{H_2}}{R_{\text{GMC}}} \right)^2 \quad (6.9)$$

$$\Rightarrow r_{H_2} = \sqrt{f'_{\text{mol}}}, \quad (6.10)$$

where r_{H_2} is the fractional radius, $r_{H_2} = R_{H_2}/R_{\text{cloud}}$. We find f'_{mol} by assuming $\text{HI} \leftrightarrow \text{H}_2$ equilibrium and using the analytical steady-state approach of Pelupessy et al. (2006) for inferring f'_{mol} for a logotropic cloud subjected to a radially incident FUV radiation field (see also Olsen et al., 2015). In this framework, the value of f'_{mol} (and thereby r_{H_2}) depends on:

1. The cloud boundary pressure (P_{ext}), which is calculated as explained in Section 6.4.1.

2. The metallicity (Z') of the GMC, which is inherited from its parent SPH particle and assumed constant throughout the cloud.
3. The kinetic temperature of the gas at the GMC surface ($T_k(R_{\text{GMC}})$). This quantity is calculated in an iterative process together with f'_{mol} by solving the following thermal balance equation:

$$\Gamma_{\text{PE}} + \Gamma_{\text{CR,HI}} = \Lambda_{\text{CII}} + \Lambda_{\text{OI}}, \quad (6.11)$$

where Γ_{PE} is the heating rate associated with the photoelectric ejection of electrons from dust grains by the FUV field and $\Gamma_{\text{CR,HI}}$ is the heating rate by cosmic rays in atomic gas. The main cooling agents are assumed to be due to [CII] and [OI] ($63 \mu\text{m}$ and $145 \mu\text{m}$) line emission (i.e., Λ_{CII} and Λ_{OI} , respectively). Γ_{PE} , $\Gamma_{\text{CR,HI}}$, and Λ_{CII} all depend on the electron fraction at R_{GMC} , which is determined by the degree of HI ionization by the local FUV radiation field and CR ionization rate (see below for how these quantities are derived). For analytical expressions for the heating rates, we refer to Olsen et al. (2015). For Λ_{OI} we use the expressions given in Röllig et al. (2006). The calculation of Λ_{CII} at the GMC surface is detailed in Section 6.5 and Appendix A.3.

4. The strength of the local FUV radiation field (G_0) and the CR ionization rate (ζ_{CR}) impinging on the GMCs. These quantities do not come out from the simulation directly, and instead they are calculated by scaling the Galactic FUV field ($G_{0,\text{MW}}$) and CR ionization rate ($\zeta_{\text{CR,MW}}$) with the local SFR volume density in the simulations, i.e., $G_0 \propto G_{0,\text{MW}} (\text{SFRD}_{\text{local}}/\text{SFRD}_{\text{MW}})$ and $\zeta_{\text{CR}} \propto \zeta_{\text{CR,MW}} (\text{SFRD}_{\text{local}}/\text{SFRD}_{\text{MW}})$, where $\text{SFRD}_{\text{local}}$ is estimated for each SPH particle as the volume averaged SFR within a 2 kpc radius. We have adopted Milky Way values of $G_{0,\text{MW}} = 0.6 \text{ Habing}$ (Seon et al., 2011) and $\zeta_{\text{CR,MW}} = 3 \times 10^{-17} \text{ s}^{-1}$ (Webber, 1998). For SFRD_{MW} we adopt $0.0024 \text{ M}_{\odot} \text{ yr}^{-1} \text{ kpc}^{-3}$, inferred from the average Galactic SFR ($0.3 \text{ M}_{\odot} \text{ yr}^{-1}$) within a disk 10 kpc in radius and 0.2 kpc in height (Heideman et al., 2010; Bovy et al., 2012).
5. The electron fraction at the cloud boundary. This fraction is not the previously introduced x_e , which was inherent to the SPH simulations and used to split the SPH gas into a neutral and ionized gas phase. Instead, it is the electron fraction given by the degree of ionization of HI caused by the G_0 and ζ_{CR} impinging on the cloud. This fraction (and thus the HI:HII ratio) is calculated with CLOUDY v13.03 (Ferland et al., 2013) given the hydrogen density and temperature at the cloud boundary and assuming an unattenuated G_0 and ζ_{CR} at R_{GMC} .

The [CII] emitting region in each of our GMCs is defined as the layer between the surface of the cloud and the depth at which the abundances of C and C^+ are equal. Hence, if the latter occurs at a radius R_{CI} from the cloud center, the thickness of the layer is $R_{\text{cloud}} - R_{\text{CI}}$ (Fig. 6.4). At radii $< R_{\text{CI}}$, all carbon atoms are for simplicity assumed to be in neutral form. In order to determine the fractional radius $r_{\text{CI}} (= R_{\text{CI}}/R_{\text{GMC}})$ we follow the work of Röllig et al. (2006) (but see also Pelupessy & Papadopoulos, 2009), who considers the following dominant reaction channels for the formation and destruction of C^+ :



In this case, r_{Cl} can be found by solving the following equation:

$$5.13 \times 10^{-10} \text{s}^{-1} G_0 \int_1^\infty \frac{e^{-\mu \xi_{\text{FUV}} A_V(r_{\text{Cl}})}}{\mu^2} d\mu = n_{\text{H}}(r_{\text{Cl}})[a_{\text{C}} X_{\text{C}} + 0.5 k_{\text{C}}], \quad (6.15)$$

where the left-hand side is the C^+ formation rate due to photo-ionization by the attenuated FUV field at r_{Cl} (eq. 6.12), and the right-hand side is the destruction rate of C^+ due to recombination and radiative association (eqs. 6.13 and 6.14). The constants $a_{\text{C}} = 3 \times 10^{-11} \text{cm}^{-3} \text{s}^{-1}$ and $k_{\text{C}} = 8 \times 10^{-16} \text{cm}^{-3} \text{s}^{-1}$ are the recombination and radiative association rate coefficients. Note, we have accounted for an isotropic FUV field since $\mu = \cos \theta$, where θ is the angle between the Poynting vector and the normal direction. $A_V(r_{\text{Cl}})$ is the visual extinction corresponding to the $R_{\text{cloud}} - R_{\text{Cl}}$ layer, and is given by $A_V(r_{\text{Cl}}) = 0.724 \sigma_{\text{dust}} Z' \langle n_{\text{H}} \rangle R_{\text{cloud}} \ln(r_{\text{Cl}}^{-1})$, where $\sigma_{\text{dust}} = 4.9 \times 10^{-22} \text{cm}^2$ is the FUV dust absorption cross section (Pelupessy & Papadopoulos, 2009; Mezger et al., 1982). ξ_{FUV} accounts for the difference in opacity between visual and FUV light and is set to 3.02. X_{C} is the carbon abundance relative to H and is calculated by adopting the carbon mass fractions of the parent SPH particle (self-consistently calculated as part of the overall SPH simulation) and assuming it to be constant throughout the GMC.

The temperature of the [CII]-emitting molecular gas (i.e., from the gas layer between R_{Cl} and R_{H_2}) is assumed to be constant and equal to the temperature at R_{H_2} . The latter is given by the thermal balance:

$$\Gamma_{\text{PE}} + \Gamma_{\text{CR}, \text{H}_2} = \Lambda_{\text{H}_2} + \Lambda_{\text{CII}} + \Lambda_{\text{OI}}, \quad (6.16)$$

where $\Gamma_{\text{CR}, \text{H}_2}$ is the CR heating in molecular gas, and Λ_{H_2} is the cooling due to the S(0) and S(1) rotational lines of H_2 (Papadopoulos et al. (2014); see also Olsen et al. 2015). $\Gamma_{\text{CR}, \text{H}_2}$ depends on x_{e} , which is calculated with CLOUDY for the local CR ionization rate and the attenuated FUV field at r_{H_2} , i.e. $G_0 e^{-\xi_{\text{FUV}} A_V(r_{\text{H}_2})}$. $A_V(r_{\text{H}_2})$ corresponds the extinction through the outer atomic transition layer of each GMC.

The temperature of the PDR gas (i.e., from the gas between R_{H_2} and R_{cloud}) is assumed to be constant and equal to the temperature at R_{cloud} .

For each GMC we solve in an iterative manner simultaneously for R_{H_2} (eq. 6.10) and R_{Cl} (eq. 6.15), as well as for the gas temperature at R_{cloud} and at R_{H_2} (eqs. 6.11 and 6.16, respectively)

The resulting distributions of R_{H_2} and R_{Cl} for the GMC population in G4 are shown in Fig. 6.5 (bottom panel), along with the distribution of R_{GMC} (obtained from eq. 6.3). In GMCs in general, we expect $R_{\text{Cl}} < R_{\text{H}_2}$, due to efficient H_2 selfshielding. However, as Fig. 6.5 shows some of the GMCs in our simulations have very small R_{H_2} (due to them having virtually zero molecular gas fractions), and in those cases R_{Cl} can be equal to or even exceed R_{H_2} . The latter implies that the [CII] emission is only coming from the PDR phase, with no contribution from the molecular gas.

The distributions of the kinetic temperature of the gas at R_{H_2} and R_{cloud} for the GMC population in G4 are shown in Fig. 6.6. The temperatures at the cloud surfaces range from $\sim 8 \text{K}$ to $\sim 10^{5.5} \text{K}$, and the temperatures at R_{H_2} lies between ~ 8 and 1800K .

With R_{H_2} and R_{Cl} determined for each GMC we can calculate the gas masses associated with the molecular and PDR gas phase, respectively. The resulting mass distributions are

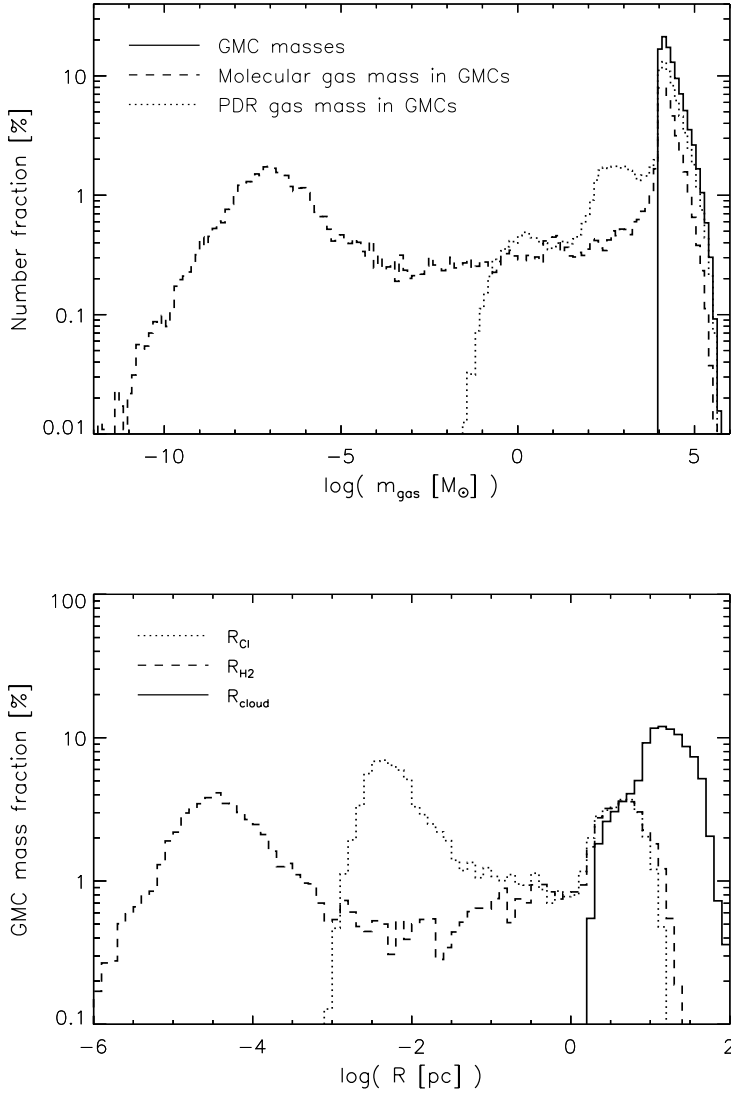


Figure 6.5 Top: the number distribution of GMC masses (solid histogram) together with the number distributions of the molecular (dashed histogram) and PDR (dotted histogram) gas component. **Bottom:** GMC-mass-weighted distributions of R_{Cl} (dotted), R_{H_2} (dashed) and R_{cloud} for GMCs in G4.

shown in the top panel of Fig. 6.5, along with the distribution of total GMC masses (m_{GMC}) as determined by the adopted GMC mass spectrum (Section 6.4.1). We see that most of the molecular and PDR gas masses follow the total GMC mass spectrum. There is, however, a fraction of GMCs with extremely small molecular gas masses (corresponding to $f'_{\text{mol}} \sim 0$). On the other hand, there are some GMCs with small PDR gas masses, i.e., clouds that are so shielded from FUV radiation that they are almost entirely molecular.

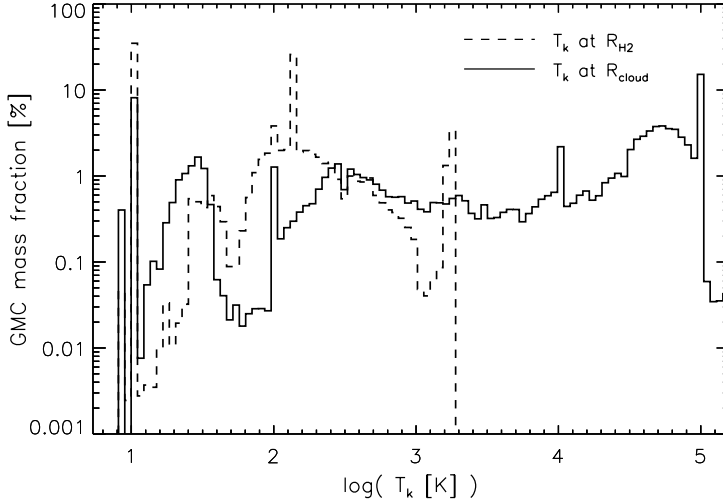


Figure 6.6 GMC-mass-weighted distributions of the temperature at R_{H_2} (dashed) and at the cloud surfaces (solid) for GMCs in G4.

6.4.2 THE IONIZED GAS

The ionized gas in our simulations (see eq. 6.2), is assumed to be distributed in spherical clouds of uniform densities and with radii (R_{HII}) equal to the smoothing lengths of the original SPH particles. These ionized regions in our simulations are furthermore assumed to be isothermal with the temperatures equal to that of the SPH gas. Fig. 6.7 shows the size (top) and temperature (bottom) distribution for the ionized clouds in G4. Cloud sizes range from ~ 0.1 to ~ 10 kpc, with more than 60 % of the ionized gas mass residing in clouds of size $\lesssim 1000$ pc. For comparison, the range of observed sizes of HII clouds in nearby galaxies is $10 - 1000$ pc (Oey & Clarke, 1997; Hodge et al., 1999). The temperatures range from $\sim 10^2$ K to $\sim 10^6$ K with the bulk of the ionized gas having temperatures $\sim 10^{4-5}$ K.

6.5 THE [CII] LINE EMISSION

The [CII] luminosity of a region of gas is the volume-integral of the effective [CII] cooling rate per volume, i.e.:

$$L_{[\text{CII}]} = \int_{\Delta V} \Lambda_{\text{CII}} dV. \quad (6.17)$$

Since we have adopted spherical symmetry in our sub-grid treatment of the clouds (both neutral and ionized), we have:

$$L_{[\text{CII}]} = 4\pi \int_{R_1}^{R_2} \Lambda_{\text{CII}} R^2 dR, \quad (6.18)$$

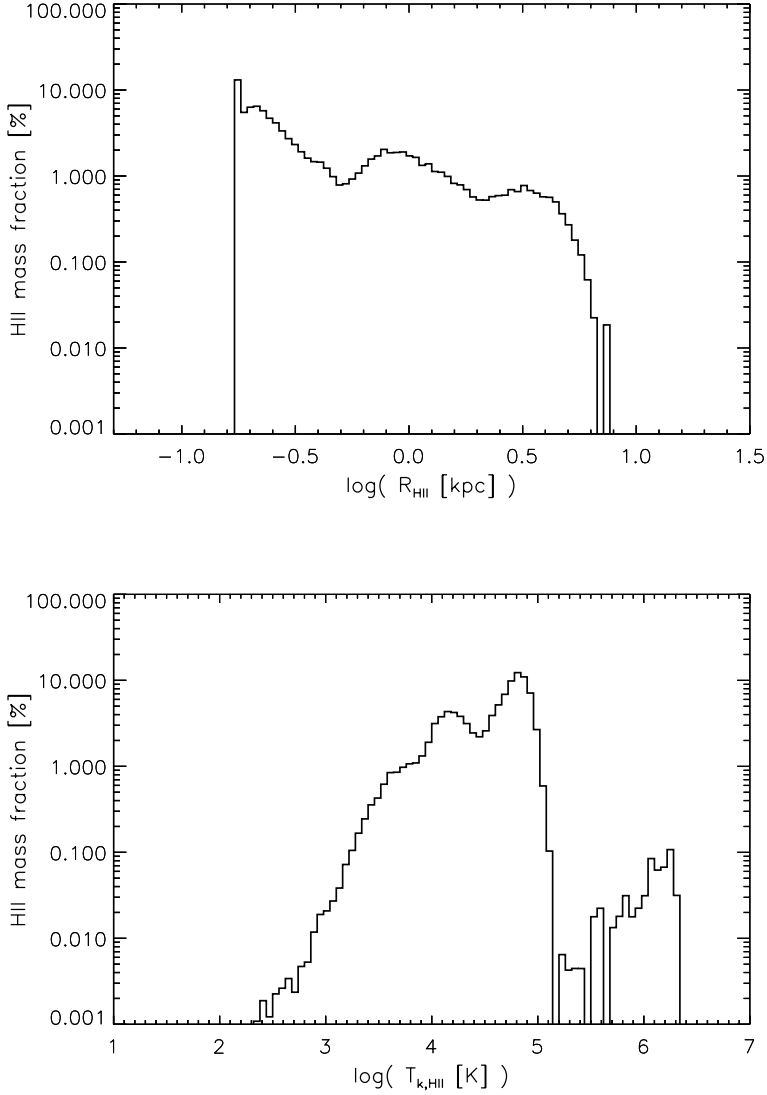


Figure 6.7 Mass-weighted histograms of the size (top) and temperature (bottom) distributions of the ionized clouds in G4.

where $R_1 = R_{C\text{I}}$ and $R_2 = R_{\text{H}_2}$ for the molecular phase; $R_1 = R_{\text{H}_2}$ and $R_2 = R_{\text{GMC}}$ for the PDR region, and $R_1 = 0$ and $R_2 = R_{\text{HII}}$ for the ionized gas.

The effective $[\text{CII}]$ cooling rate is:

$$\Lambda_{\text{CII}} = A_{\text{ul}} \beta f_{\text{u}} n_{\text{CII}} h\nu, \quad (6.19)$$

where $A_{\text{ul}} (= 2.3 \times 10^{-6} \text{ s}^{-1})^1$ is the Einstein coefficient for spontaneous decay. We ignore the

¹Einstein coefficient for spontaneous emission taken from the LAMDA database: <http://www.strw.leidenuniv.nl/~moldata/>, Schöier et al. (2005)

effects of any background radiation field from dust and the cosmic microwave background (CMB). β is the [CII] photon escape probability for a spherical geometry (i.e., $\beta = (1 - \exp(-\tau))/\tau$, where τ is the [CII] optical depth). f_u is the fraction of singly ionized carbon in the upper $^2P_{3/2}$ level and is determined by radiative processes and collisional (de)excitation (see Appendix A.3). The latter can occur via collisions with e^- , H I, or H_2 , depending on the state of the gas. In our simulations the collisional partner is H_2 in the molecular phase, H I and e^- in the PDR regions, and e^- in the ionized gas. Analytical expressions for the corresponding collision rate coefficients as a function of temperature are given in Appendix A.3. n_{CII} is the number density of singly ionized carbon and is given by $n_{\text{CII}} = X_{\text{C}} f_{\text{CII}} n_{\text{H}}$, where f_{CII} is the fraction of carbon atoms in the singly ionized state. For the latter we used tabulated fractions from CLOUDY v13.03 over a wide range in temperature, hydrogen density, FUV field strength, and CR ionization rate.

We calculate the integral in eq. 6.18 numerically by splitting the $R_2 - R_1$ region up into 100 radial bins. In each bin, n_{H} is set to be constant and – in the case of the molecular and PDR regions – given by the logotropic density profile at the radius of the given bin (Fig. 6.4). For the ionized clouds, n_{H} is constant throughout (Section 6.4.2). For the PDR regions (i.e., from R_{H_2} to R_{GMC}) we assume that the temperature, electron fraction and G_0 are kept fixed to the outer boundary value at R_{GMC} (i.e., no attenuation of the FUV field). This implies that the [CII] luminosity from the PDR gas is an upper limit. Similar for the [CII] emission from the molecular region (i.e., from R_{CI} to R_{H_2}), where we assume that the temperature throughout this region is fixed to its values at R_{H_2} . Also, throughout this region we adopt the attenuated FUV field at R_{H_2} .

6.6 RESULTS AND DISCUSSION

Having divided the ISM in our galaxies into molecular, atomic and ionized gas phases, and having devised a methodology for calculating their [CII] emission, we are now in a position to quantify the relative contributions from the aforementioned gas phases to the total [CII] emission, and examine their relationship to the on-going star formation.

6.6.1 RADIAL [CII] LUMINOSITY PROFILES

First, however, to get a sense of the distribution of gas and star formation in our simulated galaxies, we show in Fig. 6.8 surface density maps of the total SPH gas (left column) and star formation rate (middle column) when viewed face-on. The maps reveal spiral galaxy morphologies, albeit with some variety: some (G1, G2 and G3) show perturbed spiral arms due to on-going mergers with satellite galaxies; others (G4, G5, G6 and G7) have seemingly undisturbed, grand-design spiral arms; a central bar-like structure is also seen in some (G2, G4, G5 and G7). Overall, the star formation is seen to be much more centrally concentrated than the SPH gas. This is especially true for G1 and G2, which have very centrally peaked star formation. The radial SFR and [CII] luminosity profiles of G1, ..., G7 – derived by summing up the SFR and the [CII] luminosity within concentric rings (of fixed width: 0.2 kpc) – are also shown in Fig. 6.8. We have inferred the radial [CII] luminosity distribution for the full ISM as well as for the individual gas phases.

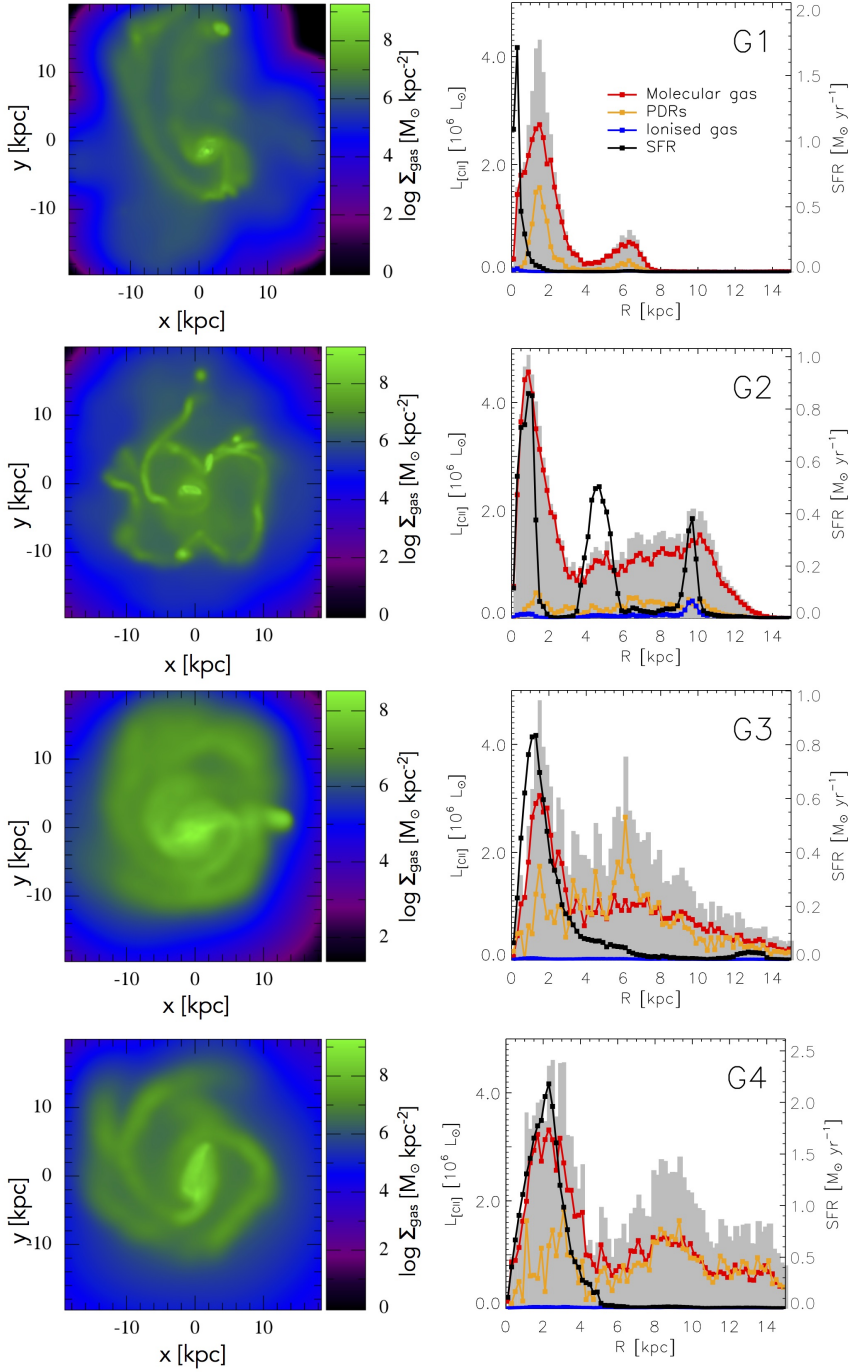


Figure 6.8 Gas and SFR surface density maps (left and middle columns, respectively) of our SPH simulated galaxies viewed face-on (G1, ..., G7 from top to bottom; see also Thompson et al. (2015)). The horizontal white bars correspond to a physical scale of 5 kpc. The right-hand column shows the radial profiles of the total [CII] luminosity (gray histogram) and the contributions from molecular gas (red curve), PDR (orange curve) and ionized gas (blue curve). The SFR radial profiles are also shown (black curve). The radial profiles were determined by summing up the [CII] luminosity and SFR within concentric rings with fixed width of 0.2 kpc.

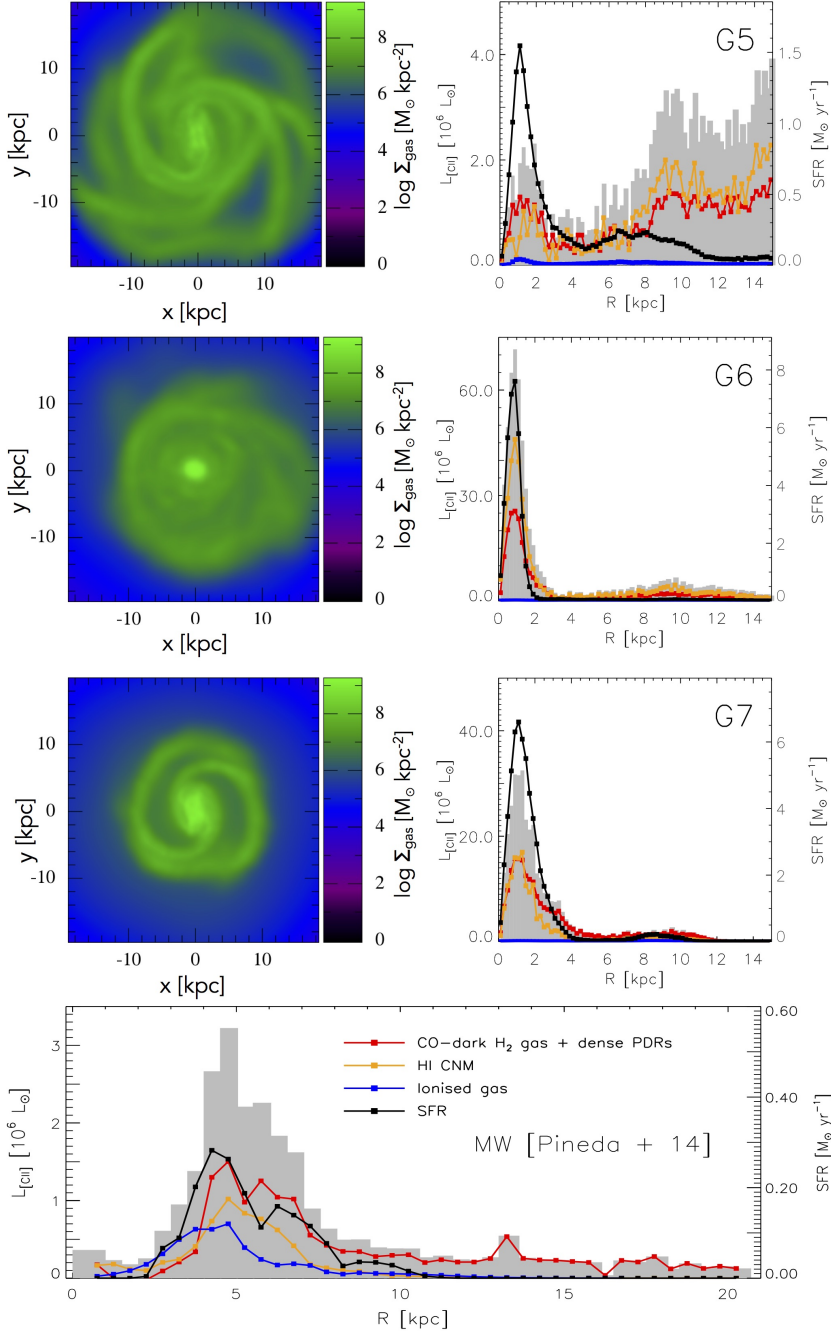


Figure 6.7 Continued. In the bottom panel we show for reference the radial L_{CII} profile of the Galaxy (gray histogram) along with the contributions from CO-dark H_2 gas and dense PDRs (red curve), cold HI (orange curve), and ionized gas (blue curve) (Pineda et al., 2014). Also shown is the radial SFR profile (black curve) inferred from the 1.4 GHz intensity distribution. Fixed radial bin widths of 0.5 kpc have been adopted (see Pineda et al. (2014) for details).

The radial SFR profiles of our model galaxies typically peak at $R \sim 0.5 \text{ kpc}$ (in G1 at $R \lesssim 0.5 \text{ kpc}$) and then tail off with radius. In some cases, local peaks in the star formation activity occur at galactocentric distances $\gtrsim 2 \text{ kpc}$, corresponding to the locations of either satellite galaxies (G2 and G3) or spiral arms (G5 and G7).

The total [CII] luminosity profiles (gray histograms) also peak at $R \sim 0.5 \text{ kpc}$, and within the central $R \lesssim 1.5 \text{ kpc}$ there is in general a good correspondence between the total [CII] emission and the star formation activity. This correspondence is driven by the molecular gas phase which dominates the [CII] emission in the central regions. The molecular [CII] emission is seen to correlate strongly with the star formation out to radii $\sim 5 \text{ kpc}$ and beyond (e.g., G3 and G4). There are cases, however, where localized enhancements in the SFR are not matched by increased [CII] emission from the molecular gas (e.g. G2, and G3). These SFR enhancements are reflected in the [CII] emission profile of the ionized gas, which at galactocentric distances $\gtrsim 2 \text{ kpc}$ follow the SFR closely (despite contributing only a small fraction to the total [CII] emission budget, see below). In contrast, the [CII] emission from the PDR gas, which dominates the total [CII] luminosity at $2.0 \text{ kpc} \lesssim R \lesssim 10 \text{ kpc}$, does not appear to be a sensitive tracer of the SFR. At $R \lesssim 1.5 \text{ kpc}$ where the SFR peaks, the [CII] emission from this phase is seen to drop. At larger radii, the PDR [CII] emission declines but at a more gradual rate than the star formation.

In the bottom right panel of Fig. 6.8 we show the Galactic SFR and [CII] luminosity radial profiles from Pineda et al. (2014), who observed the [CII] emission from (1) CO-dark H_2 gas and dense PDRs, (2) cold neutral HI gas, and (3) hot ionized gas in our own Galaxy. In order to facilitate an approximate comparison with our simulations we identify these three Galactic ISM phases with the molecular, atomic, and ionized gas in our simulations. It is important to keep in mind, however, that the ISM in our simulations has a higher pressure, is kinematically more violent, and is more actively forming stars than is the case in our Galaxy.

The SFR and [CII] profiles in our Galaxy peak at larger radii ($R \sim 4 - 5 \text{ kpc}$) than in our simulated galaxies. This is not surprising given the low content of star formation and gas in the Galactic bulge, and the fact that the bulk of star formation in our Galaxy takes place in the disk. In contrast, gas is still being funneled toward the central regions of our simulated galaxies where it is converted into stars. Thus the SFR level in our simulated galaxies is much higher (by $\gtrsim 10\times$) and more centrally concentrated than in our Galaxy, where stars form at a rate of $\lesssim 0.1 - 1 \text{ M}_\odot \text{ yr}^{-1}$ across the disk. Remarkably, significant levels of [CII] emission extend out to $R \sim 20 \text{ kpc}$ in our Galaxy, well beyond the point where star formation has ceased. Here, the emission is completely dominated by CO-dark H_2 gas and dense PDR regions. This is similar to the picture seen in our simulated galaxies where the [CII] emission at large radii is dominated by a neutral gas phase – designated PDR gas in our simulations, dubbed CO-dark $\text{H}_2 +$ dense PDR gas in Pineda et al. (2014) – that is largely uncoupled from star formation. The radial [CII] profile of the ionized gas in the Galaxy roughly follows the SFR profile, as is the case in our simulations.

Fig. 6.8 displays the fractional [CII] luminosity from the different ISM phases: top panel for the entire disk ($R < 10 \text{ kpc}$), middle panel for the central region ($R \leq 1 \text{ kpc}$), and bottom panel for the outer disk ($R > 2 \text{ kpc}$). Within $R \leq 10 \text{ kpc}$, the molecular gas can constitute from $\sim 31\%$ (G2) to $\sim 91\%$ (G7) of the total [CII] luminosity; for the PDR gas the range is $\sim 9\%$ (G7) to $\sim 67\%$ (G2). Fig. 6.8 shows that the contribution from the molecular gas to the total [CII] emission increases with the overall SFR of the galaxy. A reverse trend is seen for the PDR gas. As expected, the total [CII] emission from the central regions ($R \leq 1 \text{ kpc}$) is dominated by the

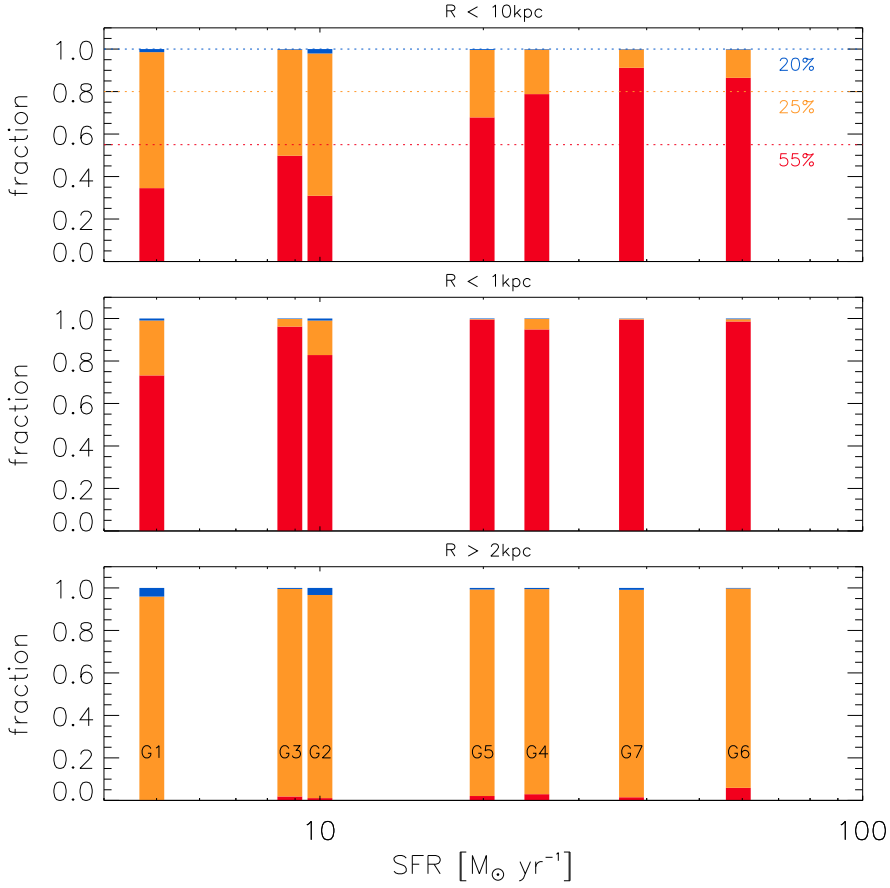


Figure 6.8 Contributions to the total [CII] luminosity from the molecular (red), PDR (yellow), and ionized (blue) gas phases for each of our simulated galaxies, ranked according to their total SFRs. The three panels show the relative contributions within $R < 10 \text{ kpc}$ (top), for $R < 1 \text{ kpc}$ (middle), and for $R > 2 \text{ kpc}$ (bottom). The horizontal dashed lines and the percentages given indicate the relative contributions to the total [CII] luminosity of our own Galaxy from CO-dark H_2 + dense PDR gas (red; 55%), cold atomic gas (yellow; 25%), and ionized gas (blue; 20%) (Pineda et al., 2014). The total SFR of the Galaxy is $1.9 M_{\odot} \text{ yr}^{-1}$ (Chomiuk & Povich, 2011).

molecular gas ($\gtrsim 70\%$) while further out ($R > 2 \text{ kpc}$) the PDR gas phase dominates ($\gtrsim 90\%$) (see Fig. 6.8, bottom two panels). For reference, we note that in our own Galaxy about 55 % of the total Galactic [CII] luminosity (within $R \lesssim 20 \text{ kpc}$) is from molecular gas and dense PDRs, 25 % from cold HI, and 20 % from the ionized gas (Pineda et al., 2014). Thus, the ionized phase is a more important contributor to the overall [CII] budget in our Galaxy than in the simulated galaxies presented here where the contribution from the ionized gas is $\lesssim 3\%$ in all cases.

6.6.2 THE INTEGRATED $L_{[\text{CII}]} - \text{SFR}$ RELATION

Fig. 6.9 shows the integrated $L_{[\text{CII}]} - \text{SFR}$ relations for our simulated galaxies: top panel for the full ISM and, in separate panels below, for each of the three ISM phases considered in our simulations.

When considering the entire ISM a tight correlation between $L_{[\text{CII}]}$ and SFR emerges, which is well fit in log-log space by a straight line with slope 1.27 ± 0.17 (solid line in the top panel). This relation is largely set by the molecular and PDR gas phases. The molecular gas phase, itself exhibiting a strong correlation between $[\text{CII}]$ and SFR with slope 1.72 ± 0.22 , drives the slope of the total correlation. The PDR gas on the other hand, shows a weaker $[\text{CII}] - \text{SFR}$ correlation with a slope of 0.43 ± 0.20 but contributes significantly to the normalization of the total $[\text{CII}] - \text{SFR}$ relation, especially at the low SFR end (see Fig. 6.9). The $[\text{CII}]$ emission from the ionized gas also shows a weak dependency on SFR (slope 0.44 ± 0.30) but does not contribute significantly to the total $[\text{CII}]$ emission, its normalization factor being $\gtrsim 10\times$ below that of the molecular and PDR gas (Fig. 6.9, bottom panel).

In the top panel of Fig. 6.9 we compare the $L_{[\text{CII}]} - \text{SFR}$ relation obtained from our simulated galaxies with samples of $[\text{CII}]$ detected galaxies in the redshift range $z \sim 0 - 6.5$ compiled from the literature. Our simulated galaxies are seen to match the observed $L_{[\text{CII}]} - \text{SFR}$ relation both in terms of the slope of the relation and its overall normalization. A power-law fit to the simulated galaxies (shown as solid line in Fig. 6.9) yields a near-linear slope (1.27 ± 0.17). Normal star-forming galaxies at $z \sim 0$, with similar levels of SFR ($\sim 0.2 - 100 \text{ M}_{\odot} \text{ yr}^{-1}$; Malhotra et al. 2001) as our simulated galaxies, are consistent with a linear correlation given by $L_{[\text{CII}]} = 1.05 \times 10^7 \text{SFR}$ (dotted line in Fig. 6.9) with a scatter of 0.3 dex (Magdis et al., 2014)². The scatter of our simulated galaxies around their best-fit relation is 0.14 dex, i.e., significantly lower. We attribute this to the fact that our simulated galaxies constitute a fairly homogeneous (and small) sample spanning a rather small range in SFR, $L_{[\text{CII}]}$, and Z' , unlike the observed samples with which we are comparing.

A direct comparison with $[\text{CII}]$ -detected galaxies at high redshifts is complicated by the fact that the latter typically have significantly larger SFRs than our model galaxies. Furthermore, high- z samples are often heterogeneous (e.g., significant AGN contribution, cf. Gullberg et al., 2015). One exception, however, is the recent $[\text{CII}]$ -detected sample of star-forming galaxies at $z \simeq 5 - 6$ presented by Capak et al. (2015) (shown as magenta stars in Fig. 6.9), which span the same range in SFR as our simulations. These galaxies are seen to be in excellent agreement with the $L_{[\text{CII}]} - \text{SFR}$ relation defined by our simulations, both in terms of slope and normalization.

Extrapolating our best-fit relation to SFRs $\gtrsim 300 \text{ M}_{\odot} \text{ yr}^{-1}$ in order to compare with other high- z samples, the relation is seen to overshoot the data. A power-law fit to the $z > 1$ star-forming galaxies with $\text{SFR} \gtrsim 300 \text{ M}_{\odot} \text{ yr}^{-1}$ compiled by D14 yields: $L_{[\text{CII}]} = 1.7 \times 10^7 \text{SFR}^{0.85}$ (D14; shown as the dashed line in Fig. 6.9), i.e., formally, a shallower relation than that of our simulated galaxies and that of the $z \sim 0$ sample (albeit less so). Finally, we stress that the $[\text{CII}]$ -detected galaxies at $z > 1$ with SFRs $\gtrsim 300 \text{ M}_{\odot} \text{ yr}^{-1}$ likely derive from rather complex environments (e.g. Narayanan et al., 2015), which may not correspond to the relatively quiescent MS star-forming galaxies modeled here.

²This expression is inferred from a power-law fit by Magdis et al. (2014) to the $[\text{CII}]$ and FIR ($42.5 - 122.5 \mu\text{m}$) luminosities (in units of L_{\odot}) of the Malhotra et al. (2001) sample: $L_{[\text{CII}]} = 10^{-2.51 \pm 0.39} L_{\text{FIR}}$, where we have made use of the conversion $\text{SFR} = L_{\text{FIR}}/3.4 \times 10^9$.

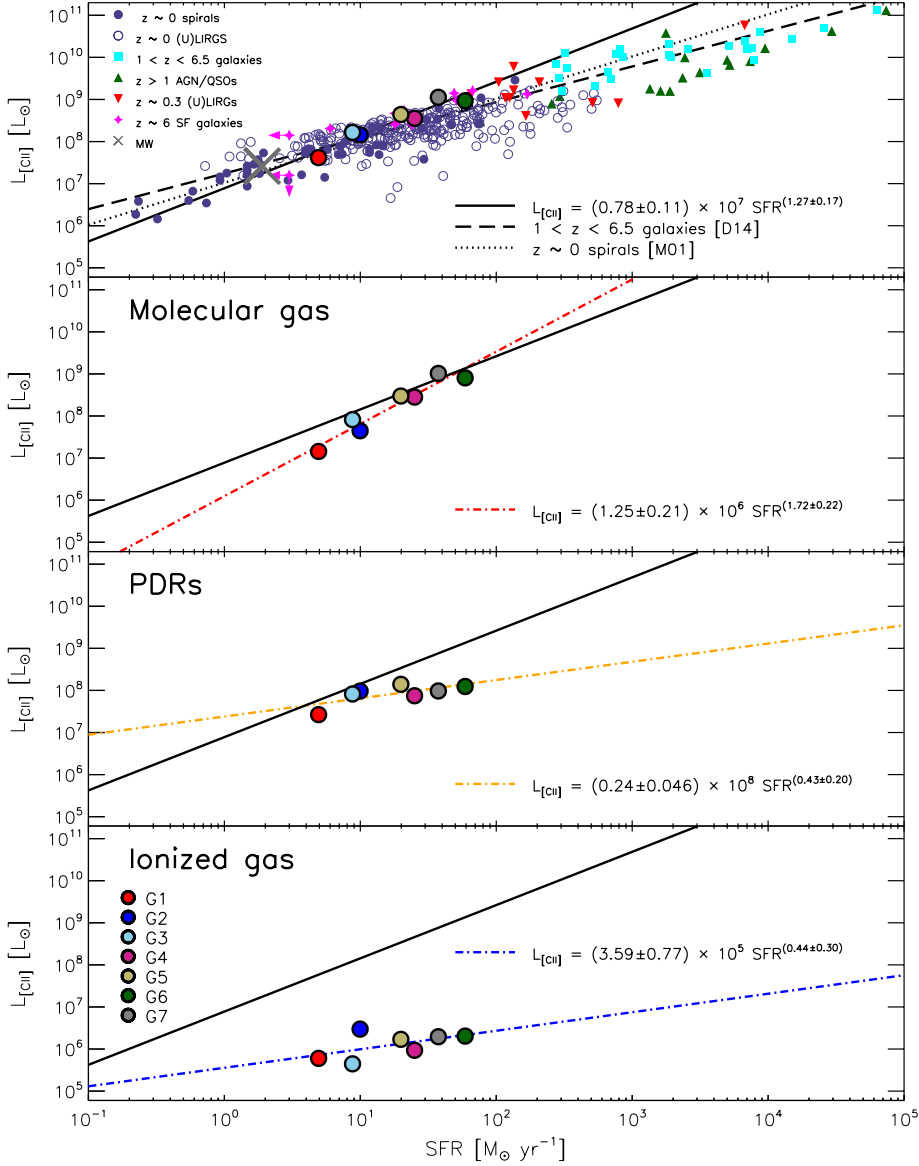


Figure 6.9 $L_{\text{[CII]}}$ vs. SFR for our simulated galaxies (big filled circles). The same color-coding as in Fig. 6.2 is used and listed again for convenience in the bottom panel. From top to bottom panel we show the [CII] luminosity from the full ISM (gray), the molecular gas (red), PDRs (orange), and ionized gas (blue). For comparison, we show individual [CII] observations of 54 $z \sim 0$ spirals (purple filled circles; Malhotra et al., 2001), with the best fit to this sample given by the dotted line (see main text for details). Also shown are 240 $z \sim 0$ (U)LIRGs (purple open circles; Díaz-Santos et al., 2013; Farrah et al., 2013), and 12 $z \sim 0.3$ (U)LIRGs (red triangles; Magdis et al., 2014). The high- z comparison samples include 25 $1 < z < 6$ star-forming galaxies (cyan squares; D14) and the dashed line indicate the best fit to this sample. Also shown are 16 $z \sim 4 - 7$ quasars (green triangles; Iono et al., 2006; Walter et al., 2009; Wagg et al., 2010; Gallerani et al., 2012; Wang et al., 2013; Venemans et al., 2012; Carilli et al., 2013; Willott et al., 2013), and 10 normal star-forming $z \sim 5 - 6$ galaxies (magenta stars) observed by Capak et al. (2015). The Galaxy is shown for reference with a gray cross (Pineda et al., 2014).

6.6.3 THE RESOLVED $\Sigma_{\text{[CII]}} - \Sigma_{\text{SFR}}$ RELATION

In Fig. 6.10 we show the combined $\Sigma_{\text{[CII]}} - \Sigma_{\text{SFR}}$ relation of all seven simulated galaxies in their face-on configuration. The relation is shown for the entire ISM (top panel) and for each of the separate gas phases (bottom three panels). Surface densities were determined within $1 \text{ kpc} \times 1 \text{ kpc}$ regions. Contours reflect the number of regions at a given $(\Sigma_{\text{SFR}}, \Sigma_{\text{[CII]}})$ -combination and are given as percentages of the peak number of regions.

Given the variations in the local star formation conditions within our model galaxies, we can explore the relationship between [CII] and star formation over a much wider range of star formation intensities than is possible with the integrated quantities. A $\Sigma_{\text{[CII]}} - \Sigma_{\text{SFR}}$ correlation spanning more than five decades in Σ_{SFR} is seen for the entire ISM as well as for the individual ISM phases. Similar to the integrated [CII] vs. SFR relations in the previous section, the molecular and PDR phases dominate the resolved [CII] emission budget at all SFR surface densities, and with the molecular relation being steepest and exhibiting the largest degree of scatter. The resolved [CII] emission from the ionized phase, while clearly correlated with Σ_{SFR} , is largely negligible at all star formation densities.

We compare the $\Sigma_{\text{[CII]}} - \Sigma_{\text{SFR}}$ relation for our simulated galaxies to that of three resolved surveys of nearby galaxies: (1) the $\sim 50 \text{ pc}$ -scale relation derived from five $3' \times 3'$ fields toward M31 (K15; shown as green points in Fig. 6.10), (2) the kpc-scale relation obtained for 48 local dwarf galaxies covering a wide range in metallicities ($Z/Z_{\odot} = 0.02 - 1$, D14; cyan crosses), and (3) the kpc-scale relations for local, mostly spiral, galaxies (H15; magenta contours). The data from these surveys have been converted to the Chabrier IMF assumed by our simulations by multiplying Σ_{SFR} with a factor 0.94 when a Kroupa IMF was adopted (D14; K15) or 0.92 when a truncated Salpeter IMF was used (H15), following Calzetti et al. (2007) and Speagle et al. (2014). Regarding the observations by H15, we adopt the raw $\Sigma_{\text{[CII]}}$ measurements rather than the IR-color-corrected ones. From Fig. 6.10 we see that over the range in Σ_{SFR} ($\sim 0.001 - 1 \text{ M}_{\odot} \text{ yr}^{-1} \text{ kpc}^{-2}$) spanned by these three surveys, the $\Sigma_{\text{[CII]}} - \Sigma_{\text{SFR}}$ relation defined by our simulations is in excellent agreement with the observations. Also, the majority of our simulated $1 \text{ kpc} \times 1 \text{ kpc}$ regions fall within the observed Σ_{SFR} and $\Sigma_{\text{[CII]}}$ ranges. A small fraction (a few percent) of regions in our simulations exhibit an excess in $\Sigma_{\text{[CII]}}$ for a given Σ_{SFR} relative to the observed relations, but the majority coincide with the observations. We note that the observed relations exhibit significant scatter ($\sim 0.2 - 0.3 \text{ dex}$; D14, H15, K15) as well as small systematic offsets relative to each other (in particular in the case of D14). The $\Sigma_{\text{[CII]}} - \Sigma_{\text{SFR}}$ relations observed in the five fields in M31 by K15 yield best-fit power-law slopes in the range $\sim 0.67 - 1.03$, with an average of 0.77 (shown as dashed-dotted line in Fig. 6.10). Similar power-law fits to the samples of D14 and H15 yield slopes of ~ 1.07 and ~ 0.88 , respectively (shown as dashed and dotted lines in Fig. 6.10). In comparison, a power-law fit to our simulations – across the full Σ_{SFR} -range – results in a slope of ~ 0.60 , i.e., on the low side of the observed range. However, if instead we fit only to simulated regions within the $\Sigma_{\text{SFR}} = 0.001 - 0.1 \text{ M}_{\odot} \text{ yr}^{-1} \text{ kpc}^{-2}$ range, thereby matching the range with the most observations, we find a slope of ~ 0.75 , i.e., well within the observed range.

Beyond the above Σ_{SFR} -range a comparison with the observations has to rely on extrapolations of the simple power-law fits to the observed $\Sigma_{\text{[CII]}} - \Sigma_{\text{SFR}}$ relations. At low Σ_{SFR} ($\lesssim 0.001 \text{ M}_{\odot} \text{ yr}^{-1} \text{ kpc}^{-2}$), the simulations broadly follow the extrapolations of the observed relations, except for D14 where the systematic offset noted at higher Σ_{SFR} is compounded at the lower Σ_{SFR} values owing to the relatively steep slope of the fit to the D14 data. At these low Σ_{SFR} levels a larger (but still minor, overall) fraction of the simulated regions display ex-

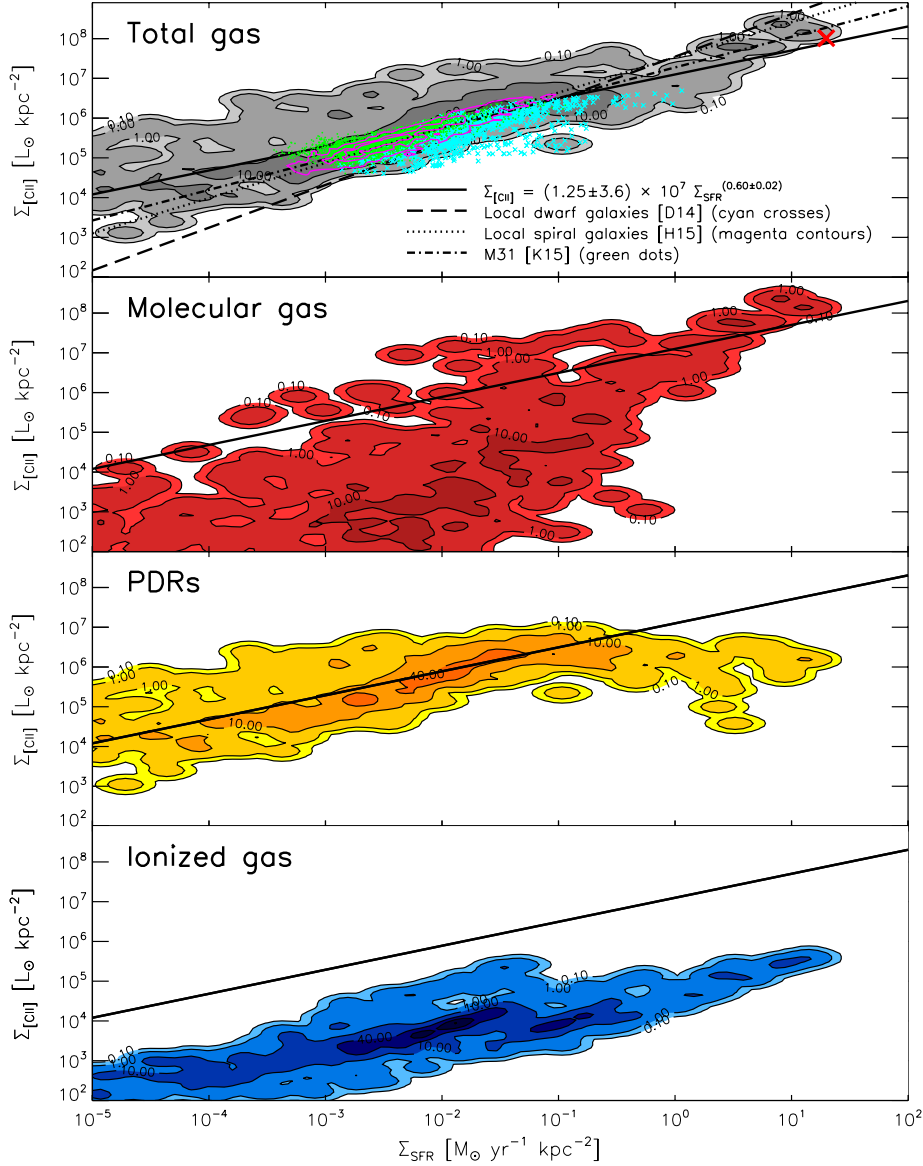


Figure 6.10 $[\text{CII}]$ luminosity surface density ($\Sigma_{[\text{CII}]}$) vs. SFR surface density (Σ_{SFR}) for the full ISM in our simulated galaxies (top panel), and for each of the three ISM phases (bottom three panels). $\Sigma_{[\text{CII}]}$ and Σ_{SFR} are determined over $1 \text{ kpc} \times 1 \text{ kpc}$ regions within all 7 galaxies. The filled colored contours indicate the number of such regions with this combination of Σ_{SFR} and $\Sigma_{[\text{CII}]}$ as a percentage (at 0.1%, 1%, 10%, 40% and 70%) of the maximum number of regions. The solid line shown in all panels is the best-fit power-law to the total gas $\Sigma_{[\text{CII}]}$ vs. Σ_{SFR} (see legend). For comparison we show observed $\Sigma_{[\text{CII}]}$ vs. Σ_{SFR} for individual 20 pc regions in M31 (green dots; K15), 1 kpc regions in nearby (mostly spiral) galaxies (magenta contours, indicating regions containing 25%, 45%, and 95% of the total number of data points; H15), and 1 kpc regions in local dwarf galaxies (cyan crosses; D14). The best-fit power-laws to these three data-sets are shown as dashed-dotted, dotted, and dashed lines, respectively. In the case of M31 the power-law is fitted to 50 pc regions (see K15). We also show the galaxy-averaged $\Sigma_{[\text{CII}]}$ and Σ_{SFR} of ALESS 73.1 (red cross), a $z = 4.76$ submillimeter-selected galaxy which was marginally resolved in $[\text{CII}]$ and in the FIR continuum with ALMA, revealing a source size of $R \sim 2 \text{ kpc}$, $L_{[\text{CII}]} = 5.15 \times 10^9 L_{\odot}$, and $\text{SFR} \sim 1000 M_{\odot} \text{ yr}^{-1}$ (De Bruck et al., 2014).

cess [CII] emission levels ($\gtrsim 10\times$) compared to the survey-based power-law fits. This excess [CII] emission is driven by the PDR gas in our simulations (second panel in Fig. 6.10), which dominates the [CII] emission at these Σ_{SFR} levels. Interestingly, in at least two of the five fields in M31 studied by K15, a similar [CII]-excess relative to the power-law fit is observed at $\Sigma_{\text{SFR}} \lesssim 0.001 \text{ M}_{\odot} \text{ yr}^{-1} \text{ kpc}^{-2}$ (see Fig. 7 in K15). K15 argues that the excess is due to a contribution from diffuse, ionized gas (HII), although they cannot discount the possibility that the larger dispersion is at least partly due to being close to the sensitivity limit of their survey at such low $\Sigma_{\text{[CII]}}$. Our simulations, however, clearly show no significant contribution from the diffuse HII gas phase at low Σ_{SFR} .

At high Σ_{SFR} ($\gtrsim 1 \text{ M}_{\odot} \text{ yr}^{-1} \text{ kpc}^{-2}$), the scatter in the $\Sigma_{\text{[CII]}} - \Sigma_{\text{SFR}}$ relation from our simulations decreases significantly, and is seen to broadly match the extrapolated locally observed relations. Furthermore, the simulation contours are seen to agree with the few galaxies observed to date to have $\Sigma_{\text{SFR}} \gtrsim 1 \text{ M}_{\odot} \text{ yr}^{-1} \text{ kpc}^{-2}$: a few sources from the D14 sample (there are two D14 galaxies with $\Sigma_{\text{SFR}} \gtrsim 1 \text{ M}_{\odot} \text{ yr}^{-1} \text{ kpc}^{-2}$) and ALESS 73.1, a $z = 4.76$ sub-millimeter selected galaxy, marginally resolved in [CII] and with a disk-averaged Σ_{SFR} of $\sim 80 \text{ M}_{\odot} \text{ yr}^{-1} \text{ kpc}^{-2}$ (De Breuck et al. 2014; indicated by a red cross in Fig. 6.10).

The aforementioned studies of local galaxies typically measure both obscured (e.g. from $24 \mu\text{m}$) and un-obscured (from either FUV or $\text{H}\alpha$) SFRs in order to estimate the total Σ_{SFR} and, while intrinsic uncertainties are inherent in the empirical $24 \mu\text{m}/\text{FUV}/\text{H}\alpha \rightarrow \text{SFR}$ calibrations, the Σ_{SFR} values should be directly comparable to those from our simulations. Nonetheless, some caution is called for when comparing our simulations to resolved observations, primarily regarding the determination of Σ_{SFR} on $\lesssim \text{kpc}$ -scales. In particular, as pointed out by D14, the emission from old stellar populations in diffuse regions with no ongoing star formation can lead to overestimates of the SFR when using the above empirical SFR calibrations. Both K15 and H15 account for this by subtracting the expected cirrus emission from old stars in $24 \mu\text{m}$ (using the method presented in Leroy et al. 2012), although on scales $\ll 1 \text{ kpc}$ this correction for $24 \mu\text{m}$ cirrus emission becomes particularly challenging as it was calibrated on $\gtrsim 1 \text{ kpc}$ scales. K15 further points to the problem arising from the possibility of photons leaking between neighboring stellar populations, meaning that average estimates of the SFR on scales $< 50 \text{ pc}$ might not represent the true underlying SFR.

6.6.4 PHYSICAL UNDERPINNINGS OF THE $L_{\text{[CII]}}$ -SFR RELATION

The SFRs of galaxies at both low and high redshifts is observed to strongly correlate with their molecular gas content (typically traced by CO or dust emission) (e.g. Kennicutt, 1998; Daddi et al., 2010; Genzel et al., 2010; Narayanan et al., 2012). This SFR – H_2 dependency is incorporated into our SPH simulations (see Section 6.3), and it is therefore natural to ask whether the integrated [CII] – SFR relation examined in Section 6.6.2 might simply be a case of galaxies with higher SFRs having larger (molecular) gas masses with higher associated [CII] luminosities. To investigate this, we show in Fig. 6.11 [CII] luminosity vs. gas mass for the full ISM in our simulated galaxies and for the individual gas phases separately. For the molecular gas phase we see a significant luminosity–mass scaling (red curve), which would explain the strong $L_{\text{[CII]}} - \text{SFR}$ relation for this phase and, at least in part, the $L_{\text{[CII]}} - \text{SFR}$ relation for the full ISM. The PDR gas and the ionized gas do not exhibit similar luminosity–mass scaling relations. Since, on average, significantly more mass resides in each of these two phases than in the molecular phase, this has the effect of weakening the correlation between $L_{\text{[CII]}}$ and SFR

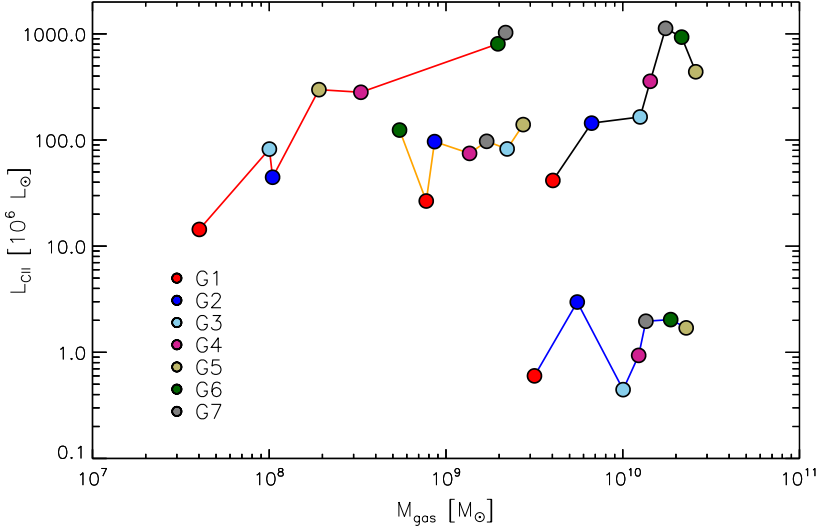


Figure 6.11 [CII] luminosity versus gas mass of the total ISM (black line), the molecular (red line), the PDR (orange line), and the HII (blue line) gas phase for each of our seven simulated galaxies. The [CII] emission from the molecular gas is seen to increase with the amount of molecular gas available, whereas this is not the case for gas associated with PDR and HII regions.

when considering the full ISM.

The abundances of metals in the ISM is expected to affect the [CII] emission. In their study of low-metallicity dwarf galaxies, D14 compared total (IR+UV) SFRs to SFRs derived using the best-fit $L_{\text{[CII]}}$ – SFR relation to their entire sample. They found an increase in the $\text{SFR}_{\text{IR+UV}}/\text{SFR}_{\text{[CII]}}$ fraction, corresponding to weaker [CII] emission, toward lower metallicities. In Fig. 6.12 we show $\text{SFR}/L_{\text{[CII]}}$ as a function of $Z_{\text{[O/H]}}$ ($= 12 + \log [\text{O}/\text{H}]$) for our simulated galaxies as well as for the dwarf galaxy sample of D14. As D14 points out, $Z_{\text{[O/H]}}$ does not take into account potential deficits of carbon relative to the [O/H] abundance, potentially obscuring any potential correlation between [CII] luminosity and actual carbon abundance. In Fig. 6.12 we therefore also plot $\text{SFR}/L_{\text{[CII]}}$ as a function of $Z_{\text{[C/H]}}$ ($= 12 + \log [\text{C}/\text{H}]$) for our simulated galaxies. Arguably, our simulated galaxies exhibit a weak trend in $\text{SFR}/L_{\text{[CII]}}$ with metallicity (in particular for [C/H]). Certainly, there is a very good overall agreement with the findings of D14. The lack of a strong trend within our simulation sample is not surprising, however, since our galaxies span a limited range in metallicity ($Z_{\text{[O/H]}} = 8.03 - 8.96$) and, as we saw in Section 6.6.2, form a tight $L_{\text{CII}} - \text{SFR}$ relation.

To better understand how the metallicity and also the ISM pressure affects the [CII] emission, we define a ‘[CII] emission efficiency’ ($\epsilon_{\text{[CII]}}$) of a given gas phase as the [CII] luminosity of the gas phase divided by its mass, and examine how it depends on Z' and $P_{\text{ext}}/k_{\text{B}}$. Specifically, we create a grid of (Z' , $P_{\text{ext}}/k_{\text{B}}$) values, and in each grid point the median $\epsilon_{\text{[CII]}}$ of all clouds in our simulated galaxies is calculated. The resulting $\epsilon_{\text{[CII]}}$ contours as a function of Z' and $P_{\text{ext}}/k_{\text{B}}$ are shown in Fig. 6.13 for the molecular (top) and PDR (middle), and Fig. 6.14 for the HII gas phases. For comparison, we also show the median Z' - and $P_{\text{ext}}/k_{\text{B}}$ -values for each of our galaxies.

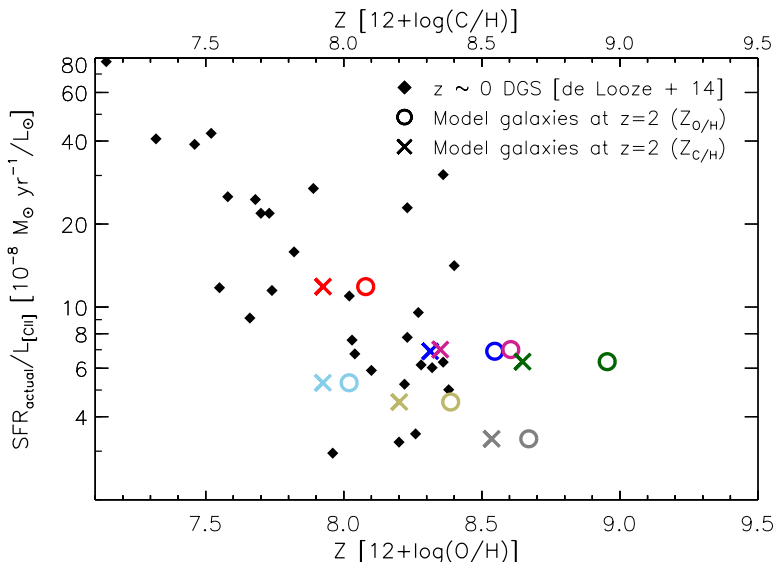


Figure 6.12 $\text{SFR}/L_{[\text{CII}]}$ as a function of metallicity for our simulated galaxies. The metallicity is parametrized both relative to the oxygen (circles) and the carbon (crosses) abundance. The galaxies are color coded in the usual manner. For comparison, we show $\text{SFR}/L_{[\text{CII}]}$ vs. $Z_{[\text{O/H}]}$ for the local dwarf galaxy sample of D14, where SFRs are from combined UV and $24\,\mu\text{m}$ measurements.

The molecular phase in our simulations is seen to radiate most efficiently in [CII] at relatively high metallicities ($\log Z' \sim 0.5$) and cloud external pressures ($P_{\text{ext}}/k_B \sim 10^6\,\text{cm}^{-3}\,\text{K}$). The PDR and ionized phases, however, have their maximal $\epsilon_{[\text{CII}]}$ at $\log Z' \gtrsim 0$ and $P_{\text{ext}} \sim 10^4\,\text{cm}^{-3}\,\text{K}$, i.e. at $\sim 100\times$ lower pressures than the molecular phase, and can maintain a significant [CII] efficiency ($\gtrsim 20\%$) even at $P_{\text{ext}}/k_B \sim 10^2\,\text{cm}^{-3}\,\text{K}$ provided $\log Z' \gtrsim 0$. This is consistent with our finding in Section 6.6.1, that the molecular phase dominates the [CII] emission in the central, high-pressure regions, while the PDR gas dominates further out in the galaxy where the ISM pressure is less extreme. In all three panels, G6 and G7 lie in regions of high $\epsilon_{[\text{CII}]}$ ($\gtrsim 50\%$ for the molecular and PDR gas). Thus, the reason why these two galaxies have the highest total [CII] luminosities is in part due to the fact that they have the highest molecular gas masses (by nearly an order of magnitude, see Fig. 6.11), and in part due to the bulk of their cloud population (GMCs or ionized clouds) having sufficiently high metallicities (on average $\gtrsim 5\times$ higher than G2) and experiencing external pressures ($\sim 100\times$ higher on average than the remaining galaxies) which drives their [CII] efficiencies up.

6.7 COMPARING WITH OTHER [CII] SIMULATIONS

A direct quantitative comparison with other [CII] emission simulation studies in the literature (Nagamine et al., 2006; Vallini et al., 2013, 2015; Popping et al., 2014b; Muñoz & Furlanetto, 2014) is complicated by the fact that there is not always overlap in the masses and/or redshifts of the galaxies simulated by the aforementioned studies and our model galaxies. Furthermore, there are fundamental differences in the simulation approach, with some adopting semi-analytical models (Popping et al., 2014b; Muñoz & Furlanetto, 2014) and others adopt-

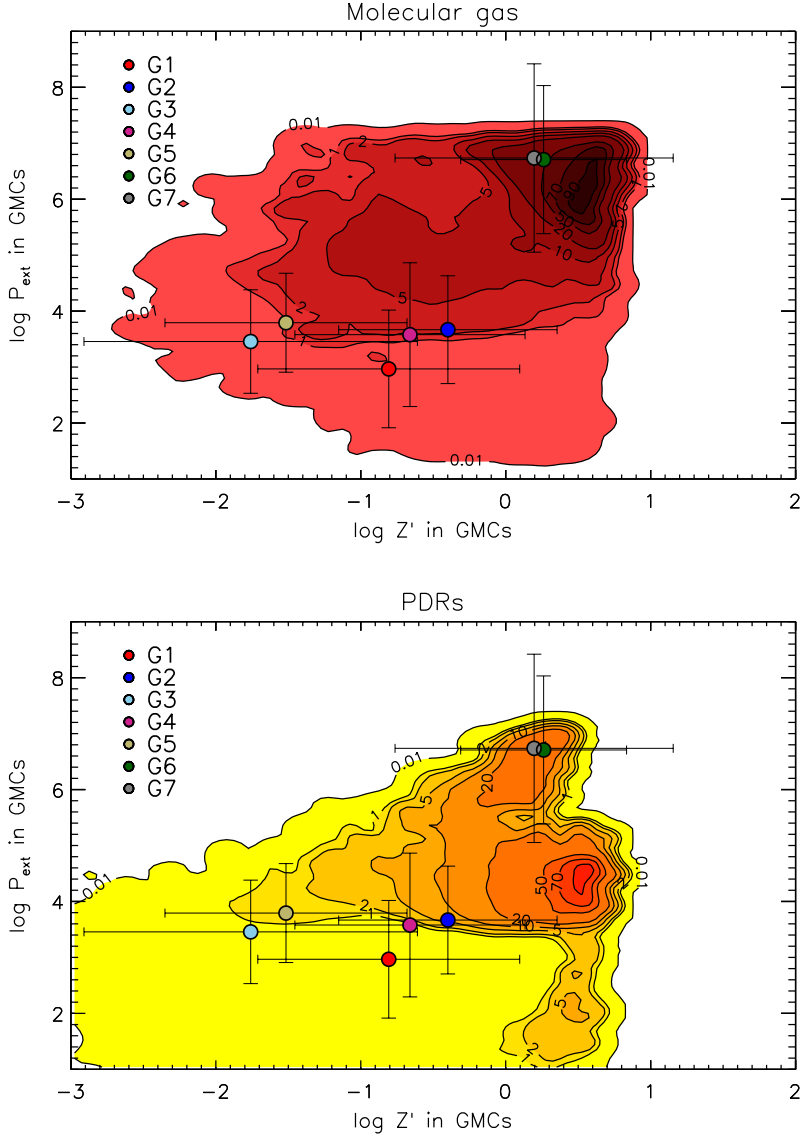


Figure 6.13 Contours of (median) $\epsilon_{[\text{CII}]}$ (i.e. [CII] luminosity per gas mass) as a function of Z' and P_{ext}/k_B for the molecular (top) and PDR (bottom) gas phases in our model galaxies. In each panel the contours indicate 0.01%, 1%, 2%, 5%, 10%, 20%, 50%, 70%, and 90% percentages of the maximum efficiency. For reference, the maximum (median) $\epsilon_{[\text{CII}]}$ for the molecular and PDR gas phases are: 3.7 and $6.6 L_{\odot}/M_{\odot}$, respectively. Median values of Z' and P_{ext}/k_B and for the GMC and ionized cloud population in each model galaxies are indicated as colored circles (error bars are the 1σ dispersion of the distributions).

ing SPH simulations (Nagamine et al., 2006; Vallini et al., 2013, 2015). Also, differences in the numerical resolution of both types of simulations, and in the specifics of the sub-grid physics implemented, can lead to diverging results and make comparisons difficult.

The simulations presented here combine cosmological SPH galaxy simulations with a sub-grid treatment of a multi-phase ISM that is locally heated by FUV radiation and CRs in a man-

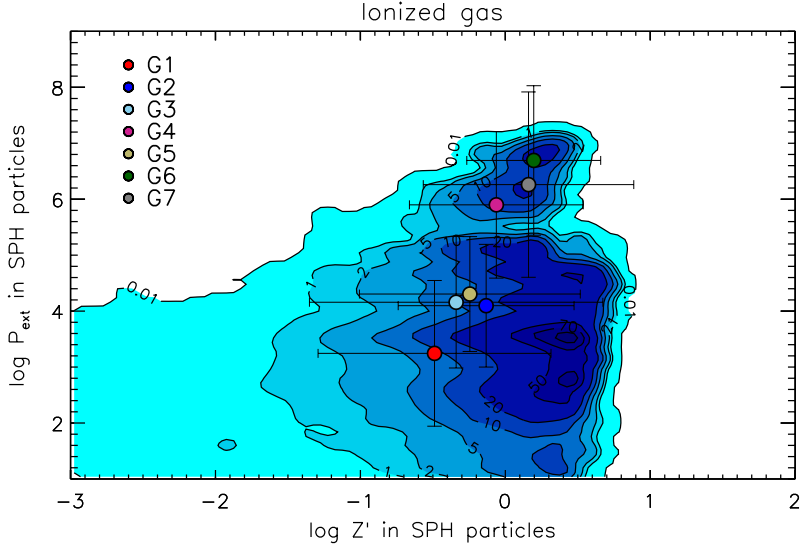


Figure 6.14 Contours of (median) $\epsilon_{[CII]}$ (i.e. [CII] luminosity per gas mass) as a function of Z' and P_{ext}/k_B for the HII gas phases in our model galaxies. The contours and galaxy positions are defined as in Fig. 6.13. The maximum (median) ionized gas phase is: $0.02 L_{\odot}/M_{\odot}$.

ner that depends on the local SFR density within the galaxies. We have applied our method to a high resolution ($\delta m_{SPH} \simeq 1.7 \times 10^4 M_{\odot}$) cosmological SPH simulation of $z = 2$ star-forming galaxies (i.e., baryonic mass resolution $\delta m_{SPH} \simeq 1.7 \times 10^4 M_{\odot}$ and gravitational softening length $\simeq 0.6 h^{-1}$ kpc, see Section 6.3). A novel feature of our simulations is the inclusion of molecular, neutral and ionized gas as contributors to the [CII] emission. Another unique feature of our model is the inclusion of CRs as a route to produce C^+ deep inside the GMCs where UV photons cannot penetrate (see Section 6.5).

Our simulations probably come closest – both in terms of methodology and galaxies simulated – to those of Nagamine et al. (2006) who employed cosmological simulations with GADGET-2 (the precursor for GADGET-3 used here) to predict total [CII] luminosities from dark matter halos associated with $z \simeq 3$ LBGs with $M_* \sim 10^{10} M_{\odot}$ and $SFR \gtrsim 30 M_{\odot} \text{ yr}^{-1}$ (see also Nagamine et al., 2004). Their simulations employed gas mass resolutions in the range $\delta m_{SPH} \simeq 3 \times 10^{5-8} M_{\odot}$ and gravitational softening lengths of typically $> 1 h^{-1}$ kpc. In their simulations the ISM consist of a CNM ($T \sim 80$ K and $n \sim 10 \text{ cm}^{-3}$) and a warm neutral medium ($T \sim 8000$ K and $n \sim 0.1 \text{ cm}^{-3}$) in pressure-equilibrium, and the assumption is made that the [CII] emission only originates from the former phase. The thermal balance calculation of the ISM includes heating by grain photo-electric effect, CRs, X-rays, and photo-ionization of C I – all of which are assumed to scale on the local SFR surface density. Their simulations predict $L_{[CII]} \sim (0.3 - 1) \times 10^8 L_{\odot}$ for their brightest LBGs ($SFR \gtrsim 30 M_{\odot} \text{ yr}^{-1}$) which is slightly below the prediction of our integrated [CII] – SFR relation ($L_{[CII]} \sim 6 \times 10^8 L_{\odot}$; Fig. 6.9).

Employing a semi-analytical model of galaxy formation, Popping et al. (2014b) made predictions of the integrated [CII] luminosity from galaxies at $z = 2$ with $M_* \sim 10^8 - 10^{12} M_{\odot}$ and $SFR \sim 0.1 - 100 M_{\odot} \text{ yr}^{-1}$ (see also Popping et al., 2014c). The galaxies are assumed to have exponential disk gas density profiles, with randomly placed ‘over-densities’ mimicking GMCs

(constituting $\sim 1\%$ of the total volume). The gas is embedded in a background UV radiation field of 1 Habing, with local variations in the radiation field set to scale with the local SFR surface density. The C^+ abundance is set to scale with the abundance of carbon in the cold gas. The excitation of [CII] occurs via collisions with e^- , H, and H_2 , and the line emission is calculated with a 3D radiative transfer code that takes into account the kinematics and optical depth effects of the gas. For galaxies with SFRs similar to our model galaxies ($\sim 5 - 50 M_\odot \text{ yr}^{-1}$) their simulations predict ensemble-median [CII] luminosities of $\lesssim (1 - 6) \times 10^7 L_\odot$.³ This is lower than the [CII] luminosities predicted by our simulations and also somewhat on the low side of the observed $z \sim 0$ $L_{\text{[CII]}} - \text{SFR}$ relation (Fig. 6.9). Allowing for the $+2\sigma$ deviation from the median of the Popping et al. (2014b) models results in $L_{\text{[CII]}} \lesssim (2 - 30) \times 10^7 L_\odot$ for $\text{SFR} \sim 5 - 50 M_\odot \text{ yr}^{-1}$, which matches the observed $L_{\text{[CII]}} - \text{SFR}$ relation.

The remaining [CII] simulation studies in the literature focus on $z \gtrsim 6$ galaxies (Vallini et al., 2013, 2015; Muñoz & Furlanetto, 2014). Vallini et al. (2013) uses a GADGET-2 cosmological SPH simulation with a mass resolution $\delta m_{\text{SPH}} = 1.32 \times 10^5 M_\odot$ and gravitational softening length $\sim 2 h^{-1} \text{ kpc}$. They adopt a two-phased ISM model (CNM+WNM), and heating and cooling mechanisms similar to that of Nagamine et al. (2006), in order to predict the [CII] emission from a $z = 6.6$ Lyman alpha emitter (LAE) with $\text{SFR} \simeq 10 M_\odot \text{ yr}^{-1}$. They investigated two cases of fixed metallicity: $Z' = 1$ and $Z' = 0.02$. In their simulations, the CNM ($T \sim 250 \text{ K}$ and $n \sim 50 \text{ cm}^{-3}$) is found to be responsible for $\sim 95\%$ of the total [CII] emission, with the WNM phase ($T \sim 500 \text{ K}$ and $n \sim 1 \text{ cm}^{-3}$) contributing the remaining 5%. Vallini et al. (2015) presents an update to their 2013 model, in which the same $z = 6.6$ SPH simulation as in Vallini et al. (2013) is considered but now with the implementation of a density-dependent prescription for the metallicity of the gas, and the inclusion of [CII] contributions from PDRs (in addition to their previous two-phased CNM+WNM ISM model), and accounting for the effect of the CMB on the [CII] emission. As a result of these updates, it is found that the [CII] emission is now dominated by the PDRs, with $< 10\%$ coming from the CNM. This is qualitatively consistent with the results from our simulations at $z = 2$ where the PDR gas dominates the total [CII] emission at least at the low SFR end ($\lesssim 10 M_\odot \text{ yr}^{-1}$). However, our simulations do not incorporate the CNM to the same extent as that of Vallini et al. (2015), as the lowest densities found in the neutral gas in our simulations is of order $\sim 100 \text{ cm}^{-3}$, i.e., above typical CNM densities of $\sim 20 - 50 \text{ cm}^{-3}$. It is therefore reassuring that Vallini et al. (2015) find the CNM contribution to the total [CII] emission to be benign. Assuming that $\Sigma_{\text{SFR}} \propto \Sigma_{\text{H}_2}$ and $\Sigma_{\text{H}_2} \propto \Sigma_{\text{[CII]}}$, Vallini et al. (2015) scale the [CII] luminosity of their fiducial LAE model ($\text{SFR} = 10 M_\odot \text{ yr}^{-1}$) in order to generate a $L_{\text{[CII]}} - \text{SFR}$ relation.

Muñoz & Furlanetto (2014) make analytical predictions of the [CII] luminosities for a range of galaxy types at $z \gtrsim 6$ (e.g., Lyman-alpha emitters, starburst galaxies and quasars, spanning a range in SFR from tens of $M_\odot \text{ yr}^{-1}$ to several thousand) as part of their efforts to develop an analytical framework for disk galaxy formation and evolution at these early epochs. In their study, the [CII] emitting gas is assumed to come from photo-dissociation regions only. Throughout their models, the metallicity is kept fixed at solar. By tuning their models, i.e., either increasing the star formation efficiency at high redshifts or lowering the depletion of metals onto dust grains, they arrive at the [CII] – SFR relation: $L_{\text{[CII]}}/L_\odot = 5 \times 10^8 (\text{SFR}/100 M_\odot \text{ yr}^{-1})^{0.9}$. While this is essentially a linear relation, it struggles to match the expected [CII] luminosities

³Since Popping et al. (2014b) plots $L_{\text{[CII]}}$ against L_{IR} and not SFR, we have converted our SFRs to L_{IR} in order to crudely estimate their predicted [CII] luminosities (see their Fig. 11). For the $\text{SFR} \rightarrow L_{\text{IR}}$ conversion we have used (Bell, 2003). Not all the star formation will be obscured and so the IR luminosities, and thereby the [CII] luminosities given here will be upper limits.

based on observations due to the somewhat lower normalization.

6.8 CONCLUSION

We have adapted `SÍGAME` (described in previous Chapter) to include simulations of the [CII] emission from star-forming galaxies. `SÍGAME` was applied to SPH simulations of seven star-forming galaxies at $z = 2$ with stellar masses in the range $\sim (0.4 - 6.6) \times 10^{10} M_{\odot}$ and SFRs $\sim 5 - 60 M_{\odot} \text{ yr}^{-1}$ in order to make predictions of the [CII] line emission from MS galaxies during the peak of the cosmic star formation history.

A key result of our simulations is that the total [CII] emission budget from our galaxies is dominated by the molecular gas phase ($\gtrsim 70\%$) in the central regions ($R \lesssim 1 \text{ kpc}$) where the bulk of the star formation occurs and is most intense, and by PDR regions further out ($R \gtrsim 1 - 2 \text{ kpc}$) where the molecular [CII] emission has dropped by at least an order of magnitude compared to their central values. The PDR gas phase, while rarely able to produce [CII] emission as intense as the molecular gas in the central regions, is nonetheless able to maintain significant levels of [CII] emission from $R \sim 2 \text{ kpc}$ all the way out to $\sim 8 \text{ kpc}$ from the center. The net effect of this is that on global scales the PDR gas can produce between 8% and 67% of the total [CII] luminosity with the molecular gas responsible for the remaining emission. We see a trend in which galaxies with higher SFRs also have a higher fraction of their total [CII] luminosity coming from the molecular phase. Our simulations consistently show that the ionized gas contribution to the [CII] luminosity is negligible ($\lesssim 3\%$), despite the fact that this phase dominates the ISM mass budget (see Fig. 6.11). Therefore, the ionized gas phase is an inefficient [CII] line emitter in our simulations.

The integrated [CII] luminosities of our simulated galaxies strongly correlate with their SFRs, and in a manner that agrees well (both in terms of slope and overall normalization) with the observed $L_{[\text{CII}]} - \text{SFR}$ relations for normal star-forming galaxies at both low and high redshifts. We have also examined the relationship between the 1 kpc -averaged surface densities of $L_{[\text{CII}]}$ and SFR across our simulated galaxies. The resulting $\Sigma_{[\text{CII}]} - \Sigma_{\text{SFR}}$ relation spans six orders of magnitude in Σ_{SFR} ($\sim 10^{-5} - 10 M_{\odot} \text{ yr}^{-1} \text{ kpc}^{-2}$), extending beyond the observed ranges at both the low and high end of the relation. In the Σ_{SFR} -range where a direct comparison with observations can be made ($\sim 0.001 - 1 M_{\odot} \text{ yr}^{-1} \text{ kpc}^{-2}$) we find excellent agreement with our simulations.

Our simulations suggest that the correlation between [CII] and SFR – both the integrated and the resolved versions – is determined by the combined [CII]-contribution from the molecular and PDR phases (the ionized gas makes a negligible contribution), with the former exhibiting the steepest slope and dominating the [CII] emission at the high-SFR-end. We argue that this is due to the fact that the [CII] luminosity scales with the amount of molecular gas present in our simulated galaxies. A similar luminosity-mass scaling is not seen for the other phases. Our work therefore suggest that the observed [CII] – SFR relation is a combination of the line predominantly tracing the molecular gas (i.e., the star formation ‘fuel’) at high SFR levels/surface densities, while at low SFRs/surface densities the line is tracing PDR gas being exposed to a weaker, interstellar UV-field. As a consequence, we hypothesize that galaxies with large mid-plane pressures and large molecular gas fractions will display a steeper [CII] – SFR relationship than galaxies where a larger fraction of the ISM is atomic/ionized gas. In the future we will extend this study to a larger sample of model galaxies, in particular with a larger spread in SFRs and metallicities.

In the future we feel strongly encouraged to extend this study to a larger sample of galaxies, in particular with a larger spread in SFRs.

7

OUTLOOK

7.1 IMPROVEMENTS ON SÍGAME

The aim of SÍGAME is to model line emission from the ISM of galaxies at any redshift. Such a code has to be as true as possible to the observations of gas and dust, on small and large scale. At high- z (and assuming that physical laws do not change in time), this turns into a limitation in how well we can resolve the ISM spatially or spectroscopically, sometimes leading to rather crude assumptions based on what can be observed locally. As a recently developed code, SÍGAME has several such assumptions with room for improvement, of which three are listed below.

7.1.1 DUST TEMPERATURES WITH A RADIATIVE TRANSFER CODE

With SÍGAME we have demonstrated a new method that takes into account local FUV fields and CR intensities in galaxies. However, our method of scaling these fields to the local SFR and total stellar mass, can be made much more realistic with the inclusion of an actual dust radiative transfer (RT) code. One such code, developed recently, is Hyperion¹ (Robitaille, 2011) for which Powderday² can be used as an interface between Hyperion and galaxy formation simulations. And many alternatives exist as evident from the review by Steinacker et al. (2013). Implementing one of these would allow us to self-consistently derive dust temperatures, taking into account anisotropic scattering, absorption and (re-)emission by interstellar dust, all based on the distribution of stars and dust in the galaxy.

7.1.2 MODELING OF ASYMMETRIC GMCS

At present, there exists a gap between simulations of the ISM on galaxy-scales and those on scales relevant for the formation of individual stars. On galaxy-scales, simulations are typically restricted to model star formation using empirical correlations between gas density and star formation rate. However, more detailed simulations are emerging, following dense gas from kpc-scales down to ~ 0.1 pc where star clusters are formed (Butler et al., 2014; Dobbs, 2015). With modifications, SÍGAME could be applied to resolved simulations of single star formation such as those of Vázquez-Semadeni et al. (2010, 2011) and Dale et al. (2013), in order to make a more precise grid in CO line intensities as a function of more global parameters. The move

¹<http://www.hyperion-rt.org/>

²<https://bitbucket.org/desika/powderday>

from spherically symmetric GMC models towards the clumpy, filamentary clouds observed is an important step forward for SÍGAME.

7.1.3 INCLUDING HEATING BY X-RAYS AND TURBULENT DISSIPATION

Particularly towards the Galactic center, observations demand the presence of non-photon driven heating such as cosmic rays and turbulent dissipation (Ao et al., 2014). But also in normal star-forming GMCs, turbulent dissipation has been suggested as a cause for most of the observed excess in CO lines at $J_{\text{upper}} \geq 6$ (Pon et al., 2012, 2014). In AGNs, the circum-nuclear disks can act like an X-ray Dominated Region (XDR), and X-ray heating is therefore important when modeling these central regions (e.g. Aalto et al., 2007; García-Burillo et al., 2010). We have focused our research projects on normal star-forming galaxies, but if SÍGAME is to work more generally on starburst and AGNs, turbulent dissipation and X-ray heating must be included in the model.

7.2 GOING TO HIGHER REDSHIFT

7.2.1 THE EVOLUTION OF X_{CO} WITH REDSHIFT

Gas mass estimates depend crucially on the dust-to-gas mass ratio or the X-factor, X_{CO} . At $z \sim 2$, SÍGAME predicts X_{CO} factors about half that of the MW for massive star-forming galaxies, and applying the same method to simulations at higher redshift, we could investigate how X_{CO} changes with redshift. Such predictions will be important for future observational campaigns trying to pin down the evolution of f_{gas} with redshift. X_{CO} could also readily be applied to observations of any CO line, if we knew the shape of the CO ladder beforehand. Narayanan & Hopkins (2012) developed a parametrization of the CO ladder with Σ_{SFR} that SÍGAME can now improve on by seeing how it changes at $z > 2$ for normal star-forming galaxies.

7.2.2 THE FULL CALIBRATION TO NORMAL GALAXIES AT $z \sim 2$

As evident from the study of CO and [CII] line emission in normal star-forming $z \sim 2$ galaxies, we are in need of more observations, in particular of the full CO SLED, in order to test models, such as SÍGAME, and use them to their fullest. I plan to continue my involvement in the HELLO (*Herschel* Extreme Lensing Line Observations) project which takes advantage of powerful lensing (by e.g. foreground groups of galaxies) in order to detect [CII] line emission from normal galaxies at $z \sim 2$. With the high spectral resolution of *Herschel*, kinematic studies of the line profiles are used to estimate rotation speed and gas velocity dispersion (Rhoads et al., 2014). Follow-up observations of CO lines with JVLA and ALMA make these galaxies excellent calibrators for SÍGAME, which itself will help in the interpretation of these future line observations.

7.2.3 GALAXIES DURING THE EPOCH OF RE-IONIZATION

In the early universe, at redshifts above 7, spectroscopic observations in the FIR might be our only way to characterize the modest MS galaxies responsible for most star formation, that are otherwise proving difficult to capture in rest-frame UV with existing spectrographs. Observing and modeling the gas conditions during the Epoch of Re-ionization (EoR) will enable us to

answer questions such as: *How did galaxies first acquire their gas masses? When did the gas become enriched by the first supernovae? What role did the gas play in setting the SFR?*

Observing with band 7 of ALMA, Capak et al. (2015) found $> 3\sigma$ detections of [CII] in a sample of 9 normal ($\text{SFR} < 3$ to $\sim 170 M_{\odot} \text{ yr}^{-1}$) galaxies at $z \sim 5 - 6$, of which only 4 are detected in dust continuum, underlining the importance of [CII] as a tracer of the ISM at high redshift. However, many attempts with ALMA (and PdBI) pointing at $z \sim 7$ star-forming MS galaxies for hours, have only resulted in upper limits on both [CII] line emission and dust continuum (Ouchi et al., 2013; Maiolino et al., 2015; Ota et al., 2014; Schaerer et al., 2015; González-López et al., 2014). One preferred explanation is low metallicity because the galaxies might not have had enough time to enrich the primordial gas with metallicities to a degree that their line emission is strong enough for detection (Ouchi et al., 2013; Ota et al., 2014; González-López et al., 2014; Schaerer et al., 2015). Another explanation based on recent simulations, is that molecular clouds in these primeval systems are destroyed and dispersed by strong stellar feedback, pushing most of the carbon to higher ionization states (Maiolino et al., 2015; Vallini et al., 2013). A difference in PDR structure or physical states of the ISM between star-forming galaxies at high-redshift and local ones, might also be enough to explain the low luminosity in [CII] and FIR (Ota et al., 2014).

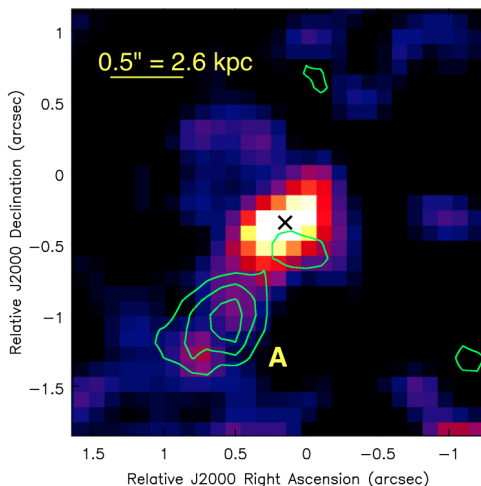


Figure 7.1 Image in rest frame UV stellar continuum and $\text{Ly}\alpha$ emission of the $z = 7.109$ galaxy BDF3299. Green contours show the levels of 2, 3 and 4 times the noise per beam in the [CII] map. The detected clump at 4 kpc distance from the galaxy center (black cross) is marked 'A' (Maiolino et al., 2015).

Interestingly, Maiolino et al. (2015) detect a strong (7σ) [CII] signal from a position which is offset from the actual galaxy, BDF3299 at $z = 7.109$, as shown in Fig. 7.1. This is interpreted as an accreting/satellite gas clump of neutral gas about 4 kpc from the galaxy itself. At slightly higher redshift, Watson et al. (2015) managed to detect dust continuum emission from the galaxy A1689-zD1 of $\text{SFR} \sim 10 M_{\odot} \text{ yr}^{-1}$. Such observations nourish the hope that we are but few steps away from using [CII] observations to characterise the gas in normal galaxies and/or the mass assembly from the Circumgalactic Medium (CGM) in the early universe.

With this motivation, I have recently made preliminary attempts at simulating [CII] emission from halos at high redshift, in collaboration with Kristian Finlator, here at the Dark Cosmology Centre. As a simple test, we adopted a NFW profile for the radial halo density profile, and, since little is known about the metal abundance at these redshifts, assumed three values for the abundance of carbon, going from pessimistic to optimistic: $Z'_C = [10^{-4.5}, 10^{-4}, 10^{-3.5}]$. The resulting rough estimate of [CII] luminosity as a function of halo mass at $z = 6$ is shown in Fig. 7.2 together with a surface brightness map for a halo mass of $5 \times 10^9 M_{\odot}$. With the use of actual cosmological simulations, rather than simple spherically symmetric halo models or constant metallicity and temperature, we can make much more precise predictions for the detectability of the CGM.

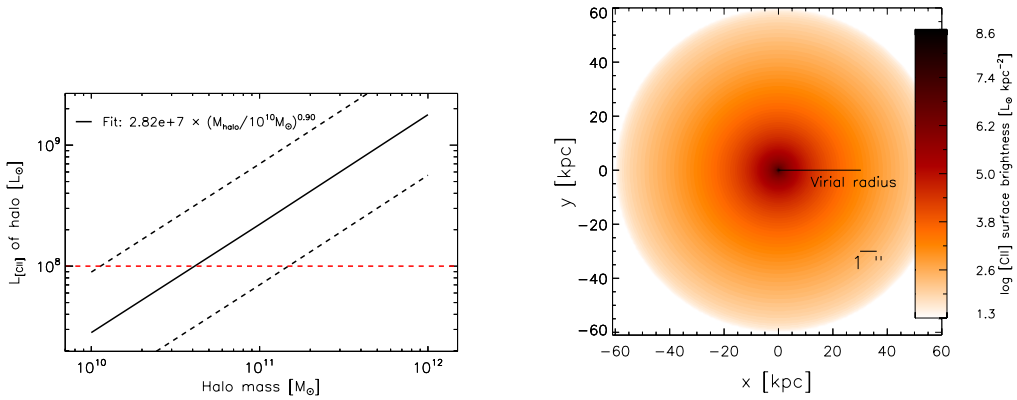


Figure 7.2 *Left*: [CII] luminosity as a function of stellar mass for our fiducial case (solid line) and the optimistic and pessimistic cases (dashed lines). *Right*: Map of [CII] surface brightness from a galaxy of stellar mass $5 \times 10^9 M_{\odot}$ at $z = 6$ (corresponding to a halo mass of $2.7 \times 10^{11} M_{\odot}$ within the virial radius, marked on the figure).

7.3 REFERENCES

- Aalto, S., Spaans, M., Wiedner, M. C., & Hüttemeister, S. 2007, *A&A*, 464, 193
- Abel, N. P., Dudley, C., Fischer, J., Satyapal, S., & van Hoof, P. A. M. 2009, *ApJ*, 701, 1147
- Ao, Y., Henkel, C., Menten, K. M., et al. 2014, in *IAU Symposium*, Vol. 303, *IAU Symposium*, ed. L. O. Sjouwerman, C. C. Lang, & J. Ott, 89–91
- Bell, E. F. 2003, *ApJ*, 586, 794
- Blitz, L., Fukui, Y., Kawamura, A., et al. 2007, *Protostars and Planets V*, 81
- Boselli, A., Gavazzi, G., Lequeux, J., & Pierini, D. 2002, *A&A*, 385, 454
- Bovy, J., Rix, H.-W., & Hogg, D. W. 2012, *ApJ*, 751, 131
- Brauer, J. R., Dale, D. A., & Helou, G. 2008, *ApJS*, 178, 280
- Butler, M. J., Tan, J. C., & Van Loo, S. 2014, *ArXiv e-prints*
- Calzetti, D., Kennicutt, R. C., Engelbracht, C. W., et al. 2007, *ApJ*, 666, 870
- Capak, P. L., Carilli, C., Jones, G., et al. 2015, *ArXiv e-prints*
- Carilli, C. L., Riechers, D., Walter, F., et al. 2013, *ApJ*, 763, 120
- Casey, C. M., Narayanan, D., & Cooray, A. 2014, *arXiv/1402.1456*
- Chomiuk, L., & Povich, M. S. 2011, *AJ*, 142, 197
- Crawford, M. K., Genzel, R., Townes, C. H., & Watson, D. M. 1985, *ApJ*, 291, 755
- Croxall, K. V., Smith, J. D., Wolfire, M. G., et al. 2012, *ApJ*, 747, 81
- Daddi, E., Elbaz, D., Walter, F., et al. 2010, *ApJ*, 714, L118
- Dale, J. E., Ngoumou, J., Ercolano, B., & Bonnell, I. A. 2013, *MNRAS*, 436, 3430
- Dartois, E., & Muñoz-Caro, G. M. 2007, *A&A*, 476, 1235
- Davé, R., Katz, N., Oppenheimer, B. D., Kollmeier, J. A., & Weinberg, D. H. 2013, *MNRAS*, 434, 2645
- De Breuck, C., Maiolino, R., Caselli, P., et al. 2011, *A&A*, 530, L8
- De Breuck, C., Williams, R. J., Swinbank, M., et al. 2014, *A&A*, 565, A59
- de Looze, I., Baes, M., Bendo, G. J., Cortese, L., & Fritz, J. 2011, *MNRAS*, 416, 2712
- De Looze, I., Cormier, D., Lebouteiller, V., et al. 2014, *ArXiv e-prints*
- Díaz-Santos, T., Armus, L., Charmandaris, V., et al. 2013, *ApJ*, 774, 68
- Dobbs, C. L. 2015, *MNRAS*, 447, 3390
- Durier, F., & Dalla Vecchia, C. 2012, *MNRAS*, 419, 465

Elmegreen, B. G. 1989, *ApJ*, 344, 306
 Esteban, C., García-Rojas, J., Carigi, L., et al. 2014, *MNRAS*, 443, 624
 Farrah, D., Lebouteiller, V., Spoon, H. W. W., et al. 2013, *ApJ*, 776, 38
 Ferkinhoff, C., Brisbin, D., Nikola, T., et al. 2011, *ApJ*, 740, L29
 Ferland, G. J., Porter, R. L., van Hoof, P. A. M., et al. 2013, *RxMAA*, 49, 137
 Ford, A. B., Werk, J. K., Dave, R., et al. 2015, *ArXiv e-prints*
 Gallerani, S., Neri, R., Maiolino, R., et al. 2012, *A&A*, 543, A114
 García-Burillo, S., Usero, A., Fuente, A., et al. 2010, *A&A*, 519, A2
 Genzel, R., Tacconi, L. J., Gracia-Carpio, J., et al. 2010, *MNRAS*, 407, 2091
 Goldsmith, P. F., Langer, W. D., Pineda, J. L., & Velusamy, T. 2012, *ApJS*, 203, 13
 González-López, J., Riechers, D. A., Decarli, R., et al. 2014, *ApJ*, 784, 99
 Graciá-Carpio, J., Sturm, E., Hailey-Dunsheath, S., et al. 2011, *ApJ*, 728, L7
 Gullberg, B., De Breuck, C., Vieira, J. D., et al. 2015, *MNRAS*, 449, 2883
 Hahn, O., & Abel, T. 2011, *MNRAS*, 415, 2101
 Hailey-Dunsheath, S., Nikola, T., Stacey, G. J., et al. 2010, *ApJ*, 714, L162
 Heiderman, A., Evans, II, N. J., Allen, L. E., Huard, T., & Heyer, M. 2010, *ApJ*, 723, 1019
 Herrera-Camus, R., Bolatto, A. D., Wolfire, M. G., et al. 2015, *ApJ*, 800, 1
 Hodge, P. W., Balsley, J., Wyder, T. K., & Skelton, B. P. 1999, *PASP*, 111, 685
 Hollenbach, D. J., & Tielens, A. G. G. M. 1999, *Reviews of Modern Physics*, 71, 173
 Hopkins, P. F. 2013, *MNRAS*, 428, 2840
 Ibar, E., Lara-López, M. A., Herrera-Camus, R., et al. 2015, *ArXiv e-prints*
 Iono, D., Yun, M. S., Elvis, M., et al. 2006, *ApJ*, 645, L97
 James, B. L., Aloisi, A., Heckman, T., Sohn, S. T., & Wolfe, M. A. 2014, *ApJ*, 795, 109
 Kanekar, N., Wagg, J., Ram Chary, R., & Carilli, C. L. 2013, *ApJ*, 771, L20
 Kapala, M. J., Sandstrom, K., Groves, B., et al. 2015, *ApJ*, 798, 24
 Katz, N., Weinberg, D. H., & Hernquist, L. 1996, *ApJS*, 105, 19
 Kennicutt, Jr., R. C. 1998, *ARA&A*, 36, 189
 Kramer, C., Abreu-Vicente, J., García-Burillo, S., et al. 2013, *A&A*, 553, A114
 Krumholz, M. R., McKee, C. F., & Tumlinson, J. 2008, *ApJ*, 689, 865
 —. 2009, *ApJ*, 693, 216
 Krumholz, M. R., & Tan, J. C. 2007, *ApJ*, 654, 304
 Kurtz, N. T., Smyers, S. D., Russell, R. W., Harwit, M., & Melnick, G. 1983, *ApJ*, 264, 538
 Lada, C. J., Lombardi, M., & Alves, J. F. 2010, *ApJ*, 724, 687
 Larson, R. B. 1981, *MNRAS*, 194, 809
 Lebouteiller, V., Cormier, D., Madden, S. C., et al. 2012, *A&A*, 548, A91
 Leech, K. J., Völk, H. J., Heinrichsen, I., et al. 1999, *MNRAS*, 310, 317
 Leroy, A. K., Bigiel, F., de Blok, W. J. G., et al. 2012, *AJ*, 144, 3
 Luhman, M. L., Satyapal, S., Fischer, J., et al. 2003, *ApJ*, 594, 758
 —. 1998, *ApJ*, 504, L11
 Madden, S. C., Genzel, R., Herrmann, F., et al. 1992, in *Bulletin of the American Astronomical Society*, Vol. 24, American Astronomical Society Meeting Abstracts, 1268
 Magdis, G. E., Rigopoulou, D., Hopwood, R., et al. 2014, *ApJ*, 796, 63
 Magrini, L., Stanghellini, L., Corbelli, E., Galli, D., & Villaver, E. 2010, *A&A*, 512, A63
 Maiolino, R., Carniani, S., Fontana, A., et al. 2015, *ArXiv e-prints*
 Malhotra, S., Helou, G., Stacey, G., et al. 1997, *ApJ*, 491, L27
 Malhotra, S., Kaufman, M. J., Hollenbach, D., et al. 2001, *ApJ*, 561, 766
 McKee, C. F., & Krumholz, M. R. 2010, *ApJ*, 709, 308

Mezger, P. G., Mathis, J. S., & Panagia, N. 1982, *A&A*, 105, 372
 Muñoz, J. A., & Furlanetto, S. R. 2014, *MNRAS*, 438, 2483
 Nagamine, K., Springel, V., Hernquist, L., & Machacek, M. 2004, *MNRAS*, 350, 385
 Nagamine, K., Wolfe, A. M., & Hernquist, L. 2006, *ApJ*, 647, 60
 Narayanan, D., Cox, T. J., Shirley, Y., et al. 2008a, *ApJ*, 684, 996
 Narayanan, D., & Hopkins, P. 2012, *ArXiv e-prints*
 Narayanan, D., Krumholz, M. R., Ostriker, E. C., & Hernquist, L. 2012, *MNRAS*, 421, 3127
 Narayanan, D., Cox, T. J., Kelly, B., et al. 2008b, *ApJS*, 176, 331
 Narayanan, D., Turk, M., Feldmann, R., et al. 2015, *Nature*, 525, 496
 Oey, M. S., & Clarke, C. J. 1997, *MNRAS*, 289, 570
 Olsen, K. P., Greve, T. R., Narayanan, D., et al. 2015, *ApJ*, 814, 76
 Oppenheimer, B. D., & Davé, R. 2008, *MNRAS*, 387, 577
 Ota, K., Walter, F., Ohta, K., et al. 2014, *ApJ*, 792, 34
 Ouchi, M., Ellis, R., Ono, Y., et al. 2013, *ApJ*, 778, 102
 Papadopoulos, P. P., Zhang, Z.-Y., Xilouris, E. M., et al. 2014, *ApJ*, 788, 153
 Pelupessy, F. I., & Papadopoulos, P. P. 2009, *ApJ*, 707, 954
 Pelupessy, F. I., Papadopoulos, P. P., & van der Werf, P. 2006, *ApJ*, 645, 1024
 Pineda, J. L., Langer, W. D., & Goldsmith, P. F. 2014, *A&A*, 570, A121
 Pineda, J. L., Langer, W. D., Velusamy, T., & Goldsmith, P. F. 2013, *A&A*, 554, A103
 Planck Collaboration, Ade, P. A. R., Aghanim, N., et al. 2014, *A&A*, 571, A16
 Pon, A., Johnstone, D., & Kaufman, M. J. 2012, *ApJ*, 748, 25
 Pon, A., Johnstone, D., Kaufman, M. J., Caselli, P., & Plume, R. 2014, *MNRAS*, 445, 1508
 Popping, G., Pérez-Beaupuits, J. P., Spaans, M., Trager, S. C., & Somerville, R. S. 2014a, *MNRAS*, 444, 1301
 —. 2014b, *MNRAS*, 444, 1301
 Popping, G., Somerville, R. S., & Trager, S. C. 2014c, *MNRAS*, 442, 2398
 Rhoads, J. E., Malhotra, S., Allam, S., et al. 2014, *ApJ*, 787, 8
 Robertson, B. E., & Kravtsov, A. V. 2008, *ApJ*, 680, 1083
 Robitaille, T. P. 2011, *A&A*, 536, A79
 Röllig, M., Ossenkopf, V., Jeyakumar, S., Stutzki, J., & Sternberg, A. 2006, *A&A*, 451, 917
 Russell, R. W., Melnick, G., Gull, G. E., & Harwit, M. 1980, *ApJ*, 240, L99
 Saitoh, T. R., & Makino, J. 2009, *ApJ*, 697, L99
 —. 2013, *ApJ*, 768, 44
 Sanders, N. E., Caldwell, N., McDowell, J., & Harding, P. 2012, *ApJ*, 758, 133
 Sargsyan, L., Leboutteiller, V., Weedman, D., et al. 2012, *ApJ*, 755, 171
 Schaerer, D., Boone, F., Zamojski, M., et al. 2015, *A&A*, 574, A19
 Schaye, J., & Dalla Vecchia, C. 2008, *MNRAS*, 383, 1210
 Schmidt, M. 1959, *ApJ*, 129, 243
 Schöier, F. L., van der Tak, F. F. S., van Dishoeck, E. F., & Black, J. H. 2005, *A&A*, 432, 369
 Seon, K.-I., Edelstein, J., Korpela, E., et al. 2011, *ApJS*, 196, 15
 Speagle, J. S., Steinhardt, C. L., Capak, P. L., & Silverman, J. D. 2014, *ApJS*, 214, 15
 Spergel, D. N., Verde, L., Peiris, H. V., et al. 2003, *ApJS*, 148, 175
 Springel, V. 2005, *MNRAS*, 364, 1105
 Springel, V., & Hernquist, L. 2003, *MNRAS*, 339, 289
 Stacey, G. J., Geis, N., Genzel, R., et al. 1991, *ApJ*, 373, 423
 Stacey, G. J., Hailey-Dunsheath, S., Ferkinhoff, C., et al. 2010, *ApJ*, 724, 957
 Stacey, G. J., Smyers, S. D., Kurtz, N. T., & Harwit, M. 1983, *ApJ*, 268, L99

- Steinacker, J., Baes, M., & Gordon, K. D. 2013, *ARA&A*, 51, 63
- Swinbank, A. M., Papadopoulos, P. P., Cox, P., et al. 2011, *ApJ*, 742, 11
- Swinbank, A. M., Karim, A., Smail, I., et al. 2012, *MNRAS*, 427, 1066
- Thompson, R., Davé, R., Huang, S., & Katz, N. 2015, *ArXiv e-prints*
- Thompson, R., Nagamine, K., Jaacks, J., & Choi, J.-H. 2014, *ApJ*, 780, 145
- Tielens, A. G. G. M., & Hollenbach, D. 1985, *ApJ*, 291, 722
- Vallini, L., Gallerani, S., Ferrara, A., & Baek, S. 2013, *MNRAS*, 433, 1567
- Vallini, L., Gallerani, S., Ferrara, A., Pallottini, A., & Yue, B. 2015, *ApJ*, 813, 36
- Vázquez-Semadeni, E., Banerjee, R., Gómez, G. C., et al. 2011, *MNRAS*, 414, 2511
- Vázquez-Semadeni, E., Colín, P., Gómez, G. C., Ballesteros-Paredes, J., & Watson, A. W. 2010, *ApJ*, 715, 1302
- Venemans, B. P., McMahon, R. G., Walter, F., et al. 2012, *ApJ*, 751, L25
- Wagg, J., Carilli, C. L., Wilner, D. J., et al. 2010, *A&A*, 519, L1
- Walter, F., Riechers, D., Cox, P., et al. 2009, *Nature*, 457, 699
- Wang, R., Wagg, J., Carilli, C. L., et al. 2013, *ApJ*, 773, 44
- Watson, D., Christensen, L., Knudsen, K. K., et al. 2015, *Nature*, 519, 327
- Webber, W. R. 1998, *ApJ*, 506, 329
- Whitaker, K. E., Labbé, I., van Dokkum, P. G., et al. 2011, *ApJ*, 735, 86
- Wiersma, R. P. C., Schaye, J., Theuns, T., Dalla Vecchia, C., & Tornatore, L. 2009, *MNRAS*, 399, 574
- Willott, C. J., Omont, A., & Bergeron, J. 2013, *ApJ*, 770, 13

Part II

The AGN-galaxy co-evolution at $z \sim 2$

8

HOW TO DETECT AN AGN

A general concern when estimating the SFR by fitting the broadband SED of a galaxy with stellar population synthesis models, is the relative dominance of AGN versus star formation. The dominant contributor to the mid-infrared (MIR) light is from UV-light reprocessed by dust, but the UV light can be emitted by either young stars or an AGN. At $z \sim 2$ it is not clear, without the aid of high spatial and spectral resolution, what is causing the observed MIR emission from massive galaxies; is dust in the central regions being heated by AGN activity, is dust across a larger region of the galaxy being heated by star formation, or is a combination of the two scenarios taking place?

X-ray emission, on the other hand, does not suffer from strong dust obscuration. Observing in X-ray can thus lift the apparent degeneracy in interpreting the origin of the MIR light, and thereby help to give the true AGN fraction of a sample of galaxies. A galaxy dominated by AGN activity can be distinguished from a galaxy dominated by star formation by having a harder X-ray spectrum if the AGN is obscured by dust, or by simply having a very high X-ray luminosity, $L_{0.5-8\text{ keV}}$. The most heavily obscured ‘Compton-thick’ AGNs, with column densities $N_{\text{H}} > 10^{24} \text{ cm}^{-2}$, might be missed by X-ray selection, but can instead be identified via an excess of MIR emission over that expected from purely star-forming galaxies (e.g., Daddi et al., 2007; Treister et al., 2009).

The shape of the MIR spectrum can also reveal AGNs, as the intense nuclear emission re-emitted by dust leads to a power-law spectrum in the MIR. For this purpose, color cuts have been devised using the *Spitzer* data (e.g., Stern et al., 2005; Donley et al., 2012). While this technique has the capability of detecting even Compton-thick AGNs, otherwise missed in X-ray, it has a low efficiency for low- to moderate-luminosity AGNs and its robustness has yet to be verified at $z \gtrsim 2$ (Cardamone et al., 2008).

In a galaxy where star formation is dominant, the total hard band X-ray luminosity, $L_{2-10\text{ keV}}$, can be used to estimate the SFR (e.g., Grimm et al., 2003; Ranalli et al., 2003; Lehmer et al., 2010). An AGN will reveal itself if the X-ray SFR inferred this way is much larger than the SFR derived from other tracers such as $\text{H}\alpha$, UV, or MIR luminosity. Also, if star formation dominates the radiation output, the $L_x \rightarrow \text{SFR}$ conversion will give an upper limit on the SFR as has been obtained for sub-mm galaxies (Laird et al., 2010) and for massive, star-forming galaxies at $1.2 < z < 3.2$ (Kurczynski et al., 2012).

At redshifts around 2, high-ionization lines in the rest-frame UV can be used as AGN indicators, but X-ray observations remain a more efficient way of identifying AGNs (Lamareille, 2010).

8.1 DISSECTING THE X-RAY EMISSION FROM AN AGN

I will focus this section on X-ray emission generated by the accretion of matter onto a SMBH, as described in Section 1.3.1, since it is this characteristic that I use for detecting AGN in my study of the presence of AGN at high- z (Part II).

Fig. 8.1 shows the X-ray part of the SED of a type I AGN, together with individual contributions from its components, the nature of which is elaborated on below.

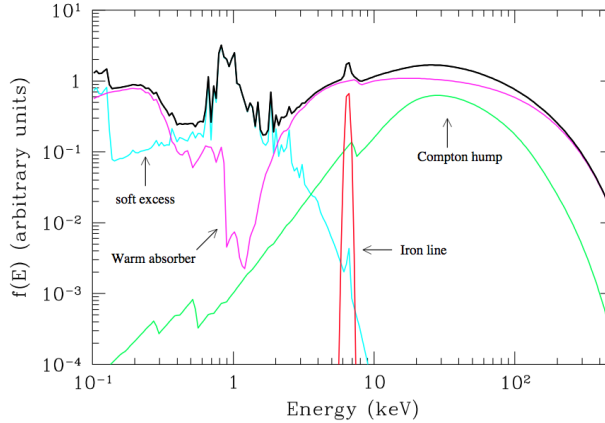


Figure 8.1 The X-ray spectrum (black) of a typical type I AGN, with curves showing the contribution from a primary continuum component (pink) resembling a power law but absorbed at soft energies by warm gas, a cold reflection component (green; Compton hump) and a soft excess (cyan). Also shown is iron $K\alpha$ emission – the most relevant narrow feature (red), arising in the inner parts of the accretion disk. Figure from the review by Risaliti & Elvis (2004).

At high X-ray energies (~ 30 keV), the SED is dominated by reflection component (‘Compton hump’) consisting of primary emission from the accretion disk being scattered by ionized gas, i.e. electrons. This component will be largest if the reflector is Compton-thick but smaller in the Compton-thin case in which case some of the incident radiation escapes without interaction (Risaliti & Elvis, 2004). An additional hard component is sometimes present, most likely caused by inverse-Compton scattering of the radio-synchrotron photons off of electrons in the relativistic jet itself. At lower energies ($\lesssim 2$ keV) with an almost universal effective temperature of $\sim 0.1 - 0.2$ keV, a ‘soft excess’ is often observed but less understood. Models suggest that the strongest soft excesses are found in AGNs with low mass accretion rates Done et al. (2012), and typically atomic processes are invoked to explain the soft excess via either ionized reflection with light bending or the remaining part of a high-energy power law subject to ionized absorption (Vasudevan et al., 2014). But also comptonization models have been proposed, in which the soft excess consists of UV/soft-X-ray photons by a population of hot electrons Matt et al. (2014). The joint NuSTAR/XMM program as well as future X-ray missions such as ASTRO-H and ASTROSAT (to be launched this year) are likely to break the degeneracy between these models (see Section 1.5). Finally a warm, ionized absorber exists that reflects the incident continuum without changing its spectral shape.

To first order though, the intrinsic or ‘primary’ emission from the central engine is a power law extending from 1 to 100 keV, with the slope determined by the different components described. The slope of the power law can be used to determine the amount of obscuration in the AGN, as more obscuration will result in a steeper power law (harder). In order to estimate the column density of obscuring material, one has to take a guess at the spectral slope, Γ , of the

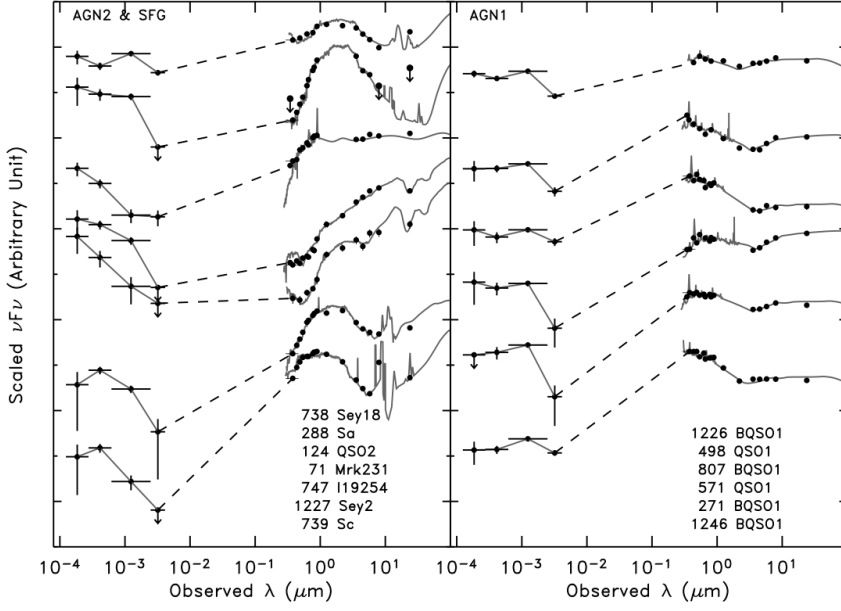


Figure 8.2 X-ray spectra of 13 galaxies from the work of Tajer et al. (2007). *Left*: Top two spectra are consistent with star-forming template SEDs shown, while the following 4 galaxies have type 2 AGN SEDs. *Right*: Type 1 AGN SEDs.

intrinsic emission from the obscured source:

$$dN/dE[\text{photons cm}^{-2} \text{ s}^{-1} \text{ keV}^{-1}] \propto E^{-\Gamma} \quad (8.1)$$

where dN is the number of photons with energy in the dE energy range. Note that a harder spectrum has *lower* Γ as shown in the left-hand plot of Fig. 8.3. A value of $\Gamma = 1.9$ is usually adopted, based on observations showing that Γ is roughly constant for large samples of low-luminosity Seyfert galaxies and bright QSOs for redshifts up to ~ 5 (e.g. Nandra & Pounds, 1994; Reeves & Turner, 2000; Piconcelli et al., 2005).

Fig. 8.2 shows 13 SEDs from X-ray to FIR ($100 \mu\text{m}$) of type I and type II AGN with best-fit galaxy templates. The X-ray part consists of data from XMM (see Section 1.5) sampled with 4 bands at 0.3-0.5, 0.5-2, 2-4.5, 4.5-10 and 2-10 keV.

The high angular resolution ($\sim 0.5''$) of *Chandra* combined with the high sensitivity in the deep fields CDF-N and CDF-S (see Section 1.4), makes these fields advantageous for searches of AGN at low and high redshift (Bauer et al., 2004; Xue et al., 2011; Treister et al., 2009; Alexander et al., 2011). For those studies, the observed X-ray spectra of *Chandra* are typically divided into a full (0.5 – 8 keV), a soft (0.5 – 2 keV) and a hard (2 – 8 keV) band. A proxy for the powerlaw slope is the ‘hardness ratio’, HR, defined as:

$$\text{HR} = (H - S)/(H + S) \quad (8.2)$$

where H and S are the counts in hard and soft band respectively. Hardness ratio has the advantage, in comparison to Γ , of avoiding any assumptions regarding the shape of the spectrum.

Assuming an intrinsic obscured power law with $\Gamma = 1.9$, HR converts into a column density that increases with the ‘hardness’ of the spectrum as shown in the right-hand plot of Fig. 8.3.

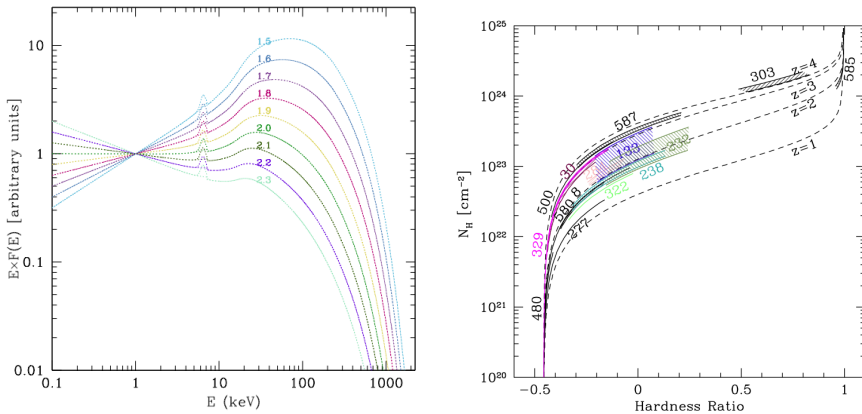


Figure 8.3 Measures of intrinsic power law slope in AGN. *Left:* SED templates for unobscured Seyferts normalized at 1 keV (Gilli et al., 2007). *Right:* Column density of obscuring material as a function of hardness ratio, HR (Treister et al., 2009).

The criteria for finding an AGN are a high full-band X-ray luminosity ($\gtrsim 2 \times 10^{42}$ ergs/s) of a hard spectrum with $HR > -0.2$ for sources of lower luminosity. These criteria are meant to rule out galaxies with SEDs consistent with star formation processes only. However, a third possible origin of a bright X-ray component in the area-integrated SED, is a hot gas halo embracing the galaxy (Mulchaey & Jeltima, 2010). Such a component can be ruled out, if the observed X-ray source is predominantly point-like, rather than extended.

8.1.1 THE AGN FRACTION AT $z \gtrsim 2$ FROM OBSERVATIONS IN X-RAY

Several studies of massive $z \sim 2$ galaxies have therefore been made with the aim of uncovering AGN fractions, using the *Chandra* X-ray observatory. Rubin et al. (2004) performed a study of 40 massive ($M_* = (1-5) \times 10^{11} M_\odot$) red ($J_s - K_s \geq 2.3$) galaxies at $z \gtrsim 2$ by analyzing a 91 ks *Chandra* exposure. Roughly 5% of these were found to host an AGN with intrinsic $L_{2-10 \text{ keV}} > 1.2 \times 10^{43} \text{ erg s}^{-1}$. Assuming that the stacked X-ray signal from the remaining X-ray undetected galaxies in X-ray comes from star formation alone, they derived a mean SFR broadly consistent with the typical mean SFRs estimated from SED fits. Alexander et al. (2011) analyzed the 4Ms *Chandra* observations of 222 $z \approx 2$ star-forming BzK galaxies ($M_* \sim 10^{10}-10^{11} M_\odot$, Daddi et al., 2007) in the Chandra Deep Field-South (CDF-S). 10%(23) showed X-ray emission consistent with AGN dominance, of which 5%(11) were found to contain heavily obscured AGNs, 4%(9) to have luminous, unobscured AGNs, and 3 out of 27 low-luminosity systems showed excess variability over that expected from star formation processes, indicating that at least some low-luminosity (rest-frame $L_{2-10 \text{ keV}} < 10^{43} \text{ erg s}^{-1}$) systems may contain AGNs.

ON THE PREVALENCE OF AGN AT $z \sim 2$ (PAPER III)

9.1 AIM OF THIS PROJECT

The aim of this project was to determine the AGN fraction in massive $z \sim 2$ galaxies, and reveal any differences between quiescent and star-forming galaxies.

9.2 OUR METHOD AND GALAXY SAMPLE

We addressed the matter by analyzing the X-ray emission from a mass-complete ($M_* > 5 \times 10^{10} M_\odot$) sample of $1.5 \leq z \leq 2.5$ galaxies residing in the CDF-S. The CDF-S, observed for 4 Ms, is currently the deepest X-ray view of the universe and so provides the best opportunity to study high- z galaxies across a relatively large area (464.5 arcmin²).

We selected our galaxies from the FIREWORKS¹ catalog (Wuyts et al., 2008), which covers a field situated within the CDF-S and contains photometry in 17 bands from the U band to the MIR. For this study we extracted a mass-complete sample of $M_* > 5 \times 10^{10} M_\odot$ galaxies at $1.5 \leq z \leq 2.5$ in a way similar to that of Franx et al. (2008) and Toft et al. (2009). We used spectroscopic redshifts when available (Vanzella et al., 2008; Xue et al., 2011), and photometric redshifts from the FIREWORKS catalog otherwise. In order to maximize the signal-to-noise (S/N) on results from X-ray stacking (Zheng et al., 2012) and ensure a relatively homogeneous PSF across the *Chandra* field employed, we considered only galaxies that lie within 6' of the average *Chandra* aimpoint.

We adopted galaxy stellar masses from the SED fitting results of Franx et al. (2008) and Toft et al. (2009). In short, the SED fits were carried out with models by Bruzual & Charlot (2003), choosing the best fit from adopting three different star formation histories (a single stellar population with no dust, an exponentially declining star formation history of timescale 300 Myr with dust, and a constant star formation history with dust). In cases where the spectroscopic redshift differed by more than 0.1 from the original FIREWORKS photometric redshift, we re-did the SED fits in FAST² using an exponentially declining star formation history with a range of possible timescales from 10 Myr to ~ 1 Gyr. As a quality parameter of the SED modeling, we demanded an upper limit on the reduced χ^2_ν of 10 on the best-fit model. The SED fits pro-

¹<http://www.strw.leidenuniv.nl/fireworks/>

²<http://astro.berkeley.edu/~mariska/FAST.html>

vide SFR estimates, but we used SFRs derived from rest-frame UV+IR luminosities (see Section 9.2.3) as these include obscured star formation and are subject to less assumptions. From the observed photometry, rest-frame fluxes in U , V , J band and at 2800 \AA have been derived using InterRest³ (Taylor et al., 2009).

We divided the resulting sample of 123 galaxies into quiescent and star-forming galaxies using the rest-frame U , V and J (falling roughly into the observed J , K and IRAC $4.5 \mu\text{m}$ bands at $z \sim 2$) colors. Dust-free but quiescent galaxies differ from dust-obscured starburst galaxies in that they obey the following criteria by Williams et al. (2009):

$$U - V > 1.3 \quad (9.1)$$

$$V - J < 1.6 \quad (9.2)$$

$$(U - V) > 0.88 \times (V - J) + 0.49 \quad (9.3)$$

The fraction of quiescent galaxies identified within our sample using this method is $22\% \pm 5\%$ (27/123). This is rather low compared to the 30–50% found by Toft et al. (2009) for the same redshift and mass limit, but under the requirement that the sSFR ($=\text{SFR}/M_*$) from SED fitting is less than 0.03 Gyr^{-1} . If applying this criterion, we would have arrived at a fraction of $42\% \pm 7\%$ (51/123). A possible reason for the discrepancy between the two methods may be that we were using the UVJ criterion in the limits of the redshift range in which it has so far been established. As the redshift approaches 2, the quiescent population moves to bluer $U - V$ colors, possibly crossing the boundaries of Equation (9.3). However, we preferred the UVJ selection technique in contrast to a cut in sSFR, because rest-frame colors are more robustly determined than star formation rates from SED fits.

9.2.1 X-RAY DATA AND STACKING ANALYSIS

The raw X-ray data from the CDF-S survey consist of 54 individual observations taken between 1999 October and 2010 July. We build our analysis on the work of Xue et al. (2011), who combined the observations and reprojected all images. They did so in observed full band (0.5–8 keV), soft band (0.5–2 keV) and hard band (2–8 keV), and the resulting images and exposure maps are publicly available.⁴

We extracted source and background count rates in the X-ray maps for all galaxies using the method of Cowie et al. (2012). Source counts were determined within a circular aperture of fixed radii: $0''.75$ and $1''.25$ at off-axis angles of $\theta \leq 3'$ and $\theta > 3'$ respectively. Background counts were estimated within an annulus $8''$ – $22''$ from the source, excluding nearby X-ray sources from the catalog of Xue et al. (2011).

Each galaxy was classified as ‘X-ray detected’ if detected in at least one band at $\geq 3\sigma$ significance, thereby creating 4 subsamples containing 8 quiescent and detected, 19 quiescent and undetected, 43 star-forming and detected, and 53 star-forming and undetected galaxies.

While the X-ray detected galaxies could be analyzed individually, we stacked the X-ray non-detected galaxies in order to constrain the typical X-ray flux from these. Stacked X-ray images of the 4 subsamples are shown in Figure 9.1 with all galaxies aligned to their K_s band galaxy center positions from FIREWORKS. Representative count rates and associated errors for these stacks were calculated using the optimally weighted mean procedure of Cowie et al.

³<http://www.strw.leidenuniv.nl/~ent/InterRest>

⁴<http://www2.astro.psu.edu/users/niel/cdfs/cdfs-chandra.html>

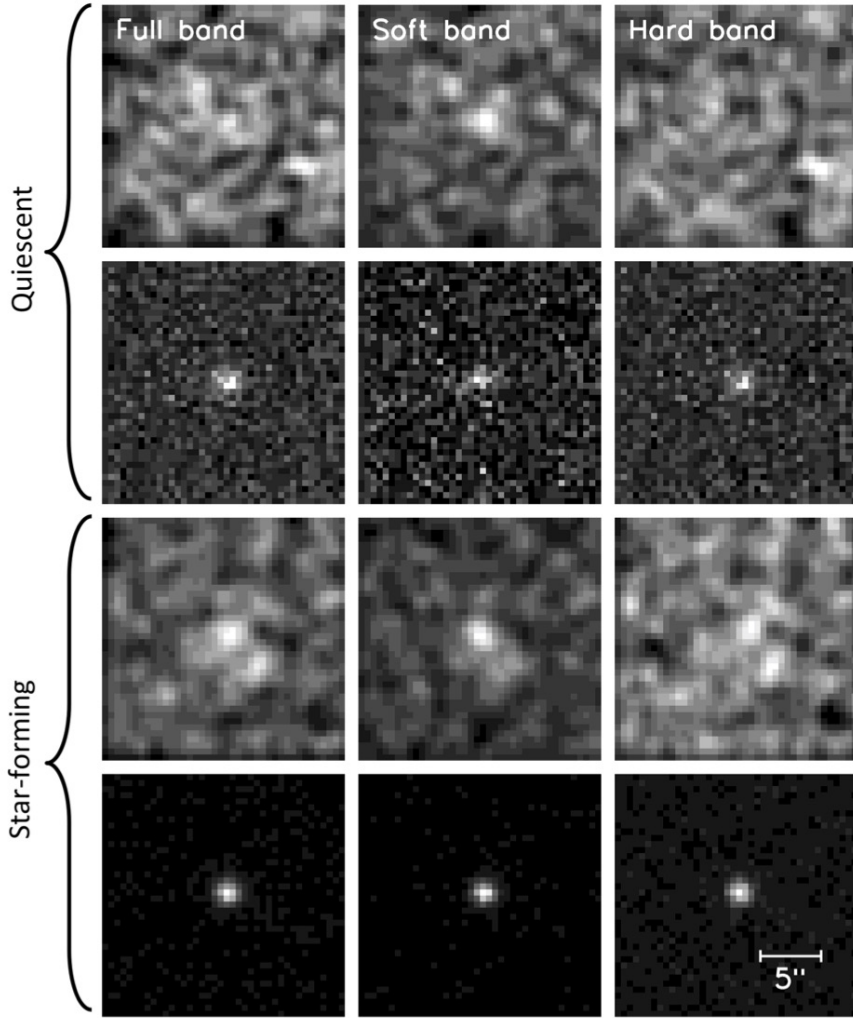


Figure 9.1 Stacked, background-subtracted and exposure-corrected $20'' \times 20''$ images in the three energy bands (columns) for the individually non-detected (top row) and detected (bottom row) quiescent and star-forming galaxies. Images of the non-detections have been smoothed with a Gaussian of width 2 pixels.

(2012) and tabulated in Table 9.1 together with S/N values.

	Count Rate $\pm 1\sigma$ (10^{-6} s^{-1}) in		
	Full Band	Soft Band	Hard Band
Q	0.71 ± 0.96 (0.7)	2.01 ± 0.41 (4.9)	-1.67 ± 0.86 (-1.9)
SF	2.51 ± 0.55 (4.5)	1.08 ± 0.24 (4.5)	1.29 ± 0.49 (2.7)

Table 9.1 Stacking results for Quiescent (Q) and Star-forming (SF) galaxies not detected individually in X-Rays (in Parentheses the corresponding S/N)

The reliability of our chosen method for X-ray stacking and source count extraction was

tested with Monte Carlo (MC) simulations. With 500 MC simulations of 53 (corresponding to the number of star-forming galaxies not detected in X-rays) randomly selected positions having no X-ray detections nearby, we obtained a histogram of stacked S/N values that is well fitted by a normal distribution with a center at -0.02 ± 0.8 , that is, consistent with no detection. Similar results were obtained using a sample size of 19, the number of quiescent non-detections.

$L_{0.5-8 \text{ keV}}$ (erg s^{-1})	HR	Classification
$> 3 \times 10^{42}$	< -0.2	Unobscured AGNs ($N_{\text{H}} < 10^{22} \text{ cm}^{-2}$)
$> 3 \times 10^{42}$	> -0.2 and < 0.8	Moderately obscured AGNs ($10^{22} < N_{\text{H}} < 10^{24} \text{ cm}^{-2}$)
$> 3 \times 10^{42}$	> 0.8	Compton-thick AGNs ($N_{\text{H}} > 10^{24} \text{ cm}^{-2}$)
$< 3 \times 10^{42}$	< -0.2	Star-forming galaxy
$< 3 \times 10^{42}$	> -0.2	Low-luminosity obscured AGNs or star-forming galaxy

Table 9.2 Classification scheme used in this work, with limits from Szokoly et al. (2004), Wang et al. (2004), and Treister et al. (2009)

We quantified the hardness of the X-ray spectra using the hardness ratio (see eq. 8.2). Assuming a power-law spectrum, we also derived a photon index, Γ , with the online mission count rate simulator WebPIMMS⁵ using a Galactic H I column density of $8.8 \times 10^{19} \text{ cm}^{-2}$ (Stark et al., 1992) and not including intrinsic absorption. Whenever the S/N in either soft or hard band was below 2, we used the corresponding 2σ upper limit on the count rate to calculate a limit on both HR and Γ , leading to a limit on the luminosity as well. When neither a hard- nor a soft-band flux was detected with an S/N above 2, a typical faint source value of $\Gamma = 1.4$ (Xue et al., 2011) was assumed, corresponding to $\text{HR} \sim -0.3$ for an intrinsic powerlaw spectrum of $\Gamma = 1.9$ (Wang et al., 2004).

We derived the unabsorbed flux from the count rate by again using the WebPIMMS tool, now with the Γ tied to the observed value of either the individually detected galaxy or the stack in question. With this method, a count rate of $\sim 10^{-5} \text{ counts s}^{-1}$ corresponds to a flux of nearly $10^{-16} \text{ erg cm}^{-2} \text{ s}^{-1}$ in full band at a typical value of $\Gamma = 0.8$. Finally, the flux was converted into luminosity in the desired rest-frame bands using XSPEC version 12.0.7 (Arnaud, 1996).

9.2.2 LUMINOUS AGN IDENTIFICATION

In the top panel of Figure 9.2 are shown the rest-frame X-ray full band luminosities, $L_{0.5-8 \text{ keV}}$, not corrected for intrinsic absorption, versus observed hardness ratio, HR, for all X-ray detected galaxies as well as stacked non-detections. A typical detection limit on $L_{0.5-8 \text{ keV}}$ has been indicated with a dotted line in Figure 9.2, calculated as two times the background noise averaged over all source positions. A few detected galaxies were found below this limit due to these residing at relatively low z and/or in regions of lower-than-average background. Galaxies with $L_{0.5-8 \text{ keV}} > 3 \times 10^{42} \text{ erg s}^{-1}$ were selected as luminous AGN, since star-forming galaxies are rarely found at these luminosities (Bauer et al., 2004). In addition, we adopted the HR criteria in Table 9.2 in order to identify obscured and unobscured AGNs.

About 53%(27/51) of the X-ray detected galaxies were identified as luminous AGNs, with 22 moderately to heavily obscured ($-0.2 < \text{HR} < 0.8$) and 5 unobscured ($\text{HR} < -0.2$) AGNs.

⁵<http://heasarc.nasa.gov/Tools/w3pimms.html>

The rest had X-ray emission consistent with either low-luminosity AGNs or star formation. We did not identify any Compton-thick AGNs directly, but three galaxies had lower limits on their hardness ratios just below $\text{HR} = 0.8$, thus potentially consistent with Compton-thick emission (see Table 9.2). In total, we detected a luminous AGN fraction of $22\% \pm 5\%$ (27/123), a fraction which is $23\% \pm 5\%$ (22/96) for the star-forming and $19\% \pm 9\%$ (5/27) for the quiescent galaxies.

Stacking the non-detections resulted in average X-ray source properties that exclude high luminosity AGNs. However, the inferred limits on their HR were consistent with a contribution from low-luminosity AGNs, the importance of which cannot be determined from this plot alone.

9.2.3 X-RAY INFERRED SFR

From the rest-frame hard band luminosity, $L_{2-10\text{ keV}}$ it is possible to derive estimates of the SFR, as the number of high-mass X-ray binaries (HMXBs) is proportional to the SFR (Ranalli et al., 2003). Kurczynski et al. (2012) made a comparison of different SFR indicators, by applying three different $L_x \rightarrow \text{SFR}$ conversions to 510 star-forming BzK galaxies at $1.2 < z < 3.2$, selected as having $L_{2-10\text{ keV}} < 10^{43} \text{ erg s}^{-1}$. While relations by Persic et al. (2004) and Lehmer et al. (2010) overestimated the true SFR (from rest-frame UV and IR light) by a factor of ~ 5 , the relation by Ranalli et al. (2003) provided a good agreement at $1.5 < z < 3.2$. But, as pointed out by Kurczynski et al. (2012), all relations might lead to an overestimation due to contamination by obscured AGNs in the sample of SF galaxies. As we did not know the exact amount of obscured AGN contamination in the stacks, we chose to use the following relation by Ranalli et al. (2003) as a conservative estimate of the SFR:

$$\text{SFR}_{2-10\text{ keV}} = 2.0 \times 10^{-40} L_{2-10\text{ keV}} \quad (9.4)$$

with SFR measured in $M_\odot \text{ yr}^{-1}$ and $L_{2-10\text{ keV}}$ in erg s^{-1} . Another reason for not using the more recent relation by Lehmer et al. (2010) is that this relation was constructed for galaxies with $\text{SFR} > 9 M_\odot \text{ yr}^{-1}$ only, whereas a large part of our sample had very low SFRs as inferred from SED fitting ($< 1 M_\odot \text{ yr}^{-1}$). Following Kurczynski et al. (2012), we used the observed soft band flux to probe the rest-frame hard band luminosity. The uncertainty on the SFR is estimated from the error on the observed soft-band flux together with a systematic error in the relation itself of 0.29 dex, as given by Ranalli et al. (2003).

For comparison, the ‘true’ SFR is inferred from rest-frame UV and IR light, $\text{SFR}_{\text{UV+IR}}$, following the method of Papovich et al. (2006):

$$\text{SFR}_{\text{UV+IR}} = 1.8 \times 10^{-10} (L_{\text{IR}} + 3.3 L_{2800}) / L_\odot \quad (9.5)$$

where L_{IR} is the total infrared luminosity and L_{2800} is the monochromatic luminosity at rest-frame 2800 Å. L_{2800} comes from the rest-frame UV flux, $f_{2800\text{ Å}}$, and in this context, the errors on $f_{2800\text{ Å}}$ are negligible. We derived L_{IR} from the observed 24 μm flux, $f_{24\mu\text{m}}$, using redshift-dependent multiplicative factors, $a(z)$, from the work of Wuyts et al. (2008), Section 8.2 in that paper):

$$L_{\text{IR}}[L_{\odot, 8-1000\mu\text{m}}] = 10^{a(z)} \cdot f_{24\mu\text{m}} \quad (9.6)$$

The errorbars on L_{IR} derive from the errors on $f_{24\mu\text{m}}$ and we further assume an uncertainty

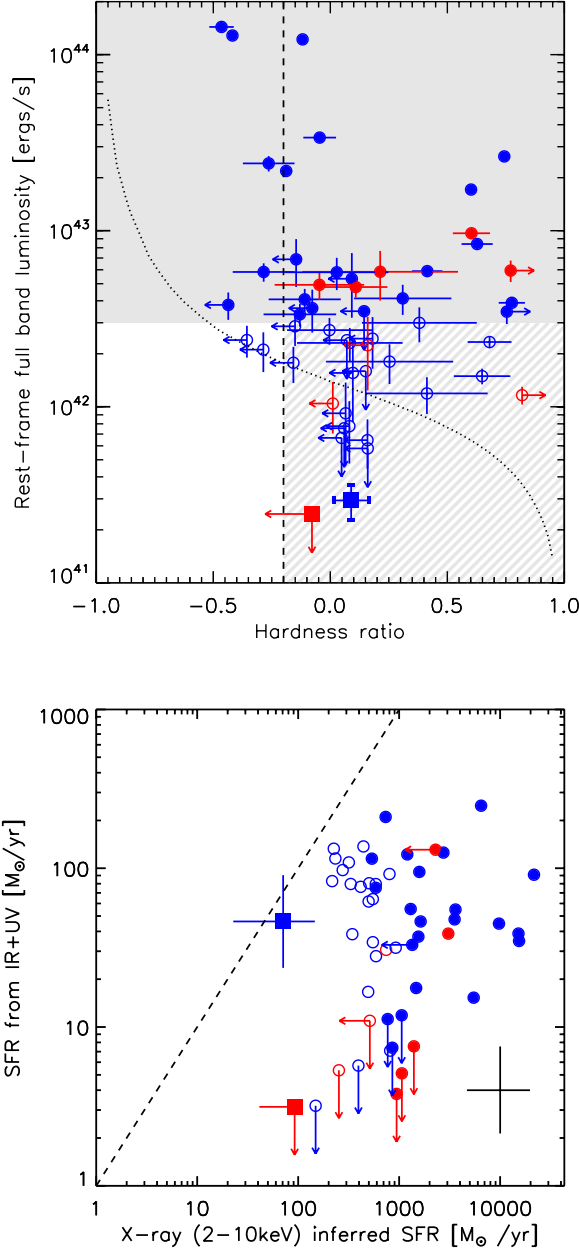


Figure 9.2 Top: $L_{0.5-8 \text{ keV}}$ vs. HR for all galaxies. Red: quiescent galaxies. Blue: star-forming galaxies. Squares: stacks of non-detected samples. Filled circles: luminous AGNs (selected with the X-ray criteria indicated by a shaded area). Open circles: galaxies dominated by low-luminosity AGNs or star formation processes alone (selected with X-ray criteria indicated by a hatched area). Dashed line: separating obscured ($N_{\text{H}} \gtrsim 10^{22} \text{ cm}^{-2}$) from unobscured AGNs. Dotted line: typical detection limit. Errorbars display 2σ errors and limits are indicated with arrows. Bottom: $\text{SFR}_{\text{UV+IR}}$ vs. $\text{SFR}_{2-10\text{keV}}$ (see the text). Dashed line: equality. Typical errors on X-ray detected galaxies are shown in the lower right corner. Symbols are as above.

of 0.3 dex in the relation of Papovich et al. (2006) as found by Bell (2003) when comparing to H α - and radio-derived SFRs. The X-ray undetected quiescent galaxies were not detected with $S/N > 3$ in 24 μm either (except in one case) leading to a mean flux of $1.2 \pm 1.7 \mu\text{Jy}$, of which we adopted a 2σ upper limit for the remaining analysis.

In the bottom panel of Figure 9.2, $\text{SFR}_{2-10 \text{ keV}}$ is compared to $\text{SFR}_{\text{UV+IR}}$ with the dashed line indicating equality. It is no surprise that nearly all of the individual X-ray detections have very high $\text{SFR}_{2-10 \text{ keV}}$ as compared to $\text{SFR}_{\text{UV+IR}}$, as we were largely insensitive to individual purely star-forming galaxies, given the detection limits in the top panel of Figure 9.2 and the criteria in Table 9.2.

For the star-forming stack, the X-ray inferred SFR of $71 \pm 51 M_{\odot} \text{ yr}^{-1}$ is consistent with the IR+UV inferred SFR of $46 \pm 33 M_{\odot} \text{ yr}^{-1}$, whereas the quiescent stack shows an $\text{SFR}_{2-10 \text{ keV}}$ of $92 \pm 65 M_{\odot} \text{ yr}^{-1}$ ($89 \pm 17 M_{\odot} \text{ yr}^{-1}$ when bootstrapping this sample 200 times), well exceeding $\text{SFR}_{\text{UV+IR}} \leq 3 M_{\odot} \text{ yr}^{-1}$.

9.3 AN OVERWHELMINGLY LARGE AGN POPULATION

9.3.1 LUMINOUS AGN FRACTION

In total, 22 X-ray detected galaxies have emission consistent with containing a luminous (rest-frame $L_{0.5-8 \text{ keV}} > 3 \times 10^{42} \text{ erg s}^{-1}$) and obscured ($10^{22} < N_{\text{H}} < 10^{24} \text{ cm}^{-2}$) AGN, and a further five have emission consistent with a luminous unobscured ($N_{\text{H}} < 10^{22} \text{ cm}^{-2}$) AGN. This leads to a luminous AGN fraction of the full sample of $22\% \pm 5\%$ (27/123) and of the detected galaxies only, $53\% \pm 13\%$ (27/51). The AGN fraction among both quiescent and star-forming galaxies, according to their X-ray spectra, is measured to be around 20% as Table 9.3 shows, meaning that AGNs in massive $z \sim 2$ galaxies, even quiescent ones, are common, as proposed by Kriek et al. (2009) who studied the near-IR spectrum of one quiescent galaxy.

	Quiescent (27)	Star-forming (96)
Luminous AGNs	5	22
Low-luminosity AGNs	2 (det) 12–19 (non-det)	19 (det) 0–21 (non-det)
Luminous AGN fraction	$19\% \pm 9\%$	$23\% \pm 5\%$
Total AGN fraction	70%–100%	43%–65%

Table 9.3 X-Ray derived AGN Numbers and Fractions for Quiescent and Star-forming Galaxies, Divided into Luminous AGNs and Detected and Non-detected Low-luminosity AGNs

This luminous AGN fraction is high when compared to the 5% found by Rubin et al. (2004) (see the introduction), but this is likely a consequence of their 4σ detection limit of $1.2 \times 10^{43} \text{ erg s}^{-1}$ in rest-frame 2–10 keV being about twice as high as our limit of $5.5 \times 10^{42} \text{ erg s}^{-1}$ (at $\Gamma = 1.4$), as calculated from the average background noise in the observed soft band. Adopting the detection limit of Rubin et al. (2004) and requiring an S/N of at least 4, we reduce our fraction of luminous AGN to $8\% \pm 3\%$ (10/123), consistent with the results of Rubin et al. (2004). Alexander et al. (2011), using also the 4 Ms CDF-S data, found a much lower X-ray detection fraction of $21\% \pm 3\%$ as compared to ours ($53\% \pm 7\%$), and a luminous AGN fraction of only $9\% \pm 2\%$ (20/222). We believe that the discrepancies have several reasons, the main ones being: (1) our use of a mass-complete sample, whereas the BzK selection technique used by Alexander et al. (2011) includes galaxies down to $M_{*} \sim 10^{10} M_{\odot}$ for which the total AGN fraction,

assuming a fixed Eddington ratio, is expected to be lower above our detection limit,⁶ (2) our updated source count extraction and stacking method leading to higher S/N, and (3) the use of Γ instead of HR in the AGN identification conducted by Alexander et al. (2011). For comparison, Tanaka et al. (2012) recently discovered a group of quiescent galaxies at $z = 1.6$ with only one main-sequence star-forming galaxy. This group differed from local groups in having a remarkably high AGN fraction of $38^{+23}_{-20}\%$, consistent with our result, and which they interpret as possible evidence for AGN activity quenching star formation.

9.3.2 IMPORTANCE OF LOW-LUMINOSITY AGNs

As seen in Figure 9.2, the X-ray-identified luminous AGNs in general show an excess in SFR compared to that inferred from IR+UV emission. Among the galaxies classified as being dominated by either low-luminosity AGN or star formation, about $\sim 90\%$ (21/24) have $\text{SFR}_{2-10\text{ keV}}$ more than 1σ above $\text{SFR}_{\text{UV+IR}}$.

Surprisingly, the quiescent stack also has a much larger $\text{SFR}_{2-10\text{ keV}}$ than $\text{SFR}_{\text{IR+UV}}$. Even when removing the marginally undetected galaxies with $2 < \text{S/N} < 3$, the resulting $\text{SFR}_{2-10\text{ keV}} = 62 \pm 19 M_{\odot} \text{ yr}^{-1}$ is still more than 3σ above $\text{SFR}_{\text{IR+UV}}$. This discrepancy is only further aggravated if instead assuming the $\text{SFR}-L_X$ relation of Lehmer et al. (2010). If caused by obscured star formation, we would have expected an average $24\text{ }\mu\text{m}$ flux of $90\text{ }\mu\text{Jy}$ for the individual galaxies, in order to match the lower limit on $\text{SFR}_{2-10\text{ keV}}$. This is far above the upper limit of $3.4\text{ }\mu\text{Jy}$ for the stack, suggesting that the X-ray flux of this stack is instead dominated by low-luminosity AGNs, but that their contribution to the $24\text{ }\mu\text{m}$ flux remains undetectable in the *Spitzer*–MIPS data.

We derived a lower limit on the low-luminosity AGN contribution for this stack of 19 objects by constructing a mock sample of the same size and with the same redshifts, but containing N low-luminosity AGNs with luminosities $L_{0.5-8\text{ keV}} = 10^{42} \text{ erg s}^{-1}$ just below the detection limit and $19 - N$ galaxies with $L_{0.5-8\text{ keV}} = 10^{41} \text{ erg s}^{-1}$ (all of them with $\Gamma = 1.4$). From random realizations of this mock sample we found that at least $N = 12$ low-luminosity AGNs are required to match the observed rest-frame 2–10 keV luminosity of the stack. Similarly, we found that by removing at least 12 randomly selected galaxies it is possible to match the low SFR predicted by IR+UV emission, though only with a small probability ($\sim 1\%$ of 200 bootstrappings). We therefore adopted 63% ($= 12/19$) as a conservative lower limit on the low-luminosity AGN fraction among quiescent X-ray non-detections, but we note that the data were consistent with all the quiescent galaxies hosting low-luminosity AGNs if the luminosity of these was assumed to be only $L_{0.5-8\text{ keV}} = 7 \times 10^{41} \text{ erg s}^{-1}$.

Interestingly, the quiescent stack was only detected in the soft band, cf. Table 9.1, whereas one might expect a significant contribution to the hard band flux from a low-luminosity AGN population as the one proposed above. The lack of a hard band detection can be explained by the fact that the sensitivity of the CDF-S observations drops about a factor of six from the soft to the hard band (Xue et al., 2011), meaning that the low-luminosity AGN population must be relatively unobscured ($\Gamma > 1$, consistent with the value of 1.4 assumed here), as it would otherwise have been detected in the hard band with an $\text{S/N} > 2$.

The $\text{SFR}_{2-10\text{ keV}}$ of the star-forming stack was consistent with its $\text{SFR}_{\text{UV+IR}}$, meaning that a strict lower limit to the low-luminosity AGN fraction here, is zero. However, performing the

⁶For a fixed Eddington ratio, and assuming that galaxy bulge mass increases with total stellar mass, the AGN X-ray luminosity is expected to scale with galaxy stellar mass according to the $M_{\text{bh}}-M_{\text{bulge}}$ relation (Håring & Rix, 2004)

test above with the same model parameters, a maximum of 40%(21/53) low-luminosity AGNs is possible, before the X-ray inferred SFR exceeds the upper limit on $\text{SFR}_{\text{UV+IR}}$.

It should be mentioned that the $24\ \mu\text{m}$ flux, especially at these high redshifts, is an uncertain estimator of the total rest-frame infrared luminosity, i.e., the entire dust peak, used in the conversion to SFR. As shown by Bell (2003), one should ideally use the entire 8–1000 μm range, e.g., by taking advantage of Herschel data, which can lead to systematic downward correction factors up to ~ 2.5 for galaxies with $L_{\text{IR}} \approx 10^{11} L_{\odot}$ (similar to the inferred IR luminosities of our sample galaxies detected in $24\ \mu\text{m}$, showing a median of $L_{\text{IR}} = 10^{11.5} L_{\odot}$) as demonstrated by Elbaz et al. (2010). However, using the same conversion from $f_{24\mu\text{m}}$ to L_{IR} as the one implemented in this study, Wuyts et al. (2011) showed that the resulting L_{IR} for galaxies out to $z \sim 3$ are consistent with those derived from PACS photometry with a scatter of 0.25 dex. Hence, we do not expect the inclusion of Herschel photometry in this study to significantly impact any of our results, and we leave any such analysis for future work.

Table 9.3 gives an overview of the derived AGN fractions, both at high and low X-ray luminosity. Adding the numbers of luminous AGN, X-ray-detected low-luminosity AGNs as well as the estimated lower limit on the low-luminosity AGN fraction among non-detections, we arrive at a lower limit on the total AGN fraction of

$$f_{\text{AGN}} \geq \frac{27 + 21 + 0.6 \cdot 19 + 0 \cdot 53}{123} = 0.48 \quad (9.7)$$

for all massive galaxies at $z \sim 2$. While for the star-forming galaxies this fraction lies in the range from 43%–65%, it must be 70%, and potentially 100%, for the quiescent galaxies. Using the upper limits on these numbers, a tentative upper limit on the total AGN fraction is 0.72.

9.3.3 CONTRIBUTION FROM HOT GAS HALOS

We have so far considered star formation and AGN activity as causes of the X-ray emission observed, but a third possibility is an extended hot gas halo as seen around many nearby early-type galaxies in the same mass-range as our sample galaxies (Mulchaey & Jeltema, 2010) and predicted/observed around similar spirals (Toft et al., 2002; Rasmussen et al., 2009; Anderson & Bregman, 2011; Dai et al., 2012). AGN X-ray emission is expected to come from a very small, $R < 1\ \text{pc}$, accretion disk surrounding the central black hole of the host galaxy (Lobanov & Zensus, 2007), whereas very extended star formation in the galaxy or a hot gas halo surrounding it would lead to more extended emission. We investigated the possibilities for these latter cases by comparing radial surface brightness profiles of the 51 individually X-ray detected galaxies out to a radius of $8''$ in both the stacked observed image and a correspondingly stacked PSF image.

The profiles were calculated in full band only, because of the high S/N here as compared to the other bands (cf. Figure 9.1). For each galaxy, we extracted the background subtracted source count per pixel within 10 concentric rings of width $0''.8$ around the galaxy center positions from the FIREWORKS catalog, and each profile was normalized to the mean count rate in all rings. The same procedure was applied to the corresponding PSF images, extracted with the library and tools that come with CIAO,⁷ allowing for extraction at the exact source positions on the detector. We verified the robustness of using PSF models from the CIAO calibration database

⁷<http://cxc.cfa.harvard.edu/ciao4.3/ahelp/mkpsf.html>

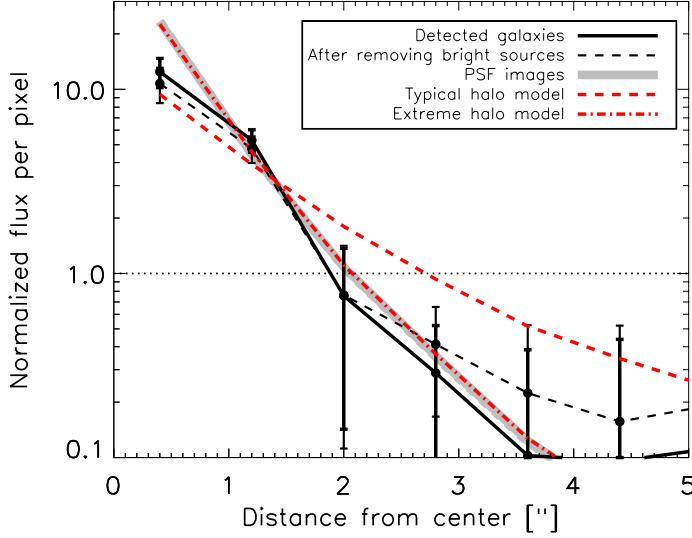


Figure 9.3 Comparison of the radial surface brightness profiles in PSF images vs. observed images in full band for all detected galaxies. Black: stacked observed image centered on K -band positions from FIREWORKS for all detected galaxies (solid line) and if excluding the three X-ray brightest sources (dashed line). Grey line: stacked PSF image. Red: stack of halo model images, with $\beta = 0.5$, $R_c = 2.5$ kpc (dashed) and $\beta = 1$, $R_c = 1$ kpc (dot-dashed).

for this purpose, by repeating the above procedure for 51 known X-ray bright point-like sources from the catalog of Xue et al. (2011), and confirming that the resulting mean profile was fully consistent with that of the corresponding model PSFs.

As can be observed in Figure 9.3, the combined radial profile of our X-ray detected galaxies in the full band is consistent with the PSF of point sources stacked at the same detector locations. A Kolmogorov-Smirnov (K-S) test yields a statistic of 0.2 and a probability of 99.96% that the two profiles are drawn from the same parent sample.

Omitting the three sources with $L_{0.5-8\text{ keV}} > 10^{44} \text{ erg s}^{-1}$ (cf. Figure 9.2) leads to a more extended profile (dashed black line in Figure 9.3), but the result still shows a high corresponding K-S probability of 70%. We also compared the profiles while recentering the images on the center of the X-ray emission as derived using WAVDETECT⁸ instead of the K -band center positions listed in the FIREWORKS catalog, in order to test for the impact of any off-set between the X-ray and optical centroids. However, the recentering only resulted in small variations within the errorbars on the original profile. The same conclusions applied to the subsample of X-ray detected star-forming galaxies only, whereas the S/N was too low to perform a similar study on the quiescent, X-ray detected sample alone.

For comparison, we also simulated the stacked profile of extended hot gas halos, using for the surface brightness profile the β -model first introduced by Cavaliere & Fusco-Femiano (1976). With default parameters of $\beta = 0.5$ and core radius $R_c = 2.5$ kpc, both taken from the study of $z \lesssim 0.05$ early-type galaxies by O’Sullivan et al. (2003), the stacked profile of the halos, convolved with the corresponding PSFs, is well outside the errorbars of the measured profile. Only if assuming an extremely compact case of $\beta = 1$ and $R_c = 1$ kpc, does the halo

⁸WAVDETECT is part of the CIAO software.

emission become sufficiently compact to mimic that of the PSF profile (see dash-dotted line in Figure 9.3), but the halo model then overpredicts the observed surface brightness on scales smaller than $1''$. In conclusion, a hot gas halo alone, described by a β -model, cannot explain the emission, unless one chooses model parameters that render the profile indistinguishable from a point-like source.

9.3.4 QUENCHING OF STAR FORMATION BY AGNs?

It remains debated whether the presence of AGN is connected with internal galaxy properties associated with secular evolution or, to a higher degree, with external processes (Darg et al., 2010). For example, the cosmic star formation rate density and the number density of AGN share a common growth history with a peak in activity around $z \sim 2-3$ (Treister & Urry, 2012; Dunlop, 2011), hinting at a co-evolution between SFR and supermassive black hole (SMBH) accretion (Schawinski, 2011). We investigated the correlation, if any, between the presence of AGNs and internal/external processes, treating luminous and low-luminosity AGNs separately. As typical internal properties governing secular evolution we focused on stellar mass, M_* , and SFR (Peng et al., 2010), while major mergers were taken as a likely case of external processes and as a phenomenon often associated with luminous AGNs (Treister et al., 2012).

Starting with our X-ray identified luminous AGNs, we found that the fraction of these does not correlate with star formation in our sample (cf. Table 9.3). In addition, the distribution of luminous AGNs and that of the rest with regards to their $\text{SFR}_{\text{IR+UV}}$ are similar, with a K-S test yielding a statistic of 0.21 with a probability of 59%. Similarly, Harrison et al. (2012) found no correlation between AGN luminosity and quenching of star formation, albeit at a higher luminosity ($L_{2-8\text{ keV}} > 10^{44} \text{ erg s}^{-1}$) than probed here. Dividing the sample according to M_* instead, by constructing two bins around the median mass of $1.1 \times 10^{11} M_\odot$, we arrived at similar luminous AGN fractions above and below this mass limit, namely $21\% \pm 7\% (13/61)$ and $23\% \pm 7\% (14/62)$, respectively. We thus find no clear evidence for the luminous AGN fraction of our sample to correlate with internal properties, suggesting that an external factor is of larger importance.

An alternative is that luminous AGNs are primarily triggered by non-secular processes such as major mergers. Treister et al. (2012) found that major mergers are the only processes capable of triggering luminous ($L_{\text{bol}} \gtrsim 10^{45} \text{ erg s}^{-1}$) AGN at $0 < z < 3$. Our luminous AGN fraction is consistent with the major merger fraction of massive ($M_* > 10^{11} M_\odot$) galaxies at $1.7 < z < 3$ found by Man et al. (2012) to be $15\% \pm 8\%$ (compared to a luminous AGN fraction of $11 \pm 3\% (13/123)$ when excluding galaxies with $M_* < 10^{11} M_\odot$). This is consistent with the idea that our luminous AGNs are triggered by major mergers, but a more direct test of this scenario would be to search for major mergers using the imaging data available in CDF-S. Indeed, Newman et al. (2012) used *HST* CANDELS imaging in the GOODS-South field residing within CDF-S (along with the UKIRT Ultra Deep Survey) to arrive at roughly equal pair fractions when comparing massive ($M_* > 10^{10.7} M_\odot$) quiescent to massive star-forming galaxies at $0.4 < z < 2$. Again, this is in agreement with our result that the luminous AGN fraction does not vary between quiescent and star-forming galaxies. A detailed morphological study of our X-ray identified luminous AGN using the *HST*/WFC3 data to search for evidence of merging is an interesting extension to the work presented here, which we leave for a future study.

Turning toward our low-luminosity AGNs, we *do* see X-ray evidence for an enhanced population among the quiescent galaxies when compared to their star-forming equivalents. The

mean masses of our non-detected samples of quiescent and star-forming galaxies are similar (14.6 ± 1.6 and $12.7 \pm 1.0 \times 10^{10} M_{\odot}$ respectively), suggesting that the relevant factor here is SFR. At $0.01 < z < 0.07$, Schawinski et al. (2009) found that massive ($M_{*} \gtrsim 10^{10} M_{\odot}$) host galaxies of low-luminosity AGNs all lie in the green valley, that is, at some intermediate state after star formation quenching has taken place and before the SED is truly dominated by old stellar populations. The observation that these host galaxies had been quiescent for ~ 100 Myr, ruled out the possibility that one short-lived, luminous AGN suppressed star formation and, at the same time, made it unlikely that the same AGN quenching star formation was still active, given current AGN lifetime estimates of $\sim 10^7$ – 10^8 yr (Di Matteo et al., 2005). Rather, the authors favored a scenario in which a low-luminosity AGN already shut down star formation, followed by a rise in luminosity, making the AGN detectable. At $z \sim 2$, SED fits of massive ($M_{*} > 10^{11} M_{\odot}$) quiescent galaxies show that the quenching typically took place ~ 1 Gyr before the time of observation (Toft et al., 2012; Krogager, J.-K. et al., in preparation), demanding an even longer delay *or* an episodic AGN activity as frequently applied in models (Croton et al., 2006). Episodic AGN activity could explain why we see evidence for a higher low-luminosity AGN fraction among quiescent as compared to star-forming galaxies, but it would also require the low-luminosity AGN phase in quiescent galaxies to last at least as long as the dormant phase. Future modeling and observations will show whether this is in fact possible.

We conclude that our data are consistent with a scenario in which luminous AGNs in massive galaxies at $z \sim 2$ are connected with major mergers or other non-secular processes, while the presence of low-luminosity AGNs in the majority of quiescent galaxies suggests that these AGNs present an important mechanism for quenching star formation and keeping it at a low level. Ultimately what happens at $z \sim 2$ has to agree with the subsequent evolution that changes size and morphology of quiescent galaxies (Barro et al., 2013).

9.4 CONCLUSIONS

Our main conclusions are on the following two topics:

1. *Luminous AGN fraction*

We find a luminous AGN fraction of $22\% \pm 5\%$ among massive ($M_{*} > 5 \times 10^{10} M_{\odot}$) galaxies at redshifts $1.5 \leq z \leq 2.5$, using their X-ray properties extracted from the 4 Ms Chandra Deep Field South observations. Among the X-ray detected galaxies, $53\% \pm 13\%$ harbor high-luminosity AGNs, while stacking the galaxies not detected in X-ray, leads to mean detections consistent with low-luminosity AGNs or pure star formation processes. The luminous AGN fraction among quiescent and star-forming galaxies is similar ($19\% \pm 9\%$ and $23\% \pm 5\%$, respectively) and does not depend on galaxy M_{*} .

We confirmed that extended X-ray emission from a hot gaseous halo is not a viable explanation for the observed X-ray emission of the X-ray detected galaxies.

2. *Limits on total AGN fraction*

We convert the rest-frame hard band X-ray luminosity into an upper limit on the star formation rate, $\text{SFR}_{2-10 \text{ keV}}$ and compare to that derived from the rest-frame IR+UV emission, $\text{SFR}_{\text{IR+UV}}$. All luminous AGNs show an excess in $\text{SFR}_{2-10 \text{ keV}}$ as expected, and so does a large fraction ($\sim 90\%$) of the remaining detected galaxies. While the star-forming galaxies not detected in X-ray have a mean X-ray inferred SFR of $71 \pm 51 M_{\odot} \text{ yr}^{-1}$, consistent with their $\text{SFR}_{\text{IR+UV}}$, the stack of quiescent galaxies shows an excess in $\text{SFR}_{2-10 \text{ keV}}$ of

a factor > 10 above the upper limit on $\text{SFR}_{\text{IR+UV}}$. For these galaxies, we find that a minimum fraction of $\sim 60\%$ must contain low-luminosity ($L_{0.5-8\text{ keV}} \approx 10^{42} \text{ erg s}^{-1}$) AGNs if the SFR estimates from X-ray are to be explained, and that low-luminosity AGNs might be present in all of them. On the other hand, for the star-forming stack, we derive a low-luminosity AGN fraction of 0–40%.

Gathering all low- and high-luminosity AGNs, we derive a lower limit to the total AGN fraction of 48%, with a tentative upper limit of 72%.

Our study was the first to present observational evidence that, at $z \sim 2$, the majority of quiescent galaxies host a low- to a high-luminosity AGN, while the AGN fraction is significantly lower in star-forming galaxies. These findings are consistent with an evolutionary scenario in which low-luminosity AGN quench star formation via the energetic output from SMBH accretion, which, if believed to continue in an episodic fashion as often invoked by models, would need to have ‘dormant’ phases at least as long as ‘active’ phases.

We find that the high-luminosity AGNs are likely related to non-secular processes such as major mergers. In the future, examining the X-ray properties of galaxies in a larger sample, cross-correlated with signs of major mergers, may shed further light on the co-evolution of AGNs and host galaxy.

10

OUTLOOK

Since we published these results in 2013, many additional observational studies have been carried out with the aim of shedding light on AGN-galaxy co-evolution at $z \sim 2$. A short summary is provided here together with future directions in this field.

10.1 THE AGN-MORPHOLOGY CONNECTION

First of all, we found no clear evidence for a correlation between the presence of a luminous AGN and the internal properties of massive galaxies at $z \sim 2$. This was interpreted as an argument for the need of external factors triggering the luminous AGN phase rather than events associated with secular evolution. However, we only considered stellar mass and SFR, whereas more recent observations have established a clear correlation between the presence (and strength) of AGN and the morphology of its host galaxy.

In this regard, Barro et al. (2013) analysed the morphologies and SFRs of $M_* > 10^{10} M_\odot$ galaxies at $z = 1.4 - 3$ in the GOODS-S and CANDELS UDS fields, for comparison with AGN activity as a function of redshift. Barro et al. (2013) found a population of compact star-forming galaxies (cSFGs; defined as having $\log(M_*/r_e^{1.5})$ below $10.3 M_\odot \text{ kpc}^{-1.5}$) at $z = 2.6 - 3.0$ that disappears before the compact quiescent galaxies (CQGs) of similar structural properties appear at lower redshifts. At the same time, the AGN fraction among cSFGs is higher at $z > 2$ than at lower redshifts and X-ray luminous ($L_{2-8 \text{ keV}} > 10^{43} \text{ erg s}^{-1}$) AGNs are found $\sim 30\%$ more frequently in cSFGs than in non-compact ones at $z > 2$. This was interpreted as a sign that at least some cSFGs evolve directly into the CQGs observed at $z \sim 2$ via the evolutionary path described in Section 2.1.5, whereas non-compact quiescent galaxies, formed later on, are the result of normal SFGs that are quenched by other mechanisms which partially preserve the structural properties.

Deriving the total IR luminosity directly from the $24 \mu\text{m}$ flux only, is a rough approximation that could possibly affect our results and those of Barro et al. (2013), as the possible contribution from an AGN to the FIR luminosity can lead to overestimates of the SFR. Mancini et al. (2015) did a more careful estimate of L_{IR} with (*Spitzer+Herschel*) photometry from $24 \mu\text{m}$ to $250 \mu\text{m}$ of $56 M_* \geq 10^{11} M_\odot$ galaxies at $1.4 \leq z \leq 2$ in the GOODS-S field, for a better estimate of $\text{SFR}_{\text{IR+UV}}$. Defining AGN as those with excess X-ray and/or radio (VLA 1.4 GHz) luminosity with respect to the expected $\text{SFR}_{\text{IR+UV}}$ or SFR_{SED} , and classifying galaxies as star-forming/quiescent based on sSFR as well as UVJ color, the authors found relatively high AGN fractions of $\sim 40 \pm 10\%$ and $\sim 22 \pm 7\%$ for star-forming and quiescent galaxies, respectively

(though fractions very close to ours when adopting the same criteria). In agreement with Barro et al. (2013), Mancini et al. (2015) also found that the presence of an AGN correlates with compactness as probed by a steep radial surface brightness profile in rest-frame optical. Over a wider redshift range, $1.4 < z < 3$ but with a similar method, Rangel et al. (2014) concluded that compact galaxies, both quiescent and star-forming, display higher intrinsic 2 – 8 keV luminosities and levels of obscuration than in extended galaxies.

These studies show that of out massive galaxies at $z \sim 2$, compact ones contain the most powerful AGN, and that when studying quiescent/star-forming galaxy samples across redshift, observations seem to promote a picture in which cSFGs evolve directly into CQGs via a relatively obscured AGN phase, albeit of high (absorption-corrected) X-ray luminosity.

10.2 DIRECT OBSERVATIONS OF AGN FEEDBACK

Direct evidence for the radiative and quasar mode of AGN feedback is now existing for a few, mostly nearby, objects (see review by Fabian, 2012). For example, in a study of the UV absorption line profiles of $226 M_* \geq 10^{11} M_\odot$ galaxies at $1 < z < 3$, Cimatti et al. (2013) found possible gas outflow velocities of up to $\sim 500 \text{ km s}^{-1}$, but only in galaxies classified as luminous AGNs (with $L_{2-8 \text{ keV}} > 10^{42.3} \text{ ergs s}^{-1}$). This indicates that the gas here is moving faster than the escape velocity of active galaxies, resulting in the ejection of part of the ISM possible decrease in SFR. With the X-ray satellite Nustar, sensitive to high energy X-rays of 3 – 79 keV, it is also possible to see such outflows in X-ray absorption and emission lines as demonstrated by Nardini et al. (2015). Likewise but at high redshift, Nesvadba et al. (2011) observed evidence for outflows of turbulent gas traced by narrow-line emission in the rest-frame UV and optical of two quasars at $z \sim 3.4$ and ~ 3.9 . In addition to observations in UV, AGN feedback has been confirmed with radio and sub-mm observations, in particular in the form of strong molecular outflows (e.g. Feruglio et al., 2010; Ciccone et al., 2014; Tombesi et al., 2015). Comparing the mass outflow (or inflow) rates of ionized or molecular gas to the accretion rate to the AGN, hints at the effect that these might have on the global SFR, as summarized by e.g. Bergmann (2012) and Storch-Bergmann (2014). However, *more observations of both jets and outflows, observationally confirmed in at least some AGNs at redshifts out to almost $z \sim 4$, are needed in order to settle how they affect the ISM of their host galaxies as a whole.*

10.3 FUTURE DIRECTIONS: DISCERNING VARIABILITY WITH TIME

In particular the arrival of new observing facilities, will open up this field towards high redshift by studying both individual cases and global properties of large samples.

Seeing the strong connection between compactness and AGN activity at high- z , as revealed over recent years, this field will benefit tremendously from the arrival of JWST, that will enable rest-frame optical imaging out to $z \sim 10$ with 3 times better angular resolution than HST at $1.6 \mu\text{m}$ (Beichman et al., 2012). That means being able to see whether AGNs are associated with compact galaxies all the way out to Epoch of Re-ionization (EoR). With the high NIR spectral resolution of JWST, the absence of poly-aromatic hydrocarbon (PAH) emission at $\sim 6 - 11 \mu\text{m}$ can also be used to select possible AGN candidates without the need of X-ray observations (Windhorst et al., 2009; Hanami et al., 2011). The combined forces of JVLA, JWST and ALMA will also allow detections of molecular outflows at high- z by measuring gas

kinematics as traced by molecular and fine structure lines (Fabian, 2012).

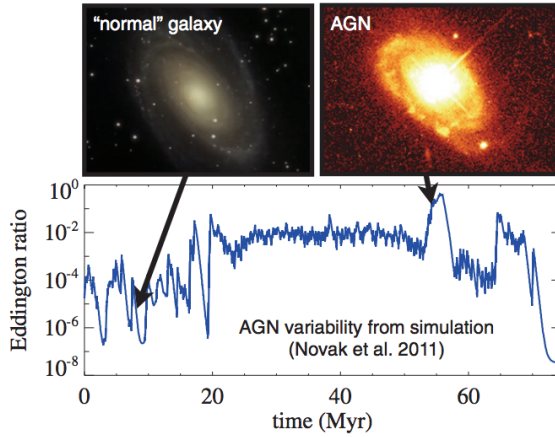


Figure 10.1 Illustration of AGN variability from Hickox et al. (2014) who took the Eddington ratio, a measure of BHAR, as a function of time from a hydrodynamic simulation presented by Novak et al. (2011) (*bottom*). Depending on the time of observation, the same galaxy can happen to be in an inactive state or a bright AGN state.

A potentially very important factor, but not completely revealed in any of the above studies, is time variation. As mentioned in Section 9.3.4, major mergers at $0 < z < 3$ have been associated with the most luminous AGNs (Treister et al., 2012), whereas moderate-luminosity ($L_{0.5-8 \text{ keV}} \sim 10^{42-44} \text{ ergs s}^{-1}$) AGNs at $z \sim 2$ are not associated with disturbed morphologies, indicative of recent mergers, any more than non-active galaxies are (Kocevski et al., 2012). This said, the apparent lack of merger signatures in AGNs cannot rule out a connection between AGNs and mergers. First of all, if mergers in the initial phase generally produce obscured AGNs, then these will be harder to detect in X-rays, unless one has access to the hard X-rays that penetrate the obscuring gas better than the soft ones. One would then expect moderate AGNs to be primarily observed in post-starburst galaxies, in agreement with our stacking of un-detected X-ray sources, that revealed a *higher* signal from quiescent galaxies than from SFGs. Another exception would be if there exists a time delay between the merger and the actual onset of the luminous AGN phase. With JWST and upcoming X-ray observatories (see Section 1.5), we can start to piece together the redshift distribution of AGNs and mergers/pairs to look for a possible delay. A second time-related issue, possibly blurring the observable relationship between AGNs and their hosts, is variability of the AGN luminosity as shown in Fig. 10.1. Models show, that when reasonable variability for the AGN luminosity is assumed, the weak correlations between SFR and L_{AGN} can be reproduced, even if there is a tight underlying correlation between SFR and BHAR (Novak et al., 2012; Hickox et al., 2014).

In conclusion, new observatories can explore the presence of AGNs at $z > 2$, with particular focus on compactness, jets and in/outflows that are crucial for the overall SFR of the host galaxy. We also need to understand the time domain of AGNs in more detail, and as Fig. 10.1 illustrates, such observations of AGN variability will be aided by a wealth of emerging simulations attempting to model the AGN-host co-evolution (e.g. Vogelsberger et al., 2013; Gabor & Bournaud, 2014; DeGraf et al., 2014).

10.4 REFERENCES

- Alexander, D. M., Bauer, F. E., Brandt, W. N., et al. 2011, *ApJ*, 738, 44
- Anderson, M. E., & Bregman, J. N. 2011, *ApJ*, 737, 22
- Arnaud, K. A. 1996, in *Astronomical Society of the Pacific Conference Series*, Vol. 101, *Astronomical Data Analysis Software and Systems V*, ed. G. H. Jacoby & J. Barnes, 17
- Barro, G., Faber, S. M., Pérez-González, P. G., et al. 2013, *ApJ*, 765, 104
- Bauer, F. E., Alexander, D. M., Brandt, W. N., et al. 2004, *AJ*, 128, 2048
- Beichman, C. A., Rieke, M., Eisenstein, D., et al. 2012, in *Society of Photo-Optical Instrumentation Engineers (SPIE) Conference Series*, Vol. 8442, *Society of Photo-Optical Instrumentation Engineers (SPIE) Conference Series*, 2
- Bell, E. F. 2003, *ApJ*, 586, 794
- Bergmann, T. S. 2012, in *Astronomical Society of the Pacific Conference Series*, Vol. 460, *AGN Winds in Charleston*, ed. G. Chartas, F. Hamann, & K. M. Leighly, 133
- Bruzual, G., & Charlot, S. 2003, *MNRAS*, 344, 1000
- Cardamone, C. N., Urry, C. M., Damen, M., et al. 2008, *ApJ*, 680, 130
- Cavaliere, A., & Fusco-Femiano, R. 1976, *A&A*, 49, 137
- Cicone, C., Maiolino, R., Sturm, E., et al. 2014, *A&A*, 562, A21
- Cimatti, A., Brusa, M., Talia, M., et al. 2013, *ApJ*, 779, L13
- Cowie, L. L., Barger, A. J., & Hasinger, G. 2012, *ApJ*, 748, 50
- Croton, D. J., Springel, V., White, S. D. M., et al. 2006, *MNRAS*, 365, 11
- Daddi, E., Dickinson, M., Morrison, G., et al. 2007, *ApJ*, 670, 156
- Dai, X., Anderson, M. E., Bregman, J. N., & Miller, J. M. 2012, *ApJ*, 755, 107
- Darg, D. W., Kaviraj, S., Lintott, C. J., et al. 2010, *MNRAS*, 401, 1552
- DeGraf, C., Dekel, A., Gabor, J., & Bournaud, F. 2014, *ArXiv e-prints*
- Di Matteo, T., Springel, V., & Hernquist, L. 2005, *Nature*, 433, 604
- Done, C., Davis, S. W., Jin, C., Blaes, O., & Ward, M. 2012, *MNRAS*, 420, 1848
- Donley, J. L., Koekemoer, A. M., Brusa, M., et al. 2012, *ApJ*, 748, 142
- Dunlop, J. S. 2011, *Science*, 333, 178
- Elbaz, D., Hwang, H. S., Magnelli, B., et al. 2010, *A&A*, 518, L29
- Fabian, A. C. 2012, *ARA&A*, 50, 455
- Feruglio, C., Maiolino, R., Piconcelli, E., et al. 2010, *A&A*, 518, L155
- Franx, M., van Dokkum, P. G., Schreiber, N. M. F., et al. 2008, *ApJ*, 688, 770
- Gabor, J. M., & Bournaud, F. 2014, *MNRAS*, 441, 1615
- Gilli, R., Comastri, A., & Hasinger, G. 2007, *A&A*, 463, 79
- Grimm, H.-J., Gilfanov, M., & Sunyaev, R. 2003, *MNRAS*, 339, 793
- Hanami, H., Ishigaki, T., & Ishigaki. 2011, in *IAU Symposium*, Vol. 277, *IAU Symposium*, ed. C. Carignan, F. Combes, & K. C. Freeman, 182–185
- Häring, N., & Rix, H.-W. 2004, *ApJ*, 604, L89
- Harrison, C. M., Alexander, D. M., Mullaney, J. R., et al. 2012, in press (*ArXiv:1209.3016*)
- Hickox, R. C., Mullaney, J. R., Alexander, D. M., et al. 2014, *ApJ*, 782, 9
- Kocevski, D. D., Faber, S. M., Mozena, M., et al. 2012, *ApJ*, 744, 148
- Kriek, M., van Dokkum, P. G., Franx, M., Illingworth, G. D., & Magee, D. K. 2009, *ApJ*, 705, L71
- Kurczynski, P., Gawiser, E., Huynh, M., et al. 2012, *ApJ*, 750, 117
- Laird, E. S., Nandra, K., Pope, A., & Scott, D. 2010, *MNRAS*, 401, 2763
- Lamareille, F. 2010, *A&A*, 509, A53
- Lehmer, B. D., Alexander, D. M., Bauer, F. E., et al. 2010, *ApJ*, 724, 559
- Lobanov, A., & Zensus, J. A. 2007, *Active Galactic Nuclei at the Crossroads of Astrophysics*

(Springer-Verlag), 147–162

- Man, A. W. S., Toft, S., Zirm, A. W., Wuyts, S., & van der Wel, A. 2012, *ApJ*, 744, 85
- Mancini, C., Renzini, A., Daddi, E., et al. 2015, *ArXiv e-prints*
- Matt, G., Marinucci, A., Guainazzi, M., et al. 2014, *MNRAS*, 439, 3016
- Mulchaey, J. S., & Jeltema, T. E. 2010, *ApJ*, 715, L1
- Nandra, K., & Pounds, K. A. 1994, *MNRAS*, 268, 405
- Nardini, E., Reeves, J. N., Gofford, J., et al. 2015, *Science*, 347, 860
- Nesvadba, N. P. H., Polletta, M., Lehnert, M. D., et al. 2011, *MNRAS*, 415, 2359
- Newman, A. B., Ellis, R. S., Bundy, K., & Treu, T. 2012, *ApJ*, 746, 162
- Novak, G. S., Ostriker, J. P., & Ciotti, L. 2011, *ApJ*, 737, 26
- . 2012, *MNRAS*, 427, 2734
- O’Sullivan, E., Ponman, T. J., & Collins, R. S. 2003, *MNRAS*, 340, 1375
- Papovich, C., Moustakas, L. A., Dickinson, M., et al. 2006, *ApJ*, 640, 92
- Peng, Y.-j., Lilly, S. J., Kovač, K., et al. 2010, *ApJ*, 721, 193
- Persic, M., Rephaeli, Y., Braitto, V., et al. 2004, *A&A*, 419, 849
- Piconcelli, E., Jimenez-Bailón, E., Guainazzi, M., et al. 2005, *A&A*, 432, 15
- Ranalli, P., Comastri, A., & Setti, G. 2003, *A&A*, 399, 39
- Rangel, C., Nandra, K., Barro, G., et al. 2014, *MNRAS*, 440, 3630
- Rasmussen, J., Sommer-Larsen, J., Pedersen, K., et al. 2009, *ApJ*, 697, 79
- Reeves, J. N., & Turner, M. J. L. 2000, *MNRAS*, 316, 234
- Risaliti, G., & Elvis, M. 2004, in *Astrophysics and Space Science Library*, Vol. 308, *Supermassive Black Holes in the Distant Universe*, ed. A. J. Barger, 187
- Rubin, K. H. R., van Dokkum, P. G., Coppi, P., et al. 2004, *ApJ*, 613, L5
- Schawinski, K. 2011, in *New Horizons in Astronomy, Proceedings of the Frank N. Bash Symposium 2011*, held October 9-11, 2011. Austin, Texas, USA. Edited by S. Salviander, J. Green, and A. Pawlik. Published online at <http://pos.sissa.it/cgi-bin/reader/conf.cgi?confid=149>
- Schawinski, K., Virani, S., Simmons, B., et al. 2009, *ApJ*, 692, L19
- Stark, A. A., Gammie, C. F., Wilson, R. W., et al. 1992, *ApJS*, 79, 77
- Stern, D., Eisenhardt, P., Gorjian, V., et al. 2005, *ApJ*, 631, 163
- Storchi-Bergmann, T. 2014, *ArXiv e-prints*
- Szokoly, G. P., Bergeron, J., Hasinger, G., et al. 2004, *ApJS*, 155, 271
- Tajer, M., Polletta, M., Chiappetti, L., et al. 2007, *A&A*, 467, 73
- Tanaka, M., Finoguenov, A., Mirkazemi, M., et al. 2012, *PASJ*, in press (ArXiv:1210.0302)
- Taylor, E. N., Franx, M., van Dokkum, P. G., et al. 2009, *ApJS*, 183, 295
- Toft, S., Franx, M., van Dokkum, P., et al. 2009, *ApJ*, 705, 255
- Toft, S., Gallazzi, A., Zirm, A., et al. 2012, *ApJ*, 754, 3
- Toft, S., Rasmussen, J., Sommer-Larsen, J., & Pedersen, K. 2002, *MNRAS*, 335, 799
- Tombesi, F., Melendez, M., Veilleux, S., et al. 2015, *ArXiv e-prints*
- Treister, E., Schawinski, K., Urry, C. M., & Simmons, B. D. 2012, *ApJ*, 758, L39
- Treister, E., & Urry, C. M. 2012, *Advances in Astronomy, Seeking for the Leading Actor on the Cosmic Stage: Galaxies versus Supermassive Black Holes*, 35
- Treister, E., Cardamone, C. N., Schawinski, K., et al. 2009, *ApJ*, 706, 535
- Vanzella, E., Cristiani, S., Dickinson, M., et al. 2008, *A&A*, 478, 83
- Vasudevan, R. V., Mushotzky, R. F., Reynolds, C. S., et al. 2014, *ApJ*, 785, 30
- Vogelsberger, M., Genel, S., Sijacki, D., et al. 2013, *MNRAS*, 436, 3031
- Wang, J. X., Malhotra, S., Rhoads, J. E., & Norman, C. A. 2004, *ApJ*, 612, L109

- Williams, R. J., Quadri, R. F., Franx, M., van Dokkum, P., & Labbé, I. 2009, *ApJ*, 691, 1879
- Windhorst, R. A., Mather, J., Clampin, M., et al. 2009, in *Astronomy*, Vol. 2010, astro2010: The Astronomy and Astrophysics Decadal Survey, 317
- Wuyts, S., Labbé, I., Schreiber, N. M. F., et al. 2008, *ApJ*, 682, 985
- Wuyts, S., Förster Schreiber, N. M., van der Wel, A., et al. 2011, *ApJ*, 742, 96
- Xue, Y. Q., Luo, B., Brandt, W. N., et al. 2011, *ApJS*, 195, 10
- Zheng, Z.-Y., Malhotra, S., Wang, J.-X., et al. 2012, *ApJ*, 746, 28

SUMMARY

Piecing together the puzzle of galaxy evolution precise knowledge about *the shape of the pieces to the puzzle*, i.e. the physical conditions of the galaxies, not just of the stellar component, but of the interstellar medium (ISM) and black hole as well. This thesis focuses on deriving the actual shape of those puzzle pieces, with particular focus on characterising the ISM as well as the gas accretion onto the central black hole, in order to better understand their effects on the SFR and general evolution of massive galaxies. With this aim in mind, the following three studies were carried out:

Amount and distribution of molecular gas in the ISM

A combination of density and temperature is the main agent shaping the CO spectral line energy distribution (SLED), and observations thereof can consequently be used to probe the conditions of the star-forming, molecular gas in the ISM. However, detailed modeling is needed in order to interpret observations. For that purpose, a new method is constructed and presented here; Simulator of GALaxy Millimeter/submillimeter Emission (SÍGAME). The method is combined with the radiative transfer code LIME in order to simulate CO line emission, and by applying SÍGAME to three galaxies from cosmological simulations, the following conclusions are drawn for simulated massive galaxies at $z \sim 2$:

- The CO SLED resembles the low-excitation one of the Milky Way (MW), in that it peaks at CO(3 – 2), but also with significant line intensity at higher transitions, not seen in the MW.
- Global α_{CO} factors range from 1.4 to $1.6 \text{ M}_{\odot} \text{ pc}^{-2} (\text{K km s}^{-1})^{-1}$ or about one third of the typically assumed MW value.
- Total CO(3 – 2) luminosities are within the range of corresponding observed samples at redshifts $z \sim 1 - 2.5$, however on the low side, most likely due to relatively low molecular gas masses in our model galaxies.
- Radial profiles of line ratios within each galaxy reveal more excited gas towards the center, in agreement with observations of nearby galaxies, and suggesting ULIRG-like environments in the central ($R < 5 \text{ kpc}$) regions.
- The α_{CO} factor displays a decrease towards the center of each model galaxy, however, by a factor that is lower than what is observed in local spiral galaxies.

Tracing SFR on local and global scales

SÍGAME is expanded and adapted in order to model [CII] – the fine-structure line of singly ionized carbon (C^+), thereby being the first code to simulate the [CII] emission reliably on kpc-scales in normal star-forming galaxies. [CII] is typically the strongest cooling line in neutral ISM, and correlates strongly with SFR on global and local scales, but its origin is so far unclear. These are the major findings from applying *SÍGAME* to seven $z = 2$ star-forming galaxies from another simulation:

- *SÍGAME* is able to reproduce the observed $L_{[\text{CII}]}$ -SFR relation of normal galaxies at $z > 0.5$.
- The [CII] emission that originates in molecular gas tends to dominate the total [CII] luminosity in the central regions ($R \lesssim 1$ kpc), but contributions from PDRs dominate further out ($R \gtrsim 1 - 2$ kpc). The more diffuse HII regions always contribute with a negligible amount.
- On resolved (1 kpc) scales, an expression is provided for the $\Sigma_{[\text{CII}]}$ - Σ_{SFR} relation.
- The low scatter around the modelled $L_{[\text{CII}]}$ -SFR relation in molecular gas owes to a tight correlation between molecular gas amount and SFR. On resolved scales, [CII] contributions from all ISM phases are increased at high metallicity, but whether GMCs of PDRs dominate the net [CII] output depends on local pressure as well. PDRs can maintain high [CII] efficiency at low as well as high pressures, while GMCs require high pressures as typically present in the central regions of galaxies.
- A weak trend is found between increasing metallicity and decreasing global $\text{SFR}/L_{[\text{CII}]}$ ratio, but the study is hampered by a limited range in metallicity for our sample of galaxies. On resolved scales, $\text{SFR}/L_{[\text{CII}]}$ does increase towards the center of each galaxy together with metallicity, as also observed in local spiral galaxies.

Importance of AGNs in massive galaxies at $z \sim 2$

The deep *Chandra* X-ray survey CDF-S is analysed, and AGNs of high and low X-ray luminosity are extracted via AGN classification methods, and stacking techniques of non-detections, in X-ray. The galaxies investigated come from a mass-complete (at $M_* > 5 \times 10^{10} M_\odot$) sample at $1.5 \leq z \leq 2.5$ with stellar masses from fits of stellar population synthesis models to their spectral energy distribution. By statistical analysis, the following results are obtained:

- Among both star-forming and quiescent galaxies, a similar fraction of $22 \pm 5\%$ is found to have rest-frame X-ray luminosities ($L_{0.5-8 \text{ keV}} > 3 \times 10^{42} \text{ erg s}^{-1}$) consistent with hosting luminous AGNs.
- An excess in X-ray-inferred SFR compared to that from infrared and ultraviolet emission for the stacked non-detections, converts into even higher fractions of low- or high-luminosity AGNs among these. This fraction is higher (70 – 100 %) among quiescent galaxies than among star-forming ones (43 – 65 %).
- Hot gas halos are rejected as potential sources for the strong X-ray emission in the detected galaxies, based on the very limited spatial extent of their X-ray emission.
- The fraction of luminous AGNs does not depend on SFR nor stellar mass, suggesting that external effects are triggering the AGNs.

SAMMENFATNING

Det er et sandt puslespil at stykke galakse-udviklingen sammen ud fra observationer ved forskellige rødforskydninger. For at løse puslespillet er det først og fremmest afgørende at kende formen af brikkerne, dvs. den fysiske tilstand af galakserne – ikke bare af deres stellare del men også af deres interstellare medium (ISM) og centrale sorte hul. Med dette mål for øje, består denne afhandling af følgende tre projekter:

Mængde og fordeling af molekylær gas i ISM af galakser

Den spektrale linie energi fordeling (SLED; Spectral Line Energy Distribution) for CO molekylet er bestemt af hovedsagelig tæthed og temperatur af den gas hvor linien udsendes fra, og observationer af CO SLEDs kan derfor bruges til at bestemme tilstanden af den stjernedannende, molekylære gas i ISM af galakser. For at kunne oversætte observationer af SLED'en til sådanne gas tilstande, er detaljeret modellering nødvendig. Til det formål bliver en ny metode skabt og præsenteret her; SIMulator of GALaxy Millimeter/submillimeter Emission (SÍGAME). Denne metode kombineres med en kode for strålingstransport af millimeter og infrarød stråling (LIME) for at kunne simulere CO linie emission, og ved at anvende SÍGAME på tre galakser fra kosmologiske simulationer, bliver de følgende konklusioner draget for massive galakser ved $z \sim 2$:

- CO SLED'en minder om den lavt eksiterede SLED i Mælkevejen, i og med at den har maksimum i CO(3 – 2), men de har også signifikant linie intensitet ved højere overgange, hvilket ikke ses i Mælkevejen.
- Globale α_{CO} faktorer ligger på omkring 1/3-del af Mælkevejens, nemlig fra 1.4 til 1.6 $\text{M}_{\odot} \text{pc}^{-2} (\text{K km s}^{-1})^{-1}$.
- De totale CO(3 – 2) luminositeter er alle indenfor spredningen af sammenlignelige observerede stjernedannende galakser ved rødforskydning $z \sim 1 - 2.5$, men til den lave side, højst sandsynlig pga. relativt lave molekylære gas masser i vores model galakser.
- Radielle profiler af CO linie forhold viser at hver model galakse indeholder mere eksiteret gas i de centrale dele sammenlignet med længere ude i disken. Dette er i overensstemmelse med observationer af lokale galakser og antyder at de centrale ($R < 5 \text{ kpc}$) områder minder om de forhold man finder i ULIRGs (Ultra-Luminøse Infrarøde Galakser).
- α_{CO} faktoren aftager mod centrum i galakserne som også observeret, dog med et mindre relativt fald ift. til det man typisk observerer i lokale spiral-galakser.

Afdækning af SFR på små og store skalaer

SÍGAME udvides og adapteres til at modellere [CII]–fin-struktur linien fra enkelt-ioniseret carbon (C^+), og er dermed den første kode til troværdigt at simulere [CII] emission på kpc-skala i normale stjernedannende galakser. [CII] er typisk den linie der kraftigst køler neutral ISM, og den skalerer med SFR på globale såvel som på lokale skalaer. Men dens fysiske oprindelse i gassen er stadig uklar. Disse er de første konklusioner, som SÍGAME indtil nu har ført til på det område:

- SÍGAME kan reproducere den observerede relation mellem $L_{[CII]}$ og SFR for normale galakser ved $z > 0.5$.
- [CII] emission udspringer hovedsageligt fra molekylær gas i de centrale ($R \lesssim 1$ kpc) dele af galakserne, men bidrag fra PDRs (Photon Dominated Regions) dominerer længere ude ($R \gtrsim 1 - 2$ kpc). Den mere diffuse HII gas bidrager med negligerlig [CII] intensitet.
- På opløste (1 kpc) skalaer, opstilles et udtryk for $\Sigma_{[CII]}$ som funktion af Σ_{SFR} .
- Den lave spredning i $L_{[CII]}$ -SFR relationen for molekylær gas skyldes en tæt sammenhæng mellem molekylær gas masse og total SFR. På opløste (1 kpc) skalaer er [CII] emissionen større i områder med relativ høj metallicitet, men hvorvidt GMCs eller PDRs dominerer [CII] budgettet afhænger også af det lokale tryk. PDRs kan opretholde høj [CII] 'effektivitet' ved lavt såvel som højt tryk, hvorimod GMCs kræver højt tryk som typisk kun er at finde i de centrale områder.
- En svag korrelation findes mellem stigende metallicitet og aftagende global $SFR/L_{[CII]}$ rate, men det er svært at konkludere noget da vores galakser ikke spænder vidt nok i metallicitet. Dog ser vi på mindre skalaer at $SFR/L_{[CII]}$ raten stiger imod centrum af galakserne sammen med metalliciteten, hvilket også er blevet observeret i lokale spiralgalakser.

En vigtig rolle af AGNs i massive galakser ved $z \sim 2$

Aktive galaksekerner (AGNs; Active Galactic Nuclei) af høj og lav X-ray luminositet afdækkes i feltet CDF-S, der er blevet studeret i røntgen med lang eksponering (4 Ms) af *Chandra* rumobservatoriet. Gruppen af galakser som undersøges dækker fuldstændigt stellar masser over $5 \times 10^{10} M_{\odot}$ ved $1.5 \leq z \leq 2.5$. Ved brug af AGN klassificerings-teknikker (og opsummerings-metoder for de galakser der ikke detekteres individuelt i røntgen), opnåes de følgende resultater:

- En brøkdel på $22 \pm 5\%$ blandt stjerne-dannende såvel som blandt passive galakser, har X-ray lysterker svarende til lysstærke AGNs.
- En endnu større brøkdel blandt de ikke-detekterede galakser, viser tegn på at indeholde AGNs af lav til høj luminositet, med højere brøkdel (70 – 100 %) blandt passive galakser sammenlignet med de stjerne-dannende (43 – 65 %).
- Grundet den rumligt koncentrerede X-ray emission fra de undersøgte galakser, kan en ekstremt varm gas halo udelukkes som årsag til X-ray emissionen i de detekterede galakser.
- Brøkdelen af lysstærke AGNs afhænger ikke af SFR eller stellar masse, hvilket tyder på at eksterne faktorer spiller ind på antændelsen af deres AGNs.

ACKNOWLEDGMENTS

My passion for astronomy was sparked during long, cold nights in the observatory of my high school, Alssundgymnasiet Sønderborg, in Southern Denmark. In that way, I feel fortunate for having benefitted from an educational system that incorporates astronomy. But more so, I am grateful to my first astronomy teacher, Mogens Winther, for his incredible enthusiasm and to those classmates that made it fun to stay up at night. Since then, so many inspirational people have opened up the sky for me, both in Aarhus, where I finished my bachelors in physics, and later on in Copenhagen for my master and PhD. These past 4 years, that journey has been eased and guided by two amazing people, my supervisors Thomas and Sune. In your own very separate ways, you have taught me how to believe in myself as a researcher, and no words can describe my respect for you.

From the moment I hand in my thesis, I will miss life at Dark. Dark Cosmology Centre is nothing less of a paradise for any astronomer; daily provisions of coffee and fruit and a non-tiring staff of administration and support. Thank you for patiently answering all of my stupid questions and fixing my mistakes (even on weekends). And to the rest of my 'darklings'; thank you for all those great moments; excursions, movie nights, alleviating lunch breaks, parties or laughs at the coffee machine.

I would not have gotten very far, in astronomy or anything else, without my friends. First 'tak' to my old friends in Copenhagen that I occasionally forget how lucky I am to have; Tomatito, Lotte (x2), Helene. Thanks to my dear friends spread across the world – your warmth, generosity and wisdom still reaches and amazes me; Marty, Cat, Urs and papa-J, Sam, Chang, Rosa, Scott (the dad and the pilot), Fan-Fan, Hannah, Carol, Lila, Henry, Charlotte, Britta and Kaare to name a few, but certainly not all! I will also not forget to thank my flamenco girls; Rut, Rebecka, Elisabeth and all those crazy, lovely people I meet doing capoeira or aerial acrobatics, in Denmark and accross the world.

Towards the end of my PhD, I was blessed by meeting my own 'curandero'. From the other side of the ocean, you support me in everything I do and make me laugh on my most solemn days. I will never know how many bruises and dangers you saved me from.

Finally, I can't wait to thank my family (yes, that includes you guys, tía mía and Erk who I always wish to see more). You're there with love and encouragement (and sund fornufft), even when Als seems light years away. In particular, thank you mamita for taking those field trips to Copenhagen and reminding me how to go shopping.

Tak, gracias, obrigada, thank you!

Karen

Appendices

A

APPENDIX TO CHAPTER 4

A.1 THERMAL BALANCE OF THE ATOMIC GAS PHASE

As explained in § 4.3.2, we cool the initial hot SPH gas by requiring:

$$\Gamma_{\text{CR,HI}} = \Lambda_{\text{ions+atoms}} + \Lambda_{\text{rec}} + \Lambda_{\text{f-f}}.$$

$\Gamma_{\text{CR,HI}}$ is the heating rate of the atomic gas due to cosmic ray ionizations (Draine, 2011):

$$\begin{aligned} \Gamma_{\text{CR,HI}} = & 1.03 \times 10^{-27} n_{\text{HI}} \left(\frac{\zeta_{\text{CR,HI}}}{10^{-16}} \right) \\ & \times \left[1 + 4.06 \left(\frac{x_e}{x_e + 0.07} \right)^{1/2} \right] \text{ erg cm}^{-3} \text{ s}^{-1}, \end{aligned} \quad (\text{A.1})$$

where $\zeta_{\text{CR,HI}}$ is the primary CR ionization rate of HI atoms (determined locally in our simulations according to eq. 4.12), and x_e is the hydrogen ionization fraction calculated with a procedure kindly provided by I. Pelupessy; see also Pelupessy (2005). The term containing x_e in eq. A.1 accounts for the fact that in highly ionised gas, electrons created by primary CR ionization have a high probability of transferring their kinetic energy into heat via long-range Coulomb scattering off free electrons. For low ionization gas, this term becomes insignificant as a higher fraction of the energy of the primary electrons goes to secondary ionizations or excitation of bound states instead of heating.

$\Lambda_{\text{ions+atoms}}$ is the total cooling rate due to line emission from H, He, C, N, O, Ne, Mg, Si, S, Ca, and Fe, calculated using the publically available code of Wiersma et al. (2009) which takes T_k , n_{H} and the abundances of the above elements as input. Wiersma et al. (2009) compute the cooling rates with the photoionization package CLOUDY assuming CIE. They also adopt a value for the meta-galactic UV and X-ray field equal to that expected at $z \sim 2$ (Haardt & Madau, 2001). At $z \sim 2$, the emission rate of HI ionizing radiation is higher by a factor of about ~ 30 than at $z = 0$ (Puchwein et al., 2015), and thus plays an important role in metal line cooling calculations.

Λ_{rec} is the cooling rate due to hydrogen recombination emission (Draine, 2011):

$$\Lambda_{\text{rec}} = \alpha_B n_e n_{\text{H}^+} \langle E_{rr} \rangle \text{ ergs cm}^{-3} \text{ s}^{-1}, \quad (\text{A.2})$$

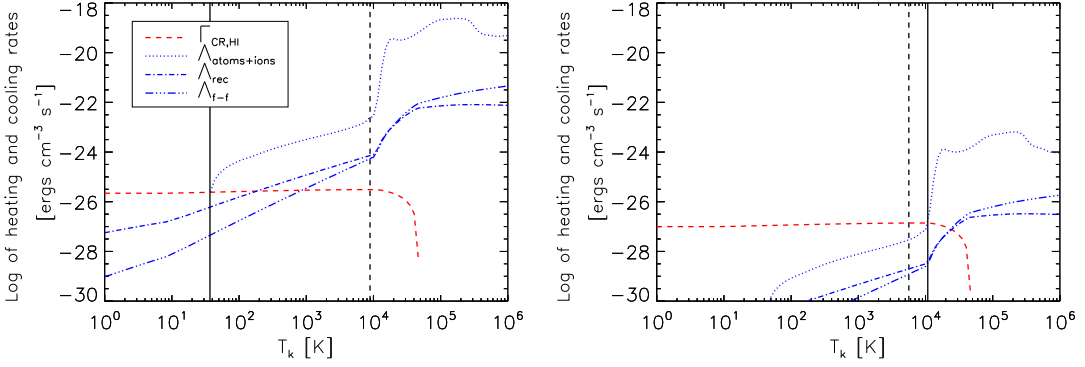


Figure A.1 Heating and cooling rates as functions of temperature for two SPH gas particles with $[n_{\text{H}} = 14.62 \text{ cm}^{-3}, \zeta_{\text{CR}} = 4.02 \times 10^{-16} \text{ s}^{-1}, x_{\text{e}} (T_{\text{k,SPH}} = 8892 \text{ K}) = 0.006]$ (left) and $[n_{\text{H}} = 0.09 \text{ cm}^{-3}, \zeta_{\text{CR}} = 3.92 \times 10^{-16} \text{ s}^{-1}, x_{\text{e}} (T_{\text{k,SPH}} = 5649 \text{ K}) = 0.001]$ (right). In both cases the metal line emission is the main cooling agent. The left-hand side plot illustrates the case of an SPH particle of high gas density and metallicity, leading to relatively efficient metal line cooling and in a low equilibrium temperature of $T_{\text{k}} = 37 \text{ K}$. The right-hand side plot shows a case of lower density and metallicity causing less cooling by metal lines, hence a higher equilibrium temperature despite a slightly lower CR heating rate. The dashed vertical lines in the two panels indicate the original SPH gas temperatures of the SPH particles, and the solid vertical lines mark their final equilibrium temperatures.

where α_B is the radiative recombination rate for hydrogen in the case of optically thick gas in which ionizing photons emitted during recombination are immediately re-absorbed. We adopt the approximation for α_B given by Draine (2011):

$$\alpha_B = 2.54 \times 10^{-13} T_4^{(-0.8163 - 0.0208 \ln T_4)} \text{ cm}^3 \text{ s}^{-1}, \quad (\text{A.3})$$

where T_4 is defined as $T_{\text{k}}/10^4 \text{ K}$. The density of ionised hydrogen, n_{H^+} , is set equal to the electron density, n_{e} , and E_{rr} is the corresponding mean kinetic energy of the recombining electrons:

$$\langle E_{\text{rr}} \rangle = [0.684 - 0.0416 \ln T_4] k_{\text{B}} T_{\text{k}} \text{ ergs}. \quad (\text{A.4})$$

$\Lambda_{\text{f-f}}$ is the cooling rate due to free-free emission from electrons in a pure H plasma (i.e., free electrons scattering off H^+), and is given by (Draine, 2011):

$$\Lambda_{\text{f-f}} = 0.54 T_4^{0.37} k_{\text{B}} T_{\text{k}} n_{\text{e}} n_{\text{H}^+} \alpha_B \text{ ergs cm}^{-3} \text{ s}^{-1}, \quad (\text{A.5})$$

where the recombination rate, α_B , is calculated in the same way as for Λ_{rec} .

Figure A.1 shows the above heating and cooling rates pertaining to two example SPH particles with similar initial temperatures ($\sim 10^4 \text{ K}$). Because of different ambient conditions (i.e., n_{H} , x_{e} , Z' , and ζ_{CR}) the equilibrium temperature solutions for the two gas particles end up being significantly different.

A.2 THERMAL BALANCE OF THE MOLECULAR GAS PHASE

As described in Section 4.3.4 *SÍGAME* assumes that the molecular gas resides exclusively in giant molecular clouds that have Plummer radial density profiles (i.e., given by eq. 4.11). Throughout the clouds the gas temperature is solved for according to the heating and cooling equilibrium requirement $\Gamma_{\text{PE}} + \Gamma_{\text{CR,H}_2} = \Lambda_{\text{H}_2} + \Lambda_{\text{CO}} + \Lambda_{\text{CII}} + \Lambda_{\text{OI}} + \Lambda_{\text{gas-dust}}$ (eq. 4.14).

Γ_{PE} is the heating rate of the gas due to photo-electric ejection of electrons from dust grains by FUV photons, and is given by (Bakes & Tielens, 1994):

$$\Gamma_{\text{PE}} = 10^{-24} \epsilon G_{0,\text{att}} n_{\text{H}} \text{ ergs cm}^{-3} \text{ s}^{-1}, \quad (\text{A.6})$$

where $G_{0,\text{att}}$ is the local attenuated FUV field in Habing units, derived following eq. 4.13, and ϵ is the heating efficiency:

$$\epsilon = \frac{4.87 \times 10^{-2}}{1 + 4 \times 10^{-3} (G_{0,\text{att}} T^{0.5} / n_e)^{0.73}} + \frac{3.65 \times 10^{-2}}{1 + 4 \times 10^{-3} (G_{0,\text{att}} T^{0.5} / n_e)^{0.73}}, \quad (\text{A.7})$$

where n_e is the electron density, calculated as $x_e n_{\text{H}}$, with x_e again calculated using the procedure of I. Pelupessy.

$\Gamma_{\text{CR,H}_2}$ is the heating rate by cosmic rays traveling through molecular gas (Stahler & Palla, 2005):

$$\Gamma_{\text{CR,H}_2} = 1.068 \times 10^{-24} \left(\frac{\zeta_{\text{CR,H}_2}}{10^{-16}} \right) \left(\frac{n_{\text{H}_2}}{10^3 \text{ cm}^{-3}} \right) \text{ ergs cm}^{-3} \text{ s}^{-1} \quad (\text{A.8})$$

where $\zeta_{\text{CR,H}_2}$ is the local CR primary ionization rate of H_2 molecules, which is approximately $1.6 \times$ higher than that of HI atoms (Stahler & Palla, 2005).

Λ_{H_2} is the H_2 line cooling rate, and we use the parameterization made by Papadopoulos et al. (2014) that includes the two lowest H_2 rotational lines ($\text{S}(0)$ and $\text{S}(1)$, the only lines excited for $T_{\text{k}} \lesssim 1000 \text{ K}$):

$$\Lambda_{\text{H}_2} = 2.06 \times 10^{-24} \frac{n_{\text{H}_2}}{1 + r_{\text{op}}} \left[1 + \frac{1}{5} e^{510 \text{ K} / T_{\text{k}}} \left(1 + \frac{n_0}{n_{\text{H}_2}} \right) \right]^{-1} \times (1 + R_{10}) \text{ ergs cm}^{-3} \text{ s}^{-1}, \quad (\text{A.9})$$

where R_{10} is defined as:

$$R_{10} = 26.8 r_{\text{op}} \left[\frac{1 + (1/5) e^{510 \text{ K} / T_{\text{k}}} \left(1 + \frac{n_0}{n_{\text{H}_2}} \right)}{1 + (3/7) e^{845 \text{ K} / T_{\text{k}}} \left(1 + \frac{n_1}{n_{\text{H}_2}} \right)} \right], \quad (\text{A.10})$$

and $n_0 \sim 54 \text{ cm}^{-3}$ and $n_1 \sim 10^3 \text{ cm}^{-3}$ are the critical densities of the $\text{S}(0):2-0$ and $\text{S}(1):3-1$ rotational lines. r_{op} is the ortho- H_2 /para- H_2 ratio (set to 3 which is the equilibrium value).

For the cooling rates due to the $[\text{C II}] 158 \mu\text{m}$ and $[\text{O I}] 63 \mu\text{m} + 146 \mu\text{m}$ fine-structure lines we adopt the parameterizations by Röllig et al. (2006). The C II cooling rate (Λ_{CII}) is:

$$\Lambda_{\text{CII}} = 2.02 \times 10^{-24} n Z' \times \left[1 + \frac{1}{2} e^{92 \text{ K} / T_{\text{k}}} (1 + 1300 / n_{\text{H}}) \right]^{-1} \text{ ergs cm}^{-3} \text{ s}^{-1}, \quad (\text{A.11})$$

where a carbon to hydrogen abundance ratio that scales with metallicity according to $\chi_{[\text{C}]} = 1.4 \times 10^{-4} Z'$ is assumed. For the parameterization of the O I cooling rate ($\Lambda_{\text{OI}} = \Lambda_{63 \mu\text{m}} + \Lambda_{146 \mu\text{m}}$) we refer to eqs. A.5 and A.6 in Röllig et al. (2006) and simply note that we adopt (in accordance

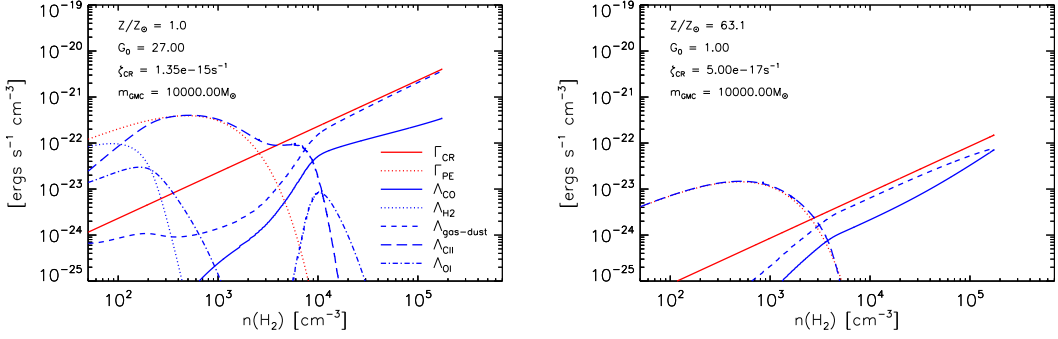


Figure A.2 Equilibrium heating (red curves) and cooling (blue curves) rates of the gas as functions of H_2 density for two different GMC models with $[m_{\text{GMC}} = 10^4 M_\odot, Z' = 1, G_0 = 27, \zeta_{\text{CR}} = 1.35 \times 10^{-15} \text{ s}^{-1}, P_{\text{ext}} = 10^4 \text{ K cm}^{-3}]$ (left) and $[m_{\text{GMC}} = 10^4 M_\odot, Z' = 63, G_0 = 1, \zeta_{\text{CR}} = 5 \times 10^{-17} \text{ s}^{-1}, P_{\text{ext}} = 10^4 \text{ K cm}^{-3}]$ (right). In the case of high FUV and CR radiation fields but low metallicity (left), the heating is dominated by cosmic ray heating (red solid) in the inner region ($n_{H_2} \gtrsim 1500 \text{ cm}^{-3}$) and photoelectric heating (red dotted) in the outer region. Cooling is dominated by gas-dust interactions (blue dashed) in the inner region ($n_{H_2} \gtrsim 10000 \text{ cm}^{-3}$) and by [CII] as well as H_2 line cooling (blue long-dashed and dotted) in the outer region. In the opposite case of low FUV and CR radiation fields but high metallicity (right), the same heating and cooling mechanisms are dominating the energy balance throughout the cloud, except in the inner region, where cooling by CO line emission (blue solid) is more important than it is in the case of low metallicity.

with Röllig et al., 2006) an oxygen to hydrogen abundance ratio of $\chi_{[\text{O}]} = 3 \times 10^{-4} Z'$.

Λ_{CO} is the cooling rate due to CO rotational transitions. We use the parameterization provided by Papadopoulos & Thi (2013):

$$\Lambda_{\text{CO}} = 4.4 \times 10^{-24} \left(\frac{n_{H_2}}{10^4} \right)^{3/2} \left(\frac{T_k}{10 \text{ K}} \right)^2 \left(\frac{\chi_{\text{CO}}}{\chi_{[\text{C}]}} \right) \text{ ergs cm}^{-3} \text{ s}^{-1}, \quad (\text{A.12})$$

where $\chi_{\text{CO}}/\chi_{[\text{C}]}$ is the relative CO to neutral carbon abundance ratio, the value of which we determine by interpolation, assuming that $\chi_{\text{CO}}/\chi_{[\text{C}]} = (0.97, 0.98, 0.99, 1.0)$ for $n_{H_2} = 5 \times 10^3, 10^4, 10^5, 10^6 \text{ cm}^{-3}$, respectively (Papadopoulos & Thi, 2013).

$\Lambda_{\text{gas-dust}}$ is the cooling rate due to gas-dust interactions and is given by (Papadopoulos et al., 2011):

$$\Lambda_{\text{gas-dust}} = 3.47 \times 10^{-33} n_H^2 \sqrt{T_k} (T_k - T_{\text{dust}}) \text{ ergs cm}^{-3} \text{ s}^{-1}, \quad (\text{A.13})$$

where the dust temperature (T_{dust}) is calculated using eq. 4.15 (Section 4.3.4).

A.3 GMC MODELS

Each SPH particle is divided into several GMCs as described in §4.3.4, and we derive the molecular gas density and temperature within each from three basic parameters which are SFR density, GMC mass, m_{GMC} , and metallicity, Z'/Z_\odot . Derived from these basic parameters are the far-UV and cosmic ray field strengths, the H_2 gas mass fraction of each SPH particles, as well as the GMC properties used to derive the CO excitation and emission; H_2 density and temperature. Histograms of the basic parameters are shown in Figure A.3, while properties derived thereof can be found in Figure A.4.

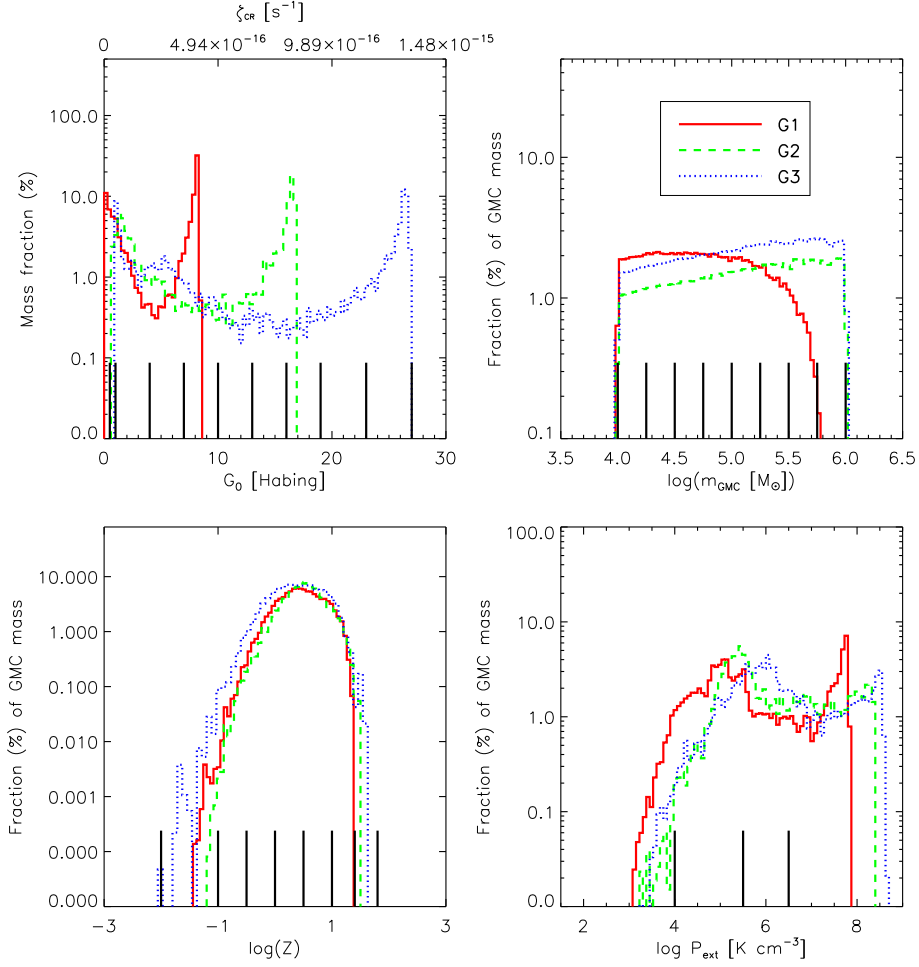


Figure A.3 Mass-weighted histograms of the basic parameters of the GMCs in G1 (red solid), G2 (green dashed), and G3 (blue dotted). From top left and clockwise: the local far-UV field (G_0) (and CR ionization rate since $\zeta_{\text{CR}} \propto G_0$), GMC mass (m_{GMC}), metallicity (Z') and external pressure (P_{ext}). Black vertical lines indicate the G_0 , m_{GMC} , Z' , P_{ext} -values for which $T_k - n_{\text{H}_2}$ curves were calculated (see Figure A.4) – a total of 630 GMCs which make up our grid GMC models. Each GMC in the galaxies is assigned the $T_k - n_{\text{H}_2}$ curve of the GMC model at the closest grid point.

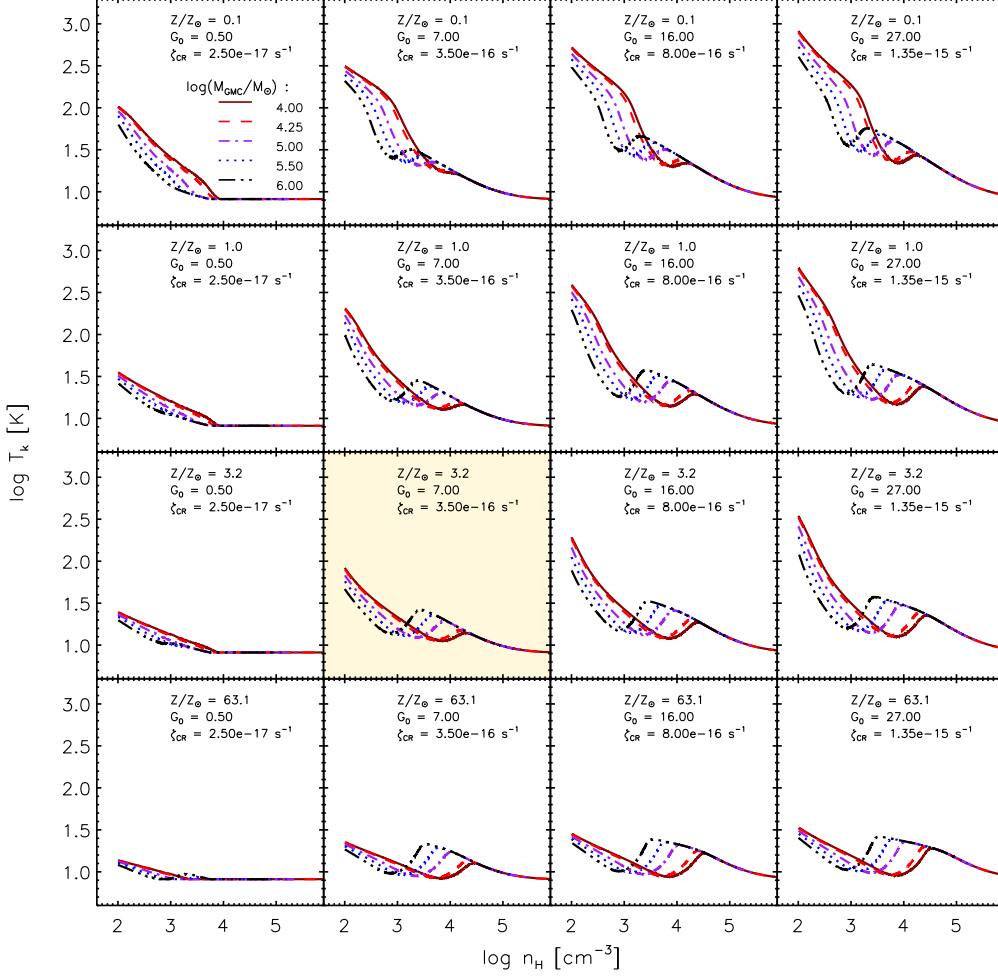


Figure A.4 Kinetic temperature versus H_2 density curves for 80 out of the 630 grid model GMCs that span the full $(G_0, M_{\text{GMC}}, Z')$ parameter space set by and marked on top of the distributions in Figure A.3 (see also Section 4.3.4) for a pressure of $P_{\text{ext}} = 10^4 \text{ K cm}^{-3}$. The grid model most often assigned to GMCs in G1 is indicated by the red dashed curve in the highlighted panel and corresponds to $G_0 = 7.0$ ($\zeta_{\text{CR}} = 3.5 \times 10^{-16} \text{ s}^{-1}$), $\log m_{\text{GMC}}/M_{\odot} = 4.25$, and $Z' = 3.2$. In general, higher metallicity (from top to bottom) leads to more cooling via emission lines of ions, atoms and molecules, and hence lower temperatures. On the other hand, higher UV and CR fields (from left to right) cause more heating and therefore higher T_k . The decreasing trend of T_k with higher values of n_{H_2} is mainly caused by the gradual attenuation of the UV field as one moves into the cloud. The ‘bump’ at $n_{H_2} \sim 10^3 - 10^4 \text{ cm}^{-3}$ corresponds to the transition from CII line cooling to the less efficient CO line cooling at higher densities. At densities above $n_{H_2} = 10^4 \text{ cm}^{-3}$, gas-dust interactions set in and eventually cools the gas down to the CMB temperature in all GMC cores.

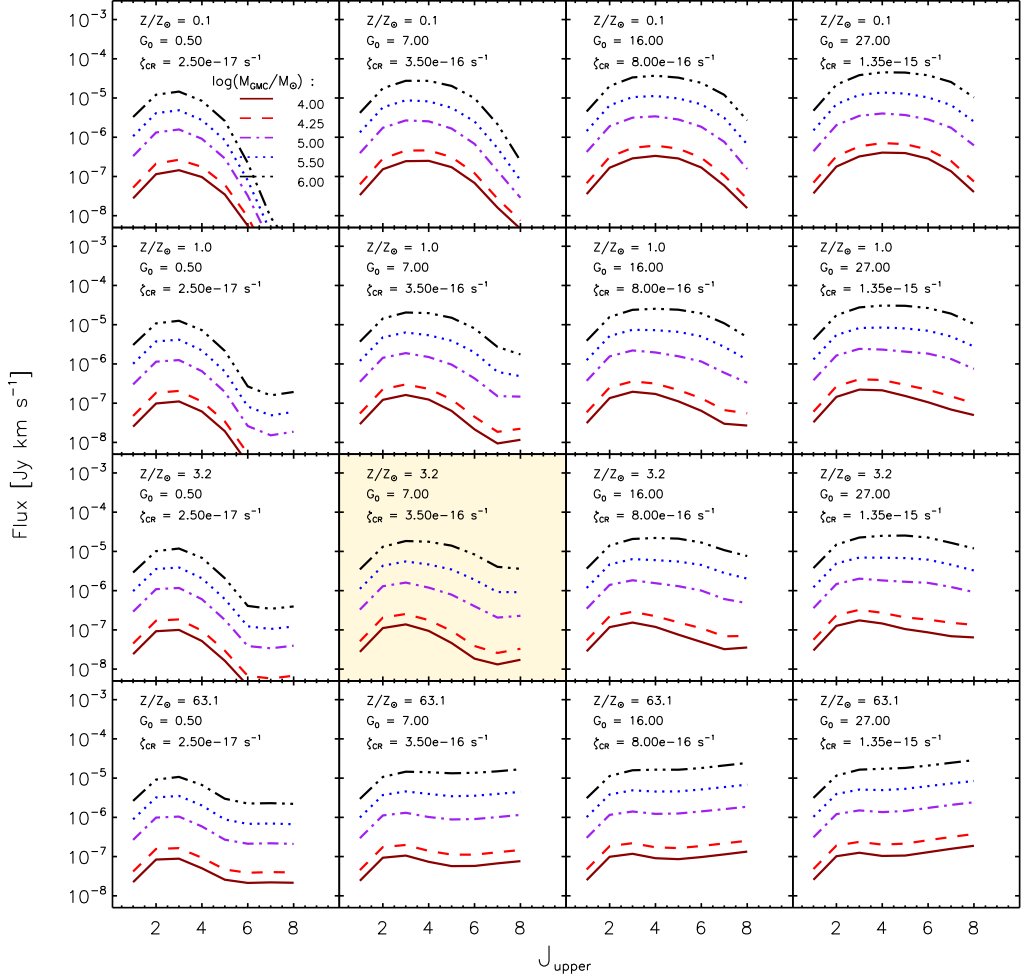


Figure A.5 CO SLEDs obtained with LIME for the 80 model GMCs whose $T_k - n_{\text{H}_2}$ curves are shown in Figure A.4. The CO SLED used most often in G1 is shown as the red dashed curve in the highlighted panel. These CO SLEDs were made for a fixed external pressure of $P_{\text{ext}}/k_B = 10^4 \text{ cm}^{-3} \text{ K}$ and a default Plummer density profile.

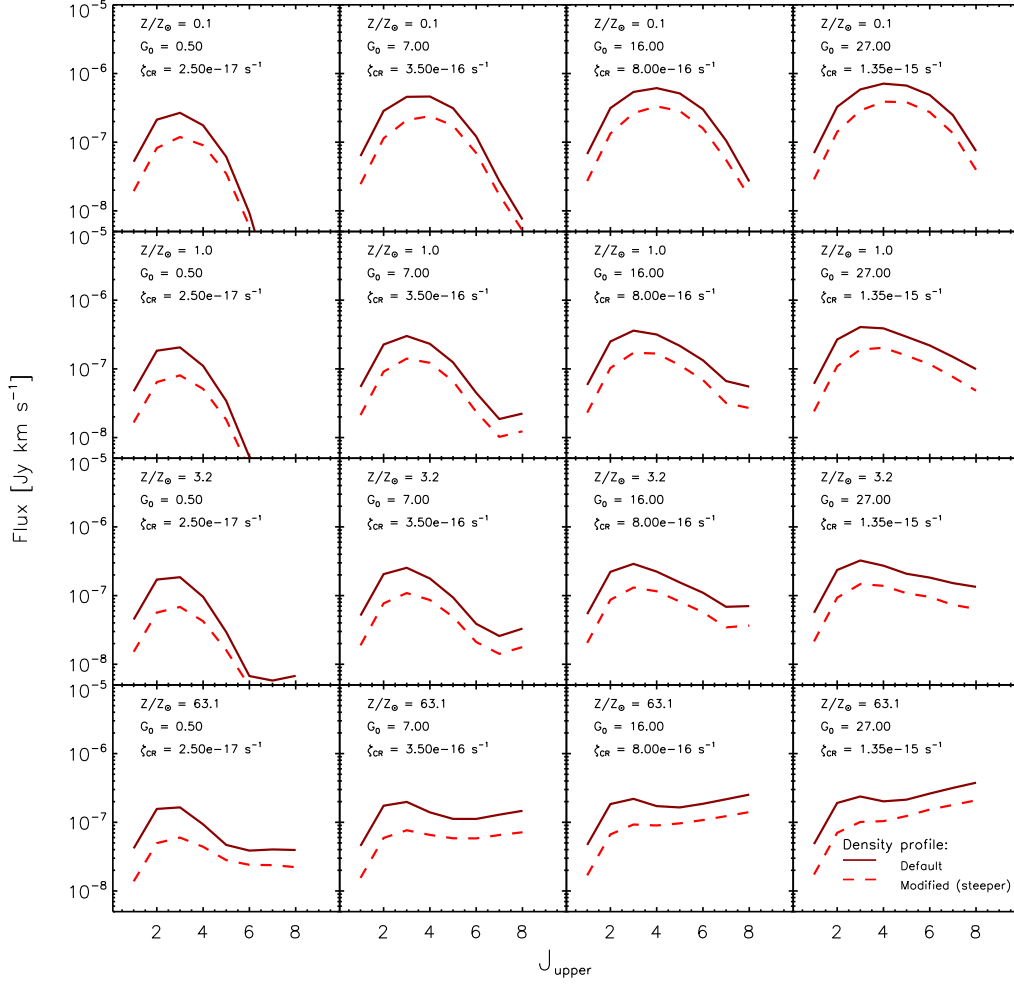


Figure A.6 CO SLEDs obtained with LIME for the same $[G_0, Z']$ values as shown in the panels of Figure A.5 for Plummer density profiles with power-law index $-5/2$ (solid curve) and $-7/2$ (dashed curve). In all panels, the external pressure has been fixed to $P_{\text{ext}}/k_B = 10^4 \text{ cm}^{-3} \text{ K}$ and the GMC mass to $m_{\text{GMC}} = 10^{4.25} M_{\odot}$.

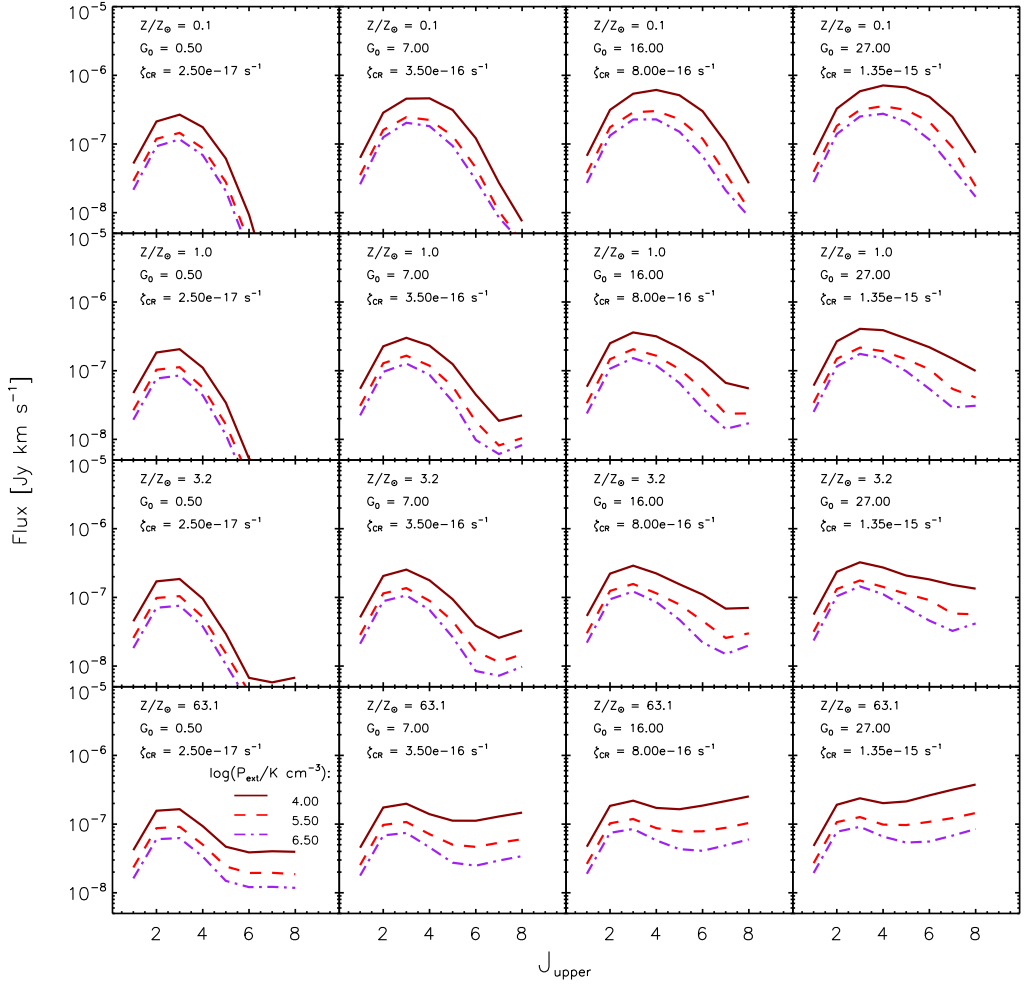


Figure A.7 CO SLEDs obtained with `LIME` for the same $[G_0, Z']$ values as shown in the panels of Figure A.5 for $P_{\text{ext}}/k_B = 10^4 \text{ cm}^{-3} \text{ K}$ (solid curves), $10^{5.5} \text{ cm}^{-3} \text{ K}$ (dashed curves), and $10^{6.5} \text{ cm}^{-3} \text{ K}$ (dot-dashed curves). In all panels, the GMC mass is fixed to $10^{4.25} M_\odot$. Higher pressure environments are seen to lead to a decrease in luminosity for all transitions.

A.4 TESTING SÍGAME ON MW-LIKE GALAXIES

As a benchmark test, SÍGAME was applied to galaxy simulations at $z = 0$ with properties similar to those of the MW. The reasoning here was that since much of the sub-grid physics adopted by SÍGAME relies on empirical relations observed in the MW (e.g., the GMC mass spectrum index), the method ought to come close to re-producing the observed CO properties of spiral galaxies, such as our MW, in the local universe.

The three galaxies (hereafter denoted MW1, MW2, and MW3 in order of increasing SFR) were selected from a more recent version of the SPH simulation described in Section 4.2. The properties of MW1, MW2, and MW3 are listed in Table A.1 and are seen to be within a factor $\sim 2 - 6$ of the stellar mass ($M_{*,\text{MW}} = 6 \times 10^{10} M_{\odot}$; McMillan, 2011) and SFR ($1.9 \pm 0.4 M_{\odot} \text{ yr}^{-1}$; Chomiuk & Povich, 2011) of the MW.

The steps outlined in Section 4.3.1 (and further described in Sections 4.3.2 to 4.3.4) were followed, but with two minor modifications: 1) the CMB temperature at $z = 0$ was set to 2.725 K rather than 8.175 K used at $z = 2$, and 2) the resolved FUV fields of our MW-like model galaxies span a range below that seen in our $z = 2$ model galaxies (cf. Figure A.3) meaning that the G_0 parameter values for our GMC grid had to be adjusted correspondingly. The following G_0 grid points were chosen: [0.05, 0.1, 0.15, 0.1, 0.2, 0.4, 0.6, 0.8, 1.0, 1.2] Habing.

In Figure A.8 we compare the resulting CO SLEDs with that of the MW from Fixsen et al. (1999), as well as with those of M51 ($M_* = 4.7 \times 10^{10} M_{\odot}$; Mentuch Cooper et al. (2012), SFR = $2.6 M_{\odot} \text{ yr}^{-1}$; Schuster et al. 2007) from Vlahakis et al. (2013), Hughes et al. (2013) and Kamenetzky et al. (2015), M83 ($M_* = 7.9 \times 10^{10} M_{\odot}$ and SFR = $3.2 M_{\odot} \text{ yr}^{-1}$; Jarrett et al. 2013) from Wu et al. (2015) and other local galaxies of IR luminosity within 20% of that of the MW ($1.8 \times 10^{10} L_{\odot}$; Wright et al. 1991) from Kamenetzky et al. (2015). M51 is a nearby galaxy slightly smaller in size and stellar mass than the MW, whereas M83 is more massive and star-forming than the MW. The dispersion in observed CO SLEDs among the MW, M83, M51 and other local galaxies, allows for a large range in normalization and shape of the CO SLED within which our model galaxies find themselves.

The CO line luminosities of the MW lie roughly in the range spanned by the CO SLEDs of MW2 and MW3 up to and including $J_{\text{up}} = 4$, but significantly above that of MW1. For the higher J transitions the line luminosities of our simulations drop off more rapidly than the MW, meaning that our model galaxies have lower luminosities compared to the MW (and other local galaxies of IR luminosities within 20% from that of the MW; long-dashed orange lines) at $J_{\text{up}} > 4$. This suggests that our simulations are missing a warm/dense component which is required to significantly excite these high- J lines. The agreement between the CO SLED of MW2 and that of M51 is good at low transitions ($J_{\text{up}} < 6$), which is encouraging given that the two galaxies have nearly identical SFR and M_* . At higher J values, the CO SLED of M51 has an excess of CO emission when compared with MW2, corresponding to a warm gas phase not captured by our models. This warm phase is more pronounced in signature when looking at the CO SLED of M83, the line ratios of which are above our model galaxies for all $J_{\text{up}} > 2$. Our models MW1, MW2 and MW3 only agree in CO luminosity with M51 at the $J_{\text{up}} = 4$ and 5 transitions.

As for brightness temperature ratios (see middle panel) of our simulated MW-like galaxies only agree with the MW within the observational errors at CO(4–3), and other wise display a CO SLED shape noticeably different from the MW. Where our model galaxies peak at the CO(3–2) transition in velocity-integrated intensity (see bottom panel), similar to M51, the MW

Table A.1 Properties of the three $z = 0$ MW-like galaxies (MW1, MW2, and MW3) used to benchmark SIGAME .

	SFR [$\text{M}_\odot \text{ yr}^{-1}$]	M_* [10^{10} M_\odot]	M_{SPH} [10^{10} M_\odot]	f_{SPH}	Z'	R_{cut} [kpc]
MW1	2.2	0.97	1.17	55%	2.07	20
MW2	4.1	3.12	1.27	29%	3.31	20
MW3	6.2	3.83	1.69	31%	3.90	20

Notes. All quantities are determined within a radius R_{cut} , which is the radius where the cumulative radial stellar mass function of each galaxy becomes flat. The gas mass (M_{SPH}) is the total SPH gas mass within R_{cut} . The metallicity ($Z' = Z/Z_\odot$) is the mean of all SPH gas particles within R_{cut} .

and M83 peak at CO(4–3). However, nowhere do the simulated line ratios differ by more than a factor of 2.

The molecular gas masses of MW1, MW2 and MW3 are 4.6, 5.4 and $8.5 \times 10^9 \text{ M}_\odot$, respectively, significantly above $(1.0 \pm 0.3) \times 10^9 \text{ M}_\odot$ for the MW (Heyer & Dame, 2015). The corresponding global ($R < 20 \text{ kpc}$) α_{CO} factors are 13.6, 7.7 and $7.0 \text{ M}_\odot \text{ pc}^{-2} (\text{K km s}^{-1})^{-1}$. For the inner disk ($R < 10 \text{ kpc}$) of the MW, $\alpha_{\text{CO,MW}} \simeq 4.3 \pm 0.1 \text{ M}_\odot \text{ pc}^{-2} (\text{K km s}^{-1})^{-1}$ (e.g., Strong & Mattox, 1996; Dame et al., 2001; Pineda et al., 2008; Bolatto et al., 2013). However, typically the measurements of α_{CO} in the MW do not probe the central ($< 1 \text{ kpc}$) region. Excluding the central $R < 1 \text{ kpc}$ region and going out to $R = 10 \text{ kpc}$, the α_{CO} factors of MW1, MW2 and MW3 are 11.6, 6.9 and $6.2 \text{ M}_\odot \text{ pc}^{-2} (\text{K km s}^{-1})^{-1}$, i.e. factors of 2.7, 1.6 and 1.4 above $\alpha_{\text{CO,MW}}$, respectively.

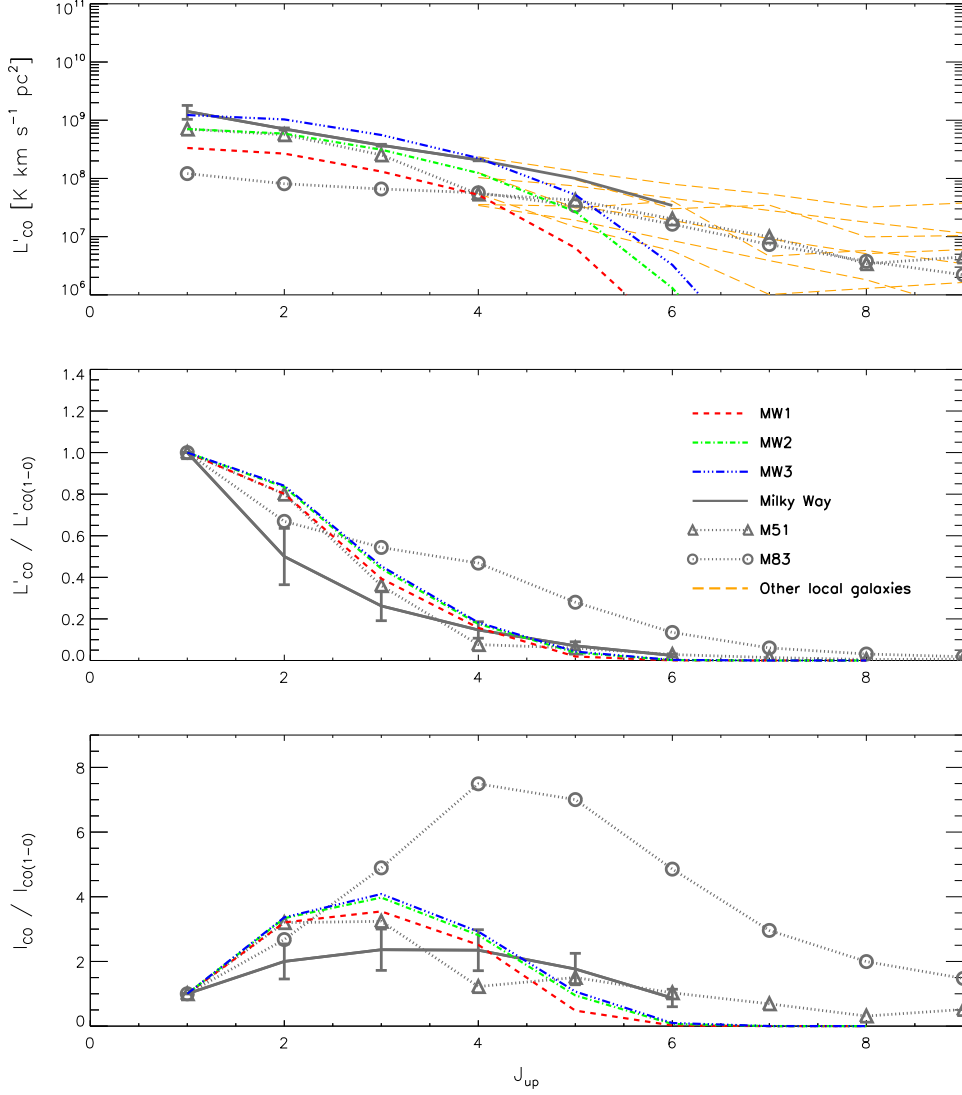


Figure A.8 Global CO SLEDs of our three model galaxies MW1, MW2 and MW3 shown as red (dashed), green (dash-dot) and blue (dash-dot-dot-dot) curves, respectively, selected to represent the MW in terms of stellar mass and SFR. The SLEDs are given as absolute line luminosities in units of $\text{K km s}^{-1} \text{pc}^2$ (top panel), as brightness temperature ratios normalised to the CO(1–0) transition (middle panel), and as velocity-integrated intensity ratios normalised to CO(1–0) (bottom panel). The observed global CO SLED of the MW is shown in grey (Fixsen et al., 1999), and global CO measurements of the local star-forming galaxy M51 are displayed with triangles. The CO observations for M51 are from Vlahakis et al. (2013) and Hughes et al. (2013). Also shown, with long-dashed orange lines, are observed CO SLEDs of local galaxies with IR luminosities within 20% of that of the MW (Kamenetzky et al., 2015).

B

APPENDIX TO CHAPTER 6

B.1 DENSITY OF SINGLY IONIZED CARBON

The strength of the [CII] emission from any gas phase depends on the fraction of total carbon atoms that are singly ionized, f_{CII} . For calculating f_{CII} , we chose to employ the microphysics code CLOUDY v13.03, that simultaneously solves the equations for statistical and thermal equilibrium for a wide range of optional elements. We set up CLOUDY to work on a small parcel of gas with a single temperature and a constant density across its volume. The incident radiation field on the gas parcel is set to the local interstellar radiation field, as provided by CLOUDY, but scaled by a factor (in practice, our G_0). In addition, a cosmic ray ionization rate can be specified in units of s^{-1} .

As a test to judge whether we are using CLOUDY correctly, the fraction of CIV, f_{CIV} , as a function of density and temperature was compared to the work of Oppenheimer & Schaye (2013) by reproducing their CIV fractions at $z = 1$ for a Haardt & Madau (2001) background radiation field. This comparison is shown in Fig. B.1 with plots of the CIV abundance (rela-

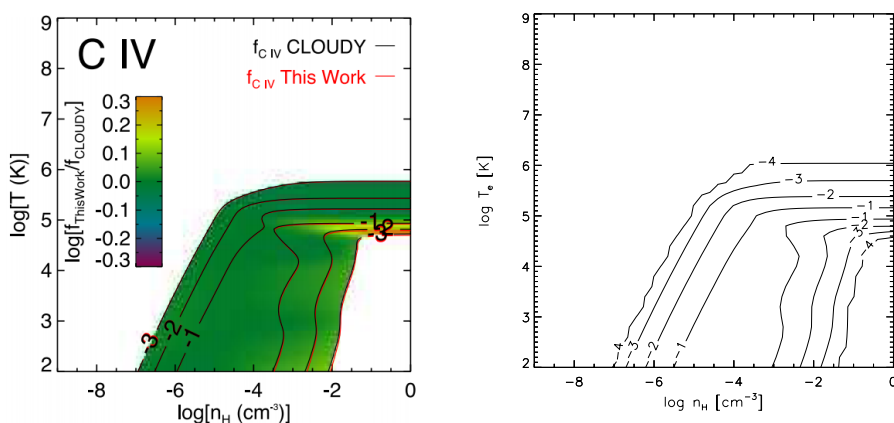


Figure B.1 A comparison of f_{CIV} as calculated by Oppenheimer & Schaye (2013) using CLOUDY v10.00 (left) and by SÍGAME using CLOUDY v13.03 (right). In both cases a Haardt & Madau 2005 background radiation field (embedded in CLOUDY) at $z = 1$ was used together with solar abundances. A good agreement is seen, in particular with decreasing f_{CIV} towards high densities and low temperatures, where carbon exists in lower ionizational states such as CII, see Fig. B.2 below.

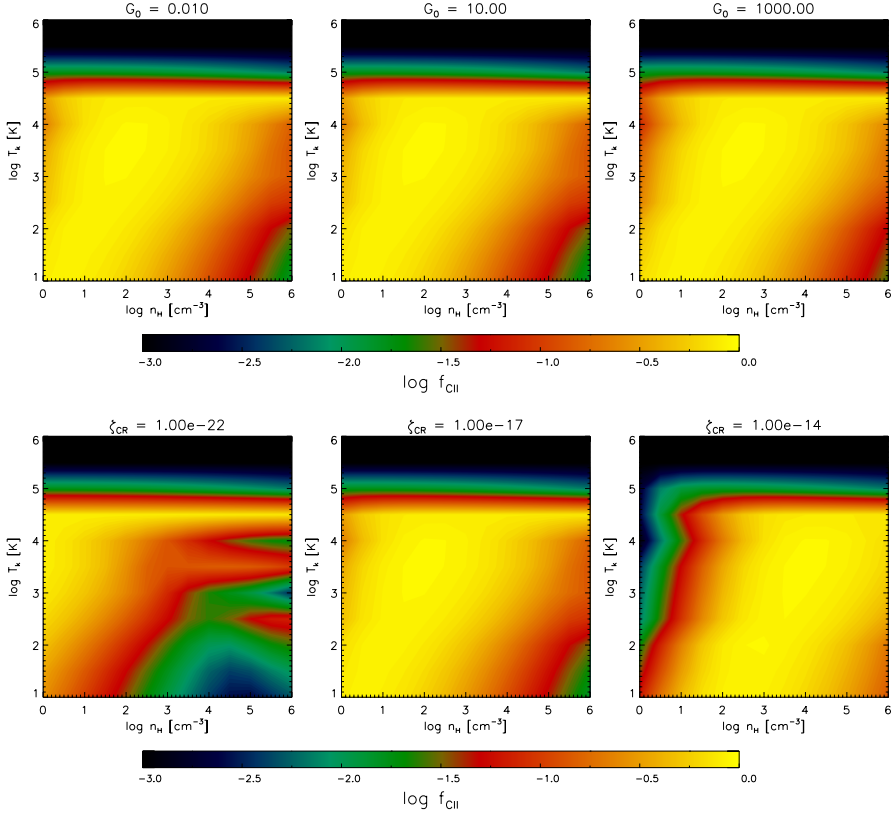


Figure B.2 Maps of f_{CII} as function of gas temperature and hydrogen density made with `CLOUDY` v13.03 as part of the grid used in `SÍGAME` to derive x_e and f_{CII} in the ISM. *Top row:* For three values of G_0 (and ζ_{CR} fixed at 10^{-17} s^{-1}). *Bottom row:* For three values of ζ_{CR} (with G_0 fixed to 1 Habing). Note how f_{CII} drops at $T_k \gtrsim 10^5 \text{ K}$ in all cases, and depends on ζ_{CR} while being largely insensitive to changes in G_0 .

tive to the total number of carbon atoms) as a function of hydrogen density and kinetic gas temperature. A good agreement with the figure of Oppenheimer & Schaye (2013) is achieved when using the build-in Haardt & Madau 2005 background of `CLOUDY` (`‘HM05’` command in `CLOUDY`, including galaxies and quasars but not the CMB) at $z = 1$ together with default solar abundances.

In order to keep the computing time of `SÍGAME` low, we set up a grid in $[n_{\text{H}}, T_k, \zeta_{\text{CR}}, G_0]$ and calculated f_{CII} with `CLOUDY` for each grid point. Though metallicity and element abundances (of C, O, Si and Fe) are followed in our simulated galaxies, we chose the default solar composition that comes with `CLOUDY` for the sake of having fewer parameters in the grid. Visualizations of this grid are shown in Fig. B.2 for three values of G_0 (and ζ_{CR} fixed at 10^{-17} s^{-1} , close to the adopted $\zeta_{\text{CR,MW}} = 10^{-17} \text{ s}^{-1}$) in the top row and three values of ζ_{CR} (with G_0 fixed to 1 Habing, close to $G_{0,\text{MW}} = 0.6 \text{ Habing}$) in the bottom row. As can be seen, f_{CII} does not seem to depend at all on G_0 , but much more on the intensity of cosmic rays.

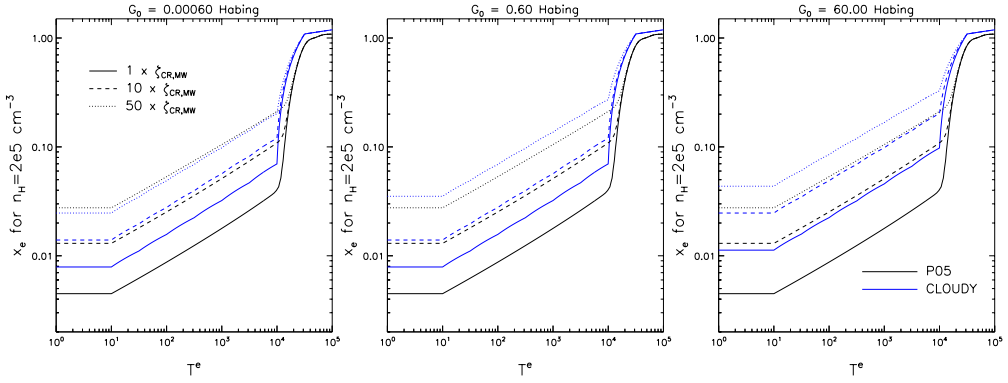


Figure B.3 A comparison of `CLOUDY` and the method described in Pelupessy (2005) for deriving x_e as a function of electron temperature, T_e , at a density of $n_H = 2 \times 10^5 \text{ cm}^{-3}$. The two methods agree about the shape of increasing x_e with T_e , including the sharp rise at $T_k \sim 10^4 \text{ K}$ due to Balmer lines. The P05 method does not include ionization by the FUV radiation field, meaning that it takes the same shape in each panel. Note that x_e rises above 1 due to the inclusion of other elements than hydrogen, that can contribute to the electron number.

B.2 ELECTRON FRACTION

In order to be consistent with the calculation of f_{CII} , we also decided to calculate the electron fraction, x_e , with `CLOUDY` v13.03 rather than the method of Pelupessy (2005) (P05) used in the previous Chapter 4. Fig. B.3 shows how `CLOUDY` and the P05 method compare as a function of electron temperature at a density of $n_H = 2 \times 10^5 \text{ cm}^{-3}$, for different combinations of interstellar radiation field (G_0) and cosmic ray ionization rate (ζ_{CR}). The P05 method is aimed for application in the interior of GMCs and therefore only considers ionization by cosmic rays that are expected to dominate the ionization of hydrogen, whereas `CLOUDY` takes G_0 and ζ_{CR} as separate variables.

Furthermore, P05 method does not depend on density, whereas the calculation with `CLOUDY` does. Fig. B.4 gives the same comparison as the previous figure, but for a lower density of $n_H = 100 \text{ cm}^{-3}$, where `CLOUDY` derives much larger electron fractions than the P05 model. This is expected, since at low densities, the gas is less shielded from the incident radiation field. We therefore consider the inclusion of the `CLOUDY`, with its sensitivity towards G_0 and n_H , an improvement of `SÍGAME` with respect to the electron fraction.

B.3 [CII] EXCITATION AND EMISSION

The cooling and heating mechanisms relevant for the generation of [CII] emission are the same as those employed in Chapter 3 and described in Appendix A.1-A.2, but we summarize them in Table B.1.

For a two-level system such as [CII] embedded in a radiation field with energy density U at the transition frequency, the general rate equation governing the population levels can be written as:

$$\frac{n_u}{n_l} = \frac{B_{lu}U + C_{lu}}{A_{ul} + B_{ul}U + C_{ul}} = \frac{gB_{ul}U + gKC_{ul}}{A_{ul} + B_{ul}U + C_{ul}}, \quad (\text{B.1})$$

where A_{ul} ($= 2.3 \times 10^{-6} \text{ s}^{-1}$) is the spontaneous emission rate, and B_{ul} and B_{lu} are the stimu-

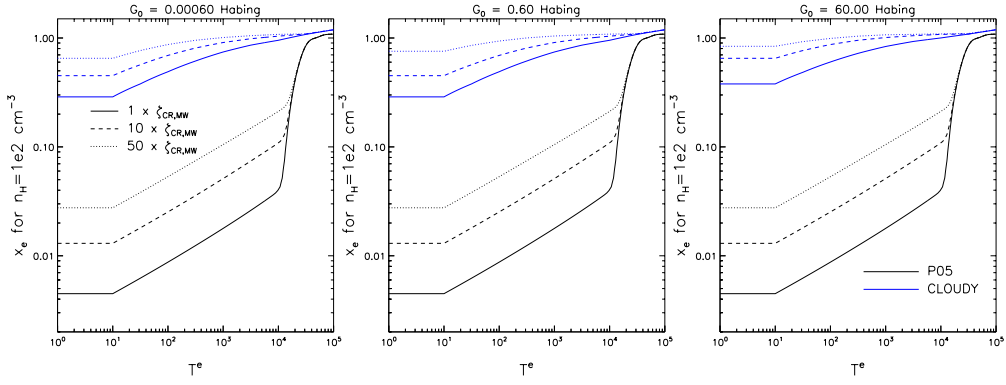


Figure B.4 Same as Fig. B.3, but for a density of $n_H = 100 \text{ cm}^{-3}$.

Table B.1 Provides a summary of the various heating and cooling mechanisms adopted in the molecular and atomic gas regions of our GMC models, along with the physical quantities on which they depend.

Cooling and Heating Rates in GMC Models			
Process		Parameters	Reference
Γ_{PE}	Photo-electric heating	G_0, T_k, n_e, n_H	Bakes & Tielens (1994)
$\Gamma_{\text{CR,HI}}$	Cosmic ray heating in atomic gas	$\zeta_{\text{CR}}, n_{\text{HI}}, x_e$	Draine (2011)
$\Gamma_{\text{CR,H}_2}$	Cosmic ray heating in molecular gas	$\zeta_{\text{CR}}, n_{\text{H}_2}$	Stahler & Palla (2005)
Λ_{H_2}	H2 line cooling	n_{H_2}, T_k	Papadopoulos et al. (2014)
Λ_{OI}	OI line cooling	n_H, T_k	Röllig et al. (2006)
Λ_{CII}	[CII] line cooling in ionized gas	$G_0, T_k, n_H, X_C, \sigma_v$	Goldsmith et al. (2012)

Note. The most important references are given, and we also refer to Olsen et al. (2015) for a detailed description.

lated emission and absorption rate coefficients, respectively (Goldsmith et al., 2012). Here we have invoked detailed balance, i.e. $B_{lu}U = gB_{ul}U$ and $C_{lu} = gKC_{ul}$, where $g (= g_u/g_l)$ is the ratio of the statistical weights and $K = e^{-h\nu/k_B T_k} = e^{-91.25 \text{ K}/T_k}$. We can then write the fraction of C^+ in the upper level, f_u , as:

$$\begin{aligned}
 f_u &= \frac{n_u}{n_l + n_u} = \frac{1}{\frac{n_l}{n_u} + 1} \\
 &= \frac{gB_{ul}U + gKC_{ul}}{A_{ul} + (1 + g)B_{ul}U + C_{ul} + gKC_{ul}} \\
 &= \frac{gK + gB_{ul}U/C_{ul}}{1 + gK + A_{ul}/C_{ul} + (1 + g)B_{ul}U/C_{ul}}.
 \end{aligned} \tag{B.2}$$

In general, $U = (1 - \beta)U(T_{\text{ex}}) + \beta U(T_{\text{bg}})$, where $U(T_{\text{bg}})$ is the energy density from a background field (e.g. CMB or radiation from dust), and β is the escape probability fraction at the [CII] frequency (see also Goldsmith et al., 2012). We shall ignore any background, however, in which

case we can write the stimulated downward rate as:

$$B_{ul}U = \frac{(1 - \beta)A_{ul}}{e^{-91.25 \text{ K}/T_{\text{ex}}} - 1}, \quad (\text{B.3})$$

and the excitation temperature as:

$$e^{-91.25 \text{ K}/T^{\text{ex}}} = K \left(1 + \frac{\beta A_{ul}}{C_{ul}} \right), \quad (\text{B.4})$$

see Goldsmith et al. (2012). For the escape probability we assume a spherical geometry with a radial velocity gradient proportional to radius, such that $\beta = (1 - \exp(-\tau))/\tau$. In calculating the integral in eq. 6.18 we split the integral up into 100 radial bins of thickness ΔR (see Section 6.5), and we approximate the optical depth in each such bin with that of a homogeneous static slab of gas of thickness ΔR (Draine, 2011):

$$\tau = \frac{g_u}{g_l} \frac{A_{ul}c^3}{4(2\pi)^{3/2}\nu^3\sigma_v} n_l \Delta R \left(1 - \frac{n_u g_l}{n_l g_u} \right), \quad (\text{B.5})$$

where σ_v is the gas velocity dispersion, which is calculated according to eq. 6.5 for the PDR and molecular gas regions in the GMCs, and is set to the local velocity dispersion in the SPH simulation in the case of the ionized clouds. We use eqs. B.2, B.3, B.4, and B.5 to iteratively solve for consistent values of f_u and β in each ΔR bin. This is done by first assuming optically thin emission ($\beta = 1$) in order to get an initial estimate of f_u (eq. B.2), which is subsequently used to calculate τ and β (eq. B.5) and from that T_{ex} and $B_{ul}U$ (eqs. B.4 and B.3), etc. Once consistent values for f_u and τ have been reached, we calculate the total cooling rate according to eq. 6.19. This cooling rate is used to determine the thermal balance at various points within the GMCs as well as the [CII] emission from the ionized clouds as described in Section 6.5. We emphasize that our methods assumes that the [CII] emission from the different ΔR bins within a cloud is radiatively de-coupled, and that the total [CII] emission from a cloud is therefore the sum of the emission from each bin.

As explained in Section 6.5 [CII] is collisionally (de)excited by H_2 in the molecular phase, by e^- and HI in the PDR region, and by e^- in the ionized gas. For a single collision partner the collision rates are equal to the density (n) of the collision partner times the rate coefficients, i.e., $C_{ul} = nR_{ul}$ and $C_{lu} = nR_{lu}$. In case of two collision partners we have $C_{ul} = n_1R_{ul,1} + n_2R_{ul,2}$ and $C_{lu} = n_1R_{lu,1} + n_2R_{lu,2}$. Fig. B.5 shows the [CII] deexcitation rate coefficients that we have adopted in our work for collisions with e^- , HI , and H_2 as a function of temperature. For collisions with electrons, we adopt the following expression for the deexcitation rate coefficient as a function of electron temperature (T_e):

$$R_{ul}(e^-) = 8.7 \times 10^{-8} (T_e/2000 \text{ K})^{-0.37} \text{ cm}^3 \text{ s}^{-1}, \quad (\text{B.6})$$

which is applicable for temperatures from $\simeq 100 \text{ K}$ to $20,000 \text{ K}$ (Goldsmith et al., 2012). At temperatures $> 20,000 \text{ K}$ we set $R_{ul}(e^-) \sim T_e^{-0.85}$ (Wilson & Bell, 2002; Langer et al., 2015). For the PDR gas, the electron density is calculated using CLOUDY and the electron temperature is set to the kinetic temperature of the gas (calculated according to eq. 6.16). For the ionized gas we assume $n_e = n_{\text{HI}}$, i.e., $x_e = 1$, and the electron temperature gas is set to the SPH gas kinetic temperature (see Section 6.4.2). For the deexcitation rate coefficient for collisions with HI we

use the analytical expression provided by Barinovs et al. (2005) and shown as the dotted curve in Fig. B.5:

$$R_{ul}(\text{HI}) = 7.938 \times 10^{11} \exp(-91.2/T_k) \left(16 + 0.344\sqrt{T_k} - 47.7/T_k \right) \text{ cm}^3 \text{ s}^{-1}. \quad (\text{B.7})$$

While Barinovs et al. (2005) cites an application range for the above expression of $15 \text{ K} < T_k < 2000 \text{ K}$, a comparison with $R_{ul}(\text{HI})$ -values found by Keenan et al. (1986) over the temperature range $10 \text{ K} < T_k < 100,000 \text{ K}$ shows that eq. B.7 provides an excellent match over this larger temperature range (Fig. B.5). For collisions with H_2 we follow Goldsmith et al. (2012) and assume that the collision rate coefficients are approximately half those for collisions with H over the relevant temperature range for the molecular gas, i.e. $R_{ul}(\text{H}_2) = 0.5 \times R_{ul}(\text{H})$.

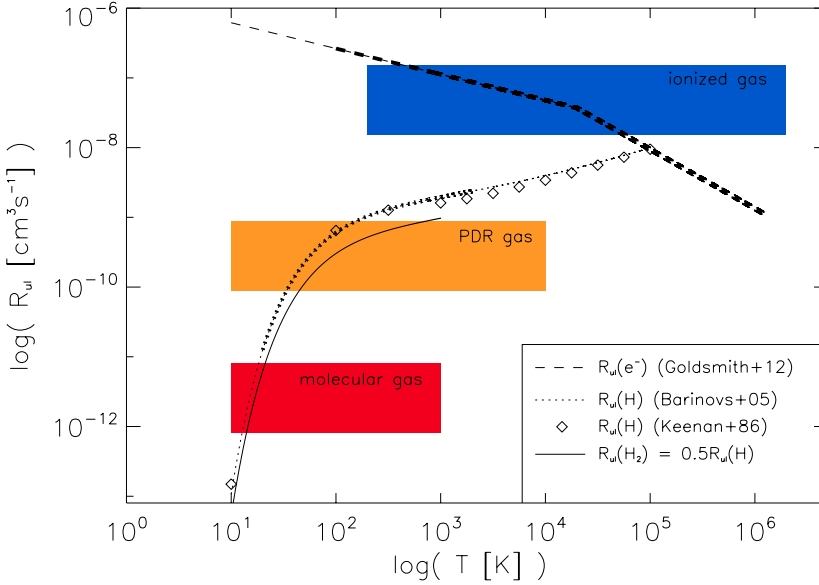


Figure B.5 [CII] deexcitation coefficients (R_{ul}) as a function of temperature for collisions with e^- (dashed line), H I (dotted line), and H_2 (solid line and diamonds). The curves are thicker over the temperature ranges where they are formally applicable. The blue, orange, and red rectangles indicate the temperature range encountered in the ionized, atomic, and molecular phase in our simulated galaxies, respectively (see sections 6.4.1 and 6.4.2).

B.4 REFERENCES

- Bakes, E. L. O., & Tielens, A. G. G. M. 1994, *ApJ*, 427, 822
- Barinova, Ğ., van Hemert, M. C., Krems, R., & Dalgarno, A. 2005, *ApJ*, 620, 537
- Bolatto, A. D., Wolfire, M., & Leroy, A. K. 2013, *ARA&A*, 51, 207
- Chomiuk, L., & Povich, M. S. 2011, *AJ*, 142, 197
- Dame, T. M., Hartmann, D., & Thaddeus, P. 2001, *ApJ*, 547, 792
- Draine, B. T. 2011, *Physics of the Interstellar and Intergalactic Medium* (Princeton University Press)
- Fixsen, D. J., Bennett, C. L., & Mather, J. C. 1999, *ApJ*, 526, 207
- Goldsmith, P. F., Langer, W. D., Pineda, J. L., & Velusamy, T. 2012, *ApJS*, 203, 13
- Haardt, F., & Madau, P. 2001, in *Clusters of Galaxies and the High Redshift Universe Observed in X-rays*, ed. D. M. Neumann & J. T. V. Tran
- Heyer, M., & Dame, T. M. 2015, *ARA&A*, 53, 583
- Hughes, A., Meidt, S. E., Schinnerer, E., et al. 2013, *ApJ*, 779, 44
- Jarrett, T. H., Masci, F., Tsai, C. W., et al. 2013, *AJ*, 145, 6
- Kamenetzky, J., Rangwala, N., Glenn, J., Maloney, P. R., & Conley, A. 2015, *ArXiv e-prints*
- Keenan, F. P., Lennon, D. J., Johnson, C. T., & Kingston, A. E. 1986, *MNRAS*, 220, 571
- Langer, W. D., Goldsmith, P. F., Pineda, J. L., et al. 2015, *ArXiv e-prints*
- McMillan, P. J. 2011, *MNRAS*, 414, 2446
- Mentuch Cooper, E., Wilson, C. D., Foyle, K., et al. 2012, *ApJ*, 755, 165
- Olsen, K. P., Greve, T. R., Narayanan, D., et al. 2015, *ApJ*, 814, 76
- Oppenheimer, B. D., & Schaye, J. 2013, *MNRAS*, 434, 1043
- Papadopoulos, P. P., & Thi, W.-F. 2013, in *Advances in Solid State Physics, Vol. 34, Cosmic Rays in Star-Forming Environments*, ed. D. F. Torres & O. Reimer, 41
- Papadopoulos, P. P., Thi, W.-F., Miniati, F., & Viti, S. 2011, *MNRAS*, 414, 1705
- Papadopoulos, P. P., Zhang, Z.-Y., Xilouris, E. M., et al. 2014, *ApJ*, 788, 153
- Pelupessy, F. I. 2005, PhD thesis, Leiden Observatory, Leiden University, P.O. Box 9513, 2300 RA Leiden, The Netherlands
- Pineda, J. E., Caselli, P., & Goodman, A. A. 2008, *ApJ*, 679, 481
- Puchwein, E., Bolton, J. S., Haehnelt, M. G., et al. 2015, *MNRAS*, 450, 4081
- Röllig, M., Ossenkopf, V., Jeyakumar, S., Stutzki, J., & Sternberg, A. 2006, *A&A*, 451, 917
- Schuster, K. F., Kramer, C., Hitschfeld, M., Garcia-Burillo, S., & Mookerjee, B. 2007, *A&A*, 461, 143
- Stahler, S. W., & Palla, F. 2005, *The Formation of Stars* (Wiley)
- Strong, A. W., & Mattox, J. R. 1996, *A&A*, 308, L21
- Vlahakis, C., van der Werf, P., Israel, F. P., & Tilanus, R. P. J. 2013, *MNRAS*, 433, 1837
- Wiersma, R. P. C., Schaye, J., & Smith, B. D. 2009, *MNRAS*, 393, 99
- Wilson, N. J., & Bell, K. L. 2002, *MNRAS*, 337, 1027
- Wright, E. L., Mather, J. C., Bennett, C. L., et al. 1991, *ApJ*, 381, 200
- Wu, R., Madden, S. C., Galliano, F., et al. 2015, *A&A*, 575, A88